

UNIVERSIDAD DE CHILE
FACULTAD DE CIENCIAS FÍSICAS Y MATEMÁTICAS
DEPARTAMENTO DE ASTRONOMÍA

**SISTEMAS DE ABSORCIÓN EN ESPECTROS ÓPTICOS DE
ESTALLIDOS DE RAYOS GAMMA**

**TESIS PARA OPTAR AL GRADO DE MAGÍSTER EN CIENCIAS
MENCIÓN ASTRONOMÍA**

NICOLÁS ANDRÉS TEJOS SALGADO

PROFESOR GUÍA:

SEBASTIÁN LÓPEZ MORALES

MIEMBROS DE LA COMISIÓN:

MARIO HAMUY WACKENHUT

PAULINA LIRA TEILLERY

ALAIN SMETTE

SANTIAGO DE CHILE

SEPTIEMBRE 2009

Resumen

Este trabajo de tesis consiste en el estudio de la primera estadística sobre el número de sistemas de absorción intervinientes de Mg II y C IV en líneas de visión hacia estallidos de rayos gamma (*gamma-ray bursts* - GRBs -).

Para ésto la técnica de líneas de absorción fue aplicada en espectros de postluminiscencias ópticas de GRBs. Dada la naturaleza de los GRBs es difícil obtener largos tiempos de exposición y hasta ahora muy pocos espectros han sido adquiridos, especialmente de alta resolución. Nuestros resultados estan basados en una muestra de 7 espectros de alta resolución ($R \equiv \lambda/\Delta\lambda \sim 30\,000 - 40\,000$) de GRBs con moderada a alta señal a ruido ($> 5 \text{ pix}^{-1}$) facilitados por la colaboración GRAASP (*Gamma-Ray Bursts Afterglows as Probes*). Por lo mismo el trabajo de esta tesis es pionero en este tipo de estudio.

Es importante comparar la estadística obtenida en líneas de visión hacia GRBs con las obtenidas en líneas de visión hacia objetos cuasi estelares (*quasi-stellar objects* - QSOs-) dado que la primera comparación de este tipo realizada por Prochter et al. (2006b) mostró una discrepancia significativa entre ambas: un factor ~ 4 más sistemas intervinientes de Mg II fuertes ($W_r > 1.0 \text{ \AA}$) en espectros de GRBs comparado con los encontrados en espectros de QSOs. En este trabajo se recupera el resultado encontrado por Prochter et al. (2006b). Además se obtiene la primera comparación en sistemas de Mg II y C IV a menores anchos equivalentes no encontrándose discrepancias significativas para estos casos.

Los posibles escenarios que han sido propuestos para explicar la discrepancia de Mg II fuertes son discutidos agregando el punto de vista de los resultados de esta tesis, así como otros recientes resultados relevantes de la literatura. Finalmente se argumenta que un sesgo por efecto de lente gravitacional es el escenario que mejor se ajusta a nuestros resultados.

Agradecimientos

Agradezco en primer lugar a mi Familia, en especial a mis padres, Pedro y Loreto. Su apoyo incondicional ha sido el pilar fundamental en mi formación como persona. Sin su constante respaldo, ni la realización de este trabajo ni el desarrollo de mi vocación científica hubiesen sido posibles.

Quiero agradecer a la Universidad de Chile y su Departamento de Astronomía por haberme dado la oportunidad de comenzar a estudiar esta motivante carrera de investigación. A mi profesor guía, Sebastián López, por sus enseñanzas y críticas constructivas, por sus excelentes consejos, y sobre todo, por la confianza depositada en mi. También agradezco a los miembros de la comisión evaluadora, por su buena disposición y por su notable contribución al enriquecimiento de este trabajo.

Un muy especial agradecimiento a mi polola Macarena, por encontrar en ella a una excelente persona y pareja. Toda su entrega y cariño, así como su ejemplo de constante dedicación y comprensión, han sido fundamentales para llegar hasta esta instancia.

A mis amigos y compañeros, por todos los buenos momentos de relax y diversión compartidos, muy necesarios para mantener la mente sana.

Finalmente agradezco a Eugenio Candia, quien me ayudó a reencontrarme y reencantarme con la matemática, en un momento crucial de mi formación vocacional. Siempre recordaré su enseñanza como un hito importante en el camino que estoy recorriendo.

"De nada vale la ciencia si no se convierte en conciencia", Carlo Dossi

Table of Contents

Table of Contents	v
List of Figures	x
List of Tables	xvii
1 Introduction	1
1.1 The IGM through QSO Lines of Sight	1
1.2 Line Formation	3
1.3 Line Characterization	4
1.3.1 Voigt Profile	4
1.3.2 Equivalent Width	4
1.3.3 Column Density	5
1.3.4 Doppler Parameter	6
1.3.5 Curve of Growth	6
1.4 Classification of Absorbers	7

1.4.1	Damped Lyman- α Absorbers (DLAS)	8
1.4.2	Sub DLAS	8
1.4.3	Lyman Limit Systems (LLS)	9
1.4.4	Lyman- α Forest Systems	9
1.4.5	Metal Systems	10
1.5	Introduction to Absorption Line Surveys	11
1.6	Basics of Gamma-ray Bursts	13
1.7	Absorption Lines in GRB Spectra	15
2	Data	17
2.1	Data on GRB	17
2.1.1	Mg II and C IV Spectral Samples	18
2.2	QSO Absorber Statistics	18
2.2.1	Mg II Reference Sample	19
2.2.2	C IV Reference Sample	19
3	Search of Absorption Systems toward GRB	20
3.1	Detection of Absorption Systems	20
3.1.1	Automatic Detection of Absorption Lines	20
3.2	Identification of Doublets	24
3.3	Testing the Sensitivity of the Automatic Detections with Simulations	26
3.4	Discarding False Systems	28

3.5	Measuring Equivalent Widths	30
3.6	Final List of Systems	30
3.6.1	Strict Criteria	30
3.6.2	Relaxed Criteria	31
3.6.3	Mg II Systems	31
3.6.4	C IV Systems	31
4	Definition of the Samples	36
4.1	Mg II Sample	36
4.1.1	Full Sample	36
4.1.2	Statistical Sample	37
4.2	C IV Samples	60
4.2.1	Full Sample	60
4.2.2	Statistical Sample	62
4.3	Comments on Measured Equivalent Widths	72
5	Redshift Path Density	90
5.1	Determination of W^{min} as a Function of Wavelength	91
5.2	Redshift Path as a Function of Equivalent Width	91
5.3	Redshift Path as a Function of Redshift	93
5.4	Removal of Telluric Lines Zones	93
5.5	Redshift Path for the Mg II Sample	93

5.6	Redshift Path for the C IV Sample	94
6	Redshift Number Density	101
6.1	Definition	101
6.1.1	Direct Calculation	101
6.1.2	Calculation Weighting Different Redshift Paths	102
6.2	Error Estimation	102
7	Results	105
7.1	Results on Mg II	105
7.1.1	Weak Mg II Absorption Systems	107
7.1.2	Strong Mg II Absorption Systems	108
7.1.3	Equivalent Width Distribution	110
7.1.4	Comments on the Upper Limits	111
7.2	C IV Results	111
7.2.1	Equivalent Width Distribution	112
7.3	Summary of the Results	112
8	Discussion of the Results	121
8.1	C IV versus Very Strong Mg II	121
8.1.1	C IV Systems and their Mg II Counterparts	123
8.2	Weak versus Strong Mg II	123
8.3	Dust Extinction	124

8.4	Gravitational Lensing	126
8.4.1	Macrolensing	126
8.4.2	Microlensing	127
8.5	Are the Mg II Absorbers Related to GRB?	128
8.6	Different Beam Sizes of the Sources and Partial Beam Coverage	129
8.7	Summary of the Discussion	132
8.8	Outlook	132
	References	137

List of Figures

1.1	Evolution of the different baryonic components of the Universe from $z = 3$ to $z = 0$ from the model of Cen & Ostriker (2006). (a) Volume fractions for each component and (b) mass fraction. The warm-hot intergalactic medium (WHIM) is modeled with and without galactic super wind (GSW). Simulations show that almost all baryons at present day are in the form of diffuse and ionized gas.	2
1.2	Examples of different lines profiles with the same equivalent width of $W = 0.21 \text{ \AA}$. The equivalent width interpretation is shown in dashed grey area. Copyright by Chris Churchill.	4
1.3	Schematic of the cloud and sightline geometry. The line of sight can cross the cloud anywhere and the observed column density represents the integrated density only along this particular direction. Copyright by Chris Churchill.	5
1.4	Theoretical curve of growth for the hydrogen Ly α line. Equivalent width, W , in \AA and column density, N , in cm^{-2} . Linear, flat and damping parts of the curve of growth are indicated. Figure from Bechtold (2001).	8
1.5	UVES spectrum of CTQ-418 at $z = 2.91$, showing two damped Ly α systems (DLA) discovered in the course of the Calan-Tololo DLA Survey (Lopez et al., 2001). Also, it is possible to see different absorption lines associated to H I (Ly α forest is clearly seen) and metal lines.	9
1.6	A schematic interpretation of different absorption line systems in an unified point of view. DLA and LLS correspond to sightlines passing through the galactic disc while Lyman- α clouds and metal systems arise from sightlines with larger impact parameters going through an extended halo.	10

1.7	Schematic of an absorption line survey. Left: Sources are <i>randomly</i> distributed at different redshifts. Different sightlines toward these sources having different redshift paths are represented by solid lines where the observer is in the center of the circles. Intervening absorbers represented by shaded points are <i>randomly</i> distributed between the background source and the observer. Right: It is possible to obtain an <i>average</i> sightline joining individual sightlines. In order to obtain an accurate dN/dz it is necessary to properly take into account the differences in redshift paths of each sightline. Copyright by Chris Churchill.	12
1.8	Histogram of the $W_r(2796)$ distribution from Nestor et al. (2005). The power laws fits (dashed and dotted lines) greatly overpredict the incidence of strong ($W_r(2796) > 2 \text{ \AA}$) systems, while the exponential fit (solid line) underpredicts the incidence of weak ($W_r(2796) < 0.3 \text{ \AA}$) systems. This suggests a transition in the distribution around $W_r(2796) \sim 0.3 \text{ \AA}$. This is possibly an indication of different populations of absorption systems.	13
1.9	Cumulative number of strong Mg II ($W_r(2796) > 1 \text{ \AA}$) systems along the GRB sight lines (black curve). The red curve shows the predicted number of systems adopting the incidence of Mg II systems measured along QSO sightlines using the result from Prochter et al. (2006a). The incidences observed for GRB and QSO sightlines are inconsistent. Figure from Prochter et al. (2006b).	16
3.1	Upper: Normalized synthetic high resolution spectrum ($S/N = 20$) with 4 Mg II doublets located at different redshifts with different shapes. Bottom: Associated significant level of <i>equivalent width spectrum</i> . Assuming a detection threshold of $N = 5$ the fourth line (at $\sim 4235 \text{ \AA}$) is not detected and only 3 doublets are found. Detection thresholds of $N = 5$ and $N = 1$ are shown with horizontal solid lines.	23
3.2	Upper: Normalized synthetic high resolution spectrum ($S/N = 5$) with a complex Mg II doublet. Bottom: Associated significant level of the <i>equivalent width spectrum</i> . Assuming a detection threshold of $N = 5$ the first component is detected as a single line while the second component is detected as two different lines.	25
3.3	Minimum rest-frame equivalent width detected with 100% efficiency for a given signal-to-noise ratio. Equivalent width values correspond to the second component (the weakest one) of each doublet.	29

3.4	Example of the <i>visualization</i> used to discard false doublets. In this case a Mg II doublet found on <i>GRB050820</i> spectrum is shown in velocity space centered at the given redshift. The upper two panels correspond to the original spectrum: red zone is the first component width and the noise is plotted in green. The second two bottom panels are the significance level of the associated <i>equivalent width spectrum</i> . The blue dashed line at zero velocity is used to take into account the relative separation of both lines.	32
3.5	Example of a false detected Mg II doublet in the <i>GRB050820</i> spectrum that was discarded from the <i>Doublet List</i> . It is clear that both lines appear at an unexpected separation at the given redshift and moreover, both lines exhibit different shapes. . .	33
3.6	Example of a false detected Mg II doublet in the <i>GRB050820</i> spectrum that was discarded from the <i>Doublet List</i> . It is clear that both component have different profiles.	34
3.7	Example of a false detected Mg II doublet in the <i>GRB050820</i> spectrum that was discarded from the <i>Doublet List</i> . It is clear that the secondary component was produced by a gap in the spectrum.	35
4.1	Absorption velocity profile of Mg II absorption system at $z_{abs} = 0.5645$	41
4.2	Absorption velocity profile of Mg II absorption system at $z_{abs} = 1.3807$	42
4.3	Absorption velocity profile of Mg II absorption system at $z_{abs} = 1.6027$	43
4.4	Absorption velocity profile of Mg II absorption system at $z_{abs} = 2.2992$	44
4.5	Absorption velocity profile of Mg II absorption system at $z_{abs} = 1.7732$	45
4.6	Absorption velocity profile of Mg II absorption system at $z_{abs} = 2.2538$	46
4.7	Absorption velocity profile of Mg II absorption system at $z_{abs} = 0.6915$	47
4.8	Absorption velocity profile of Mg II absorption system at $z_{abs} = 1.4300$	48
4.9	Absorption velocity profile of Mg II absorption system at $z_{abs} = 1.6204$	49
4.10	Absorption velocity profile of Mg II absorption system at $z_{abs} = 1.1073$	50

4.11	Absorption velocity profile of Mg II absorption system at $z_{abs} = 0.8274$	51
4.12	Absorption velocity profile of Mg II absorption system at $z_{abs} = 1.1891$	52
4.13	Absorption velocity profile of Mg II absorption system at $z_{abs} = 0.6026$	53
4.14	Absorption velocity profile of Mg II absorption system at $z_{abs} = 0.6559$	54
4.15	Absorption velocity profile of Mg II absorption system at $z_{abs} = 1.1072$	55
4.16	Absorption velocity profile of Mg II absorption system at $z_{abs} = 1.3222$	56
4.17	Absorption velocity profile of Mg II absorption system at $z_{abs} = 1.5106$	57
4.18	Absorption velocity profile of Mg II absorption system at $z_{abs} = 1.8021$	58
4.19	Absorption velocity profile of Mg II absorption system at $z_{abs} = 2.2784$	59
4.20	Absorption velocity profile of C IV absorption system at $z_{abs} = 3.254$. This system is a dubious one which was excluded for Statistical Sample.	63
4.21	Absorption velocity profile of C IV absorption system at $z_{abs} = 3.5136$	64
4.22	Absorption velocity profile of C IV absorption system at $z_{abs} = 2.1463$	65
4.23	Absorption velocity profile of C IV absorption system at $z_{abs} = 2.3589$. This system was excluded for Statistical Sample due to $W_r^{gauss}(1550) < 0.15 \text{ \AA}$	66
4.24	Absorption velocity profile of C IV absorption system at $z_{abs} = 1.5684$	67
4.25	Absorption velocity profile of C IV absorption system at $z_{abs} = 1.9891$	68
4.26	Absorption velocity profile of C IV absorption system at $z_{abs} = 2.0087$	69
4.27	Absorption velocity profile of C IV absorption system at $z_{abs} = 2.8905$	70
4.28	Absorption velocity profile of C IV absorption system at $z_{abs} = 2.9363$	71
4.29	Example of a bad Gaussian fit (red line).	73
4.30	Example of a regular Gaussian fit (red line).	73

4.31	Example of a bad Gaussian fit (red line).	74
4.32	Rest frame equivalent width of Mg II in the Strict Statistical Sample measured with Gaussian fit and with pixel integration. Systems with good, regular and bad Gaussian fits are shown as black points, green triangles and red squares, respectively. The dashed line is the identity function.	75
4.33	Same as Figure 4.32 but considering just the systems at $W_r(2796) < 0.35 \text{ \AA}$	76
4.34	Rest frame equivalent width of Mg II in the Relaxed Statistical Sample measured with Gaussian fit and with pixel integration. Systems with good, regular and bad Gaussian fits are shown as black points, green triangles and red squares, respectively. The dashed line is the identity function.	77
4.35	Rest frame equivalent width of C IV in the Statistical Sample measured with Gaussian fit and with pixel integration. The dashed line is the identity function.	78
4.36	Absorption velocity profile of Mg II absorption system at $z_{abs} = 0.5549$. This system is a dubious one and will be only used to obtain an upper limit value on number density.	79
4.37	Absorption velocity profile of Mg II absorption system at $z_{abs} = 1.2221$. This system is a dubious one and will be only used to obtain an upper limit value on number density.	80
4.38	Absorption velocity profile of Mg II absorption system at $z_{abs} = 2.3298$. This system is a dubious one and will be only used to obtain an upper limit value on number density.	81
4.39	Absorption velocity profile of Mg II absorption system at $z_{abs} = 0.6165$. This system is a dubious one and will be only used to obtain an upper limit value on number density.	82
4.40	Absorption velocity profile of Mg II absorption system at $z_{abs} = 0.4175$. This system is a dubious one and will be only used to obtain an upper limit value on number density.	83
4.41	Absorption velocity profile of Mg II absorption system at $z_{abs} = 0.6369$. This system is a dubious one and will be only used to obtain an upper limit value on number density.	84

4.42	Absorption velocity profile of Mg II absorption system at $z_{abs} = 1.1068$. This system is a dubious one and will be only used to obtain an upper limit value on number density.	85
4.43	Absorption velocity profile of Mg II absorption system at $z_{abs} = 1.1933$. This system is a dubious one and will be only used to obtain an upper limit value on number density.	86
4.44	Absorption velocity profile of Mg II absorption system at $z_{abs} = 1.9255$. This system is a dubious one and will be only used to obtain an upper limit value on number density.	87
4.45	Absorption velocity profile of Mg II absorption system at $z_{abs} = 2.3284$. This system is a dubious one and will be only used to obtain an upper limit value on number density.	88
4.46	Absorption velocity profile of Mg II absorption system at $z_{abs} = 2.4052$. This system is a dubious one and will be only used to obtain an upper limit value on number density.	89
5.1	Minimum equivalent width spectrum for the C IV and Mg II transitions as a function of redshift both at 5σ significance level for GRB060607. Blue and red lines correspond to the redshift of the GRB and the associated position of the Ly α , transition respectively. Dotted lines show a reference value of $W_{min}^{ref} = 0.03 \text{ \AA}$. It is clear how W_{min} varies with redshift and for different transitions with direct impact in the determination of the redshift path density.	92
5.2	Cumulative redshift path of the Mg II GRB survey as a function of rest-frame equivalent width.	95
5.3	Minimum equivalent width spectrum for Mg II as a function of redshift at the 2.5σ significance level. Blue lines correspond to each GRB redshift. Red lines correspond to Ly α transition and 5000 km s^{-1} from the GRB redshift (used to remove source contamination). Green lines show sky line contamination zones which were excluded from the redshift coverage. Dotted lines show a reference value of $W_{min}^{ref} = 0.07 \text{ \AA}$ which was used in further analysis.	96
5.4	Number of lines of sight in the Mg II survey and cumulative redshift path as a function of redshift for $W_{min} = 0.07 \text{ \AA}$	97

5.5	Cumulative redshift path of the C IV GRB survey as a function of rest-frame equivalent width.	98
5.6	Minimum equivalent width spectrum for C IV as a function of redshift at the 5σ significance level. Blue lines correspond to each GRB redshift. Red lines correspond to Ly α transition and 5000 km s^{-1} from the GRB redshift (used to remove source contamination). Green lines show sky line contamination zones which were excluded from the redshift coverage. Dotted lines show a reference value of $W_{min}^{ref} = 0.15 \text{ \AA}$ which was used in further analysis.	99
5.7	Number of lines of sight in the C IV survey and cumulative redshift path as a function of redshift for $W_{min} = 0.15 \text{ \AA}$	100
7.1	Redshift number density for weak Mg II ($0.07 \text{ \AA} \leq W_r(2803)$ and $W_r(2796) < 0.3 \text{ \AA}$) absorption systems in our GRB Statistical Sample. As a comparison (dashed line) we show the result obtained from the QSO survey by Narayanan et al. (2007) using the same equivalent width limits. The bins have been slightly offset in redshift for clarity.	114
7.2	Redshift number density for strong Mg II absorption systems with $W_r(2796) \geq 0.3 \text{ \AA}$ in our GRB Statistical Sample. As a comparison (dashed line) we show the result obtained from the QSO survey by Nestor et al. (2005) using the same equivalent width limit. The bins have been slightly offset in redshift for clarity.	115
7.3	Redshift number density for strong Mg II absorption systems with $W_r(2796) \geq 0.6 \text{ \AA}$ in our GRB Statistical Sample. As a comparison (dashed line) we show the result obtained from the QSO survey by Nestor et al. (2005) using the same equivalent width limit. The bins have been slightly offset in redshift for clarity.	116
7.4	Redshift number density for strong Mg II absorption systems with $W_r(2796) \geq 1.0 \text{ \AA}$ in our GRB Statistical Sample. As a comparison (black dashed line) we show the result obtained from the QSO survey by Nestor et al. (2005) using the same equivalent width limit. Also we show the previous GRB result by Prochter et al. (2006b) (blue dashed line) which is consistent with our result. The bins have been slightly offset in redshift for clarity.	117

7.5	Redshift number density of Mg II absorption systems in our GRB Statistical Sample for different equivalent width bins (see Table 7.4 for details). As a comparison we show the results obtained from the QSO surveys by Narayanan et al. (2007) (first bin) and Nestor et al. (2005) (the rest of the bins) using the same equivalent width limit (black dashed line). Also we show the previous GRB result by Prochter et al. (2006b) (blue dashed line) which is consistent with our result. The bins have been slightly offset in W_r for clarity.	118
7.6	Distribution of the number of C IV absorption systems per unit redshift in our GRB Statistical Sample. As a comparison (dashed line) we show results from QSO survey by Steidel (1990) and Misawa et al. (2002) using the same binning as that for the GRB-C IV analysis. The bins have been slightly offset in redshift for clarity.	119
7.7	Distribution of rest-frame equivalent widths $W_r(1548)$ from the C IV Statistical Sample of GRB absorption systems compared with those from Steidel (1990) for QSO absorption systems (dashed line). The bins have been slightly offset in $W_r(1548)$ for clarity.	120
8.1	Absorption velocity profile of C IV-Mg II absorption system at $z_{abs} = 1.567$	134
8.2	Absorption velocity profile of C IV-Mg II absorption system at $z_{abs} = 2.009$	135
8.3	Absorption velocity profile of C IV-Mg II absorption system at $z_{abs} = 2.785$	136

List of Tables

2.1	Spectroscopic observations of our GRB sample.	17
3.1	Feature List Example	24
3.2	Doublet List Example	26
3.3	Efficiency of Line Automatic Detection using $b = 5 \text{ km s}^{-1}$	27
3.4	Efficiency of Line Automatic Detection using $b = 15 \text{ km s}^{-1}$	28
4.1	Mg II Full Sample	38
4.1	Mg II Full Sample	39
4.2	Number of Absorbers in Statistical Mg II Subsamples	40
4.3	C IV Full Sample	61
4.3	C IV Full Sample	62
7.1	Specifications of the Strict $dN/dz _{\text{GRB}}^{\text{MgII}}$ for each Equivalent Width Range.	105
7.2	Specifications of the Relaxed $dN/dz _{\text{GRB}}^{\text{MgII}}$ for each Equivalent Width Range.	106
7.3	Comparison between $dN/dz _{\text{GRB}}^{\text{MgII}}$ for very strong Mg II systems ($W_r > 1 \text{ \AA}$) obtained from our survey and Prochter et al. (2006b).	106

7.4	Specifications of the $dN/dz _{\text{GRB}}^{\text{MgII}}$ for each Equivalent Width Bin.	110
7.5	Specifications of the $dN/dz _{\text{GRB}}^{\text{CIV}}$ for each Bin from the Statistical Sample.	112
8.1	Mg II-C IV Sample	123

Chapter 1

Introduction

1.1 The IGM through QSO Lines of Sight

Since the late sixties, quasi-stellar objects (QSOs), once established to be extragalactic sources, have been used to study the Intergalactic Medium (IGM) through the Absorption Lines technique (Greenstein & Schmidt 1967; Burbidge et al. 1968). This technique is based on the hypothesis that gas clouds located between a QSO and the Earth produce absorption lines on the background QSO continuum spectrum. Thus absorption lines of a given transition can appear at different wavelengths simply because they arise from gas clouds at different redshifts. Of course, this technique is not limited to QSO spectra and any background source sufficiently bright and blue (e.g., galaxies; afterglows of GRBs) could be used, in principle, to perform this kind of study.

After extensive studies of absorption line systems (a gas cloud at the same redshift) in spectra of QSOs it has been widely accepted that the majority of the discovered systems of neutral hydrogen and metals (Gunn & Peterson, 1965; Rauch, 1998), are intervening and that they trace the cosmological expansion of the universe. Many of the conducted surveys have focused on the cosmological evolution of metal absorption systems for different atomic transitions. A standard observational measure is the number of absorbers per unit redshift¹, dN/dz , whose behavior includes effects caused by both the cosmological evolution in the physical pathlength and the intrinsic evolution to the absorbers themselves (e.g., Lanzetta et al., 1987; Sargent et al., 1988; Steidel, 1990).

Analyzing the absorption lines allows one to study the properties of the intervening clouds and their cosmological evolution without magnitude-bias or redshift-bias. Unlike emission surveys (e.g.,

¹See Section 1.5 for its interpretation and Chapter 6 for its empirical calculation.

21-cm), using absorption lines it is possible to detect the IGM at very high redshift (at least the redshift of the most distant background source visible from Earth; until now at $z \gtrsim 8$, see Salvaterra et al., 2009) even below the critical cosmological density. This would be impossible (with current technology and instrumentation) using emission techniques given the very diffuse nature of the IGM. Although the transverse-spatial resolution is lost due to the fact that single beams can be observed, the transverse properties of the absorbers can be obtained in a statistical manner.

Since the production of heavy elements takes place in stars which are mainly grouped into galaxies, it is natural to relate metal absorbers to galaxies (although this has proven difficult to test, especially at high redshift; e.g., Churchill et al., 2005; Tripp & Bowen, 2005). Therefore, studying the evolution of metal absorbers may impact our understanding of both galaxy evolution and the physics of the IGM.

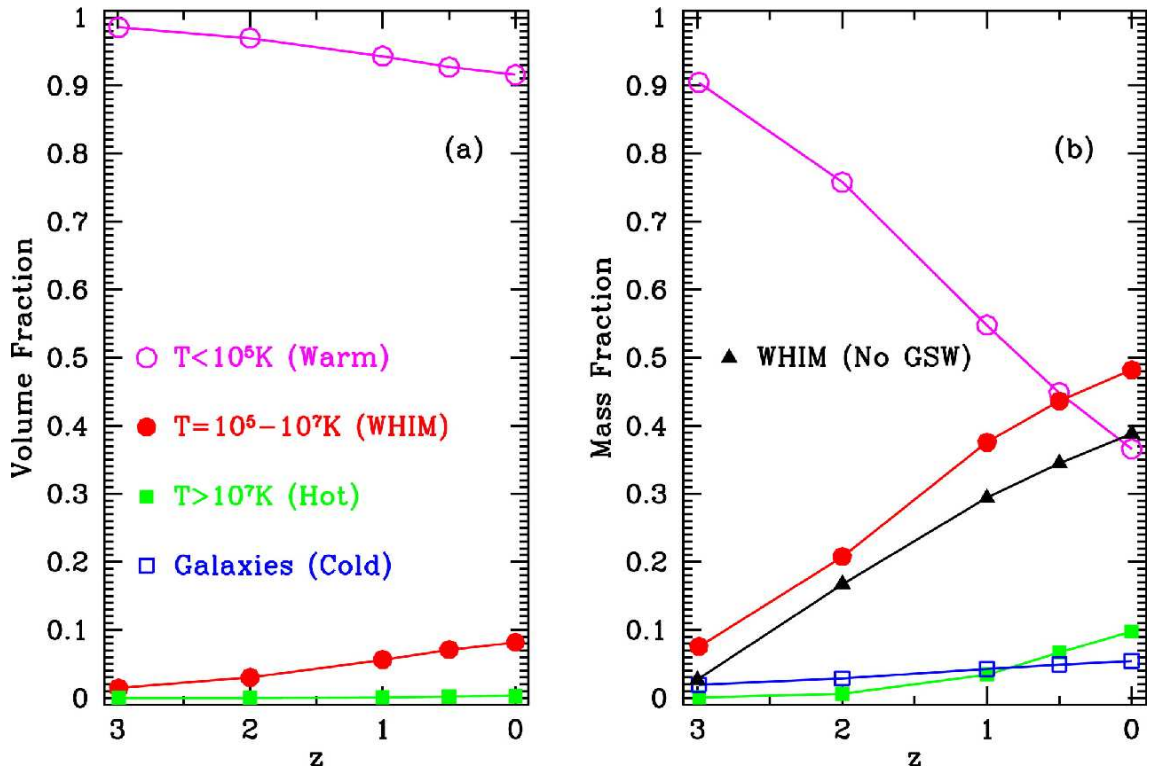


Figure 1.1 Evolution of the different baryonic components of the Universe from $z = 3$ to $z = 0$ from the model of Cen & Ostriker (2006). (a) Volume fractions for each component and (b) mass fraction. The warm-hot intergalactic medium (WHIM) is modeled with and without galactic super wind (GSW). Simulations show that almost all baryons at present day are in the form of diffuse and ionized gas.

In a global context, this kind of study is very important because it is known from observations and simulations that most of the baryons today are in the form of ionized gas (Fukugita et al., 1998). Furthermore, recent results from numerical simulations (e.g., Davé et al., 2001; Cen & Ostriker,

2006) show that at high redshift ($z \geq 2$), the vast majority of baryons is in a diffuse, photo-ionized medium (see Figure 1.1). Therefore, the study of the IGM is necessary to understand the evolution of the baryonic matter in the universe, including condensed structures like galaxies. As mentioned above, the absorption line technique is also quite important to observe and to study this gas (the IGM).

1.2 Line Formation

There are different mechanisms that produce the features of the observed lines which are used to study and interpret the intervening medium through the absorption line technique. In the following I present a brief description of each one.

- Natural Broadening

The natural broadening is caused by the physics of bound-bound transitions. According to the uncertainty principle, the energy of a quantum state is not perfectly defined and there is a dispersion around the central one, producing a Lorentz profile.

- Thermal Broadening or Doppler Broadening

The thermal broadening is caused by thermal motion of atoms within the absorbing clouds. The frequency of emission or absorption in the rest-frame of each atom corresponds to a different frequency for an observer due to the Doppler effect. The observed effect is a spread in the line with a Gaussian profile (assuming a Maxwellian velocity distribution of the gas).

- Turbulent Broadening

The turbulent broadening is caused by macroscopic motions of the host gas. This mechanism is poorly understood and it is not clear how to describe the turbulence broadening function. However, usually it is characterized by a Doppler-parameter b_{turb} and is treated as a Doppler broadening which, in contrast to Thermal broadening, is independent of the atomic mass.

- Collisional Broadening

The collisional broadening is caused by the interaction between the absorbing atom and the host ambient gas, which contains other atoms, ions, molecules, free electrons and free nuclei.

- Instrumental Broadening

The instrumental broadening is caused by the finite resolution of the spectrographs. The core of the instrumental profile defines the narrowest observable line and therefore, lines around this limit are dominated by this mechanism. The instrumental broadening or spread function is usually known.

There are many books that present detailed analysis on the physics involved in the formation of the absorption and emission lines (e.g., Griem, 1974; Rybicki & Lightman, 1979; Kitchin, 1995). I refer the reader to these sources for more in-depth descriptions.

1.3 Line Characterization

1.3.1 Voigt Profile

The observed absorption lines are dominated by the combination of Gaussian and Lorentzian profiles. The contributions of these mechanisms produce the so-called Voigt Profile (van de Hulst & Reesinck, 1947) which corresponds to the convolution of these profiles. In principle, the best way to determine the properties of the absorbers themselves is using this Voigt profile. In practice, when the lines are weak they are dominated by a Gaussian profile and when the lines are completely saturated they are dominated by a Lorentzian profile. In both extreme cases the properties of the absorbers can be well understood directly, while in intermediate cases there is a degeneracy between intrinsic parameters and no direct conclusions can be reached using a single transition.

1.3.2 Equivalent Width

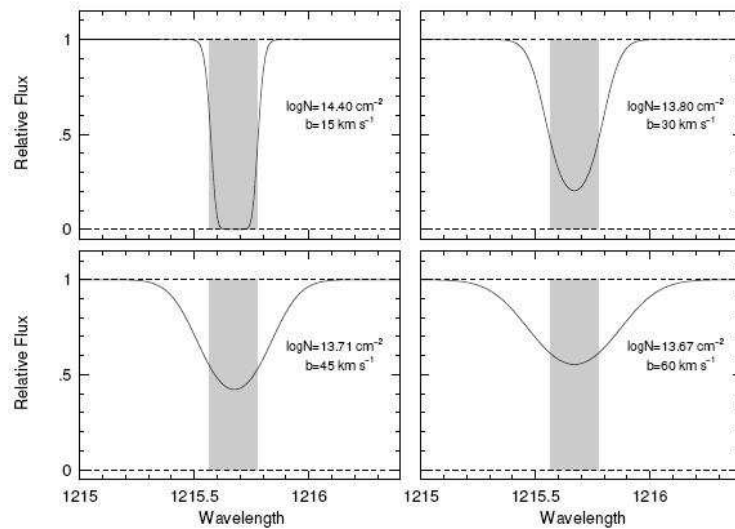


Figure 1.2 Examples of different lines profiles with the same equivalent width of $W = 0.21 \text{ \AA}$. The equivalent width interpretation is shown in dashed grey area. Copyright by Chris Churchill.

In order to characterize spectral lines (hereafter I will refer to absorption lines only, although the definitions are also valid for emission lines) the equivalent width, W , is defined. This is the total area in a spectral line divided by the continuum flux. W corresponds to the wavelength width of an absorption feature that takes out the same area (or amount of energy) but with no intensity ($I_\lambda = 0$, see Figure 1.2), i.e,

$$W = \int_{\lambda_1}^{\lambda_2} \left(1 - \frac{I_\lambda}{I_c}\right) d\lambda$$

where λ_1 and λ_2 are the wavelength bounds of the line. This characterization has the advantage of being independent of exposure time because it is normalized to the continuum. It is also independent of the line shape and spectrograph resolution (Churchill, 2008). Therefore, it permits an objective comparison between different lines (widely separated on one spectrum and/or different spectra).

1.3.3 Column Density

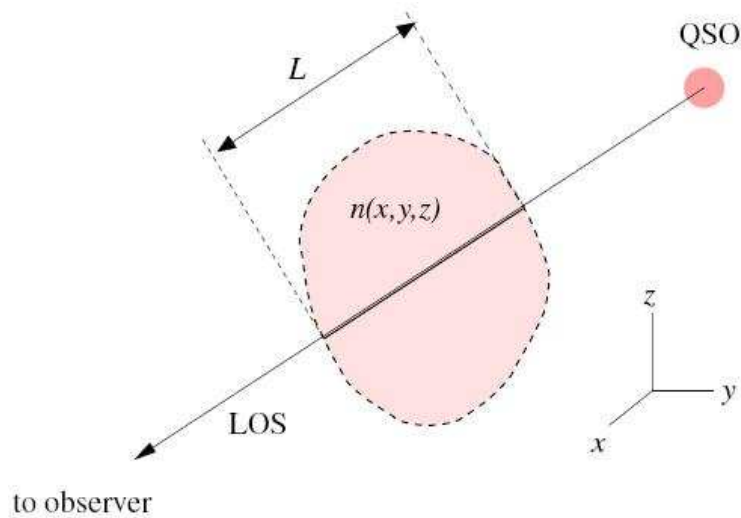


Figure 1.3 Schematic of the cloud and sightline geometry. The line of sight can cross the cloud anywhere and the observed column density represents the integrated density only along this particular direction. Copyright by Chris Churchill.

To understand the nature of the absorbers, it is necessary to know their physical properties. An appropriate way to do this is to define the column density, N , as the integrated number density along the line-of-sight (see Figure 1.3),

$$N = \int_0^L n(l) dl$$

where $n(l)$ is the volume density of the medium.

This quantity can be inferred from the observed line profile and is a measure of the number of absorbing particles along a column with a normalized area of 1 cm^2 . Although in practice there is no knowledge about $n(x, y, z)$ or L , metallicities and ionization conditions of the medium can be inferred indirectly from N .

1.3.4 Doppler Parameter

Assuming that a line profile is dominated by thermal broadening, it is possible to define the Doppler parameter $b = \sqrt{2}\sigma$ (where σ is the standard deviation of a Gaussian distribution) as

$$b = \sqrt{\frac{2k_B T}{m}}$$

where m , k_B and T are the mass of the absorbing ion, the Boltzmann constant and the temperature of the gas, respectively. Assuming a Gaussian turbulent contribution, the Doppler parameter can be written as the quadratic sum of its individual components, i.e.,

$$b = \sqrt{\frac{2k_B T}{m} + b_{\text{turb}}^2}$$

This number can be used directly to infer the temperature of the absorbing gas, but it is important to keep in mind that this is physically meaningful as long as the previous assumptions are still valid.

1.3.5 Curve of Growth

The relation between the equivalent width, W , and column density, N , is called the curve of growth (COG). While the former is a direct observable of the line (see Section 1.3.2), the latter is a physical parameter of the medium which produced the absorption line but cannot be directly observed.

This relation is useful to obtain N , and can be analyzed writing the equivalent width in terms of the optical depth², τ , as,

$$W = \int_{\lambda_1}^{\lambda_2} (1 - e^{-\tau_\lambda}) d\lambda$$

or

$$W = \int_{\lambda_1}^{\lambda_2} (1 - e^{-N\sigma(\lambda)}) d\lambda$$

given that $I_\lambda = I_c e^{-\tau}$. Therefore, the relation between W and N is unambiguous. It depends on the scattering cross section $\sigma(\lambda)$ which includes atomic and environmental parameters such as the oscillator strength³, f_{osc} , and the Doppler parameter, b .

There are three regimes in the COG as seen in Figure 1.4. In the optically thin regime ($\tau \ll 1$), $W \propto N$, and defines the linear part of the COG. In the optically thick regime ($\tau \gg 1$), $W \propto \sqrt{N}$, and defines the square root or damped part of the COW. In these two extreme cases N can be obtained directly from W . However in the intermediate case when $\tau \sim 1$, $W \propto b\sqrt{\ln(N/b)}$, and therefore there is no unique relation between N and W . In this latter case using different transitions is useful to find the intrinsic parameters⁴. I refer the reader for further details and derivation of these results to Churchill (2008) or Bechtold (2001). In this thesis I will compare results between from two different kind of surveys (see below). Therefore I will not use column densities in my analysis but only equivalent width measurements. This is the correct choice for *comparisons* between surveys because the W is a direct observable that is not affected by any extra assumption.

1.4 Classification of Absorbers

The absorption systems are classified in different categories according to the amount of observed H I Lyman- α column densities, N_{HI} , as explained below:

²The optical depth is a measure of the fraction of radiation scattered or absorbed by the medium in a given beam and can be written as $\tau_\lambda = N\sigma(\lambda)$ where N is the column density and $\sigma(\lambda)$ is the scattering cross section, both associated to the involved transition.

³The oscillator strength is a dimensionless quantity to express the strength of a given transition. This number can be obtained experimentally in the laboratory and values for different transitions can be found tabulated in literature.

⁴While a given transition may fall in the flat part, it is possible to find another transition (or single line) which falls in one of the two extreme cases.

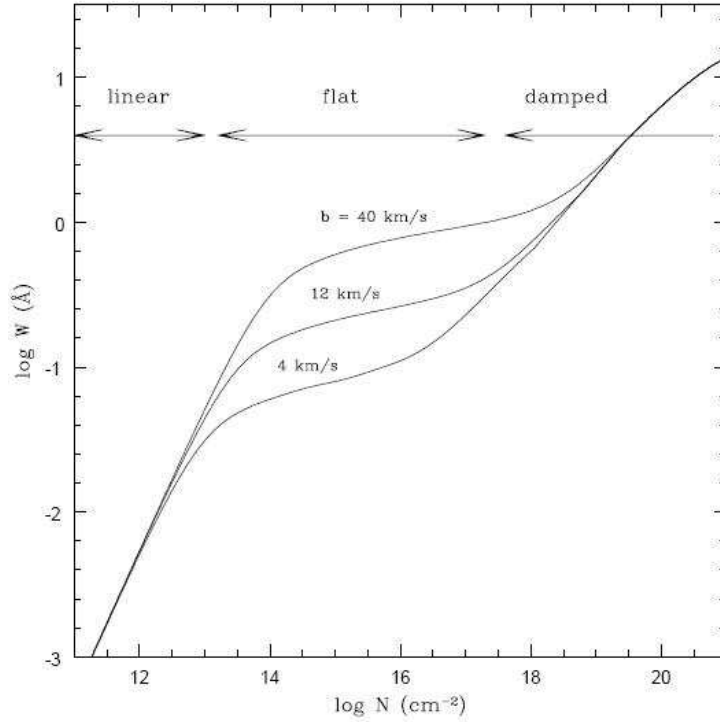


Figure 1.4 Theoretical curve of growth for the hydrogen Ly α line. Equivalent width, W , in \AA and column density, N , in cm^{-2} . Linear, flat and damping parts of the curve of growth are indicated. Figure from Bechtold (2001).

1.4.1 Damped Lyman- α Absorbers (DLAS)

Systems with column densities $N_{HI} \geq 10^{20.3} \text{ cm}^{-2}$. These systems show strongly saturated lines with extended damping wings (dominated by a Lorentzian profile). DLAS are believed to be associated with discs of spiral galaxies since our own Milky Way disc has a similar integrated column density and also because these DLAS show several metal lines associated to the same redshift.

1.4.2 Sub DLAS

Systems with column densities $10^{19} \text{ cm}^{-2} < N_{HI} < 10^{20.3} \text{ cm}^{-2}$ which lie between DLA and LLS (see definition below) are commonly called sub-DLA or super-LLS.

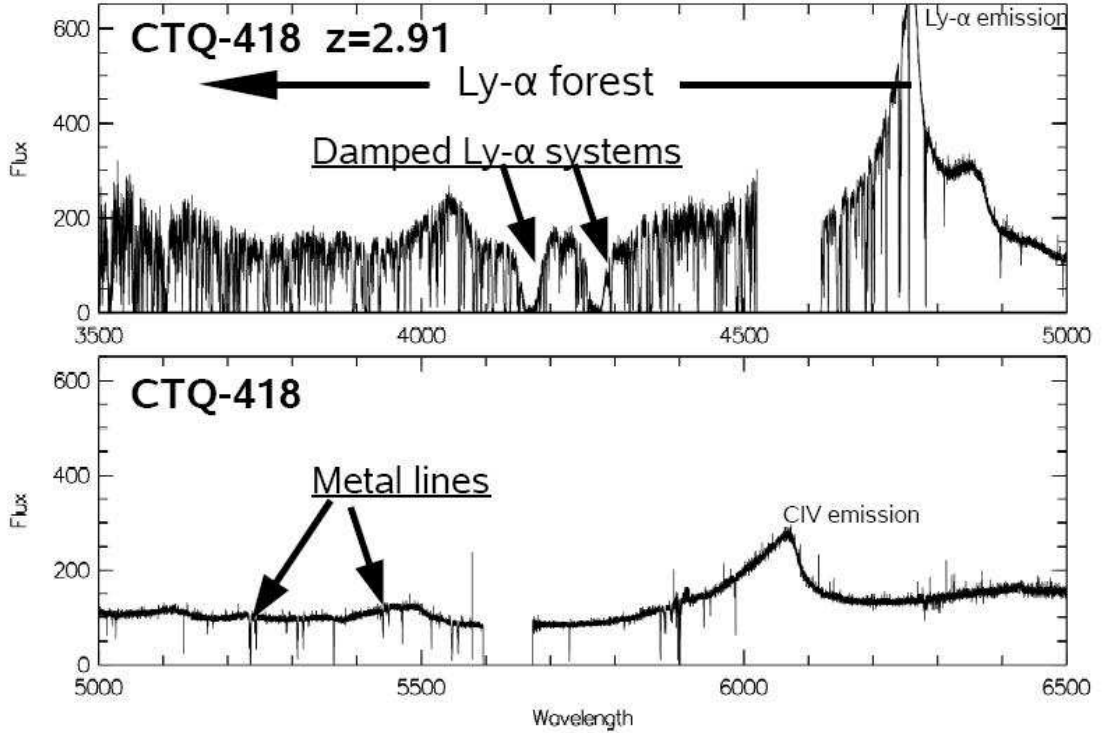


Figure 1.5 UVES spectrum of CTQ-418 at $z = 2.91$, showing two damped Ly α systems (DLA) discovered in the course of the Calan-Tololo DLA Survey (Lopez et al., 2001). Also, it is possible to see different absorption lines associated to H I (Ly α forest is clearly seen) and metal lines.

1.4.3 Lyman Limit Systems (LLS)

Systems with column densities $10^{17.2} \text{ cm}^{-2} < N_{HI} < 10^{19} \text{ cm}^{-2}$. At $N_{HI} > 10^{17.2} \text{ cm}^{-2}$ (corresponding to continuum optical depth $\tau > 1$ at $\lambda < \lambda_{LL} = 911.267 \text{ \AA}$) the background source flux is completely absorbed at wavelengths blue-ward to the Lyman limit (i.e., $\lambda < \lambda_{LL}(1 + z_{abs})$). It is also possible to observe many lines associated to the entire Lyman series itself.

1.4.4 Lyman- α Forest Systems

At lower column densities, $N_{HI} < 10^{15} \text{ cm}^{-2}$, the lines are not saturated and for the H I Lyman- α transition many of these absorption lines can be found in QSO spectra blueward of the Lyman- α emission appearing like a *forest* of lines (see Figure 1.5). The distribution of column densities shows that Ly α forest systems are $\sim 10^7$ times more frequent than DLAs. A complete review of Ly α forest systems can be found in Rauch (1998).

1.4.5 Metal Systems

Metal systems show a wide range of column densities, although they are typically found at $N_{HI} > 10^{15} \text{ cm}^{-2}$. The vast majority is associated with DLAs, sub-DLAs and/or LLS. However metal systems have been also found in Lyman- α clouds.

Different metal transitions are used to trace different IGM phases. For instance, low ionization species such as Mg II, Mg I, Fe II trace neutral gas associated to cold environments ($T \sim 10^4 \text{ K}$), while species like C IV, Si IV, O VI trace highly ionized gas associated to hotter environments ($T \sim 10^5 \text{ K}$). Systems without metals are also observed, which can be used as good tracers of primordial conditions.

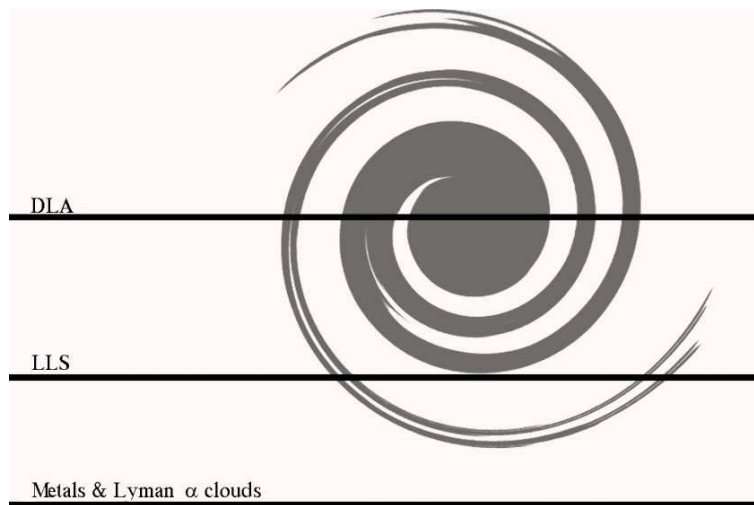


Figure 1.6 A schematic interpretation of different absorption line systems in a unified point of view. DLA and LLS correspond to sightlines passing through the galactic disc while Lyman- α clouds and metal systems arise from sightlines with larger impact parameters going through an extended halo.

Figure 1.5 shows the spectrum of CTQ-418 which illustrates the difference between the systems mentioned above. In principle these systems may not be physically connected and could be tracers of different clouds and environments, each with its own physical conditions. However, it has been suggested (e.g., Tytler, 1987) that this classification could correspond to the same cloud (associated to a single galaxy) seen along lines-of-sight at different impact parameters (see Figure 1.6). In this scenario, DLAs and LLS would be formed along lines-of-sight passing through galactic discs, and the metal and/or Lyman- α clouds would arise from in extended halos far away from the center of the galaxy. On the other hand, this scenario has been difficult to test and the *real* galaxy-absorber relation still remains unknown.

1.5 Introduction to Absorption Line Surveys

As in the majority of natural sciences there are two main approaches to study astrophysical phenomena. One is to study a single object in a great detail to understand a particular feature. Alternatively, one can study many objects in lower detail and obtain a global point of view of such phenomena. Both approaches are, of course, complementary and necessary.

The study of the IGM through the absorption line technique is not an exception to this rule and currently, there are two main types of studies of absorption systems in the literature: the study of individual systems at high spectral resolution and the study of large samples at lower spectral resolutions. Massive surveys have been carried out in both cases, either, using thousands of low-resolution QSO spectra (e.g., from SDSS⁵) or using tens of high-resolution QSO spectra (e.g., the more expensive echelle spectroscopy). In general, surveys are focused on one class of systems (e.g., Ly α forest clouds, LLS, DLAS, Mg II, C IV, etc.). In this context, it is also possible to carry out studies about different environments (and their cosmological evolution) using different kind of surveys. For example, the field is studied using intervening systems (i.e., excluding zones near the background source), the background sources are studied using systems found close to it (excluding intervening systems), etc⁶.

As mentioned in Section 1.1 a standard direct observational measure is the redshift number density, dN/dz . The fundamental underlying hypothesis to obtain an intervening dN/dz are both independency⁷ and isotropy⁸ between different lines-of-sight. A schematic of an absorption line survey is shown in Figure 1.7 which allows one to obtain an *average* dN/dz counting the number of systems in a given redshift path⁹. This quantity is the number of absorption systems per unit redshift and it is expected to vary due to both, proper evolution of the absorbers themselves and to cosmological evolution of space-time:

$$\frac{dN}{dz}(z) = \frac{c}{H_0} n(z) \sigma(z) \frac{(1+z)^2}{E(z)}$$

where c is the speed of light, H_0 is the Hubble constant and $E(z) \equiv H(z)/H_0$ with $H(z)$ the Hubble parameter. $n(z)$ and $\sigma(z)$ are the volume density and cross section of the absorbers as a function of redshift, respectively. Therefore, it is possible to infer $n(z)\sigma(z)$ from dN/dz and a cosmological model. Making assumptions on $n(z)$ it is possible to obtain $\sigma(z)$ or, on the other hand, measuring

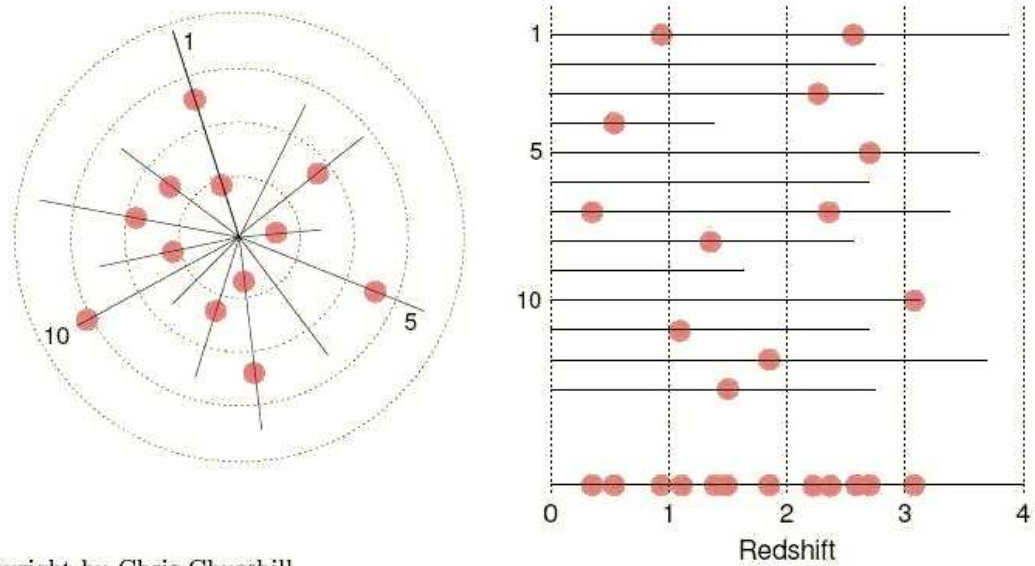
⁵Sloan Digital Sky Survey (York et al., 2000).

⁶For instance, Lopez et al. (2008) studied the galaxy clusters environments from an Mg II survey.

⁷This hypothesis is valid for sightlines which are widely spatially separated. On the other hand, very close sightlines (e.g., QSOs lensed or binaries) are useful to study absorbers lengths statistically (e.g., Smette et al., 1995).

⁸Based on Copernican principle.

⁹The redshift path is a function of both redshift and equivalent width. This number corresponds to the total redshift range in the survey where the absorption systems are searched. See Chapter 5 for further details.



Copyright by Chris Churchill.

Figure 1.7 Schematic of an absorption line survey. Left: Sources are *randomly* distributed at different redshifts. Different sightlines toward these sources having different redshift paths are represented by solid lines where the observer is in the center of the circles. Intervening absorbers represented by shaded points are *randomly* distributed between the background source and the observer. Right: It is possible to obtain an *average* sightline joining individual sightlines. In order to obtain an accurate dN/dz it is necessary to properly take into account the differences in redshift paths of each sightline. Copyright by Chris Churchill.

$\sigma(z)$ in an independent way allows one to derive $n(z)$. Finally, if one could identify a known non-evolving type of absorber, it would be possible to derive cosmological parameters. Thus, dN/dz is an important measurement, both in IGM and cosmological studies.

The completeness of the survey is determined from a rest-frame equivalent width, W_r , value. This corresponds to the fraction of the spectral coverage where the surveyed absorption system could be detected at a given W_r . It is easier to detect lines at greater W_r values than smaller. This is because the signal-to-noise ratio required to detect weak lines is greater than to detect strong ones. Therefore a survey must look for absorption systems at $W_r > W_{min}$, where W_{min} is the rest-frame equivalent width where the completeness of the survey is arbitrarily defined as acceptable (typically greater than a 90%). Likewise, the choice of a given W_{min} could imply differences in the column densities of the medium that produces the absorption features. Thus, when carrying out the analysis, different W_{min} choices can be used to look at different populations of absorption systems. For example, it is known from the equivalent width distribution that there are two population of Mg II absorption systems (See Figure 1.8) separated at an $W_r \sim 0.3 \text{ \AA}$.

The study of the IGM through absorption lines has been done almost exclusively using QSO

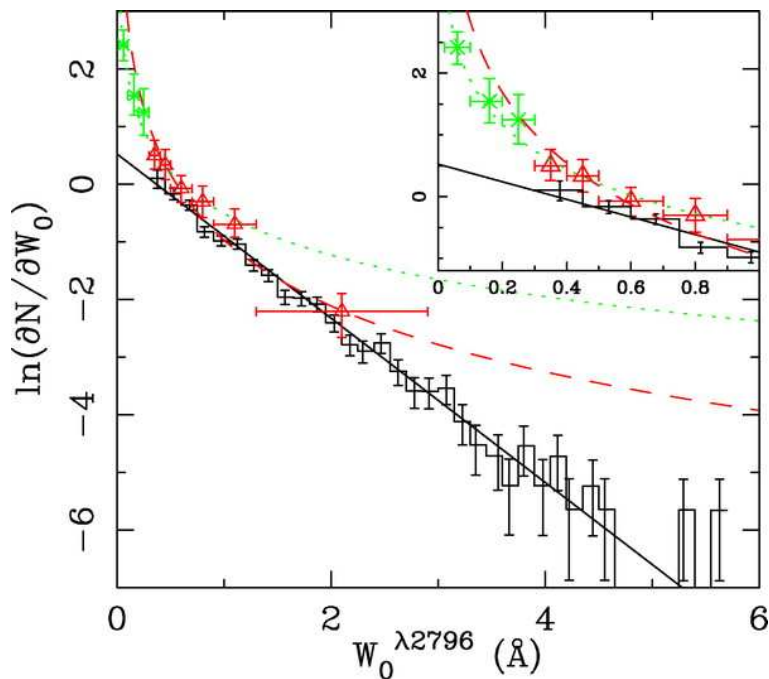


Figure 1.8 Histogram of the $W_r(2796)$ distribution from Nestor et al. (2005). The power laws fits (dashed and dotted lines) greatly overpredict the incidence of strong ($W_r(2796) > 2 \text{ \AA}$) systems, while the exponential fit (solid line) underpredicts the incidence of weak ($W_r(2796) < 0.3 \text{ \AA}$) systems. This suggests a transition in the distribution around $W_r(2796) \sim 0.3 \text{ \AA}$. This is possibly an indication of different populations of absorption systems.

as background sources. Very recently, spectra of optical GRB afterglows have begun to be used. In principle, the properties of the intervening systems should be physically independent of the background source employed but, as we will see below (see Section 1.7 and Chapter 7), there are significant differences in the first result derived from intervening Mg II toward GRBs when compared with those toward QSOs.

In this thesis I used high resolution spectra of GRB afterglows. The survey is composed of 7 high to moderate signal to noise ratio GRB echelle spectra (see Chapter 2) which are used to measure the dN/dz in intervening Mg II and C IV metal systems.

1.6 Basics of Gamma-ray Bursts

The discovery of gamma-ray bursts (GRBs) was reported by Klebesadel et al. (1973). It consisted of sixteen high energetic photons ($\sim \text{MeV}$) observed as extraterrestrial (and extra-solar) sources. The GRBs also exhibited lower-energy longer-duration afterglows (e.g., X-Ray, opti-

cal and radio) observed at similar spatial directions. With the launch of new instruments like BATSE¹⁰/CGRO¹¹ (among others) precise GRBs positions¹² were established. These measurements revealed an isotropic spatial distribution suggesting either a cosmological or Galactic halo origin.

The cosmological nature of GRBs was finally revealed when Metzger et al. (1997) measured the first cosmological redshift for the optical afterglow of GRB970508. For this fact, the GRBs are believed to be the most energetic objects known in the universe having typical luminosities $E/t \sim 10^{51} - 10^{52}$ erg s⁻¹ derived from their large apparent brightness of their optical afterglows at cosmological distances from Earth.

Nowadays, the Swift Gamma-Ray Burst Mission (launched on 2004) plays an important role in the detection of the majority of the observed GRBs. This satellite is composed by three telescopes, namely the BAT¹³, the XRT¹⁴ and the UVOT¹⁵, which permit a rapid spatial position determination of the GRBs afterglows. Therefore, the Swift mission is very useful to observe the early stages of both GRBs and their afterglows as well as to carry out ground-based follow up observations even with large telescopes (allowing high-resolution spectroscopy).

The real nature of GRBs is still unknown although there are many evidences supporting the fireball model. This model states that GRBs are produced when the kinetic energy of an ultra-relativistic flow is dissipated (Rees & Meszaros, 1992). The GRB itself is produced by internal dissipation within the flow while the afterglow is produced via external shocks with the circumburst medium. However the mechanism which supports this scenario is more uncertain suggesting that GRB could be produced by a neutron star (or black hole) merger (e.g., Eichler et al., 1989) or a high-energetic (massive) stellar collapse event (e.g., Woosley, 1993).

Despite the unknown nature of GRBs, their optical afterglows can be used as background sources to study the IGM through the absorption line technique in the same manner as QSOs. This technique can also be used as a powerful tool to study the intrinsic GRBs properties as well as their environment and the interstellar medium (ISM) of the galaxies that host them.

Differences between GRBs and QSOs are very important. GRBs afterglows are, in general, more luminous than QSOs and therefore could be observed at similar (Ciardi & Loeb, 2000) or even higher redshifts than QSOs (e.g., according to Lamb & Reichart, 2000, GRB should be detectable at $z \gtrsim 10$). Another important difference is their time duration: due to the low duration¹⁶ of GRBs

¹⁰Burst and Transient Source Experiment.

¹¹Compton Gamma-Ray Observatory.

¹²The GRB itself can not be resolved spatially. Using X-ray imaging the position is well constrained and then optical images taken from the ground help to obtain an accurate position.

¹³Burst Alert Telescope.

¹⁴X-ray Telescope.

¹⁵Ultraviolet/Optical Telescope.

¹⁶GRBs themselves last for seconds, while their afterglows can be observed for days (X-rays, optical) or even, in

these are more difficult to be observed than QSOs and high resolution spectra at high signal-to-noise ratios are very hard to obtain. On the other hand, the fact that GRBs (and their afterglows) disappear on human time-scales, makes them very useful objects to identify the foreground galaxies associated to the absorbers at small impact parameters from the background source (for QSOs this kind of study is more difficult due to their constant high brightness). Regarding continuum fitting, GRBs are easier to model using a simple power law (without prominent emission lines). Finally the different intrinsic nature of GRBs and QSOs can be used to study different environments. According to the unified model QSOs correspond to AGN¹⁷ activity in the centers of galaxies while GRBs, as mentioned, are believed to be due to a stellar collapse or an energetic merger event in star forming regions.

Summarizing, both QSOs and GRBs afterglows are useful probes of the IGM using the absorption line technique, which permit different and complementary points of view about both intrinsic environments and cosmological intervening systems. In this thesis I will restrict the analysis to the latter case.

1.7 Absorption Lines in GRB Spectra

Recently, Prochter et al. (2006b) have found a significant overabundance (a factor of ~ 4) of strong ($W_r(2796) \geq 1.0 \text{ \AA}$) Mg II absorbers in LOS toward GRBs when compared to the statistics drawn from LOS toward QSOs. They identified 14 systems in a total redshift path of $\Delta z = 15.5$ implying almost 1 strong Mg II system per unit redshift along GRB sightlines while in QSO spectra only 0.3 strong Mg II systems per unit redshift are found (see Figure 1.9). This result is striking because a key hypothesis of this experiment is that the intervening systems are independent of the background source.

Several physical effects have been proposed to explain the overabundance (Prochter et al., 2006b; Frank et al., 2007), namely:

1. dust within the Mg II absorbers may obscure faint QSOs which therefore do not appear in magnitude limited samples
2. the Mg II gas may be intrinsic to the GRBs
3. the GRBs may be gravitationally lensed by these absorbers

some cases, years (radio afterglows). However, for useful spectroscopic studies (nowadays) optical afterglows are needed.

¹⁷Active Galactic Nuclei.

4. the absorbers are small enough that different ‘beam sizes’ between GRBs and QSOs may affect the statistics

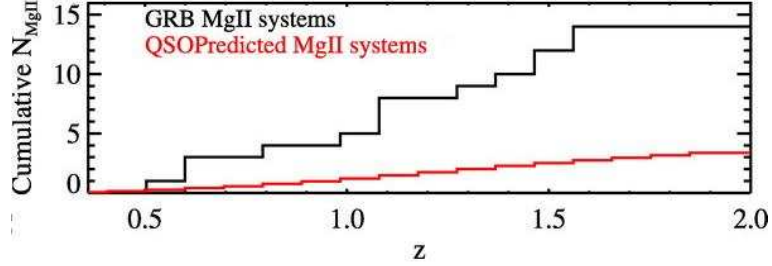


Figure 1.9 Cumulative number of strong Mg II ($W_r(2796) > 1 \text{ \AA}$) systems along the GRB sight lines (black curve). The red curve shows the predicted number of systems adopting the incidence of Mg II systems measured along QSO sightlines using the result from Prochter et al. (2006a). The incidences observed for GRB and QSO sightlines are inconsistent. Figure from Prochter et al. (2006b).

Prochter et al. (2006b) and Porciani et al. (2007) have argued that none of these explanations alone are likely to explain the full effect but it may be possible for several to contribute together to resolve the discrepancy.

Because the C IV ion has a much higher ionization potential than Mg II (47.9 eV versus 15 eV), the C IV doublet is likely to trace more diffuse and hotter gas than Mg II. Therefore, C IV systems may represent a different *population* of larger cross section absorbers and the study of their statistics may help address the problem opened by the Prochter et al. (2006b) result. On the other hand, I would also like to know whether or not this overabundance is observed in Mg II systems with equivalent widths smaller than the cutoff used by Prochter et al. (2006b). This information would be very important in order to discard or confirm possible explanations.

In this thesis, I revisit high-resolution GRB spectra and look for Mg II *and* C IV absorbers to obtain one of the first statistics of such systems in this type of lines-of-sight¹⁸. Since high resolution GRB optical afterglow spectra are not easy to obtain this might be one of the first thesis about this kind of study.

¹⁸First statistics on Mg II with $W_r < 1 \text{ \AA}$ and C IV with $W_r > 0.15 \text{ \AA}$.

Chapter 2

Data

2.1 Data on GRB

The GRB afterglows data comprises optical spectra taken with the Keck/HIRES (Vogt et al., 1994), Magellan/MIKE (Bernstein et al., 2003) and VLT/UVES (Dekker et al., 2000) echelle spectrographs, allowing high spectral resolution of $R \equiv \lambda/\delta\lambda \approx 40\,000 - 30\,000$.

The full spectral sample is comprised of 7 moderate to high signal-to-noise ratio ($> 5 \text{ pix}^{-1}$) echelle spectra observations, of the following GRB afterglows: GRB021004, GRB050730, GRB050820, GRB050922C, GRB051111, GRB060418 and GRB060607, summarized in Table 2.1. The MIKE

Table 2.1. Spectroscopic observations of our GRB sample.

GRB	RA (J2000)	Dec (J2000)	z_{GRB}	Instrument	Sample	Reference
GRB 021004	00 26 54.68	+18 55 41.6	2.335	UVES	Mg II and C IV	1
GRB 050730	14 08 17.14	-03 46 17.8	3.969	MIKE	Mg II and C IV	2,3
GRB 050820	22 29 38.11	+19 33 37.1	2.615	HIRES	Mg II and C IV	3
GRB 050922C	21 09 33.30	-08 45 27.5	2.199	UVES	Mg II and C IV	4
GRB 051111	23 12 33.36	+18 22 29.5	1.549	HIRES	Mg II	3
GRB 060418	15 45 42.40	-03 38 22.8	1.490	MIKE	Mg II	3
GRB 060607	21 58 50.40	-22 29 46.7	3.082	UVES	Mg II and C IV	5

Note. — Units of right ascension are hours, minutes and seconds, and units of declination are degrees, arcminutes and arcseconds.

References. — (1) Fiore et al. (2005); (2) Chen et al. (2005); (3) Prochaska et al. (2007); (4) Piranomonte et al. (2006); (5) Ledoux et al. (2006)

and HIRES data were acquired within the GRAASP¹ collaboration and were kindly provided to me by Dr. J. X. Prochaska. The UVES data² were retrieved from the ESO archive and processed with the standard UVES pipeline. The spectra were reduced, coadded and normalized using standard techniques. I refer the reader to the following papers for a full discussion of the observations (Fiore et al., 2005; Chen et al., 2005; Prochaska et al., 2007; Piranomonte et al., 2006; Ledoux et al., 2006).

As mentioned, in this thesis I am interested in the study of both Mg II and C IV absorption systems in GRB sightlines. Both transitions are doublets, therefore it makes them easy to be identified in a spectrum. Their rest-frame wavelengths are $\lambda\lambda$ 2796.3521, 2803.5310 Å and $\lambda\lambda$ 1548.1949, 1150.7700 Å respectively. These ultraviolet transitions appear at optical wavelengths, due to the cosmological expansion, at high redshift. Both, Carbon and Magnesium, are abundant elements which probe different phases of the gas (the ionization potential of C IV and Mg II are 47.9 eV and 15 eV, respectively). These facts explain why these transitions are commonly used in high redshift ($z \gtrsim 1$) absorption lines surveys.

2.1.1 Mg II and C IV Spectral Samples

To avoid contamination of hydrogen lines, the Mg II and C IV samples were restricted to the sightlines with coverage redward of the Ly α forest, i.e.,

$$\frac{\lambda_{Ly\alpha}(1 + z_{GRB})}{\lambda_{abs}} - 1 < z_{abs} \leq z_{GRB}$$

where $\lambda_{Ly\alpha}$ and λ_{abs} are the rest-frame wavelength of H I and the absorber (either Mg II or C IV) transition, respectively. For that reason we excluded 2 out of 7 GRB afterglows for the C IV sample, namely GRB051111 and GRB060418. Finally, the Mg II sample is composed by all previous GRB afterglows in the full spectral sample while the C IV sample is composed only by 5 of them (see column 6 on Table 2.1).

2.2 QSO Absorber Statistics

It is necessary to consider previous statistics on the incidence of Mg II and C IV absorbers toward QSOs for comparison to the GRB statistics. In what follows the QSO statistics will be used as the standard because it is based on a much larger object number and redshift paths.

¹Gamma-Ray Burst Afterglows As Probes (<http://www.graasp.org>).

²Based on observations made with ESO Telescopes at the Paranal Observatories under programs 070.A-0599(B), 075.A-0603(B) and 077.D-0661(A).

2.2.1 Mg II Reference Sample

In this case, two previous QSO samples were used to compare with our results since two different *populations* (weak and strong) of intervening Mg II systems have been identified (Churchill et al., 1999b; Rigby et al., 2002; Nestor et al., 2005). According to the equivalent width distribution (see Figure 1.8) there are two Mg II absorption system populations separated at $W_r(2796) \sim 0.3 \text{ \AA}$.

Weak Mg II population

For the *weak* Mg II population (defined as $W_r(2796) < 0.3 \text{ \AA}$), the statistics by Narayanan et al. (2007) was used as reference. In that survey, 81 QSO spectra with high spectral resolution (VLT/UVES data $R \sim 30000$) were used. I recomputed the number density from the tables published by Narayanan et al. (2007) using a greater minimum equivalent width threshold in order to match the limitations of our data (which are the poorest ones).

Strong Mg II population

For the *strong* Mg II population (defined as $W_r(2796) \geq 0.3 \text{ \AA}$), I used the results by Nestor et al. (2005). In that survey these authors used ~ 3700 low resolution QSO spectra obtained from SDSS. Their results on $dN/dz|_{\text{QSO}}^{\text{MgII}}$ are summarized in their Table 1. It is important to note that the redshift path of this survey is a factor of ~ 10 and ~ 200 larger than the GRB one at $W_r(2796) = 0.3 \text{ \AA}$ and at $W_r(2796) = 1 \text{ \AA}$, respectively.

2.2.2 C IV Reference Sample

There is a lack of C IV surveys. One of the largest published surveys of C IV along QSO sightlines was carried out by Steidel (1990). In that survey, 66 QSO spectra with low spectral resolution ($\sim 1 - 2 \text{ \AA}$) were used (55 of them were obtained from Sargent et al., 1988). I employed their result as comparison.

Steidel (1990) measured the incidence of C IV systems with $W_{min} = 0.15 \text{ \AA}$ and parameterized their results as $dN/dz|_{\text{QSO}}^{\text{CIV}} = N_0(1+z)^{-1.26}$. For comparison purposes, in what follows, I computed $dN/dz|_{\text{QSO}}^{\text{CIV}}$ directly from the tables published by Steidel (1990) and Sargent et al. (1988). I also compare with another published survey carried out more recently by Misawa et al. (2002) (18 QSO spectra with resolution of $\sim 2 \text{ \AA}$) although this survey has much lower redshift coverage and does not provide better sensitivity (they also used a $W_{min} = 0.15 \text{ \AA}$).

Chapter 3

Search of Absorption Systems toward GRB

3.1 Detection of Absorption Systems

In order to make the statistics on absorption systems reproducible, it is imperative to have a robust algorithm to detect lines over a large sample of spectra.

My search is based on a two-step selection process. Firstly, I run an automatic detection of absorption features over each spectrum that identifies possible doublets for each ion (Mg II and C IV). Secondly, I perform a visual inspection of the doublets candidates, discarding fake identifications due to noise, blends or apparent doublets composed of two different transitions with nearly identical separation.

3.1.1 Automatic Detection of Absorption Lines

For the automatic detection of line profiles in the spectra the Aperture Method (described by Wolfe et al., 1986; Churchill, 2008) was employed. The idea is to calculate the equivalent width per resolution element and detect significant features for a given confidence level. For this purpose it is necessary to define the following concepts.

Pixel Equivalent Width Spectrum

In a normalized spectrum it is possible to define an equivalent width for pixel j , e_j , as

$$e_j = \Delta\lambda_j(1 - I_j)$$

where $\Delta\lambda_j$ and I_j are the wavelength width and normalized flux of pixel j respectively. The associated error is,

$$\sigma_{e_j} = \Delta\lambda_j \sigma_{I_j}$$

where σ_{I_j} is the uncertainty in the counts of pixel j . Then, it is possible to calculate the *equivalent width spectrum*. Note that errors in λ_j and the adjustment of the continuum spectrum are not considered. In the latter case it is necessary to redefine e_j and σ_{e_j} as,

$$e_j = \Delta\lambda_j \left(1 - \frac{I_j}{I_j^c}\right)$$
$$\sigma_{e_j}^2 = (\Delta\lambda_j)^2 \left(\frac{I_j}{I_j^c}\right)^2 \left[\left(\frac{\sigma_{I_j}}{I_j}\right)^2 + \left(\frac{\sigma_{I_j^c}}{I_j^c}\right)^2 \right]$$

where I_j^c and $\sigma_{I_j^c}$ are the counts and error of fitting continuum respectively for pixel j . σ_{e_j} follows from propagation of errors.

The Aperture Method

It is necessary to define an aperture (in pixels in this case) within which the equivalent width will be calculated. It is useful to use an aperture equivalent to approximately twice the number of pixels per resolution element, p . Therefore, the equivalent width per unresolved feature at pixel j is,

$$w_j = \sum_{k=j-p}^{j+p} e_k$$

and the uncertainty of this value is,

$$\sigma_{w_j}^2 = \sum_{k=j-p}^{j+p} \sigma_{e_k}^2$$

According to this definition, $w_j > 0$ for absorption and $w_j < 0$ for emission.

Given these parameters, it is possible to detect lines (or features) automatically by adopting a detection threshold, N . Typically N is in the range 3 – 5. The next step is to find a pixel j with,

$$\left| \frac{w_j}{\sigma_{w_j}} \right| \geq N$$

Once a potential feature is identified at pixel j it is necessary to find the starting pixel j^i , and ending pixel j^f , for this particular feature. This is done by searching blueward from pixel j until the first pixel having a w_{j^i} consistent with $N = 1$ is found. The same is done for pixel j^f but searching redward from pixel j .

At this point, the identification of potential lines is complete but it is necessary to know whether the feature is significant throughout its entire profile. For that reason, the observed equivalent width, W_i , and its uncertainty, σ_{W_i} of the candidate i are calculated as,

$$W_i = \sum_{k=j^i}^{j^f} e_k$$

and,

$$\sigma_{W_i}^2 = \sum_{k=j^i}^{j^f} \sigma_{e_k}^2$$

Only features with $|W_i/\sigma_{W_i}| > N$ will be considered as potential lines. To calculate the center of the line, and considering that at high resolution it is possible to detect multiple components in one system, a convenient approach ¹ is to weight the wavelength of each pixel by e_k , i.e.,

¹In contrast with the determination of the center of the line by looking for the pixel that has the minimum w_j in the range j^i to j^f which is usually adopted for symmetric, unblended lines.

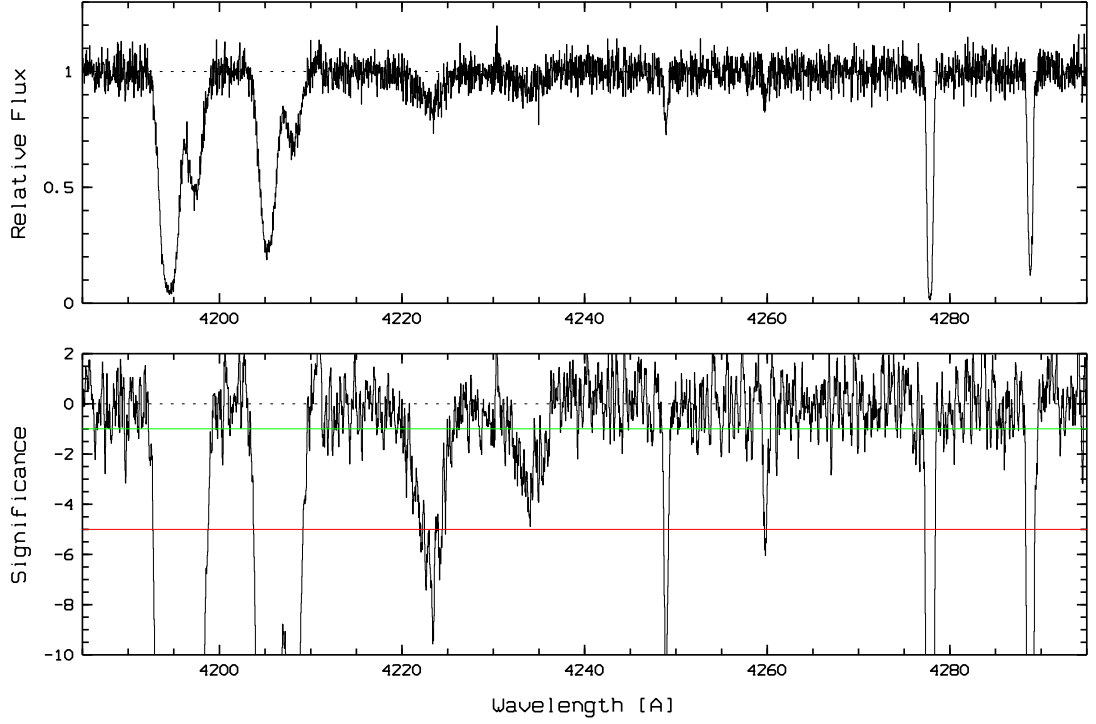


Figure 3.1 Upper: Normalized synthetic high resolution spectrum ($S/N = 20$) with 4 Mg II doublets located at different redshifts with different shapes. Bottom: Associated significant level of *equivalent width spectrum*. Assuming a detection threshold of $N = 5$ the fourth line (at $\sim 4235 \text{ \AA}$) is not detected and only 3 doublets are found. Detection thresholds of $N = 5$ and $N = 1$ are shown with horizontal solid lines.

$$\langle \lambda_i \rangle = \frac{\sum_{k=j^i}^{j^f} e_k \lambda_k}{\sum_{k=j^i}^{j^f} e_k}$$

and the associated error in $\langle \lambda_i \rangle$ is,

$$\sigma_{\langle \lambda_i \rangle}^2 = \sum_{k=j^i}^{j^f} \left(\frac{\{\lambda_k \sum_{k=j^i}^{j^f} e_k - \sum_{k=j^i}^{j^f} \lambda_k e_k\} \sigma_{e_k}}{(\sum_{k=j^i}^{j^f} e_k)^2} \right)^2$$

or, using the previous definitions,

Table 3.1. Feature List Example

ID	$\langle \lambda \rangle$ [Å]	$\sigma_{\langle \lambda \rangle}$ [Å]	W_{obs} [Å]	$\sigma_{W_{obs}}$ [Å]	SL	λ^i [Å]	λ^f [Å]	N_{pix}
0	4195.37	0.014	3.344	0.0194	172.03	4192.20	4199.24	176
1	4206.05	0.019	2.218	0.0202	109.72	4203.40	4209.64	156
2	4222.99	0.056	0.423	0.0194	21.82	4220.84	4224.96	103
3	4248.93	0.025	0.121	0.0096	12.59	4248.44	4249.44	25
4	4259.84	0.043	0.064	0.0095	6.75	4259.44	4260.36	23
5	4277.83	0.006	0.761	0.0085	89.77	4277.08	4278.52	36
6	4288.83	0.009	0.578	0.0095	60.81	4288.20	4289.64	36

Note. — Detected lines on spectrum showed in Figure 3.1.

$$\sigma_{\langle \lambda_i \rangle}^2 = \sum_{k=j^i}^{j^f} \left(\frac{\lambda_k - \langle \lambda_i \rangle}{W_i} \right)^2 \sigma_{e_k}^2$$

Figure 3.1 shows an example spectrum and the corresponding significance of its *equivalent width spectrum*. The detection threshold $N = 5$ is shown with a horizontal solid line.

Information about each detected line is saved in a text file (*Feature List*) containing the ID, $\langle \lambda \rangle$, $\sigma_{\langle \lambda \rangle}$, W_{obs} , $\sigma_{W_{obs}}$, significance level, $SL = W/\sigma_W$, starting and ending wavelength, λ^i and λ^f respectively, and number of pixels, N_{pix} as shown in Table 3.1.

3.2 Identification of Doublets

In the *Feature List* doublet candidates for a particular transition (e.g, Mg II, C IV) are found by assigning a *redshift* to each line as if it was a particular ion, and then searching for the second doublet component at the *same redshift* in the *Feature List*. Let λ_1 and λ_2 be the rest wavelengths of the doublet with $\lambda_1 < \lambda_2$, let λ_j and λ_k be the observed wavelengths on the *Feature List* with $\lambda_j < \lambda_k$ and with superscripts i and f designating beginning and ending of a feature, then

$$z = \frac{\lambda_j}{\lambda_1} - 1$$

$$\Delta\lambda = (1 + z)(\lambda_2 - \lambda_1)$$

are the *redshift* associated to the center of j th line and the expected wavelength separation of the doublet, respectively. At this point, the possible second component of the doublet is searched for, in the range

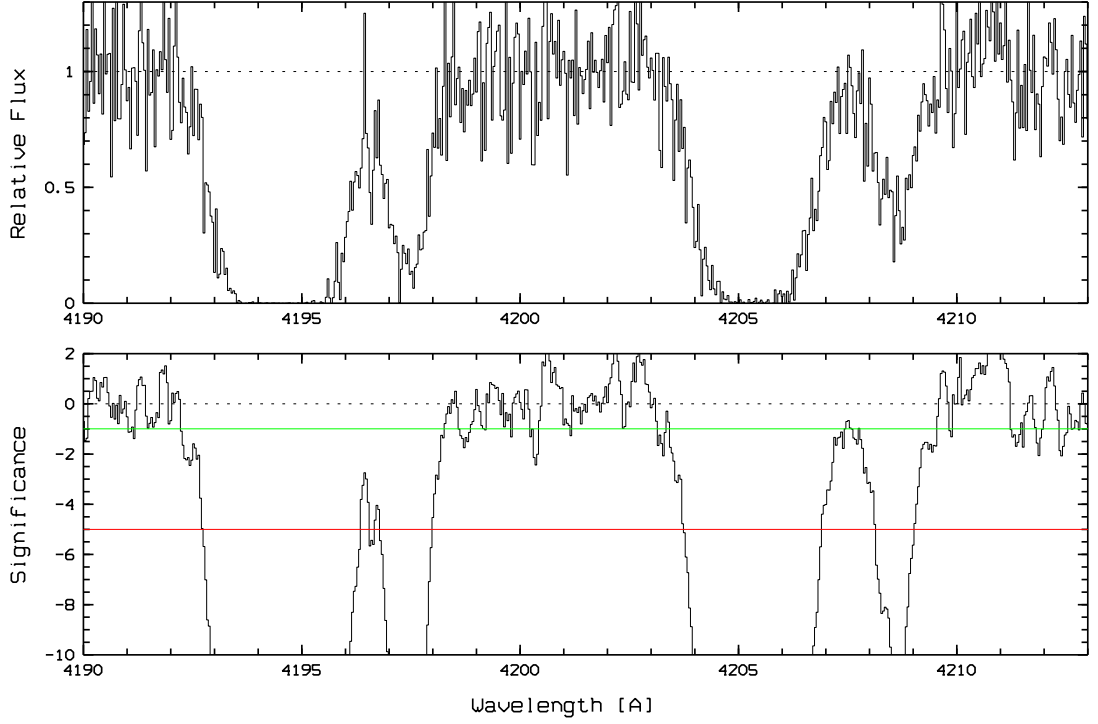


Figure 3.2 Upper: Normalized synthetic high resolution spectrum ($S/N = 5$) with a complex Mg II doublet. Bottom: Associated significant level of the *equivalent width spectrum*. Assuming a detection threshold of $N = 5$ the first component is detected as a single line while the second component is detected as two different lines.

$$\lambda_{exp}^i < \lambda_k < \lambda_{exp}^f$$

where,

$$\lambda_{exp}^{i,f} = \lambda_1^{i,f} + \Delta\lambda$$

are the expected wavelength of the bounds of the possible first component at the position of the possible second component. This method permits detections of doublets of complex systems that show only one strong line at the first component (which is typically more intense than the second) while at the position of the second component show different lines (which are separated by the noise of the spectrum. See Figure 3.2).

Table 3.2. Doublet List Example

ID _{dbl}	z	v_i, v_f [km/s]	DL	ID _{comp}	$\langle \lambda \rangle$ [Å]	W_{rest} [Å]	SL	$\Delta \lambda$ [Å]
0	0.500301	-226,277	1.51	0	4195.37	2.229 ± 0.013	172.03	7.04
				1	4206.05	1.478 ± 0.014	109.72	6.24
1	0.519453	-34,36	1.89	3	4248.93	0.080 ± 0.006	12.58	1.00
				4	4259.84	0.042 ± 0.006	6.75	0.92
2	0.529788	-52,49	1.31	5	4277.83	0.497 ± 0.006	89.77	1.44
				6	4288.83	0.378 ± 0.006	60.81	1.44

Note. — Mg II doublets found on spectrum showed in Figure 3.1.

If a second component of j th line is not found, the procedure is repeated with the next line (i.e. $(j + 1)$ th) in the *Feature List*. Finally, all detected doublet candidates are saved in a *Doublet List* which contains the redshift z , starting and ending velocity of the system at redshift z , v_i, v_f , doublet ratio $DL = \frac{W_{1st}}{W_{2nd}}$, the rest frame equivalent widths calculated as $W_{rest} = \frac{W_{obs}}{(1+z)}$, significance level of each line SL , and $\Delta \lambda$ (see Table 3.2). It is important to note that there is no condition imposed on the DL of each doublet in order to avoid missing blended systems.

3.3 Testing the Sensitivity of the Automatic Detections with Simulations

In the case of an hypothetical noiseless spectrum ($S/N \rightarrow \infty$) the Aperture Method would detect all lines independently of their shape and intensity. However, real spectra always have a non negligible contribution of noise and therefore some lines (the weakest ones) could remain undetected. Also very extended and shallow lines would be lost in the noise.

For this reason, it is important to determine the efficiency of the automatic detection algorithm in order to quantify the fraction of lines lost in the noise. I checked this by running the program over high resolution synthetic spectra containing in each case a Mg II ² doublet located at an arbitrary redshift $z = 0.5$. The synthetic spectra have $R = 40\,000$, which is the typical resolution of the real spectra used in this work. I used different column densities N and Doppler parameters b of the doublet to test different equivalent widths. I also used different signal-to-noise ratios to take into account that the minimum equivalent width W_{min} of a line that can be detected at a given significance level is proportional to the noise.

²The choice of this doublet is arbitrary and does not affect the estimate of detection efficiency for a single line.

Table 3.3. Efficiency of Line Automatic Detection using $b = 5 \text{ km s}^{-1}$.

$W_{min}^{std} _{voigt}$	$\log N [\text{cm}^{-2}]$	$b [\text{km s}^{-1}]$	S/N	$(W_{min}^{obs}/W_{min}^{std}) _{pixel}$	Efficiency
0.02	12	5	20	0.02/0.02	51/51 \sim 100%
			10	0.02/0.02	16/51 \sim 31%
			8	0.03/0.02	4/51 \sim 8%
			5	...	0/51 \sim 0%
			4	...	0/51 \sim 0%
3.33	...	0/51 \sim 0%			
0.04	12.3	5	10	0.03/0.04	51/51 \sim 100%
			8	0.03/0.04	47/51 \sim 92%
			5	0.04/0.04	11/51 \sim 22%
			4	...	0/51 \sim 0%
			3.33	...	0/51 \sim 0%
0.05	12.5	5	10	0.05/0.05	51/51 \sim 100%
			8	0.05/0.05	51/51 \sim 100%
			5	0.04/0.05	39/51 \sim 77%
			4	0.05/0.05	20/51 \sim 39%
			3.33	0.07/0.05	10/51 \sim 20%
0.07	12.7	5	10	0.07/0.07	51/51 \sim 100%
			8	0.07/0.07	51/51 \sim 100%
			5	0.07/0.07	51/51 \sim 100%
			4	0.06/0.07	43/51 \sim 84%
			3.33	0.06/0.07	23/51 \sim 45%
0.11	13	5	10	0.10/0.11	51/51 \sim 100%
			5	0.10/0.11	51/51 \sim 100%
			4	0.09/0.11	51/51 \sim 100%
			3.33	0.09/0.11	49/51 \sim 96%

A total of 2550 different synthetic spectra were created using a signal-to-noise ratio of $S/N = \{3.33, 4, 5, 8, 10, 20\}$ for a column density of $\log N = 12 \text{ cm}^{-2}$, using values of $S/N = \{3.33, 4, 5, 8, 10\}$ for column densities of $\log N = \{12.3, 12.5, 12.7\} \text{ cm}^{-2}$, and using values of $S/N = \{3.33, 4, 5, 10\}$ for a column density of $\log N = 13 \text{ cm}^{-2}$. In addition, two Doppler parameters were used $b = \{5, 15\} \text{ km s}^{-1}$ to quantify the effect of missing extended lines, i.e. the fact that W_{min} would increase for a population of lines that have a greater observed b parameter. Each of the previous cases were repeated 51 times using different *seeds* to generate the gaussian noise.

Tables 3.3 and 3.4 show the limits of automatic detection lines resulting from the simulations. The efficiency is inferred by counting how many doublets were detected of the total number of input doublets (51), for different secondary component equivalent widths obtained from a Voigt profile $W_{min}^{std}|_{voigt}$ (varying N and b) and for different S/N , always using a detection threshold of $N = 2.5$ which corresponds to a 5σ confidence level in the primary component of the doublet. It is clear that the observed equivalent width obtained from the automatic detection (using pixel integration), $W_{min}^{obs}|_{pixel}$, is not always equal to the expected equivalent width obtained from pixel integration of the same line without noise, $W_{min}^{std}|_{pixel}$. Also note that $W_{min}^{std}|_{pixel}$ is almost always equal to $W_{min}^{std}|_{voigt}$ (as expected).

Figure 3.3 shows, as an example, six synthetic Mg II doublets that can be detected by the algorithm with 100% efficiency. It is clear that as the signal-to-noise ratio decreases, the minimum equivalent width that can be detected increases.

Table 3.4. Efficiency of Line Automatic Detection using $b = 15 \text{ km s}^{-1}$.

$W_{min}^{std} _{voigt}$	$\log N [\text{cm}^{-2}]$	$b [\text{km s}^{-1}]$	S/N	$(W_{min}^{obs}/W_{min}^{std}) _{pixel}$	Efficiency
0.02	12	15	20	0.01/0.02	48/51 \sim 94%
			10	0.03/0.02	6/51 \sim 12%
			8	...	0/51 \sim 0%
			5	...	0/51 \sim 0%
			4	...	0/51 \sim 0%
3.33	...	0/51 \sim 0%			
0.04	12.3	15	10	0.03/0.04	48/51 \sim 94%
			8	0.03/0.04	35/51 \sim 69%
			5	0.05/0.04	5/51 \sim 10%
			4	...	0/51 \sim 0%
			3.33	...	0/51 \sim 0%
0.06	12.5	15	10	0.05/0.06	51/51 \sim 100%
			8	0.05/0.06	51/51 \sim 100%
			5	0.04/0.06	36/51 \sim 71%
			4	0.06/0.06	13/51 \sim 26%
			3.33	0.08/0.06	7/51 \sim 14%
0.09	12.7	15	10	0.08/0.09	51/51 \sim 100%
			8	0.08/0.09	51/51 \sim 100%
			5	0.07/0.09	51/51 \sim 100%
			4	0.07/0.09	48/51 \sim 94%
			3.33	0.07/0.09	37/51 \sim 73%
0.16	13	15	10	0.15/0.17	51/51 \sim 100%
			5	0.14/0.17	51/51 \sim 100%
			4	0.14/0.17	51/51 \sim 100%
			3.33	0.13/0.17	51/51 \sim 100%

In conclusion, the choice of $W_{min} \geq 0.07 \text{ \AA}$ guarantees a 100% detection of lines for $S/N \geq 5$ which is representative of our spectral GRB sample ($\gtrsim 90\%$ of the surveyed redshift paths).

3.4 Discarding False Systems

The *Doublet List* may contain false identifications. Thus, the candidate doublets were inspected by eye in order to discard those that were clear mis-identifications.

This was done using a *visualization* program which displays simultaneously the original spectrum and the significant level of the *equivalent width spectrum* in velocity space centered at the redshift of each doublet candidate. This scanning provides a robust way to filter all fake doublets since it is possible to see the shapes, relative line position, spectrum noise and understand why each candidate was detected according to the chosen detection threshold (see Figure 3.4).

To be conservative and systematic all doublet candidates were scanned, regardless of doublets with values far from the expected ones (e.g., doublets with $DR \gg 2$ or $DR \ll 1$).

The criteria to discard fake doublets were the following:

Synthetic MgII doublets at $z=0.5$

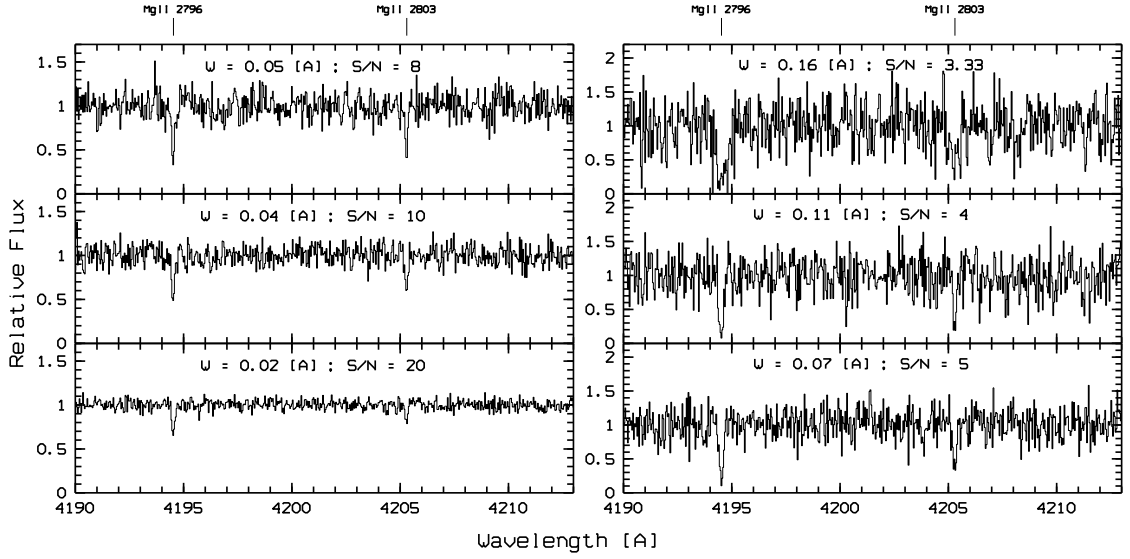


Figure 3.3 Minimum rest-frame equivalent width detected with 100% efficiency for a given signal-to-noise ratio. Equivalent width values correspond to the second component (the weakest one) of each doublet.

1. The doublet lines exhibit very different profiles (same profiles are expected).
2. The doublet lines do not appear with the expected relative separation according to the redshift (excluding blended systems).
3. One of the *lines* is evidently not a line (e.g., gaps and bad pixels).

Figures 3.5, 3.6 and 3.7 show examples of false doublets that were discarded from the *Doublet List*.

It is well known that the identification of real systems is a difficult task in moderate signal-to-noise spectra, which is the case of the GRB sample. For that reason I preferred to adopt a low detection threshold in order to not lose any possible line. The subsequent consequence is that the vast majority of the detected doublets are spurious. With this candidate line removal, the *Doublet List* is considerably reduced. The next step is to construct a *Final List* according to more certain criteria.

3.5 Measuring Equivalent Widths

Equivalent widths were calculated using both a direct pixel integration, W^{pixel} , and a Gaussian fit, W^{gauss} . I obtained W^{pixel} over the smallest velocity window that contains the whole system. The rest frame equivalent width W_r was calculated as $W_r = W_{obs}/(1+z)$.

To obtain W^{gauss} , I fitted a single or multiple Gaussian profile to the absorption lines, and summed each component of an individual system. In the case of multiples components, the associated error is, $\sigma_{system}^2 = \sum_i \sigma_i^2$, where σ_i is the individual error of component i .

I found that the equivalent widths yielded by both methods are, in general, self-consistent. Hereafter, I will use only W^{gauss} because of its robustness (continuum and blended systems are fitted, independently of the velocity window) except for poor fits (typically for saturated lines), in which case W^{pixel} will be adopted and properly indicated. See Section 4.3 for further details.

3.6 Final List of Systems

Given the impossibility to increase the signal-to-noise ratio and the relatively low number of useful optical GRB afterglow spectra, it is necessary to push the data to the limit.

For this purpose two sets of criteria were used in order to identify real systems and to create the *Final Lists*. First, a set of *strict* criteria where the systems have very high probability to be real and second, a set of *relaxed* criteria where I allow for some contamination by unreal systems. While the former gives a meaningful number density of absorption systems, the latter yields an upper limit to this number.

3.6.1 Strict Criteria

- Systems must show other transitions at the same redshift: H I and associated metal lines (e.g., Mg I and Fe II for Mg II; C III and Si IV for C IV) where the spectrum coverage allows it.
- Systems must show doublet ratios between 2:1 (unsaturated regime) and 1:1 (saturated regime).
- Systems must show exactly the expected separation between doublet components.
- Both components of the doublet must show similar profiles.

- Systems that show blended features, either produced by other lines or produced by noise, are discarded unless all previous criteria are satisfied.

3.6.2 Relaxed Criteria

- Systems must show *signs* of other transitions at the same redshift: H I and associated metal lines (e.g., Mg I and Fe II for Mg II; C III and Si IV for C IV) where the spectrum coverage allows it.
- There is no restriction on the doublet ratio value.
- Both components of the doublet must show similar profiles.
- Differences in the expected separation between doublet components are allowed if their profiles are similar.
- Systems that show blended features are not discarded.

3.6.3 Mg II Systems

For the Mg II analysis I will use both the *strict* and *relaxed* criteria in order to improve the limits on the number density of systems due to *weak* systems immersed in poor signal-to-noise data. The GRB dataset does not permit reliable detection of lines at $W_r < 0.07 \text{ \AA}$ (in contrast, previous surveys in QSO spectra have used $W_{min} = 0.02 \text{ \AA}$ for the *weak* population which is quite more sensitive than ours. See Chapter 2). Therefore, the *relaxed* criteria permits us to obtain a solid upper limit on the number density of absorption systems.

3.6.4 C IV Systems

For the C IV analysis I will use only systems that satisfy the *strict* criteria. In this case it is not necessary to use the *relaxed* criteria since the GRB data have enough signal-to-noise ratio to properly detect all systems with $W_r > 0.15 \text{ \AA}$ (this limit corresponds to W_{min} used in previous surveys in QSO spectra to define the strong C IV population which is studied in this work. See Chapter 2).

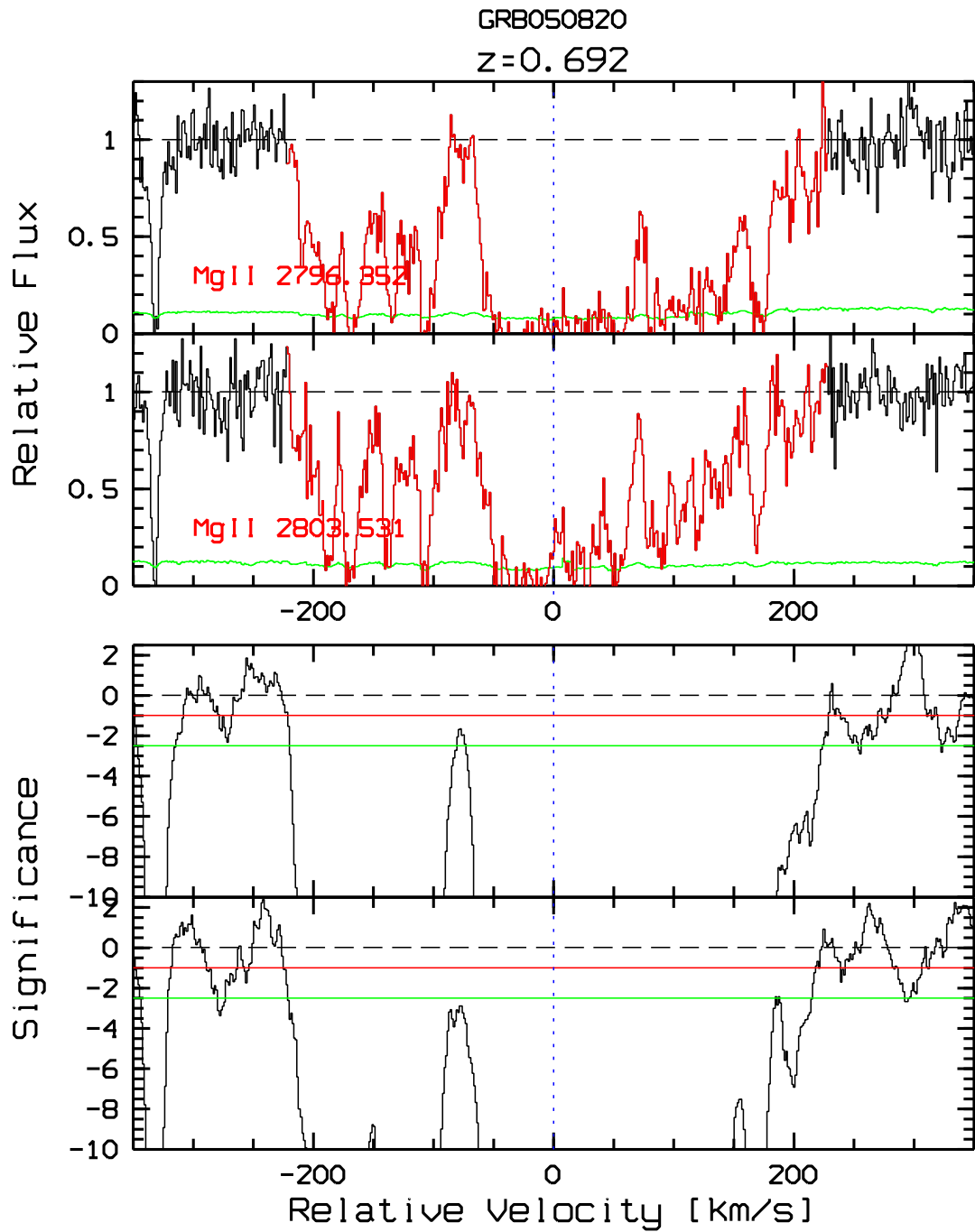


Figure 3.4 Example of the *visualization* used to discard false doublets. In this case a Mg II doublet found on *GRB050820* spectrum is shown in velocity space centered at the given redshift. The upper two panels correspond to the original spectrum: red zone is the first component width and the noise is plotted in green. The second two bottom panels are the significance level of the associated *equivalent width spectrum*. The blue dashed line at zero velocity is used to take into account the relative separation of both lines.

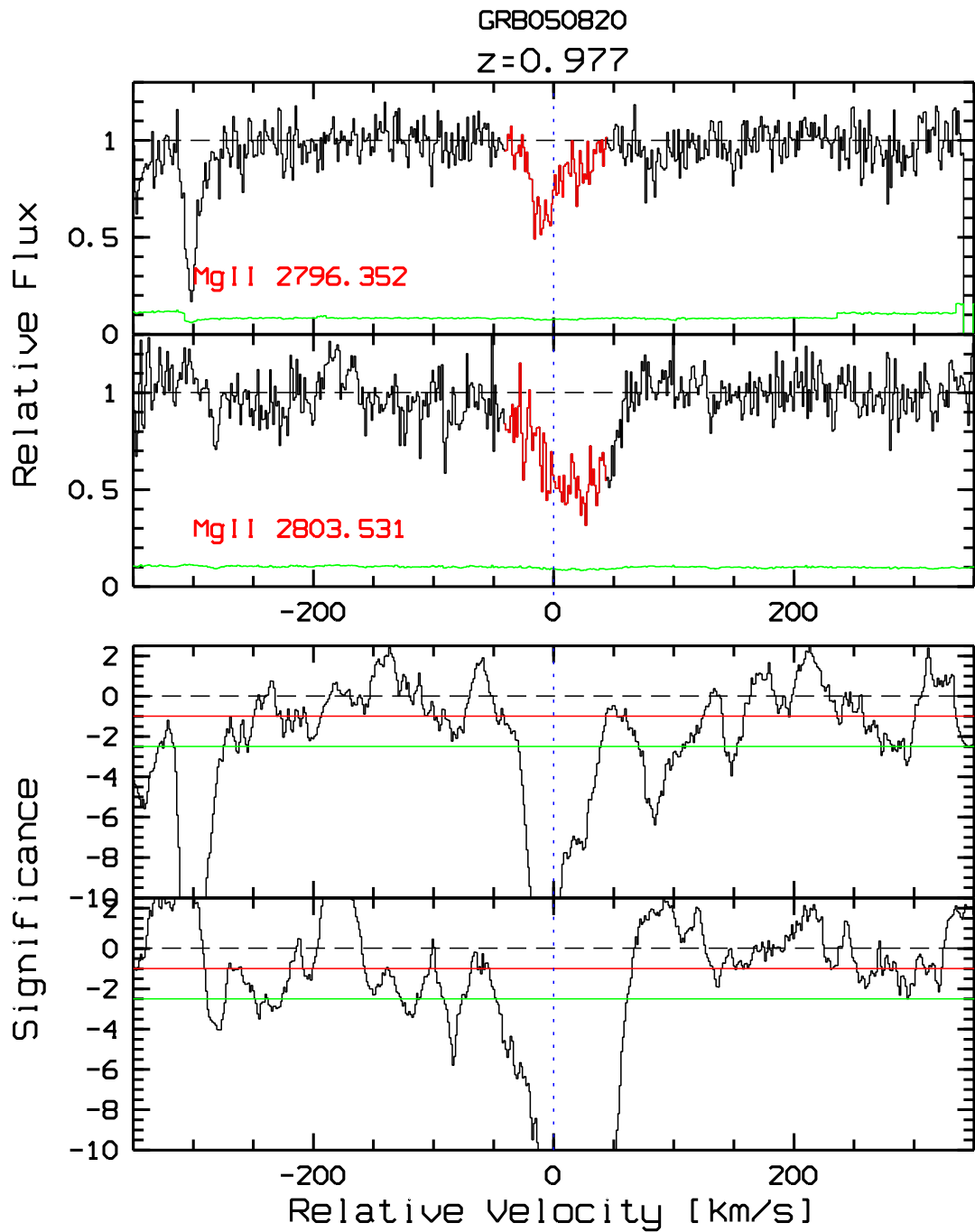


Figure 3.5 Example of a false detected Mg II doublet in the *GRB050820* spectrum that was discarded from the *Doublet List*. It is clear that both lines appear at an unexpected separation at the given redshift and moreover, both lines exhibit different shapes.

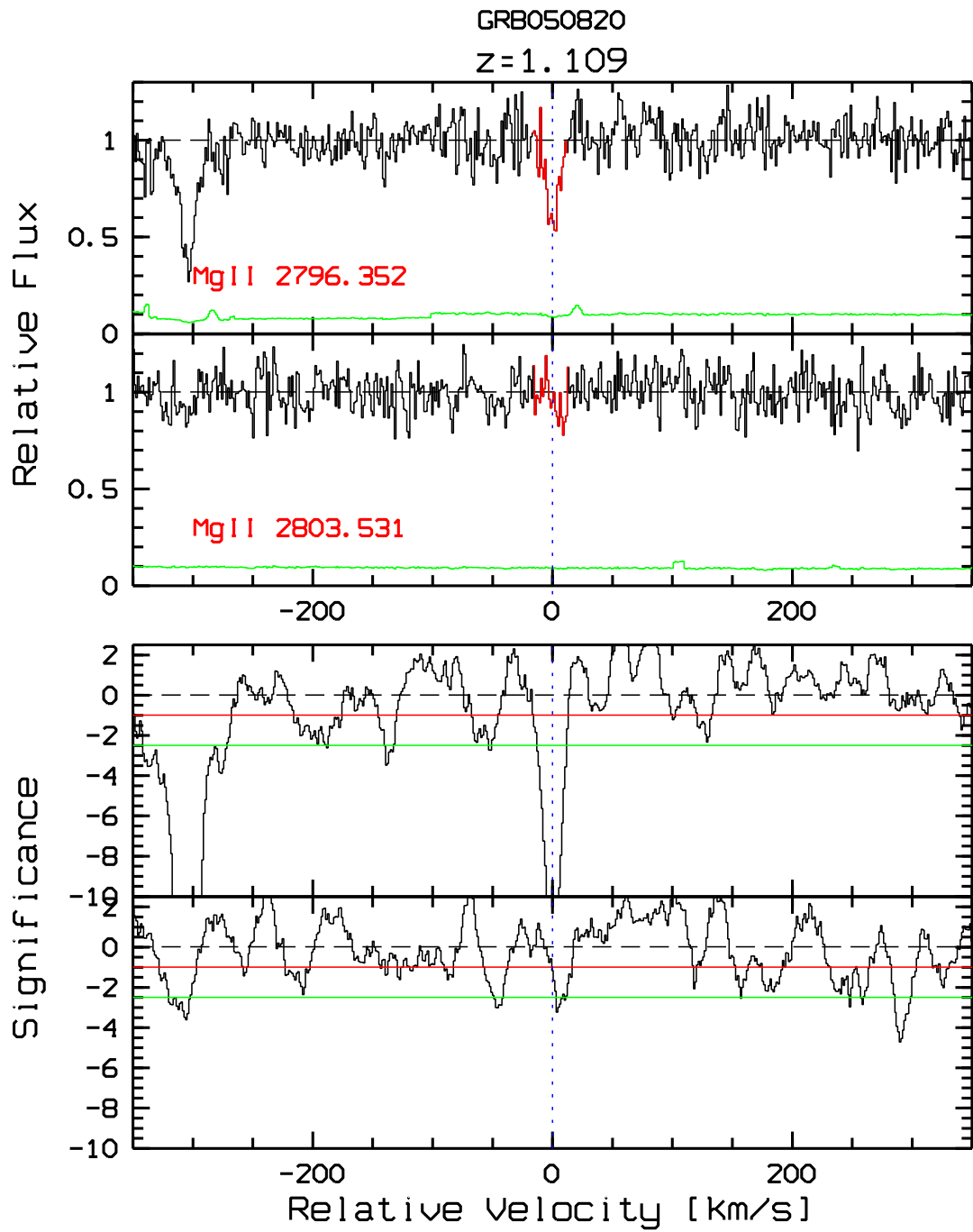


Figure 3.6 Example of a false detected Mg II doublet in the *GRB050820* spectrum that was discarded from the *Doublet List*. It is clear that both component have different profiles.

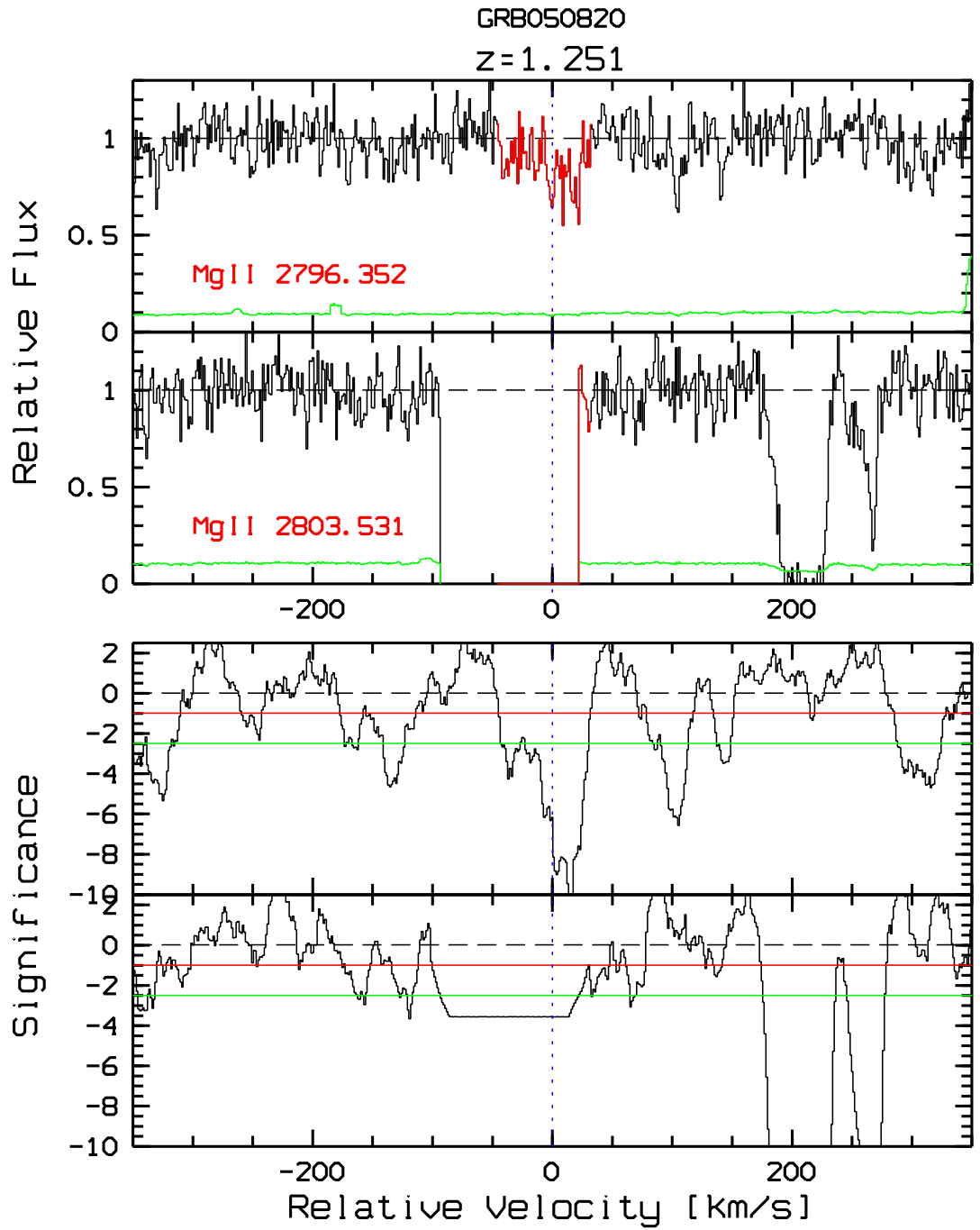


Figure 3.7 Example of a false detected Mg II doublet in the *GRB050820* spectrum that was discarded from the *Doublet List*. It is clear that the secondary component was produced by a gap in the spectrum.

Chapter 4

Definition of the Samples

In this section I define the different samples used to study the incidence of absorption systems. The Full Samples correspond to all the systems found in the GRB spectra, therefore this sample is incomplete and is contaminated by noise. Statistical Samples, subsets of Full Samples, are defined in the same way as previous studies with certain W_{min} , significance level of detection and an adequate source decontamination. Also, as mentioned in Section 2, to discount contamination by hydrogen lines, systems in the Full Samples were searched redward of the Ly α forest. Only Statistical Samples are used to compare results between QSOs and GRBs absorption systems.

4.1 Mg II Sample

4.1.1 Full Sample

1. Systems searched between $z_{start} < z_{abs}^{MgII} \leq z_{GRB}^{MgII}$ where,

$$z_{start} = \frac{1215.67}{2796.35}(1 + z_{GRB}) - 1$$

Therefore, the Full Sample includes lines associated with the GRB host galaxy (later I will restrict the analysis to intervening Mg II systems).

2. The equivalent width of the Mg II doublet must be detected at the 5σ significance level or higher for the primary component and at 2.5σ s.l. for the secondary component.
3. A complex system is considered a single system if the velocity components are grouped within

500 km s⁻¹. This last condition is necessary to compare with previous surveys (for instance, Narayanan et al., 2007, used a velocity window of 500 km s⁻¹ to group components of a single system, however a weak Mg II absorber must be at least 1000 km s⁻¹ from any strong Mg II absorption).

The Full Sample is listed in Table 4.1 which shows the information on redshift limits for each line-of-sight, z_{abs}^{MgII} , and W_r .

4.1.2 Statistical Sample

To compare the statistics of Mg II absorption along GRB sightlines with those of QSO sightlines, one must define a sample with identical equivalent width limits. Previous surveys have used $W_{min} = 0.02 \text{ \AA}$ in the rest frame (Narayanan et al., 2007). The sample of GRB spectra, however, can not be used to confidently detect lines with $W_{min} < 0.07 \text{ \AA}$ (see Figure 5.2) and also considering that the efficiency of automatic line detection falls considerably below this limit (See Tables 3.3 and 3.4). Therefore I adopt $W_{min} > 0.07 \text{ \AA}$ for *both* lines of the Mg II doublet.

In addition, to avoid contributions from galaxies clustered around the GRB hosts and wind features that might be associated with the GRB environment, I define a Statistical Sample with the same z_{start} as in the Full Sample but z_{end} at 5000 km s⁻¹ from z_{GRB} (i.e., to remove possible source contamination). Note that these criteria is exactly the same used in previous QSO surveys.

Table 4.1. Mg II Full Sample

GRB	z_{GRB}	z_{start}	$z_{end}^{\beta c=5000 km s^{-1}}$	z_{abs}^{MgII}	$W_r^{pixel}(2796)$ $W_r^{pixel}(2803)$	$W_r^{gauss}(2796)$ $W_r^{gauss}(2803)$	Comments
021004	2.335	0.44795	2.27938	0.554904††	0.562 ± 0.016	0.561 ± 0.037	$DR > 2$
					0.199 ± 0.014	0.172 ± 0.016	
				0.56446†	0.140 ± 0.013	0.097 ± 0.011	
					0.129 ± 0.014	0.093 ± 0.013	
				0.91485	0.095 ± 0.007	r 0.062 ± 0.006	a
					0.061 ± 0.007	0.066 ± 0.006	
				1.31633	0.049 ± 0.008	d 0.053 ± 0.013	
					0.017 ± 0.006	b 0.014 ± 0.009	
				1.38067† † †	1.633 ± 0.016	r 1.675 ± 0.087	
					1.305 ± 0.020	b 0.895 ± 0.060	
				1.60274† † †	r 1.389 ± 0.026	1.500 ± 0.017	
					1.132 ± 0.010	r 1.150 ± 0.015	
				1.76437	0.041 ± 0.004	b 0.037 ± 0.008	
					0.029 ± 0.005	r 0.024 ± 0.006	
2.29920††	0.335 ± 0.016	r 0.424 ± 0.035					
	0.197 ± 0.013	r 0.264 ± 0.028					
2.32893	0.814 ± 0.078	r 1.003 ± 0.114	host				
	0.783 ± 0.032	b 1.157 ± 0.150					
050730	3.97	1.5781	3.88711	1.22208†	0.142 ± 0.026	0.122 ± 0.030	g
					0.328 ± 0.020	0.106 ± 0.027	
				1.77317† † †	0.923 ± 0.019	0.946 ± 0.042	
					0.792 ± 0.020	0.783 ± 0.032	
				2.25378† † † ~	1.125 ± 0.034	b 0.979 ± 0.050	
	0.789 ± 0.042	b 0.815 ± 0.053					
2.32977†	0.181 ± 0.019	0.170 ± 0.029	a				
	0.175 ± 0.022	0.191 ± 0.036					
050820	2.6147	0.5694	2.55441	0.616511††	0.325 ± 0.015	r 0.316 ± 0.020	g, $DR < 1$
					0.498 ± 0.013	r 0.499 ± 0.019	
				0.69153† † †	2.988 ± 0.022	r 2.922 ± 0.149	
					2.335 ± 0.025	b 1.672 ± 0.113	
				1.43000† † †	
					1.262 ± 0.016	1.292 ± 0.022	
				1.56400	0.040 ± 0.006	0.027 ± 0.005	g, $DR < 1$
	0.069 ± 0.007	0.065 ± 0.012					
1.61126	0.021 ± 0.004	b 0.024 ± 0.008	a,g				
	0.019 ± 0.004	r 0.014 ± 0.006					
1.62040†	0.226 ± 0.007	0.228 ± 0.008					
					
050922C	2.199	0.3889	2.14565	0.41750†	0.264 ± 0.029	0.212 ± 0.042	a,g
					0.292 ± 0.027	b 0.324 ± 0.042	
				0.63691†	0.177 ± 0.013	0.167 ± 0.015	g, $DR > 2$
					0.079 ± 0.017	0.078 ± 0.013	
				1.10731† † † ~	0.532 ± 0.031	r 0.628 ± 0.054	
					0.359 ± 0.020	r 0.388 ± 0.052	
				1.56689	0.102 ± 0.008	0.109 ± 0.017	
					0.049 ± 0.008	0.059 ± 0.011	
2.00859	0.171 ± 0.015	0.128 ± 0.024	$DR > 2$				
	0.044 ± 0.017	0.044 ± 0.016					
2.19950	1.062 ± 0.058	r 1.162 ± 0.097	$DR < 1$, host				
	1.518 ± 0.035	r 1.517 ± 0.179					

Table 4.1 (cont'd)

GRB	z_{GRB}	z_{start}	$z_{end}^{\beta c=5000 km s^{-1}}$	z_{abs}^{MgII}	$W_r^{pixel}(2796)$ $W_r^{pixel}(2803)$	$W_r^{gauss}(2796)$ $W_r^{gauss}(2803)$	Comments
051111	1.549	0.1067	1.50649	0.82735††	0.369 ± 0.010	0.358 ± 0.011	
					0.297 ± 0.012	0.287 ± 0.017	
				1.10680†	0.173 ± 0.011	0.169 ± 0.009	a,g,DR < 1
					0.233 ± 0.004	0.242 ± 0.007	
				1.18910†††	2.091 ± 0.011	r 2.288 ± 0.037	
					1.741 ± 0.010	b 2.047 ± 0.062	
060418	1.49	0.0811	1.44847	1.19325††	0.334 ± 0.005	0.328 ± 0.007	g,DR > 2
					0.162 ± 0.005	0.146 ± 0.006	
				1.54913	2.343 ± 0.010	b 2.470 ± 0.028	host
					2.118 ± 0.010	b 2.187 ± 0.038	
060418	1.49	0.0811	1.44847	0.60259†††	1.299 ± 0.015	b 1.425 ± 0.024	
					1.233 ± 0.015	b 1.344 ± 0.023	
				0.65593†††	0.975 ± 0.010	r 0.989 ± 0.030	
					0.788 ± 0.011	r 0.794 ± 0.021	
				1.10724†††	1.832 ± 0.020	r 1.863 ± 0.255	
					1.499 ± 0.017	b 1.660 ± 0.031	
060607	3.082	0.7723	3.01392	1.32221†	0.214 ± 0.009	0.210 ± 0.012	
					0.133 ± 0.010	0.130 ± 0.013	
				1.48964	1.968 ± 0.017	2.126 ± 0.023	host
					1.711 ± 0.017	1.889 ± 0.022	
				0.94246	0.051 ± 0.003	0.030 ± 0.007	
					0.023 ± 0.003	0.023 ± 0.006	
				1.51057†	0.197 ± 0.010	0.204 ± 0.009	
					0.116 ± 0.011	0.129 ± 0.011	
				1.80208†††	1.906 ± 0.011	b 2.166 ± 0.052	
					1.552 ± 0.016	b 1.877 ± 0.034	
				1.92549†	0.144 ± 0.009	...	a
					0.075 ± 0.011	...	
2.21271	0.073 ± 0.007	0.061 ± 0.006	a,g,DR ~ 1				
	0.069 ± 0.009	0.065 ± 0.011					
2.24431	0.064 ± 0.010	0.059 ± 0.007	g				
	0.029 ± 0.010	0.027 ± 0.011					
2.27840†† ~	0.293 ± 0.015	0.310 ± 0.015					
	0.286 ± 0.017	0.282 ± 0.019					
2.32841† ~	0.081 ± 0.011	0.059 ± 0.010	g				
	0.106 ± 0.011	0.095 ± 0.011					
2.33922†† ~	0.306 ± 0.014	0.270 ± 0.015	g,DR < 1				
	0.400 ± 0.012	0.390 ± 0.020					
2.37052	0.125 ± 0.013	0.084 ± 0.008	g				
	0.067 ± 0.016	0.058 ± 0.011					
2.39882	0.218 ± 0.006	0.217 ± 0.014	a,g,DR > 2				
	0.064 ± 0.009	0.069 ± 0.010					
2.40517††	0.556 ± 0.031	0.467 ± 0.039	a				
	0.232 ± 0.019	0.292 ± 0.017					
2.44767	0.070 ± 0.010	0.079 ± 0.014	a,g				
	0.036 ± 0.012	0.041 ± 0.013					
2.45071	0.119 ± 0.014	0.079 ± 0.015	a,g				
	0.048 ± 0.017	0.050 ± 0.012					
2.47550	0.057 ± 0.009	0.058 ± 0.010	g				
	0.039 ± 0.013	b 0.043 ± 0.019					

Note. — All Mg II absorption systems found between $z_{GRB}^{Ly\alpha} < z^{MgII} \leq z_{GRB}^{MgII}$.

^a minimum of lines does not match.

^b Bad fit.

^r Regular fit.

^g Different profile shapes, contamination.

Samples: † is defined as systems with $W_r(2806) \geq 0.07 \text{ \AA}$, †† is defined as systems with $W_r(2796) \geq 0.3 \text{ \AA}$, ††† is defined as systems with $W_r(2796) \geq 0.6 \text{ \AA}$ and †††† is defined as systems with $W_r(2796) \geq 1.0 \text{ \AA}$. The ~ indicates that the criteria is satisfied only by either W_r^{pixel} or W_r^{gauss} , but not both simultaneously.

Table 4.2. Number of Absorbers in Statistical Mg II Subsamples

Criteria	Sample 1	Sample 2	Sample 3	Sample 4
Strict	4	4	2	9
Relaxed	11	8	2	9

Note. — See sections 3.6 and 4.1.2 for the criteria and subsamples definitions.

Statistical Subsamples

I define four subsamples from the Statistical Sample in order to study the behavior of the different population of Mg II absorption systems. The subsamples are:

- Sample 1: Systems with $W_r(2803) \geq 0.07 \text{ \AA}$ and $W_r(2796) < 0.3 \text{ \AA}$ (labeled with † in Table 4.1)
- Sample 2: Systems with $W_r(2796) \geq 0.3 \text{ \AA}$ and $W_r(2796) < 0.6 \text{ \AA}$ (labeled with †† in Table 4.1)
- Sample 3: Systems with $W_r(2796) \geq 0.6 \text{ \AA}$ and $W_r(2796) < 1.0 \text{ \AA}$ (labeled with ††† in Table 4.1)
- Sample 4: Systems with $W_r(2796) \geq 1.0 \text{ \AA}$ (labeled with †††† in Table 4.1)

Systems labeled with \sim in Table 4.1 fall in the limit of these definitions and therefore they satisfy either the W_r^{pixel} or W_r^{gauss} condition, but not both simultaneously.

Finally, the Statistical Sample is composed of 30 absorption systems (systems labeled with daggers in Table 4.1), out of which 19 satisfy the *strict* criteria (all systems without comments on Table 4.1; see Figures 4.1 to 4.19 for velocity plots) and are used to compute the statistics (I will later study an upper limit of the number density using all systems, i.e., including systems that only satisfied the *relaxed* criteria). Sample 1 is composed of 4 systems while Samples 2, 3 and 4 are composed of 4, 2 and 9 systems, respectively. If I consider dubious systems (i.e., systems which satisfy the *relaxed* criteria labeled with daggers but with comments in Table 4.1; see Figure 4.36 to 4.46 for velocity plots) the numbers are 11 in Sample 1, 8 in Sample 2, 2 in Sample 3 and 9 in Sample 4. This information is summarized in Table 4.2.

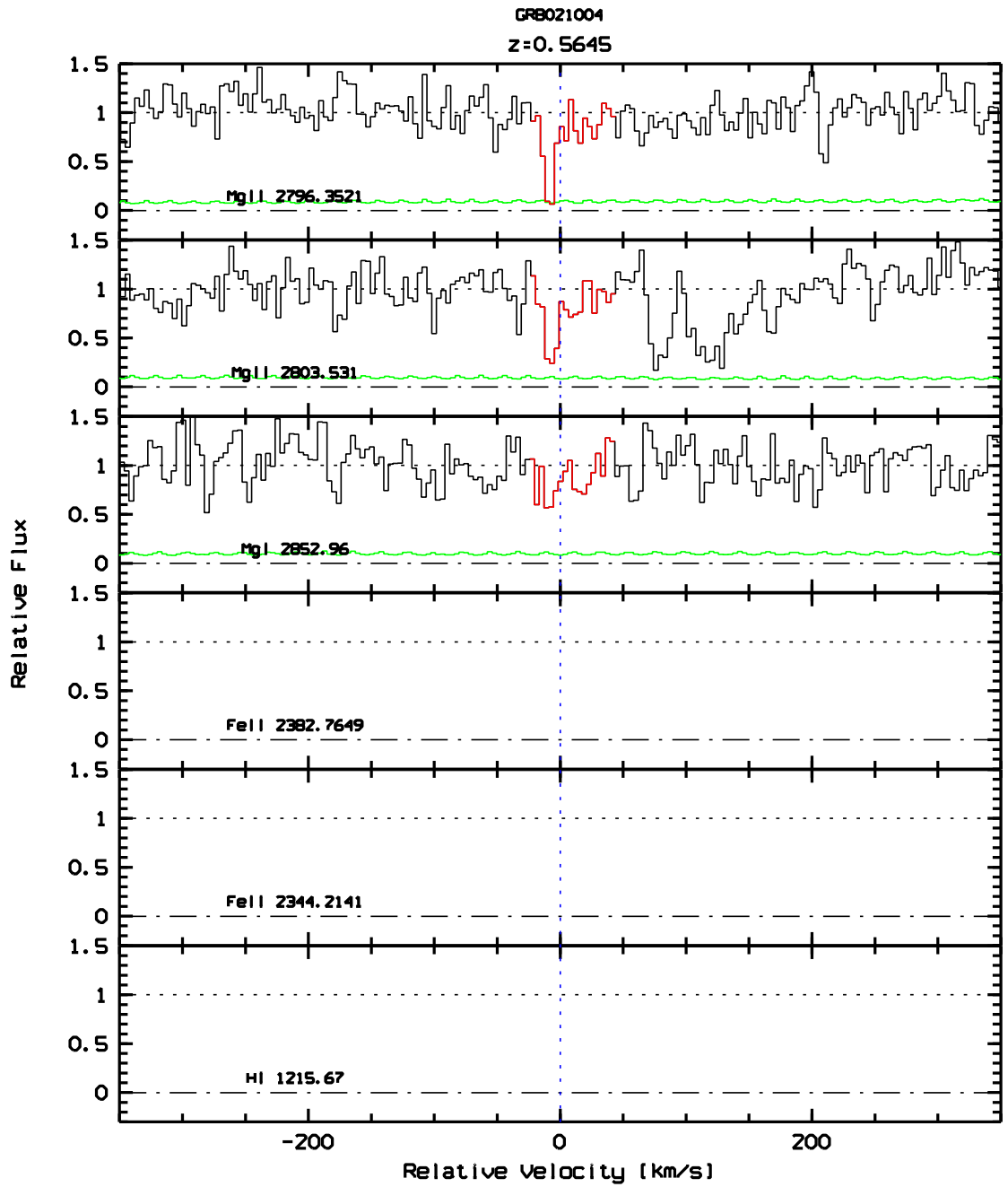


Figure 4.1 Absorption velocity profile of Mg II absorption system at $z_{abs} = 0.5645$.

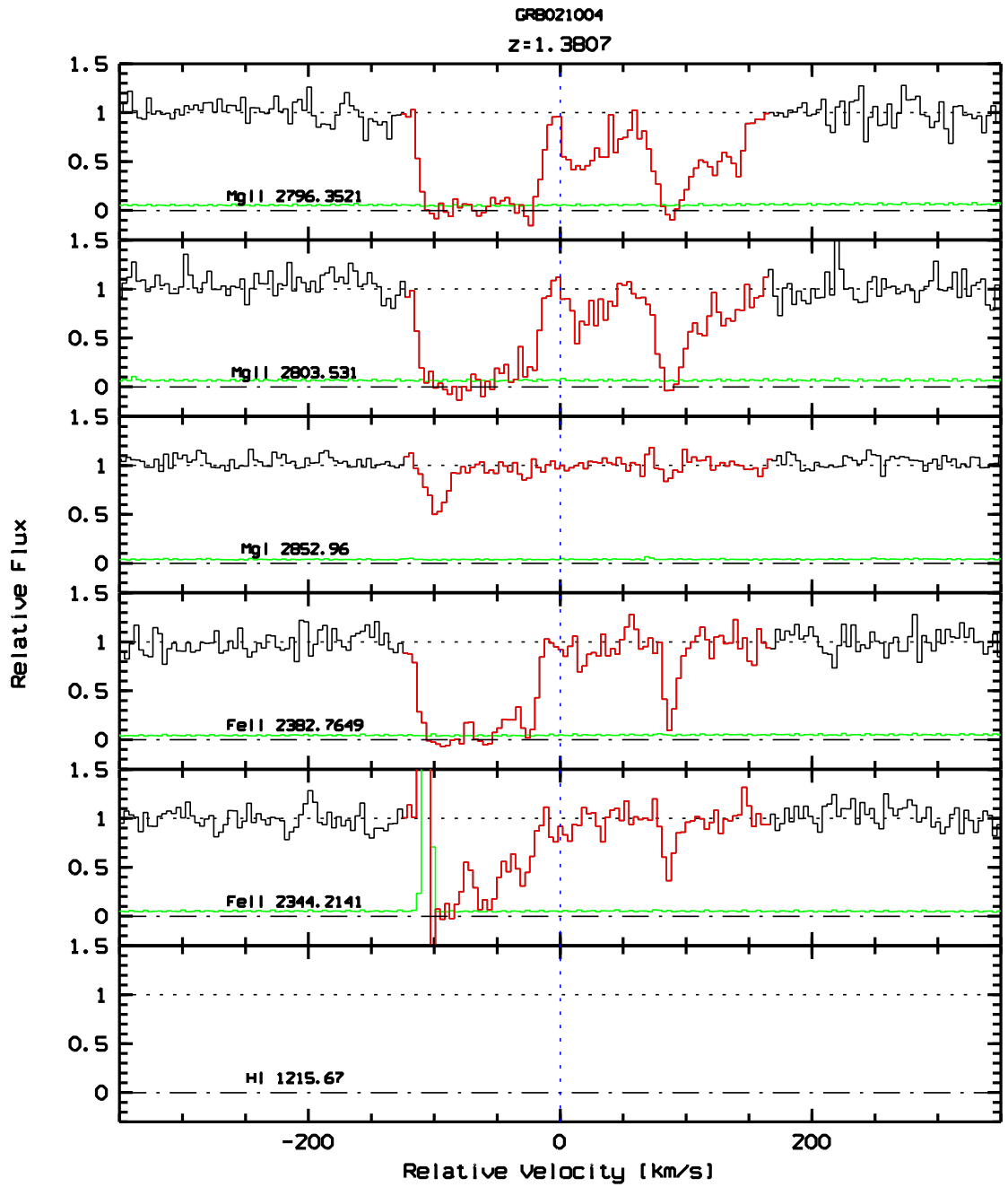


Figure 4.2 Absorption velocity profile of Mg II absorption system at $z_{abs} = 1.3807$.

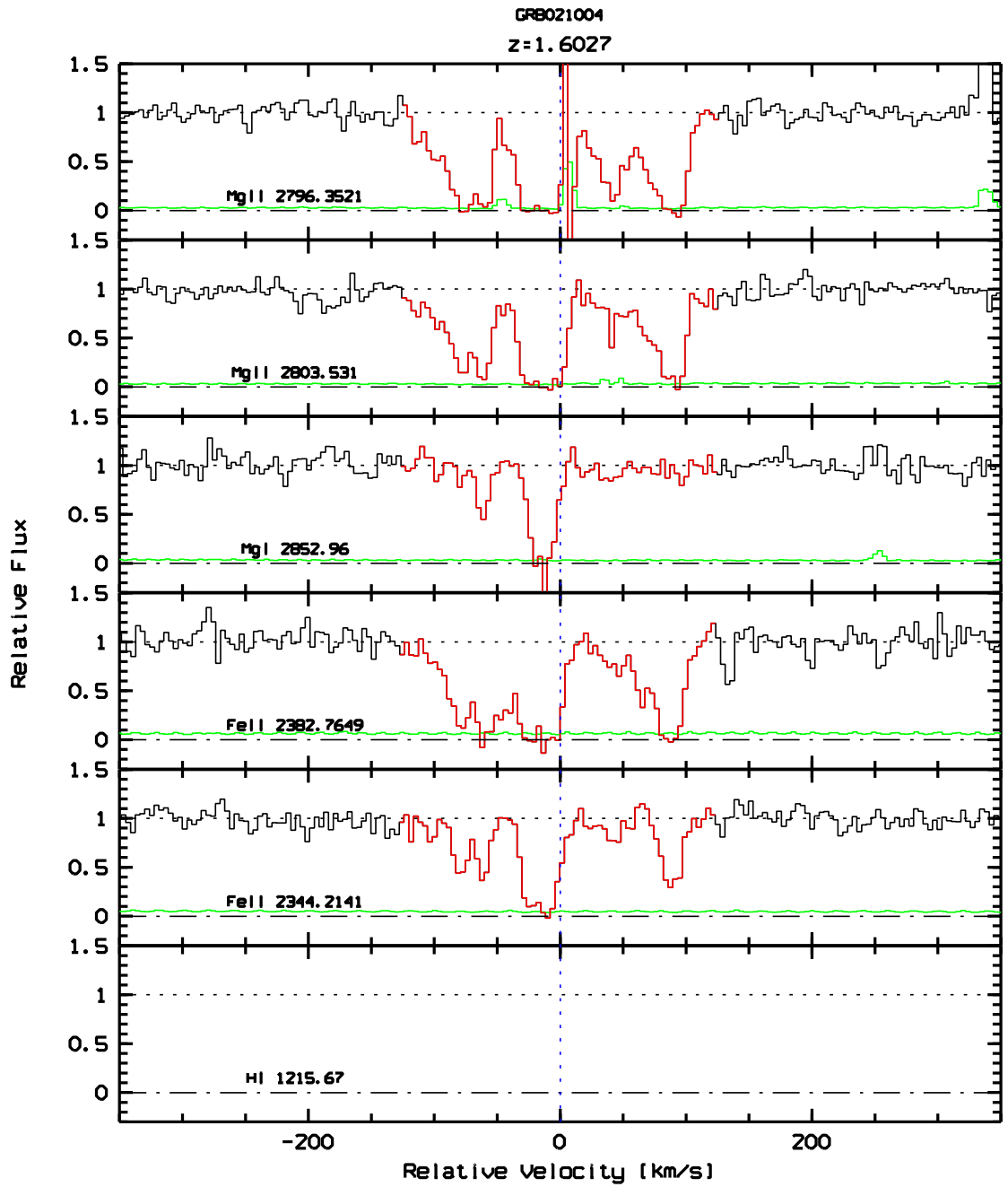


Figure 4.3 Absorption velocity profile of Mg II absorption system at $z_{abs} = 1.6027$.

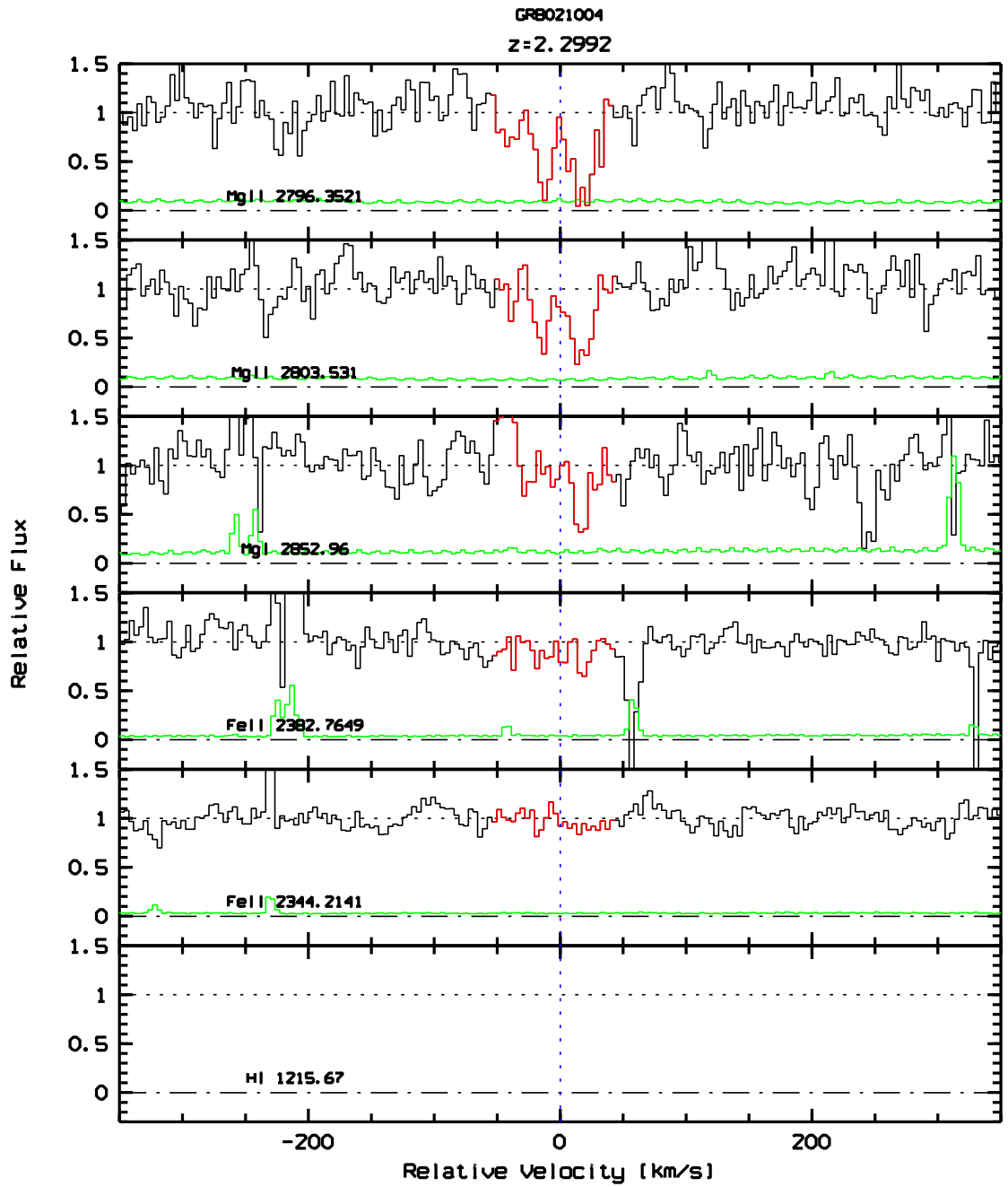


Figure 4.4 Absorption velocity profile of Mg II absorption system at $z_{abs} = 2.2992$.

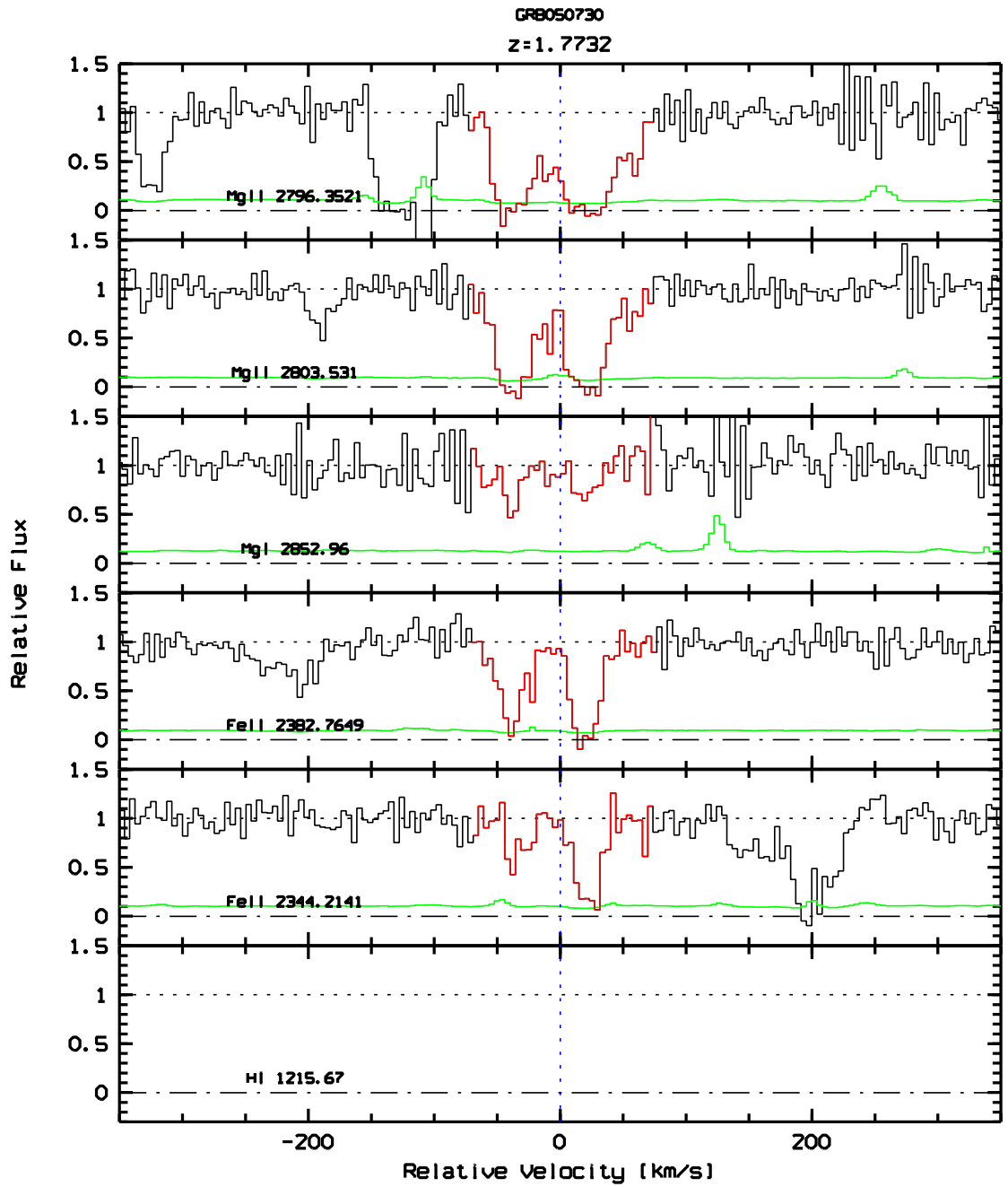


Figure 4.5 Absorption velocity profile of Mg II absorption system at $z_{abs} = 1.7732$.

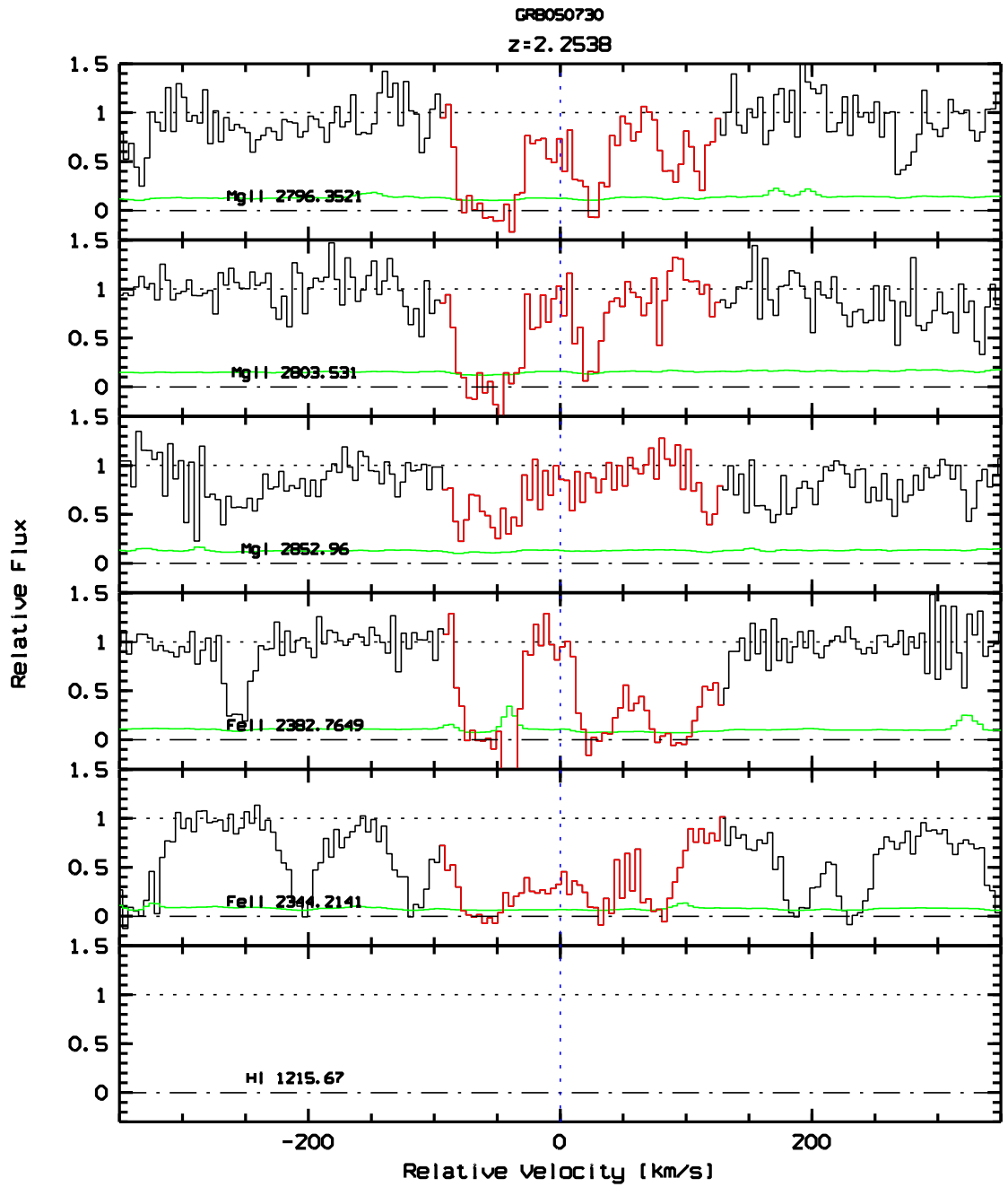


Figure 4.6 Absorption velocity profile of Mg II absorption system at $z_{abs} = 2.2538$.

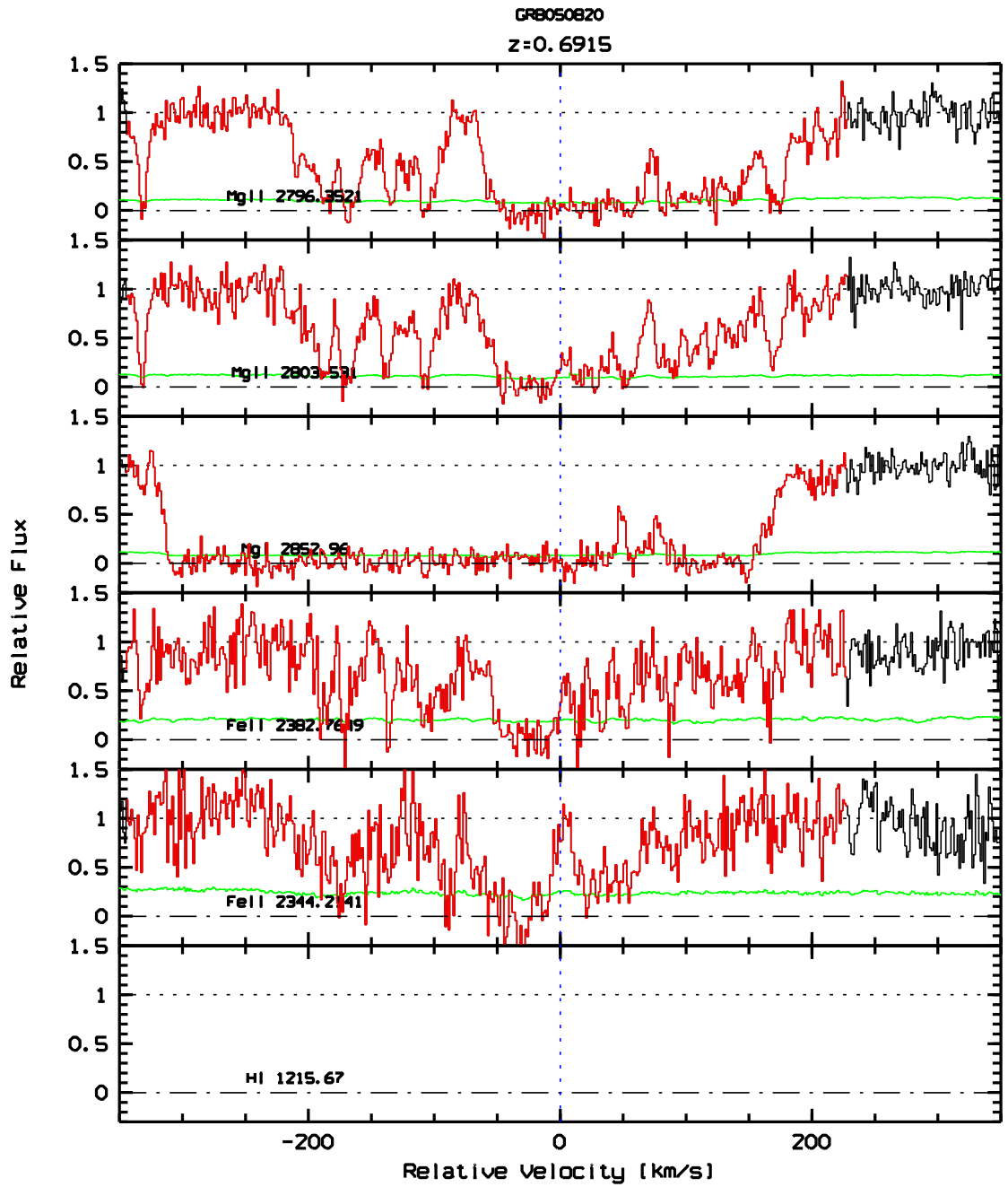


Figure 4.7 Absorption velocity profile of Mg II absorption system at $z_{abs} = 0.6915$.

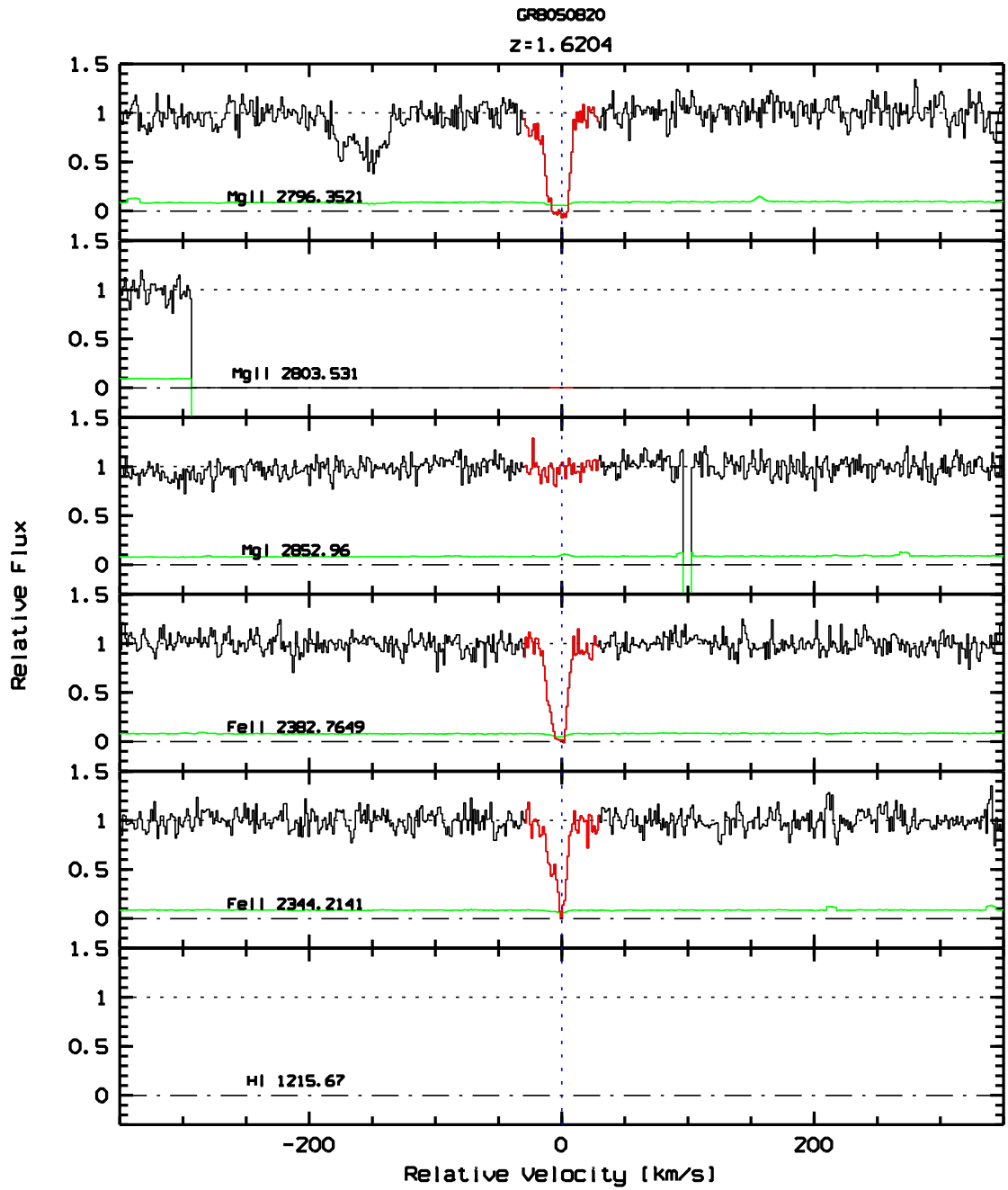


Figure 4.9 Absorption velocity profile of Mg II absorption system at $z_{abs} = 1.6204$.

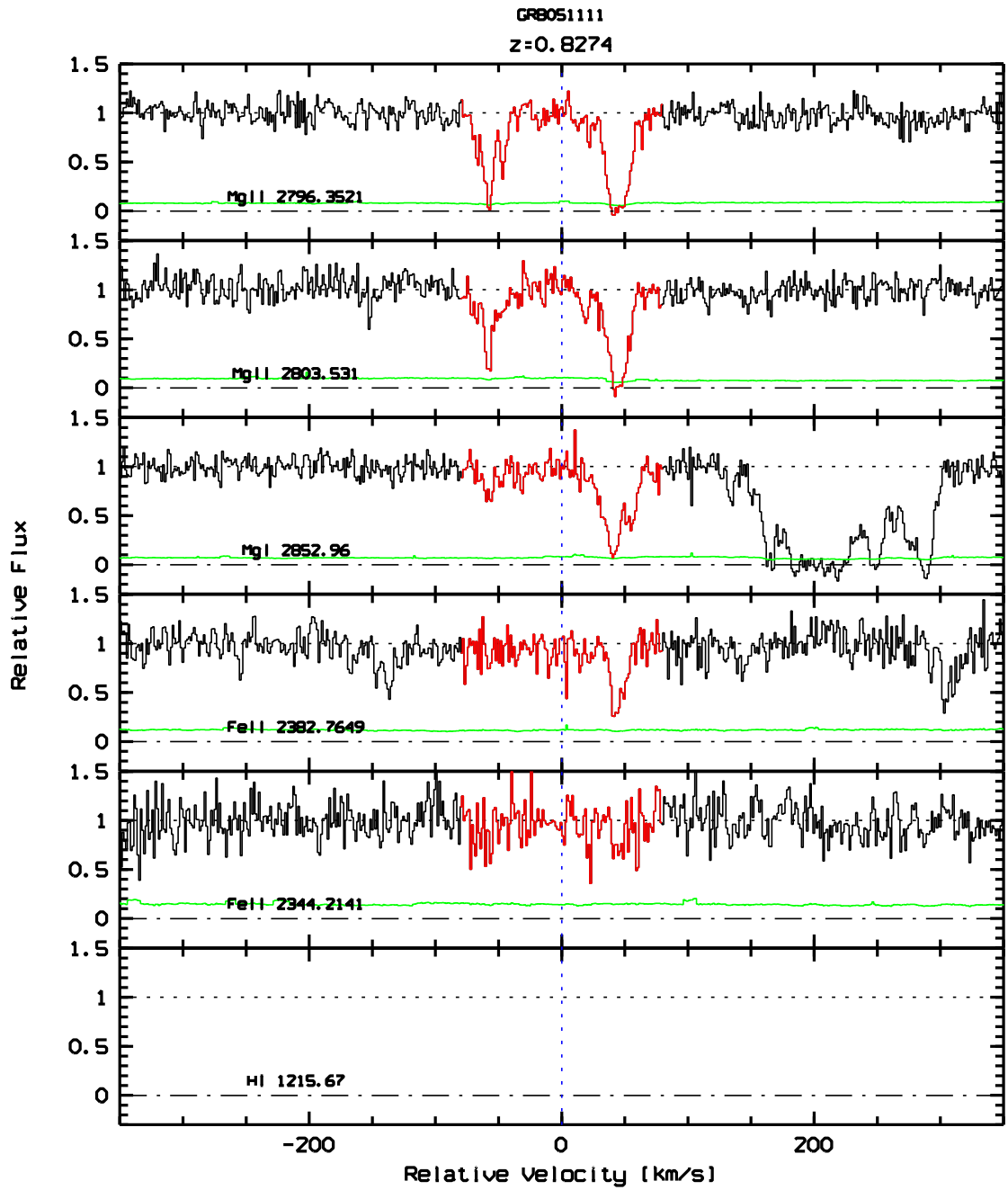


Figure 4.11 Absorption velocity profile of Mg II absorption system at $z_{abs} = 0.8274$.

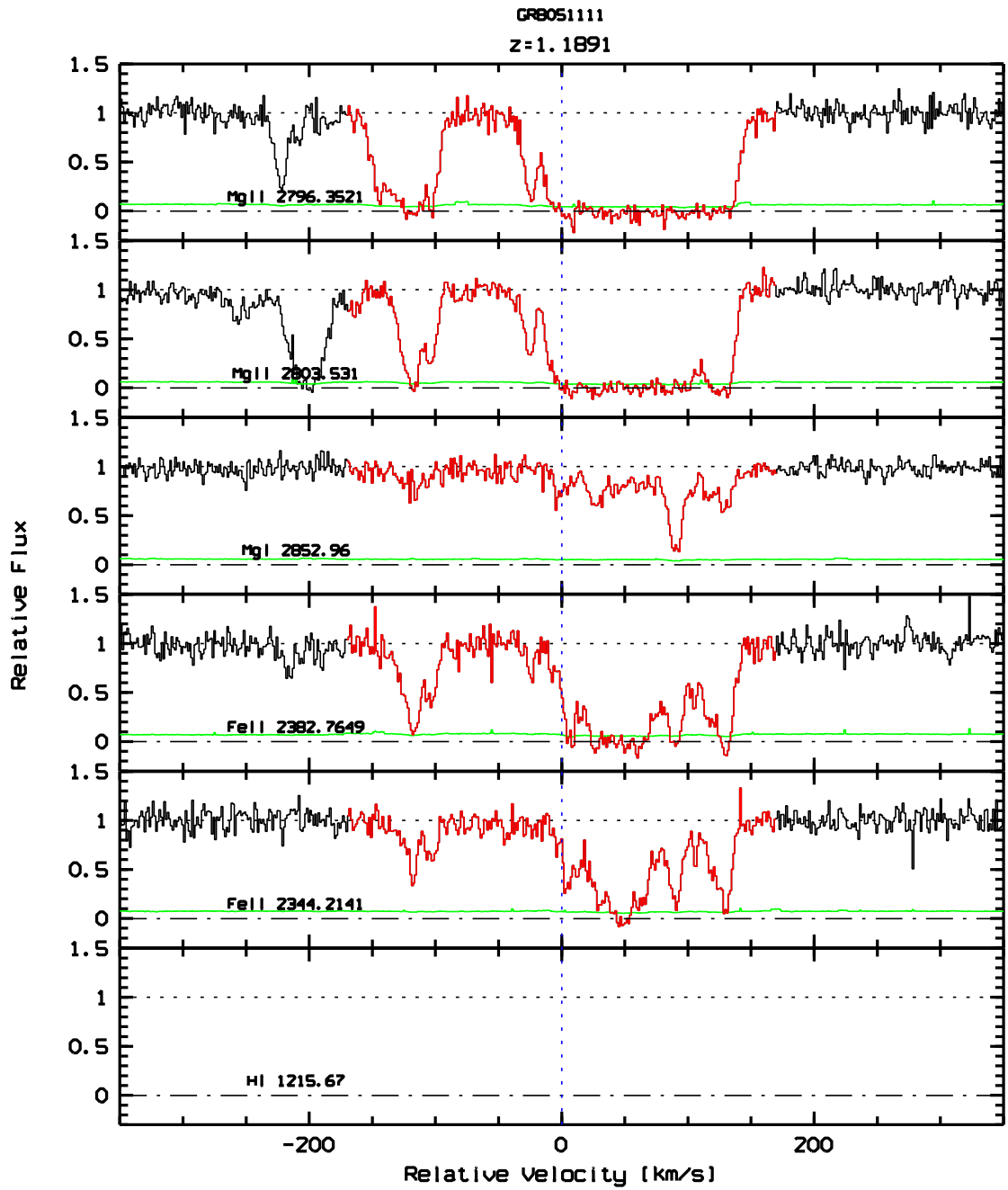


Figure 4.12 Absorption velocity profile of Mg II absorption system at $z_{abs} = 1.1891$.

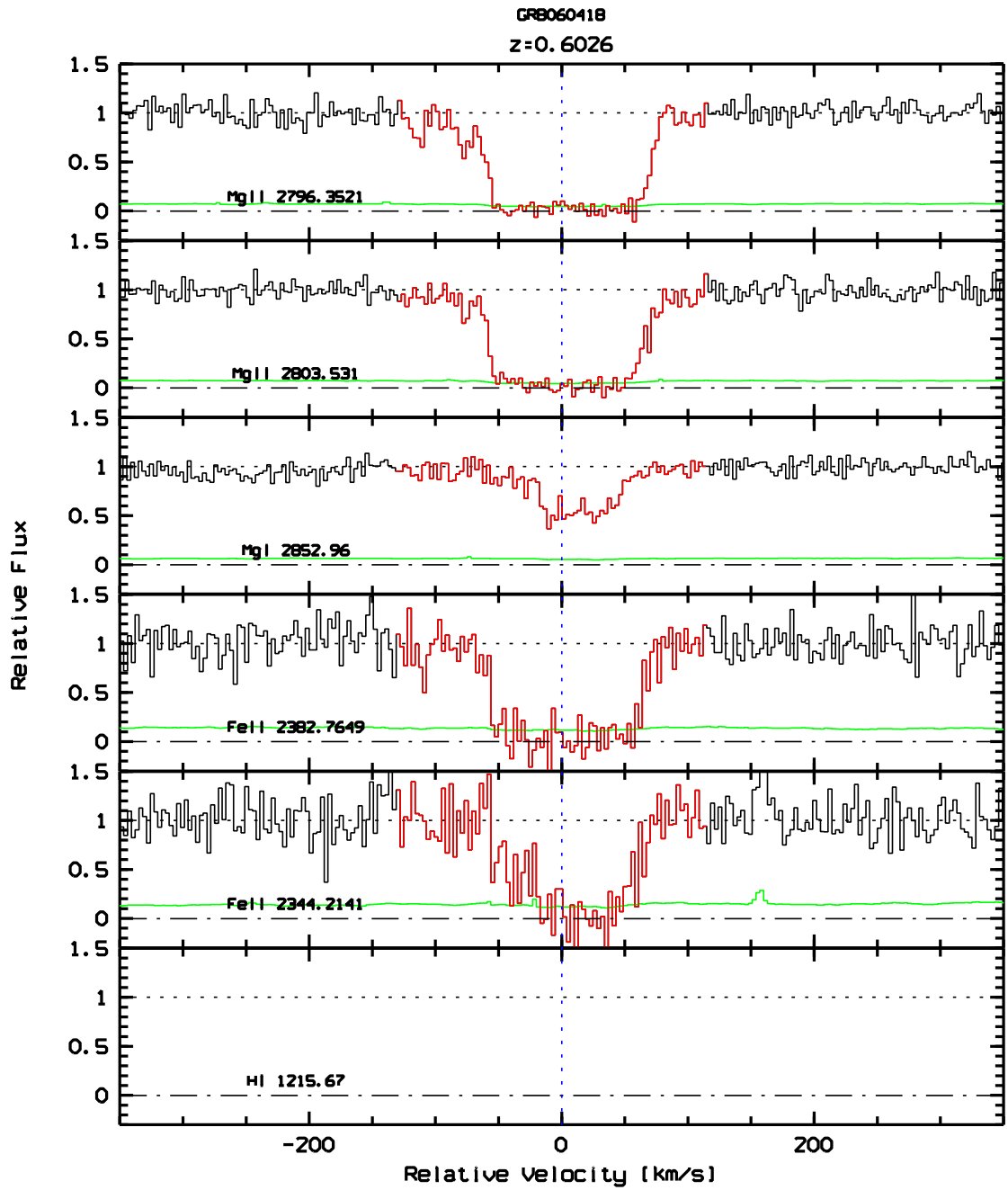


Figure 4.13 Absorption velocity profile of Mg II absorption system at $z_{abs} = 0.6026$.

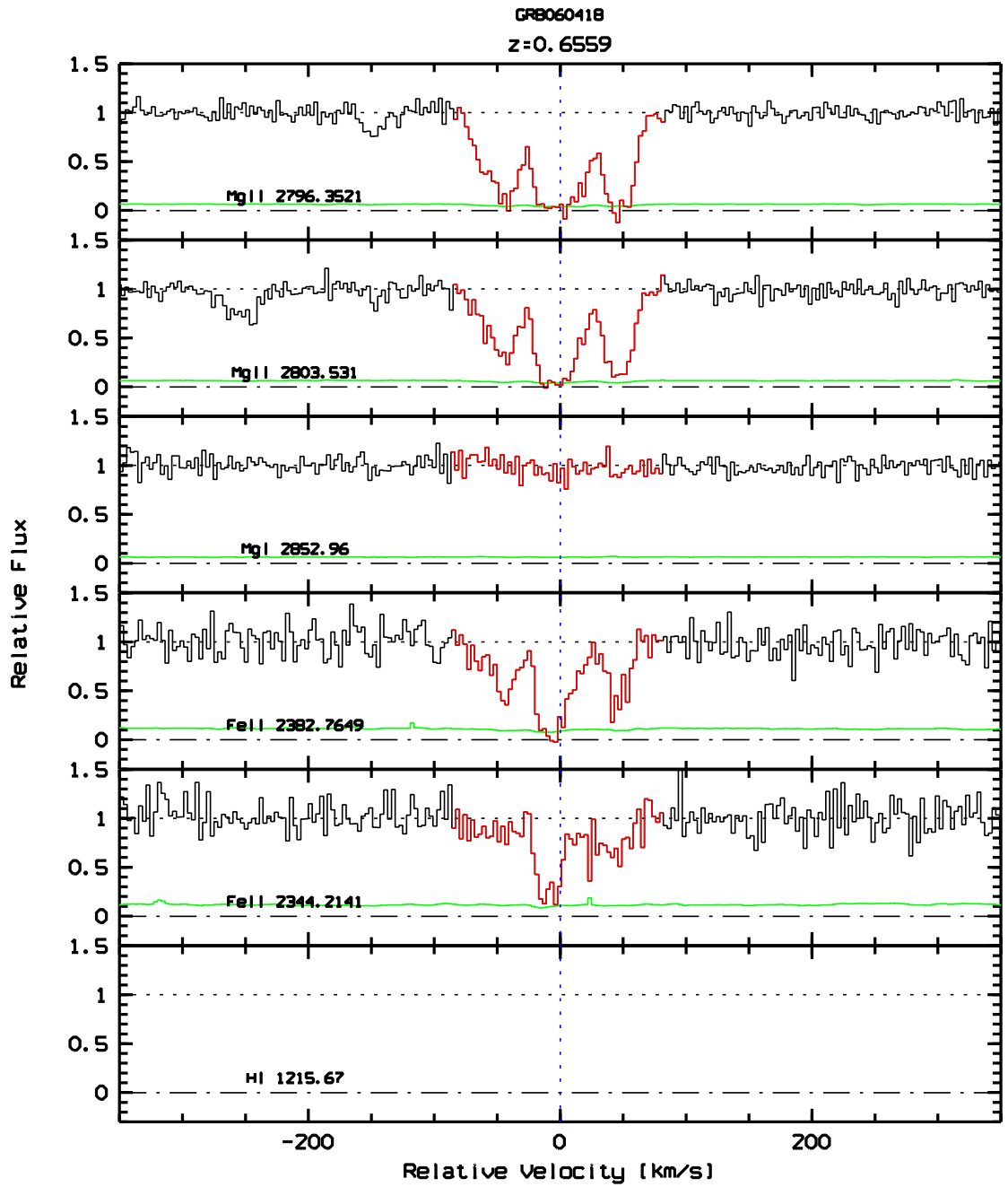


Figure 4.14 Absorption velocity profile of Mg II absorption system at $z_{abs} = 0.6559$.

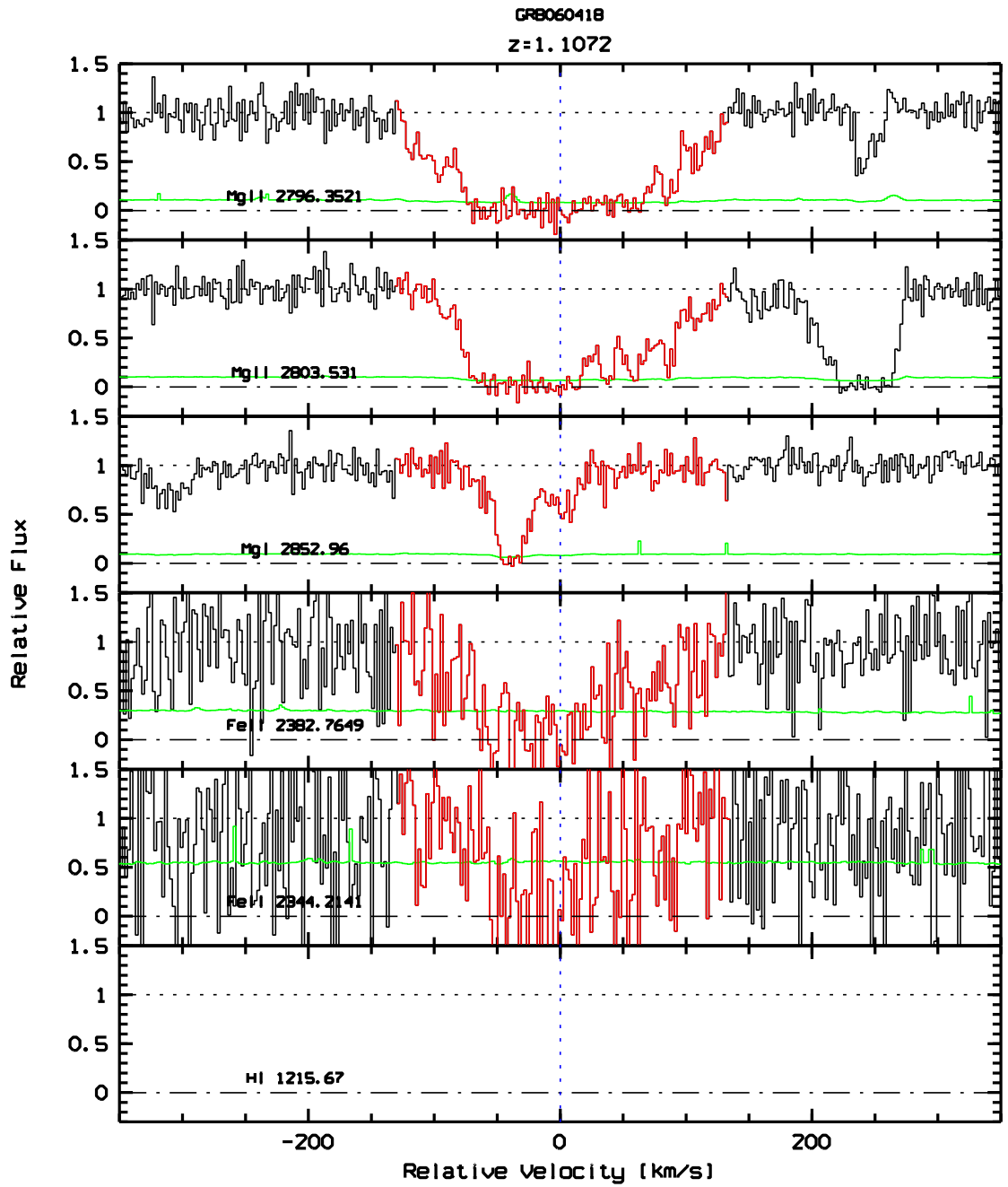


Figure 4.15 Absorption velocity profile of Mg II absorption system at $z_{abs} = 1.1072$.

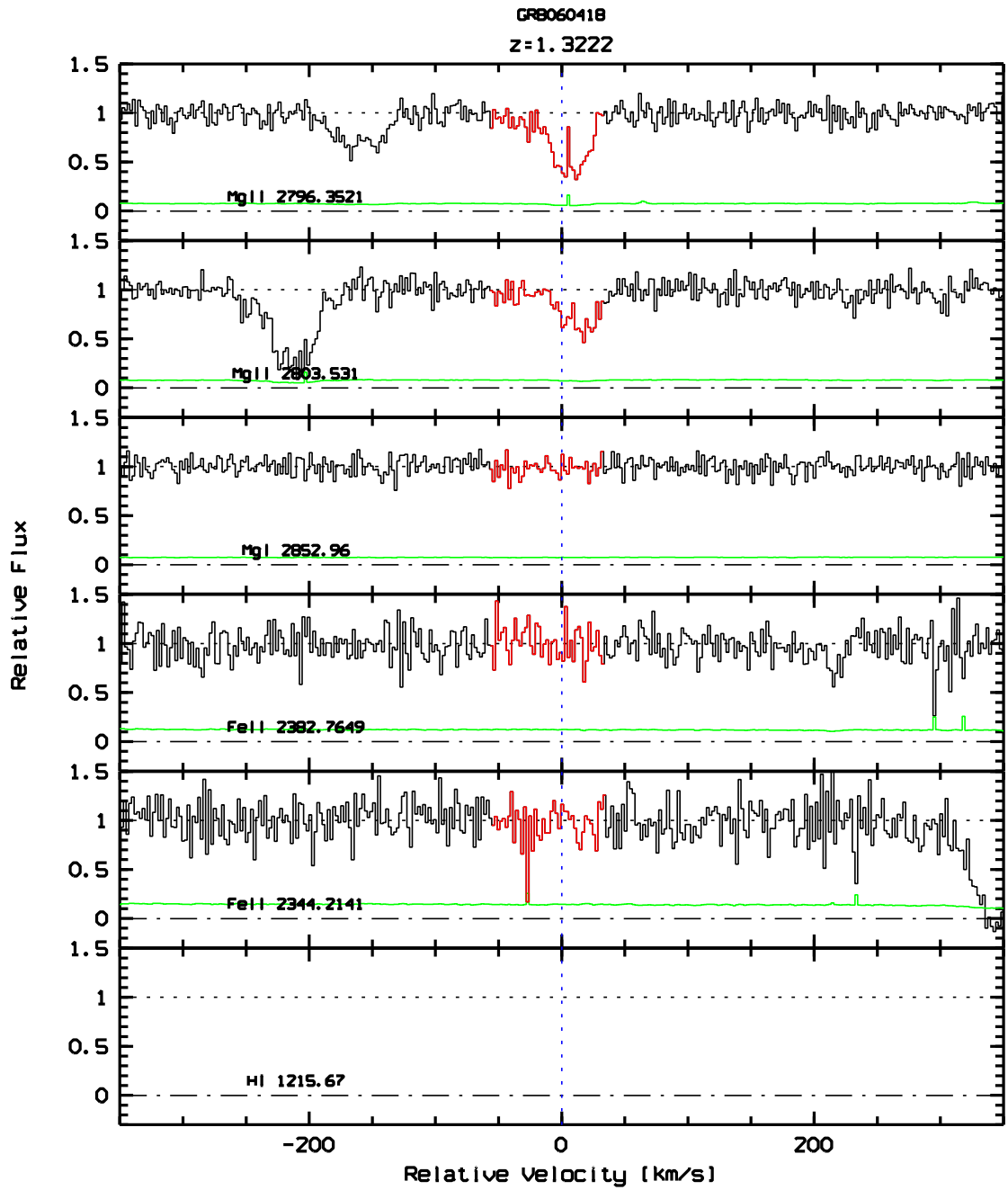


Figure 4.16 Absorption velocity profile of Mg II absorption system at $z_{abs} = 1.3222$.

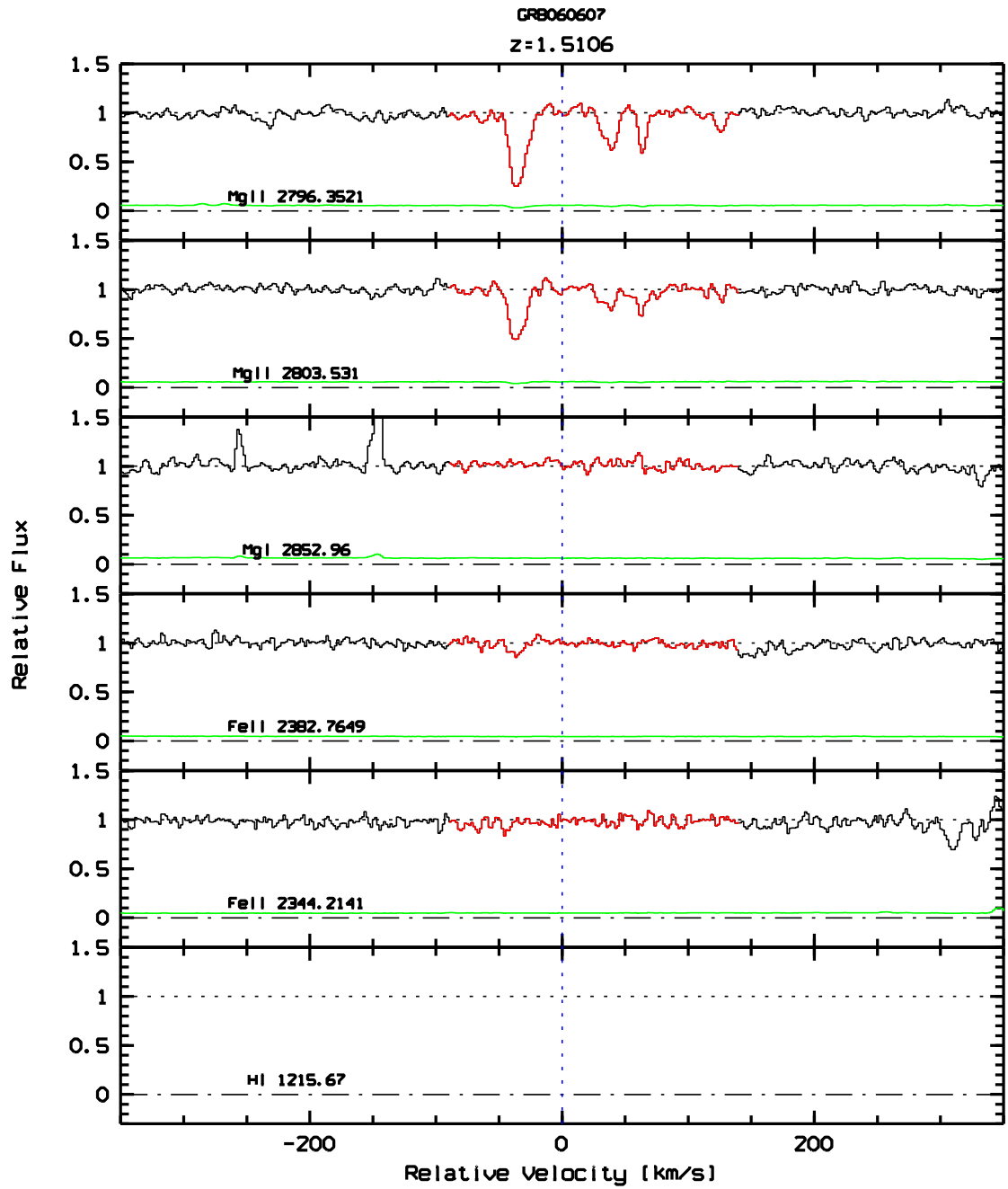


Figure 4.17 Absorption velocity profile of Mg II absorption system at $z_{abs} = 1.5106$.

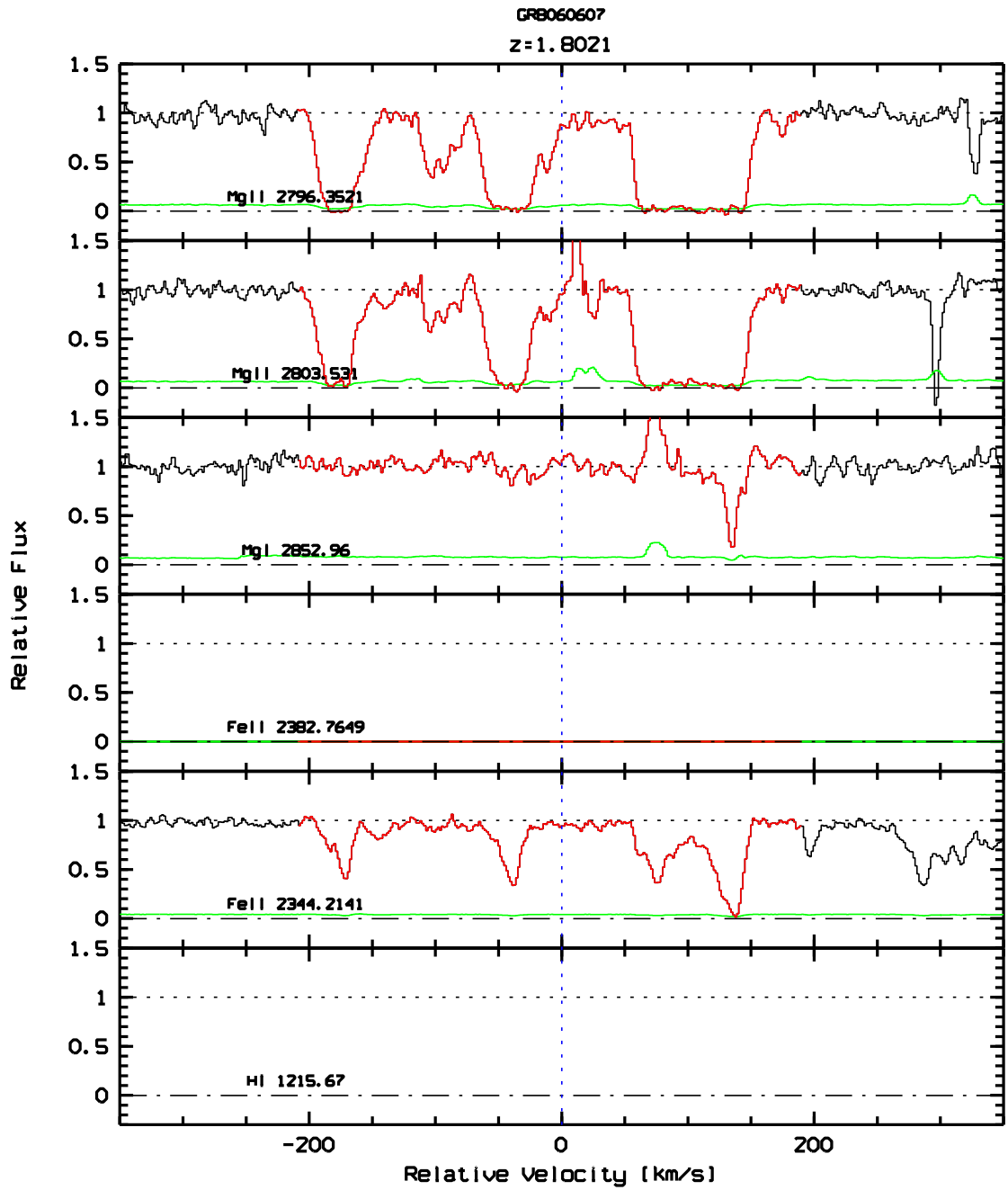


Figure 4.18 Absorption velocity profile of Mg II absorption system at $z_{abs} = 1.8021$.

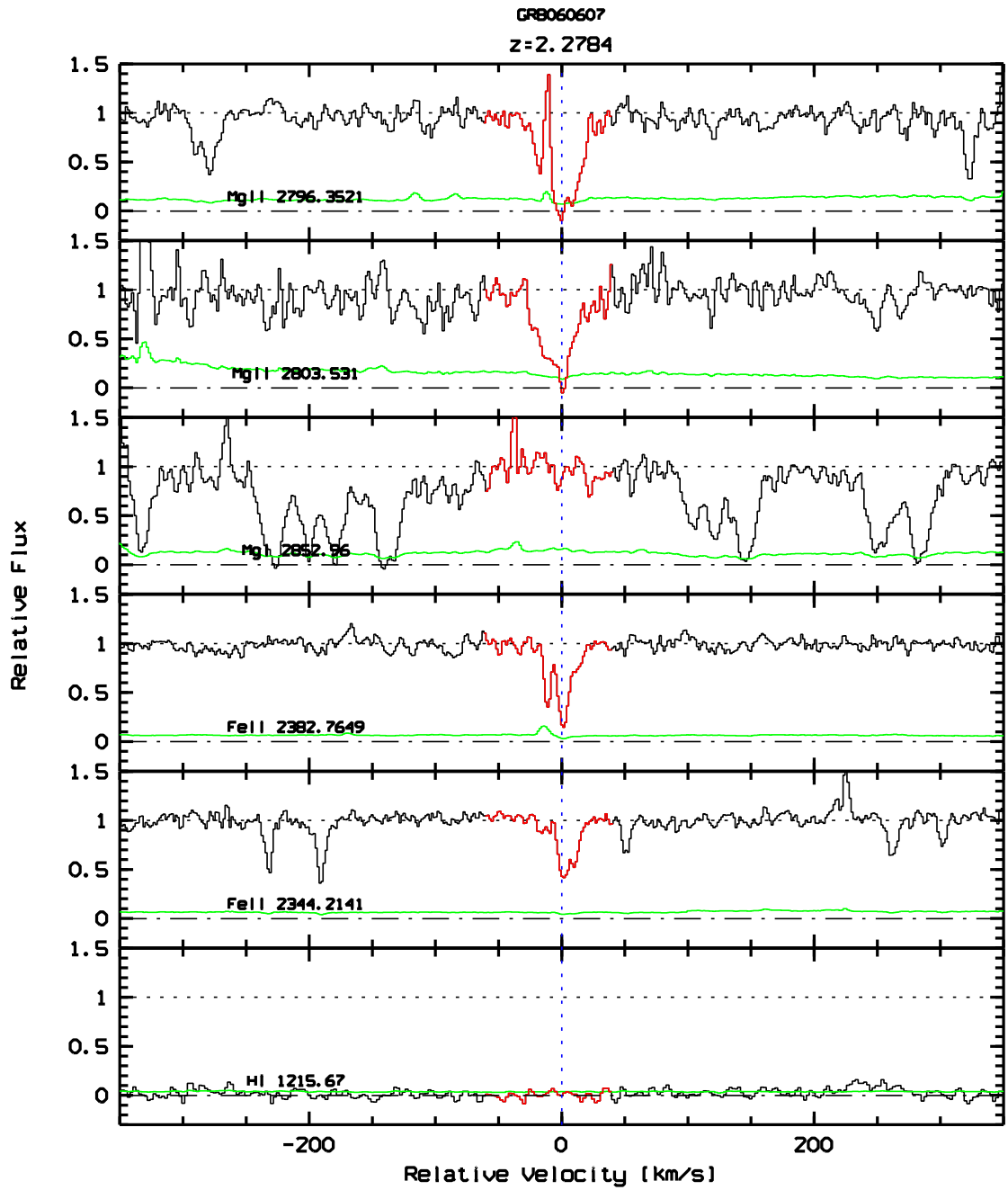


Figure 4.19 Absorption velocity profile of Mg II absorption system at $z_{abs} = 2.2784$.

4.2 C IV Samples

4.2.1 Full Sample

First I define a Full Sample of C IV absorption systems that satisfy the following criteria:

1. Systems searched between $z_{start} < z_{abs}^{CIV} \leq z_{GRB}^{CIV}$ where,

$$z_{start} = \frac{1215.67}{1550.77}(1 + z_{GRB}) - 1$$

Therefore, the Full Sample includes lines associated with the GRB host galaxy (we will later restrict the analysis to intervening C IV systems).

2. The equivalent width of the C IV doublet must be detected at the 5σ level or higher.
3. A complex system is considered a single system if the velocity components are grouped within 500 km s^{-1} . This last condition is useful to compare with previous surveys that were made at lower spectral resolution (for instance, Steidel, 1990, used a velocity window of 150 km s^{-1} to group components of a single system but then defined a statistical sample counting as a single system all components within 1000 km s^{-1} ; The Statistical Sample, defined below, does not have systems separated by less than 1000 km s^{-1} , therefore these two samples are comparable).

Although performed redward of the Ly α forest, the C IV survey has one significant contaminant: the O I 1302/Si II 1304 pair of transitions has nearly identical separation as the C IV doublet. It is trivial, however, to identify these contaminants by searching for other Si II and C II 1334 transitions.

Finally, the Full Sample is composed by 29 candidate C IV absorption systems. This number includes absorption systems with $z \sim z_{GRB}$. Table 4.3 shows the information on redshift limits for each line-of-sight, z_{abs}^{CIV} , and W_r .

Table 4.3. C IV Full Sample

GRB Comments	z_{GRB}	z_{start}	$z_{end}^{\beta_c=5000km\ s^{-1}}$	z_{abs}^{CIV}	$W_r^{pixel}(1548)$ $W_r^{pixel}(1550)$	$W_r^{gauss}(1548)$ $W_r^{gauss}(1550)$	
021004	2.335	1.715	2.279	1.74738	0.035 ± 0.006	0.031 ± 0.006	
				1.81108	0.039 ± 0.007	0.051 ± 0.014	
					0.158 ± 0.011	0.191 ± 0.014	
				1.83415	0.061 ± 0.010	0.073 ± 0.007	
					0.153 ± 0.008	0.141 ± 0.012	
					0.051 ± 0.007	0.044 ± 0.010	
				2.29800	0.898 ± 0.011	0.898 ± 0.018	
050730	3.97	2.965	3.887	2.32800	0.561 ± 0.012	0.520 ± 0.016	
					2.094 ± 0.012	2.584 ± 0.045	host
					1.695 ± 0.012	1.786 ± 0.021	
					0.233 ± 0.014	0.249 ± 0.023	$DR < 1$
050820	2.6147	1.833	2.554	3.25400 ×	0.266 ± 0.013	0.300 ± 0.023	
					0.301 ± 0.014	0.281 ± 0.022	
				3.51362 †	0.167 ± 0.013	0.178 ± 0.015	
					0.063 ± 0.007	0.059 ± 0.009	
					0.072 ± 0.007	0.062 ± 0.009	
				3.96803	0.811 ± 0.017	0.874 ± 0.026	host
					0.692 ± 0.019	0.754 ± 0.027	
050922C	2.199	1.511	2.146	1.94010	0.060 ± 0.005	0.068 ± 0.007	$DR < 1$
					0.122 ± 0.004	0.137 ± 0.009	
				2.05973	0.041 ± 0.003	0.039 ± 0.004	$DR < 1$
					0.058 ± 0.003	0.057 ± 0.006	
				2.07491	0.160 ± 0.008	0.113 ± 0.009	
					0.047 ± 0.008	0.047 ± 0.008	
				2.14629 †	0.214 ± 0.010	0.194 ± 0.014	
					0.208 ± 0.010	0.160 ± 0.012	
				2.32375	0.168 ± 0.006	0.150 ± 0.009	
					0.142 ± 0.006	0.119 ± 0.010	
060607	3.082	2.207	3.014	2.35890 ×	0.331 ± 0.013	0.292 ± 0.019	
					0.152 ± 0.013	0.143 ± 0.012	
				2.61444	1.504 ± 0.010	1.544 ± 0.040	host
					1.091 ± 0.012	1.116 ± 0.106	
				1.56843 †	0.989 ± 0.031	0.885 ± 0.053	
					0.600 ± 0.029	0.538 ± 0.058	
				1.98911 †	0.561 ± 0.020	0.555 ± 0.034	
					0.486 ± 0.022	0.407 ± 0.031	
				2.00869 †	0.479 ± 0.017	0.477 ± 0.027	
					0.366 ± 0.017	0.373 ± 0.022	
060607	3.082	2.207	3.014	2.07766	0.173 ± 0.009	0.185 ± 0.011	
					0.142 ± 0.010	0.138 ± 0.015	
				2.14204	0.040 ± 0.003	0.044 ± 0.004	
					0.037 ± 0.003	0.035 ± 0.004	
				2.19973	0.729 ± 0.009	0.735 ± 0.022	host
					0.541 ± 0.009	0.565 ± 0.016	
				2.21653	0.291 ± 0.005	0.263 ± 0.006	
060607	3.082	2.207	3.014		0.095 ± 0.007	0.106 ± 0.007	
				2.27853	0.164 ± 0.004	0.171 ± 0.008	
					0.093 ± 0.004	0.100 ± 0.008	
				2.89048 †	0.619 ± 0.005	0.843 ± 0.020	

Table 4.3 (cont'd)

GRB Comments	z_{GRB}	z_{start}	$z_{end}^{\beta c=5000 km s^{-1}}$	z_{abs}^{CIV}	$W_r^{pixel}(1548)$ $W_r^{pixel}(1550)$	$W_r^{gauss}(1548)$ $W_r^{gauss}(1550)$	
					0.532 ± 0.005	0.460 ± 0.013	
				2.91659	0.036 ± 0.003	0.031 ± 0.003	
					0.035 ± 0.003	0.037 ± 0.004	
				2.93633 †	1.554 ± 0.005	1.580 ± 0.011	
					1.111 ± 0.005	1.100 ± 0.011	
				3.04979	0.271 ± 0.005	0.233 ± 0.008	
					0.245 ± 0.005	0.224 ± 0.035	
				3.07488	0.386 ± 0.004	0.399 ± 0.009	host
					0.295 ± 0.004	0.291 ± 0.007	

Note. — All C IV absorption systems found between $z_{GRB}^{Ly\alpha} < z^{CIV} \leq z_{GRB}^{CIV}$.
Samples: † Absorption systems in the Statistical Sample.
× Excluded Systems (see Section 4.2.2).

4.2.2 Statistical Sample

To compare the statistics of C IV absorption along GRB sightlines with those for QSO sightlines, one must define a sample with identical equivalent width limits. Previous surveys have defined this limit on $W_{min} = 0.15 \text{ \AA}$ in the rest frame (Steidel, 1990; Misawa et al., 2002). I adopt the same value, i.e., $W_r \geq 0.15 \text{ \AA}$ for *both* members of the C IV doublet because our spectral GRB sample allows well detection of lines at this limit.

In addition, following the reasons explained in Section 4.1.2, I excluded from the Statistical Sample all systems with redshifts within 5000 km s^{-1} from z_{GRB} .

All the spectra included in the Statistical Sample permit detections of lines with $W_r > 0.15 \text{ \AA}$ with at least 5σ significance from $z_{GRB}^{Ly\alpha}$ to 5000 km s^{-1} within z_{GRB}^{CIV} . The Statistical Sample is composed of 7 absorption systems (those labeled with † in Table 4.3 and shown in Figure 4.20 to 4.28). We excluded 2 systems due to their dubious character (systems labeled with X in Table 4.3): $z_{abs} = 3.254$, although not saturated, it shows an equivalent width ratio < 1 (see Figure 4.20); $z_{abs} = 2.3589$ falls very close to W_{min} but $W_r^{gauss}(1550) < 0.15 \text{ \AA}$ (see Figure 4.23).

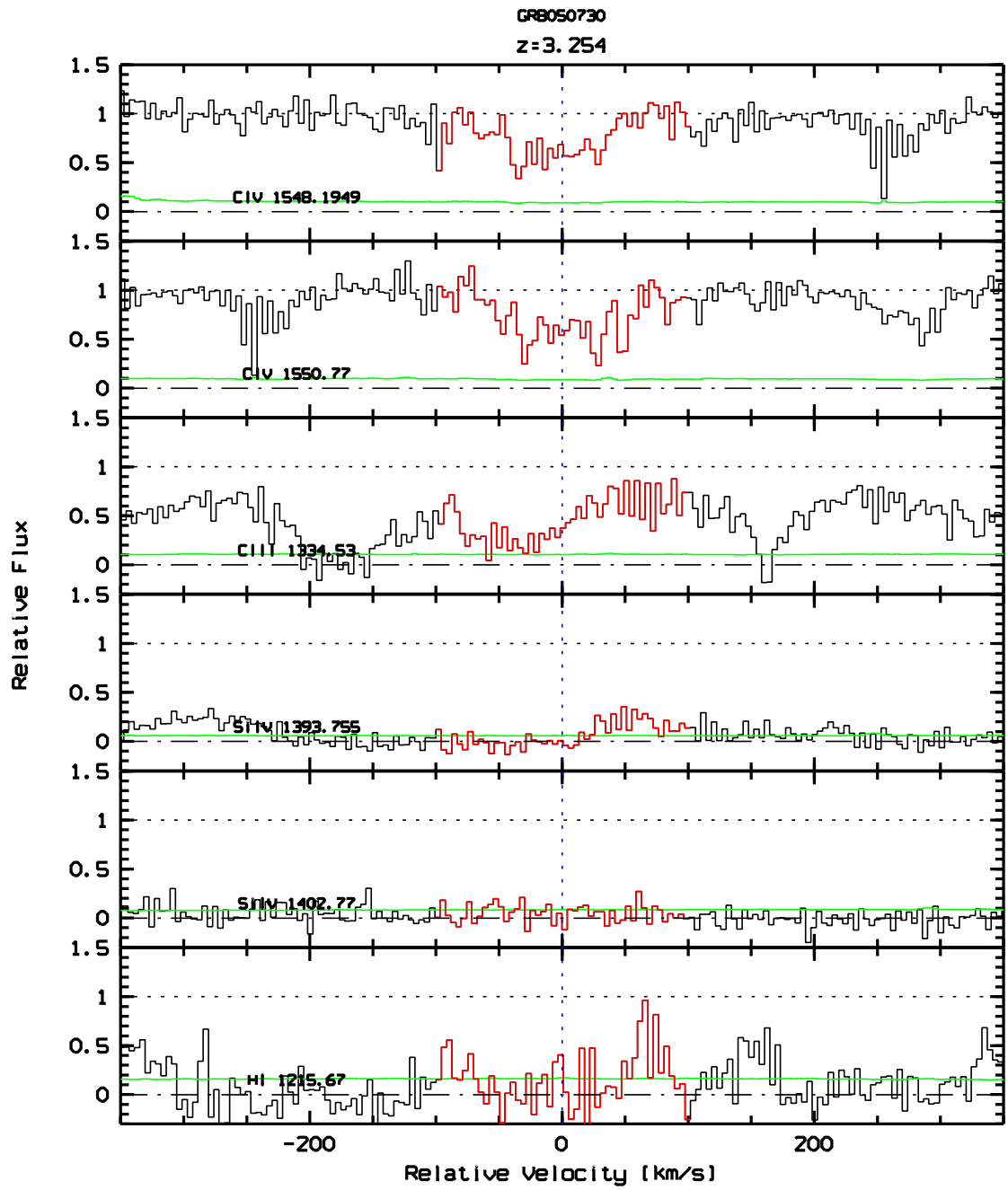


Figure 4.20 Absorption velocity profile of C IV absorption system at $z_{abs} = 3.254$. This system is a dubious one which was excluded for Statistical Sample.

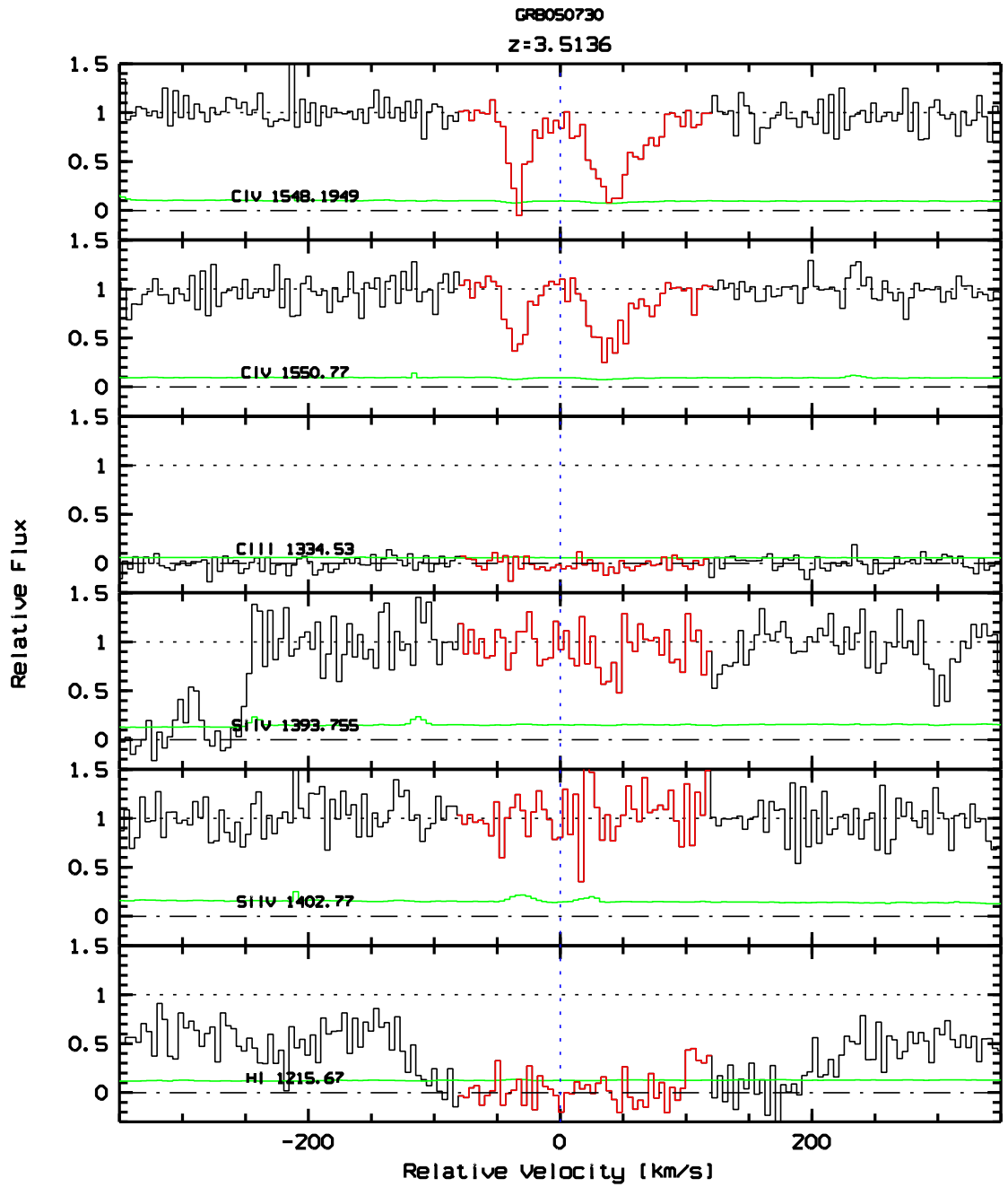


Figure 4.21 Absorption velocity profile of C IV absorption system at $z_{abs} = 3.5136$.

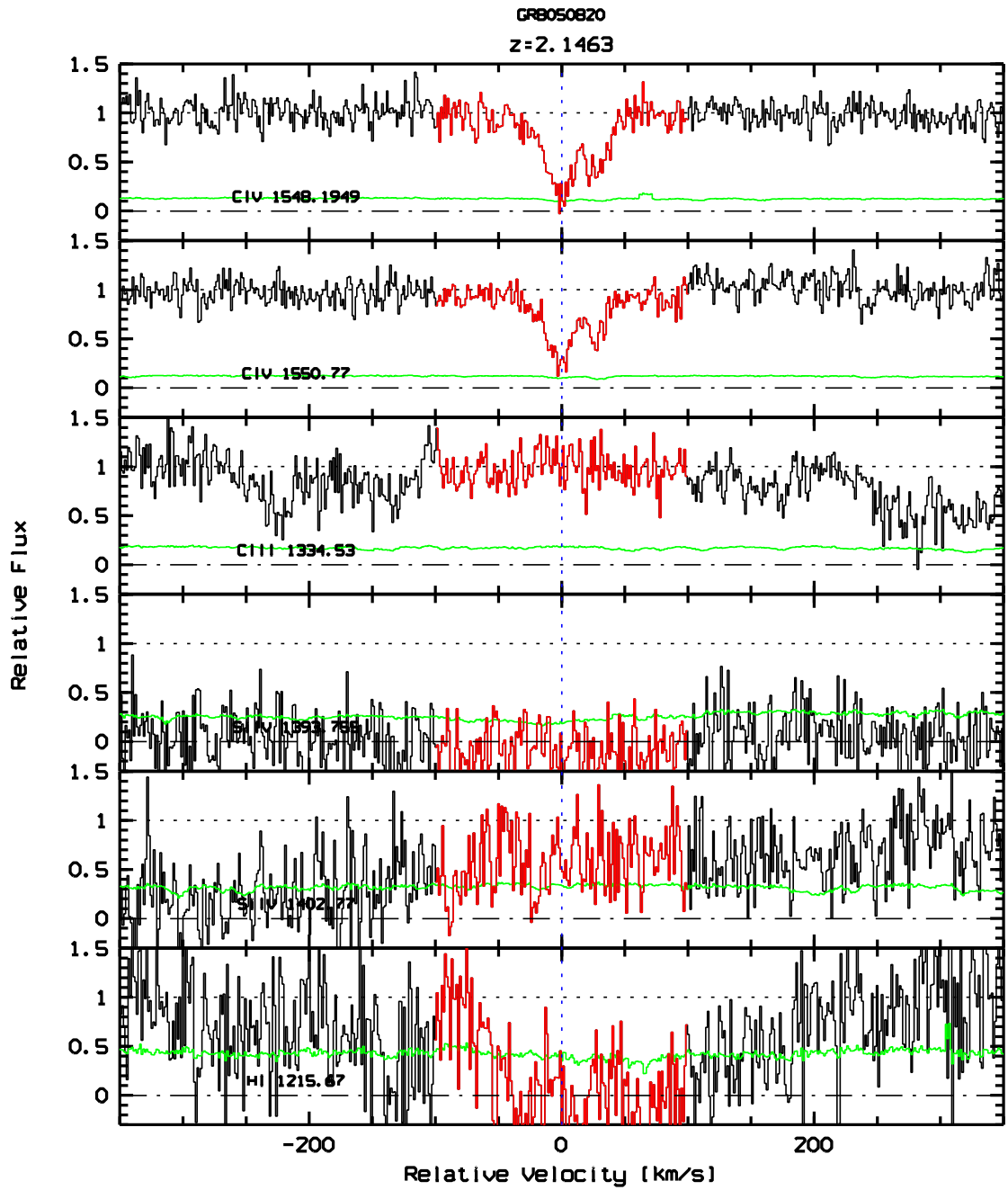


Figure 4.22 Absorption velocity profile of C IV absorption system at $z_{abs} = 2.1463$.

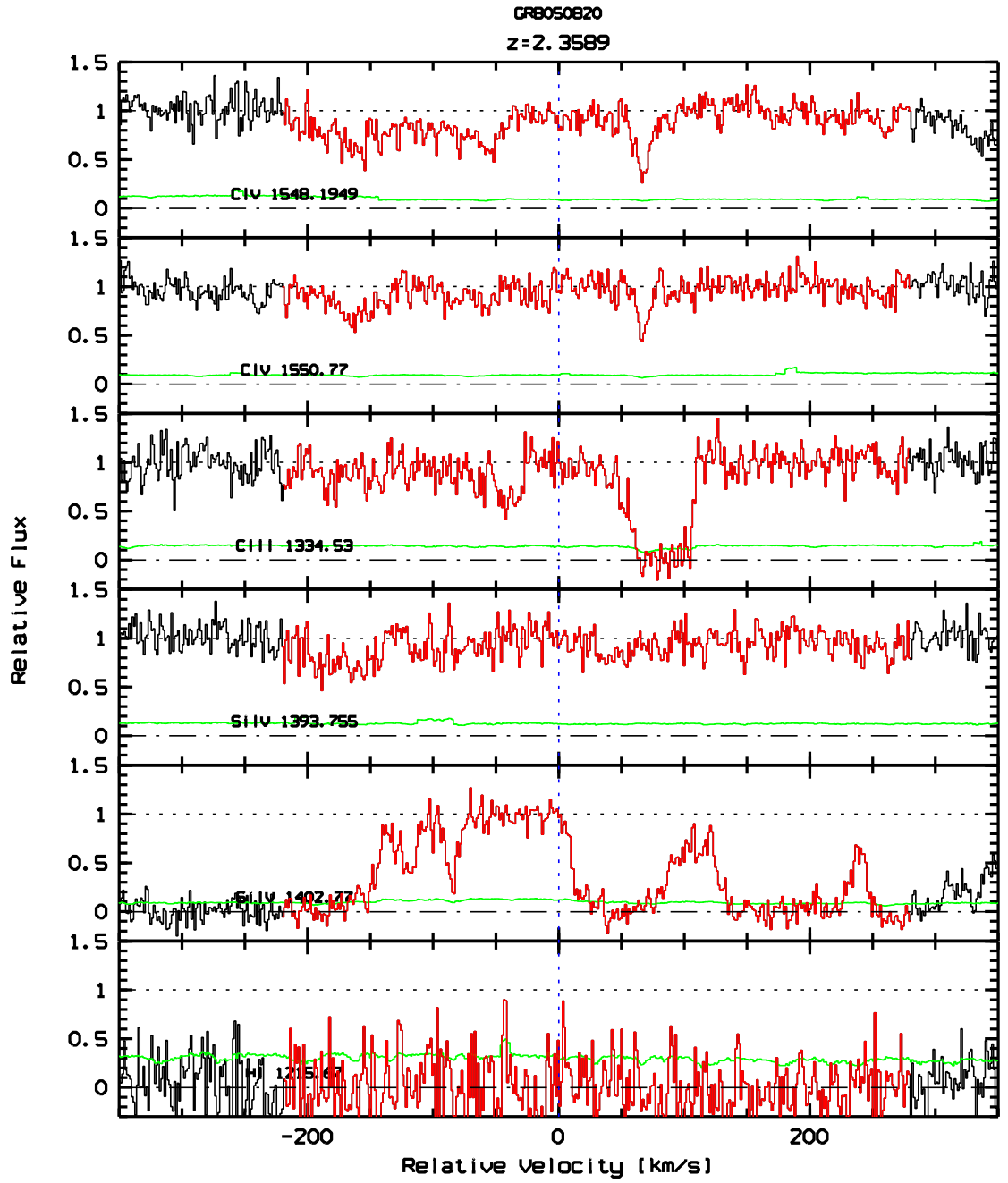


Figure 4.23 Absorption velocity profile of C IV absorption system at $z_{abs} = 2.3589$. This system was excluded for Statistical Sample due to $W_r^{gauss}(1550) < 0.15 \text{ \AA}$.

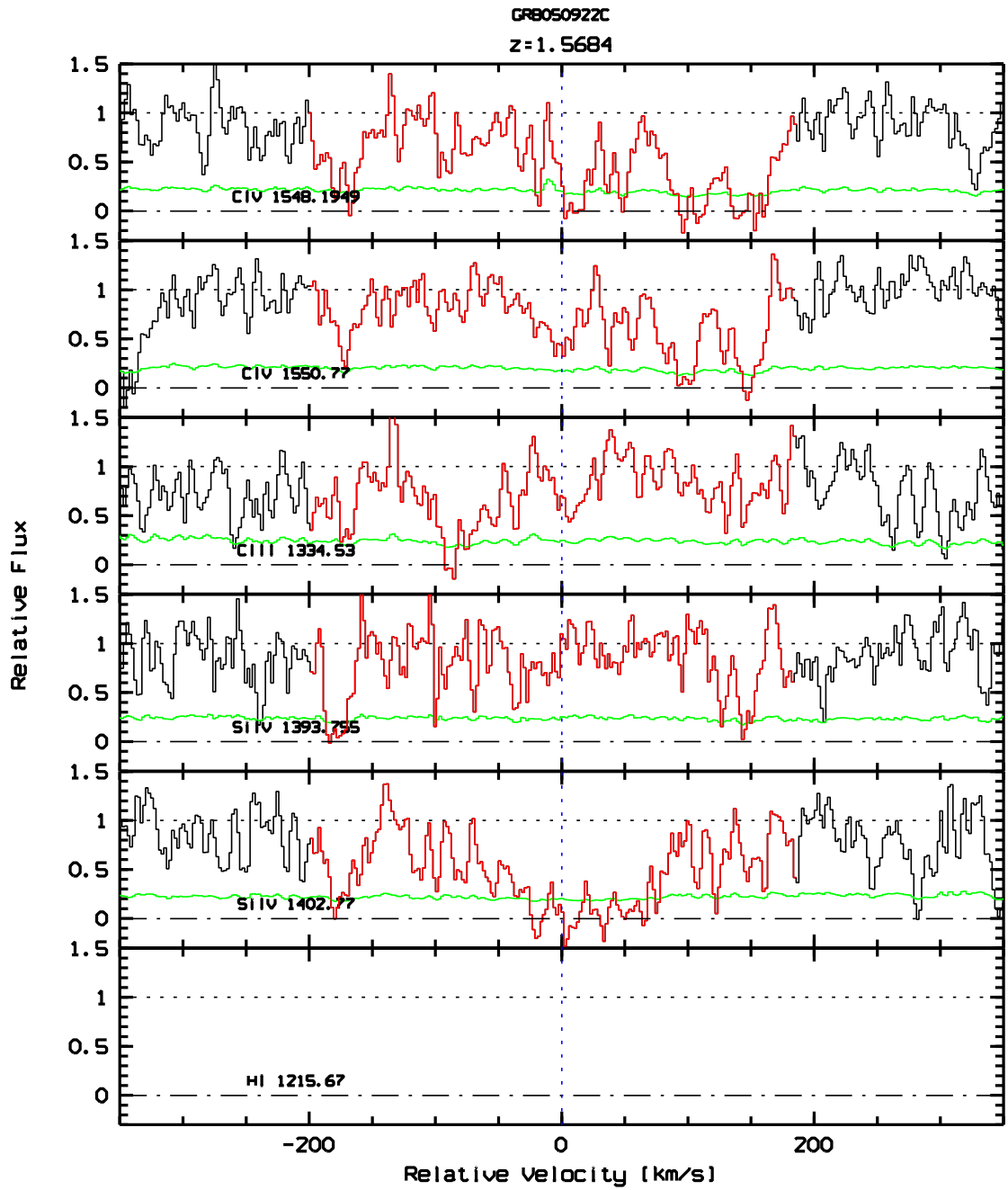


Figure 4.24 Absorption velocity profile of C IV absorption system at $z_{abs} = 1.5684$.

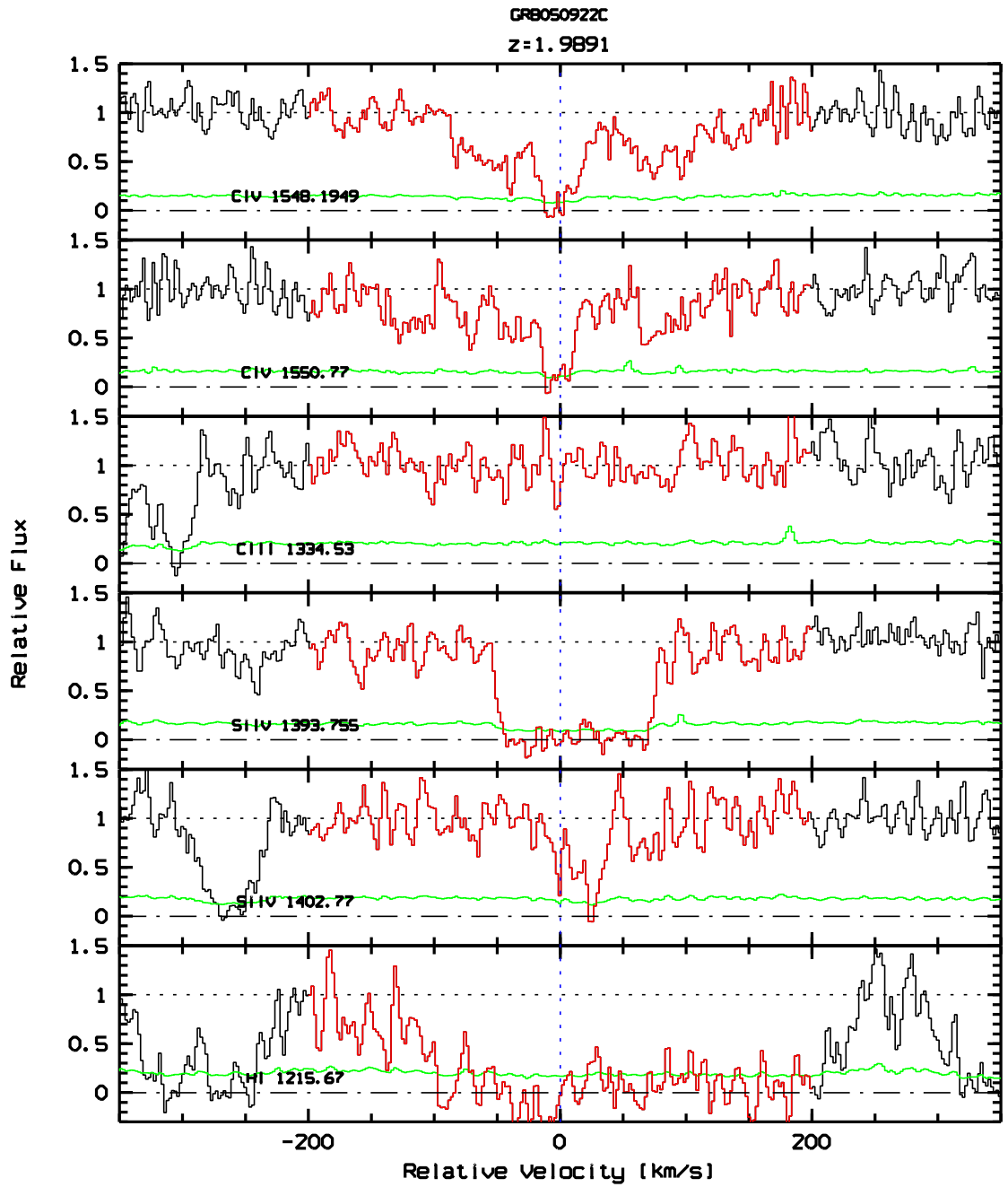


Figure 4.25 Absorption velocity profile of C IV absorption system at $z_{abs} = 1.9891$.

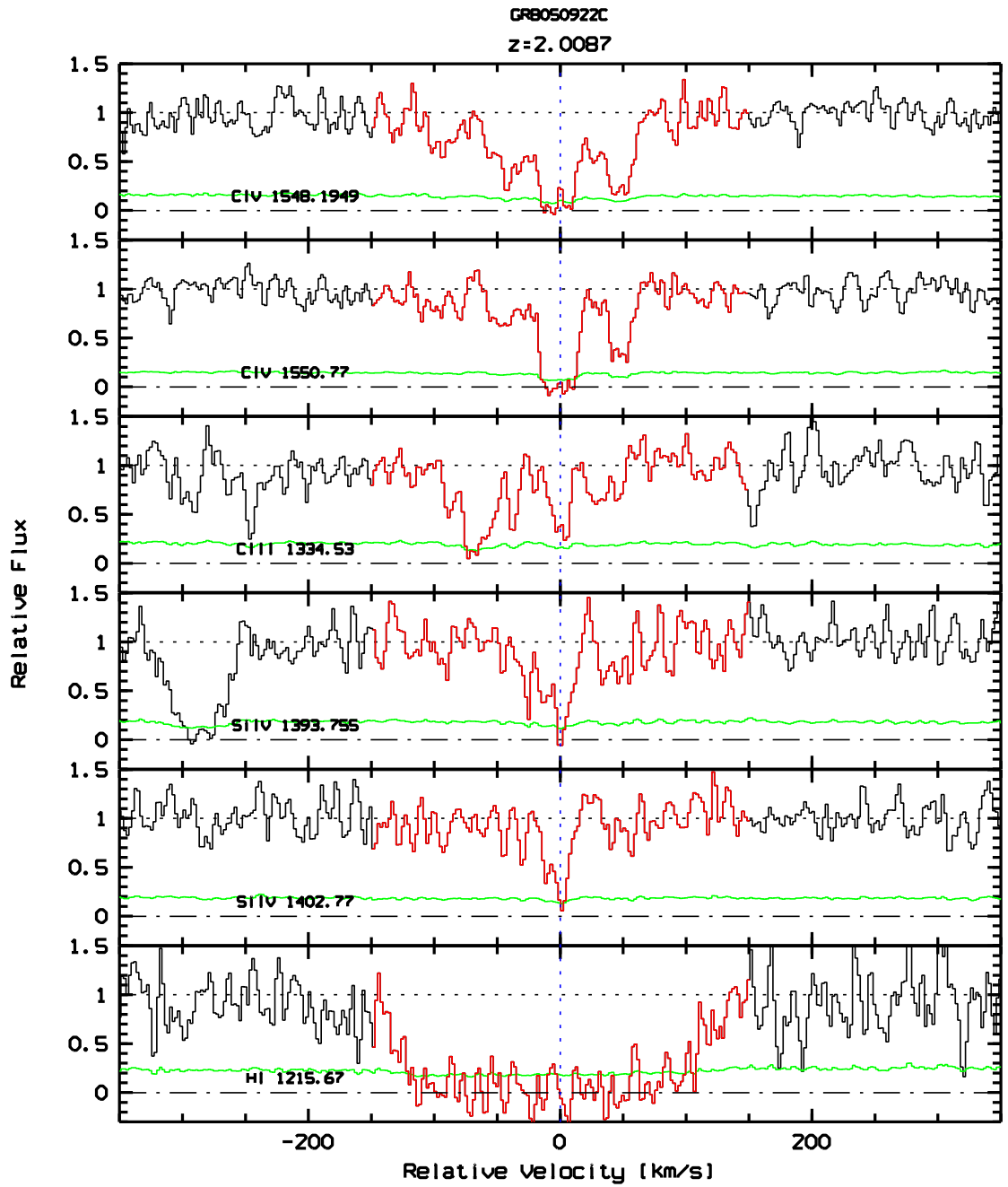


Figure 4.26 Absorption velocity profile of C IV absorption system at $z_{abs} = 2.0087$.

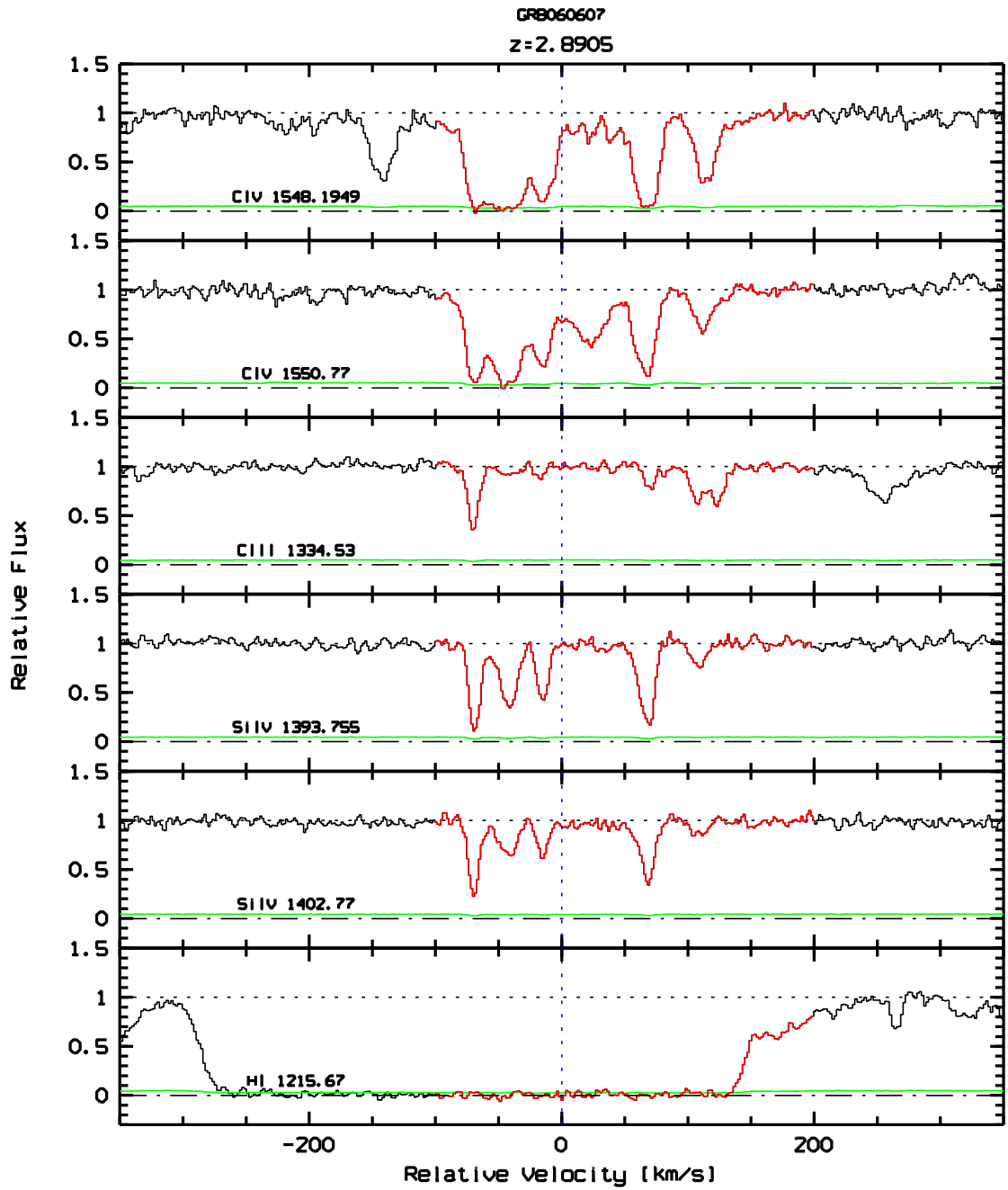


Figure 4.27 Absorption velocity profile of C IV absorption system at $z_{abs} = 2.8905$.

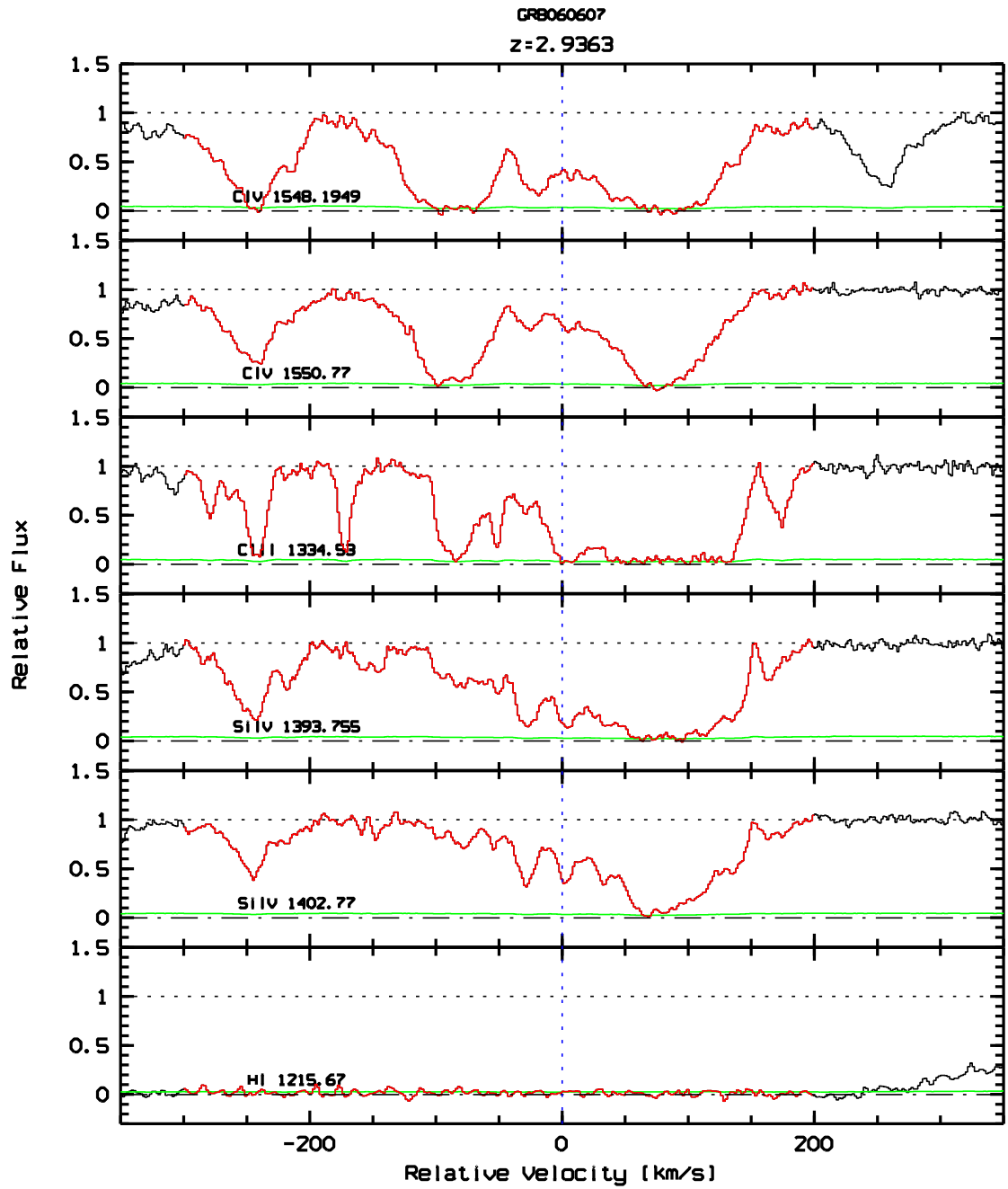


Figure 4.28 Absorption velocity profile of C IV absorption system at $z_{abs} = 2.9363$.

4.3 Comments on Measured Equivalent Widths

To be consistent with the analysis of this work, it is necessary to use a certain equivalent width method to determine if a system falls in one or another sample, especially when systems fall near the limits of sample definitions. As mentioned in Section 3.5 I chose W_r^{gauss} except for poor fits (i.e., regular and bad fits marked with the letters r and b respectively in Table 4.1) in which cases W_r^{pixel} were used. Figures 4.29 to 4.31 show examples of good, regular and bad Gaussian fits. For the C IV Statistical Sample all systems have good Gaussian fits while for Mg II Statistical Sample there are several cases with poor fits. As we will see, the fact of using W_r^{pixel} in some cases instead of W_r^{gauss} does not alter significantly the number of systems in each sample and therefore does not affect the conclusions of this work.

Figures 4.32 to 4.35 show rest frame equivalent widths values measured from pixel integration and Gaussian fit for Mg II and C IV Statistical Samples. As expected, these figures show that both methods are self-consistent except for some outlier systems, caused either by blended systems or poor Gaussian fits (typically for saturated lines).

From Figure 4.32 note that at $W_r \geq 1 \text{ \AA}$ Gaussian fits are poorer than at $W_r < 1 \text{ \AA}$. This effect is due to the fact that the absorption lines begin to saturate and the Gaussian fit is no longer appropriate to derive a W_r value. In these cases W_r obtained from a Voigt fit or pixel integration work better.

In all cases the number of systems in each Statistical Sample does not change significantly if I use either W_r^{gauss} or W_r^{pixel} . In the *worst case*, namely if I use W_r^{pixel} instead of W_r^{gauss} for systems with good fits and vice versa, the Strict Mg II Sample 1 increases by only one while the Relaxed Mg II Sample 1 remains unaffected; the Strict Mg II Sample 2 decreases by two while the Relaxed Mg II Sample 2 increases by one; the Strict and Relaxed Mg II Sample 3 is increase by two and the Strict and Relaxed Mg II Sample 4 decrease by one (see systems labeled with \sim in Table 4.1). Also, note that for C IV the number of systems does not change in the Statistical Sample despite of the outlier systems (Figure 4.35).

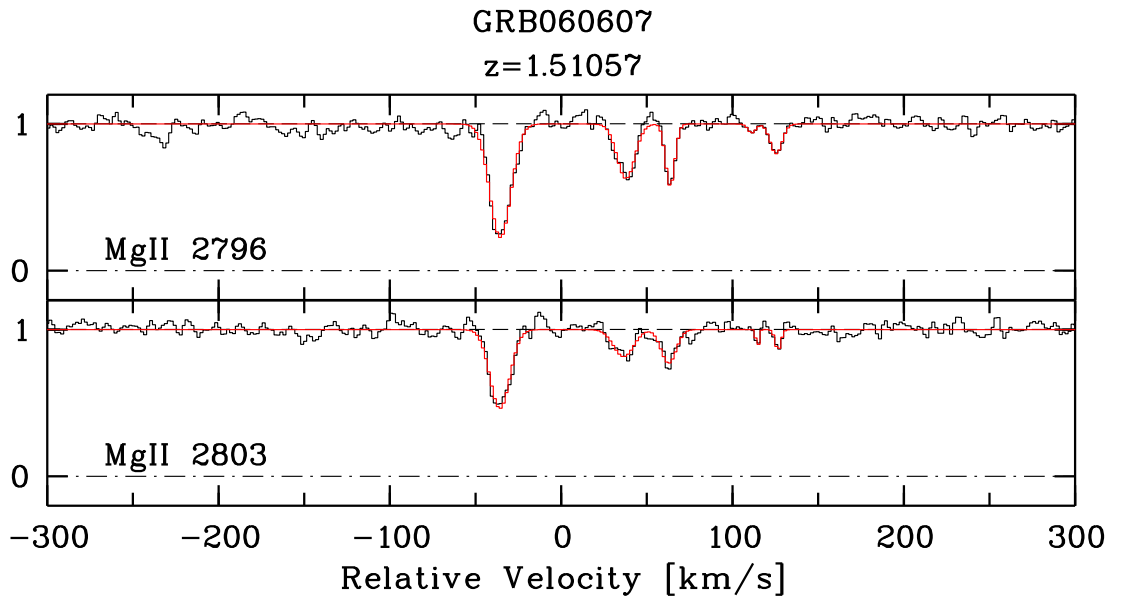


Figure 4.29 Example of a bad Gaussian fit (red line).

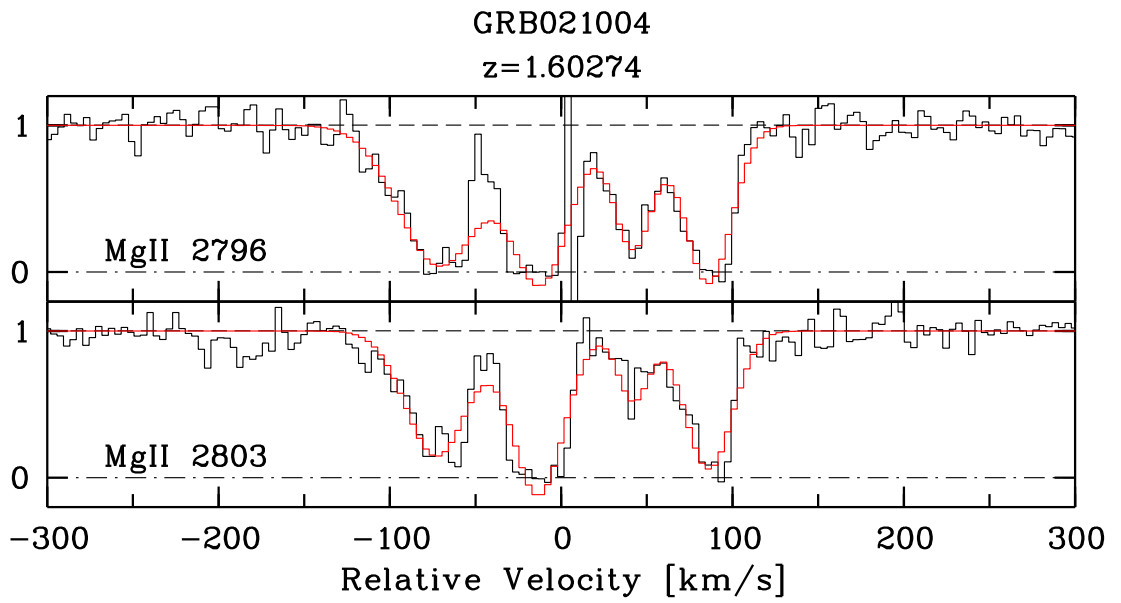


Figure 4.30 Example of a regular Gaussian fit (red line).

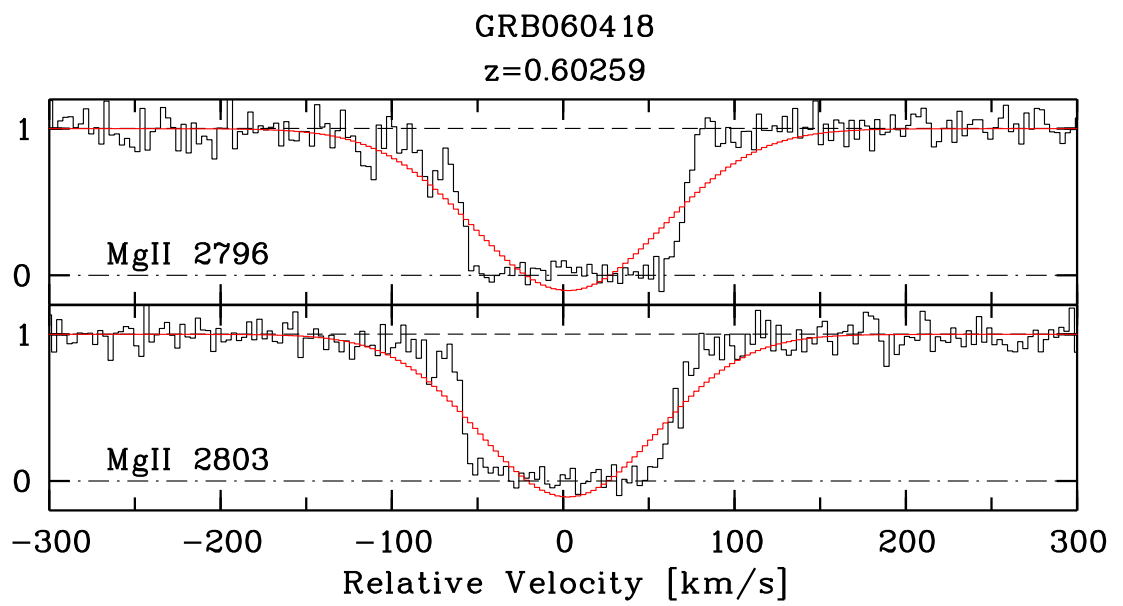


Figure 4.31 Example of a bad Gaussian fit (red line).

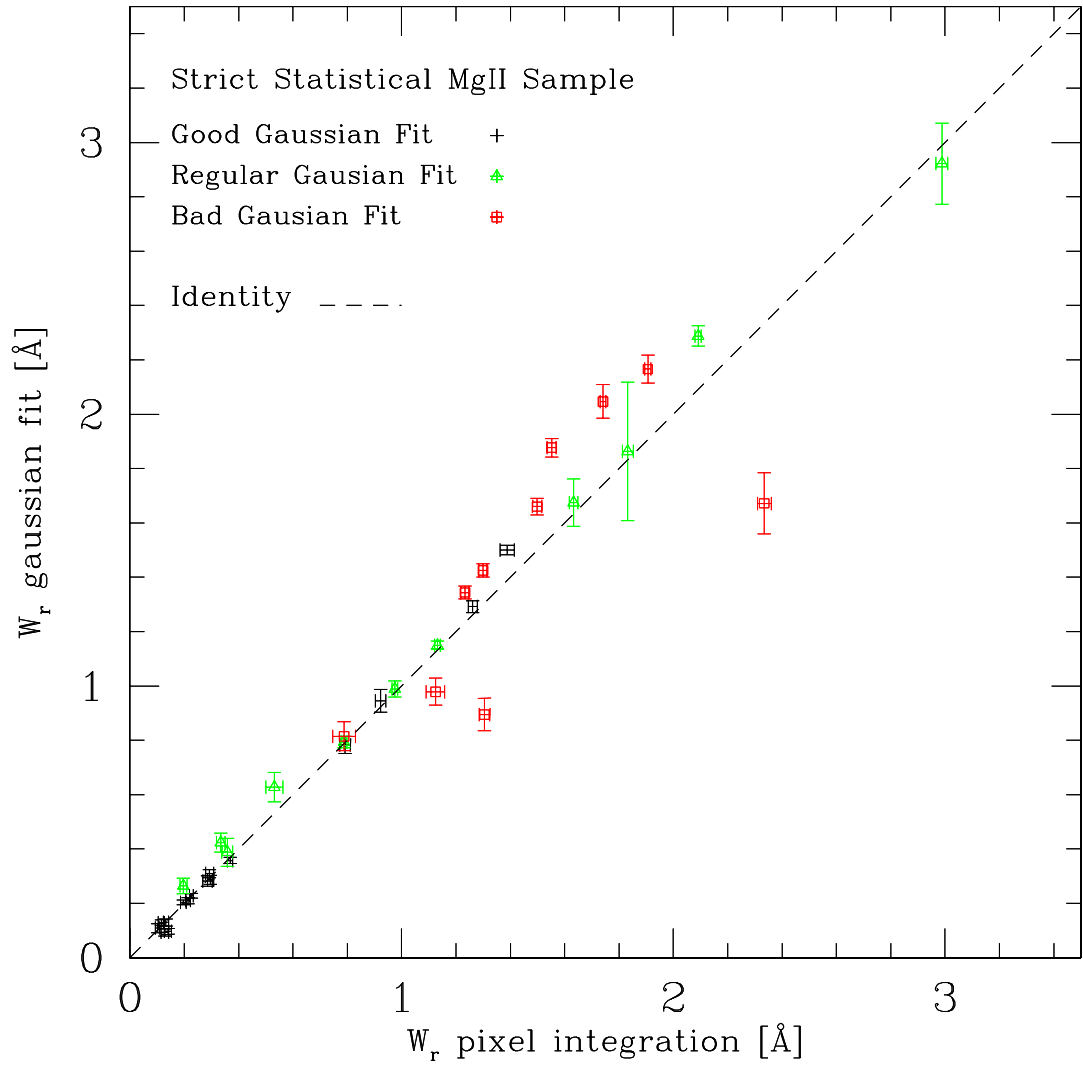


Figure 4.32 Rest frame equivalent width of Mg II in the Strict Statistical Sample measured with Gaussian fit and with pixel integration. Systems with good, regular and bad Gaussian fits are shown as black points, green triangles and red squares, respectively. The dashed line is the identity function.

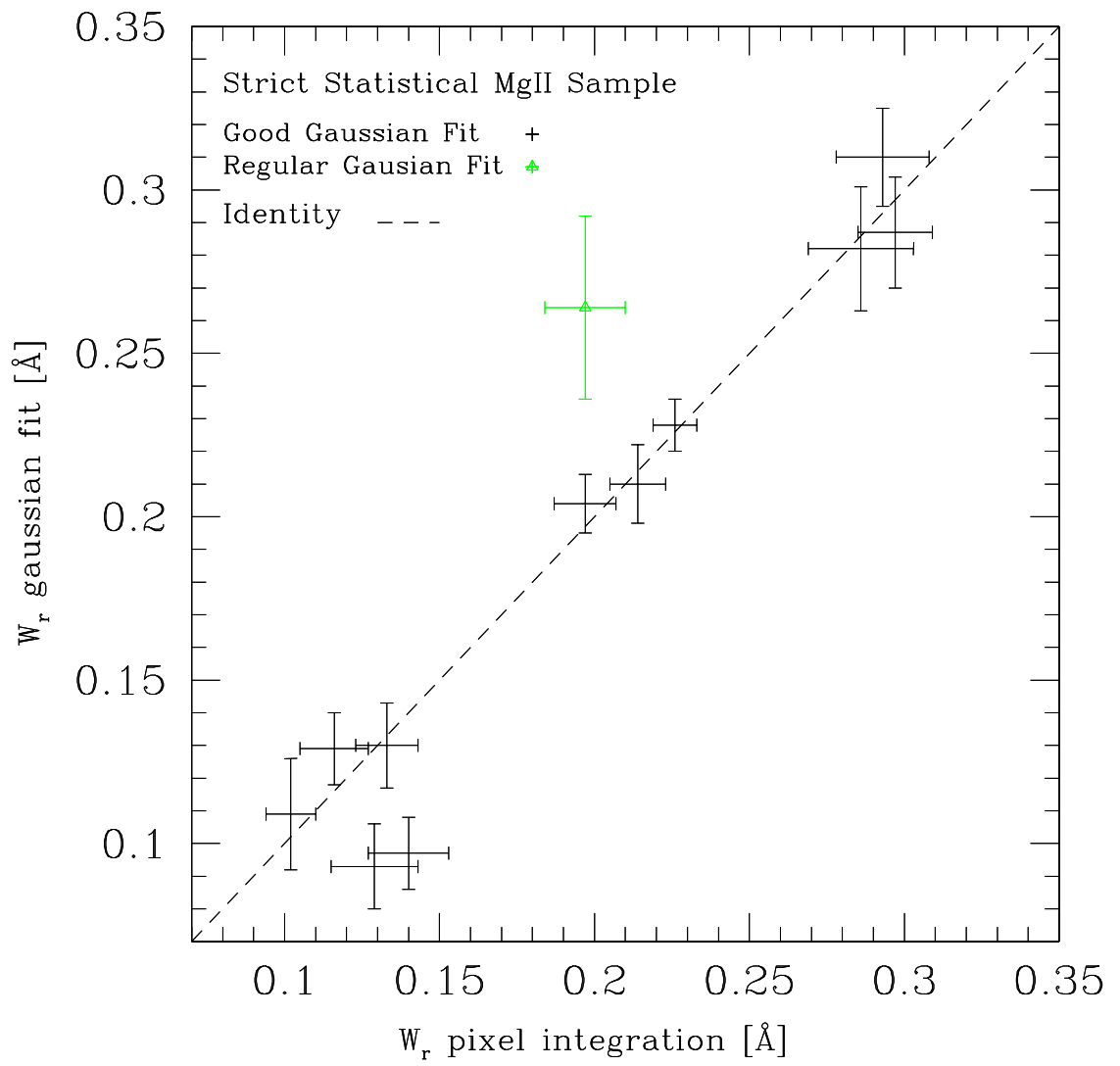


Figure 4.33 Same as Figure 4.32 but considering just the systems at $W_r(2796) < 0.35 \text{ \AA}$.

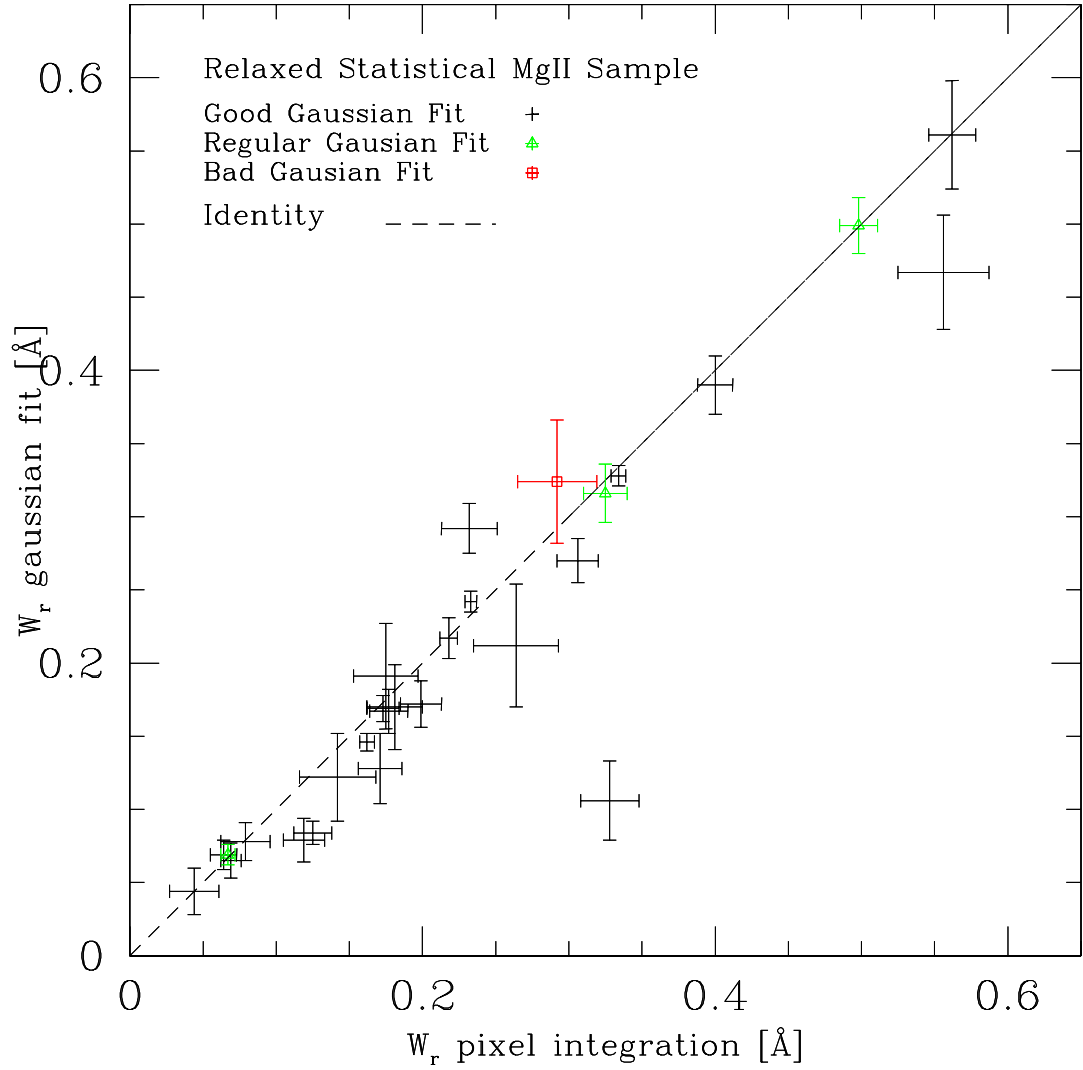


Figure 4.34 Rest frame equivalent width of Mg II in the Relaxed Statistical Sample measured with Gaussian fit and with pixel integration. Systems with good, regular and bad Gaussian fits are shown as black points, green triangles and red squares, respectively. The dashed line is the identity function.

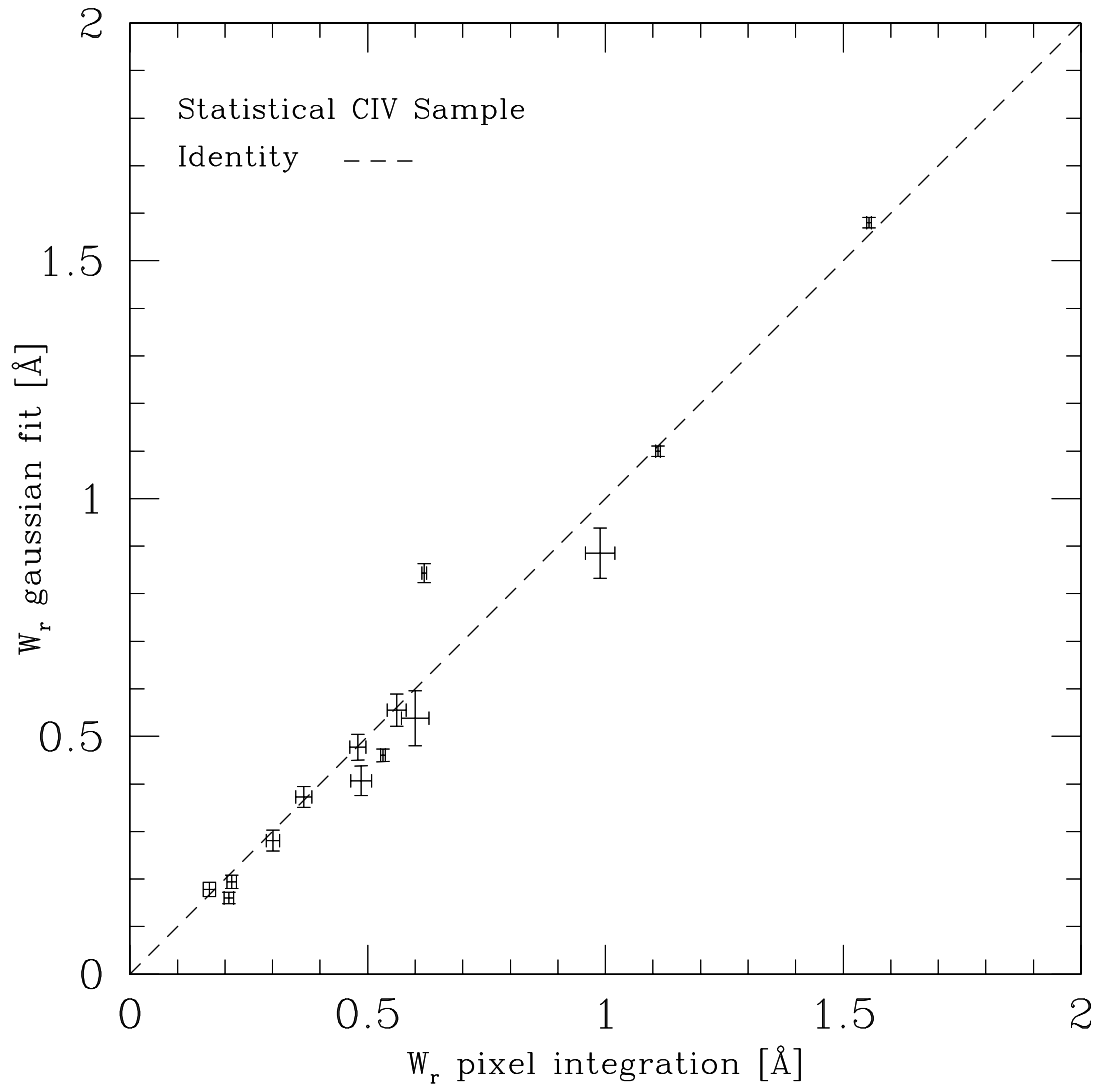


Figure 4.35 Rest frame equivalent width of C IV in the Statistical Sample measured with Gaussian fit and with pixel integration. The dashed line is the identity function.

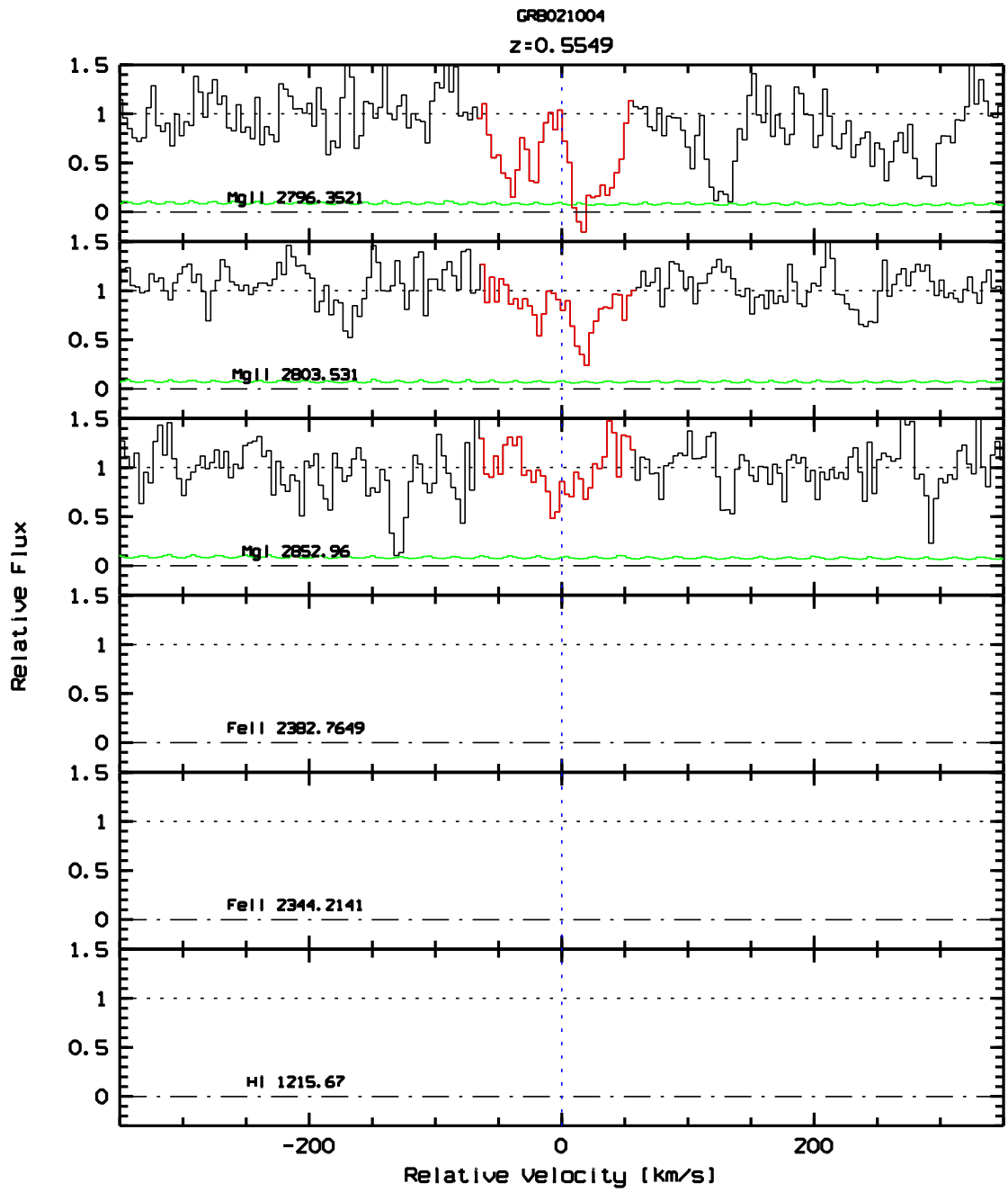


Figure 4.36 Absorption velocity profile of Mg II absorption system at $z_{abs} = 0.5549$. This system is a dubious one and will be only used to obtain an upper limit value on number density.

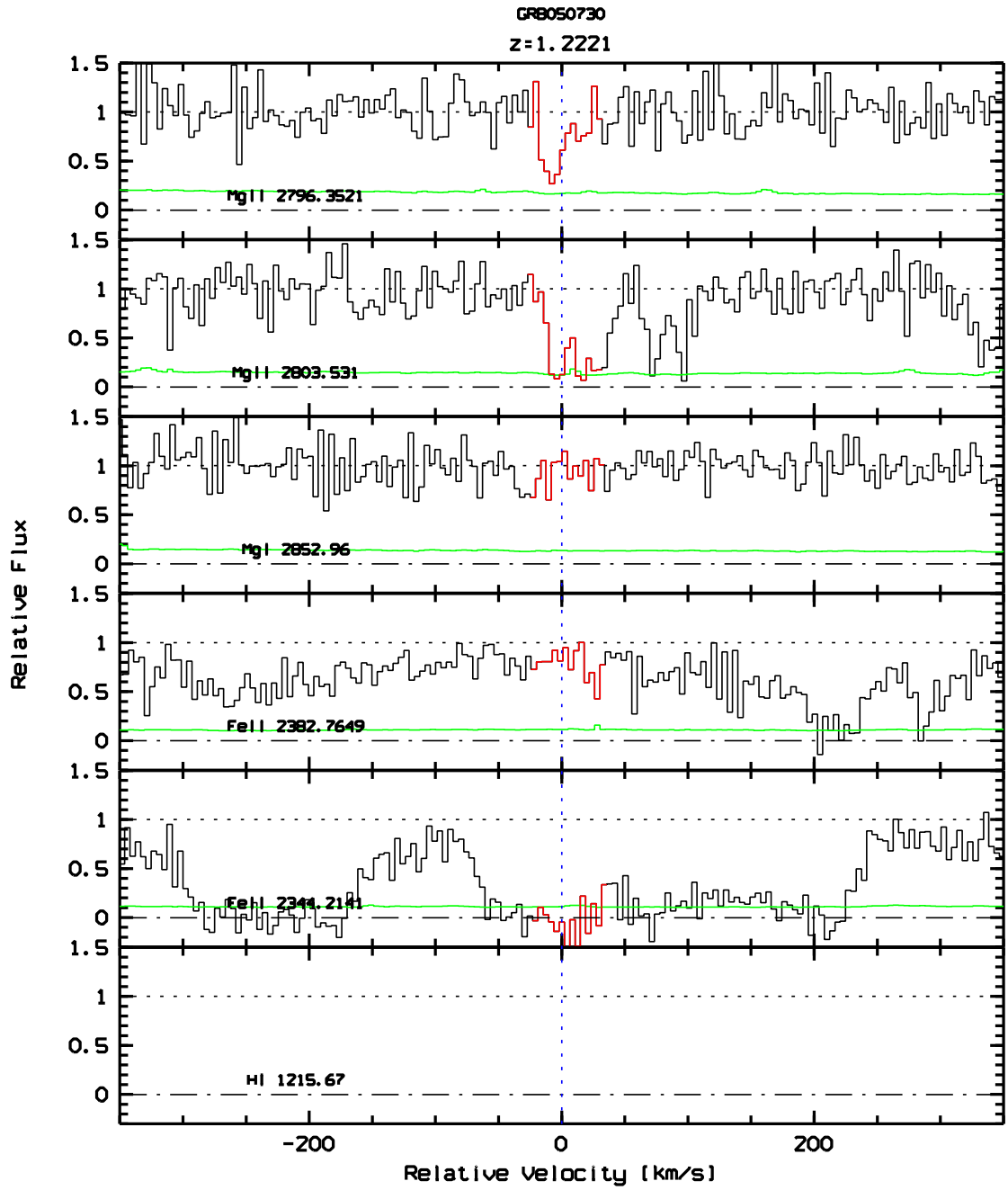


Figure 4.37 Absorption velocity profile of Mg II absorption system at $z_{abs} = 1.2221$. This system is a dubious one and will be only used to obtain an upper limit value on number density.

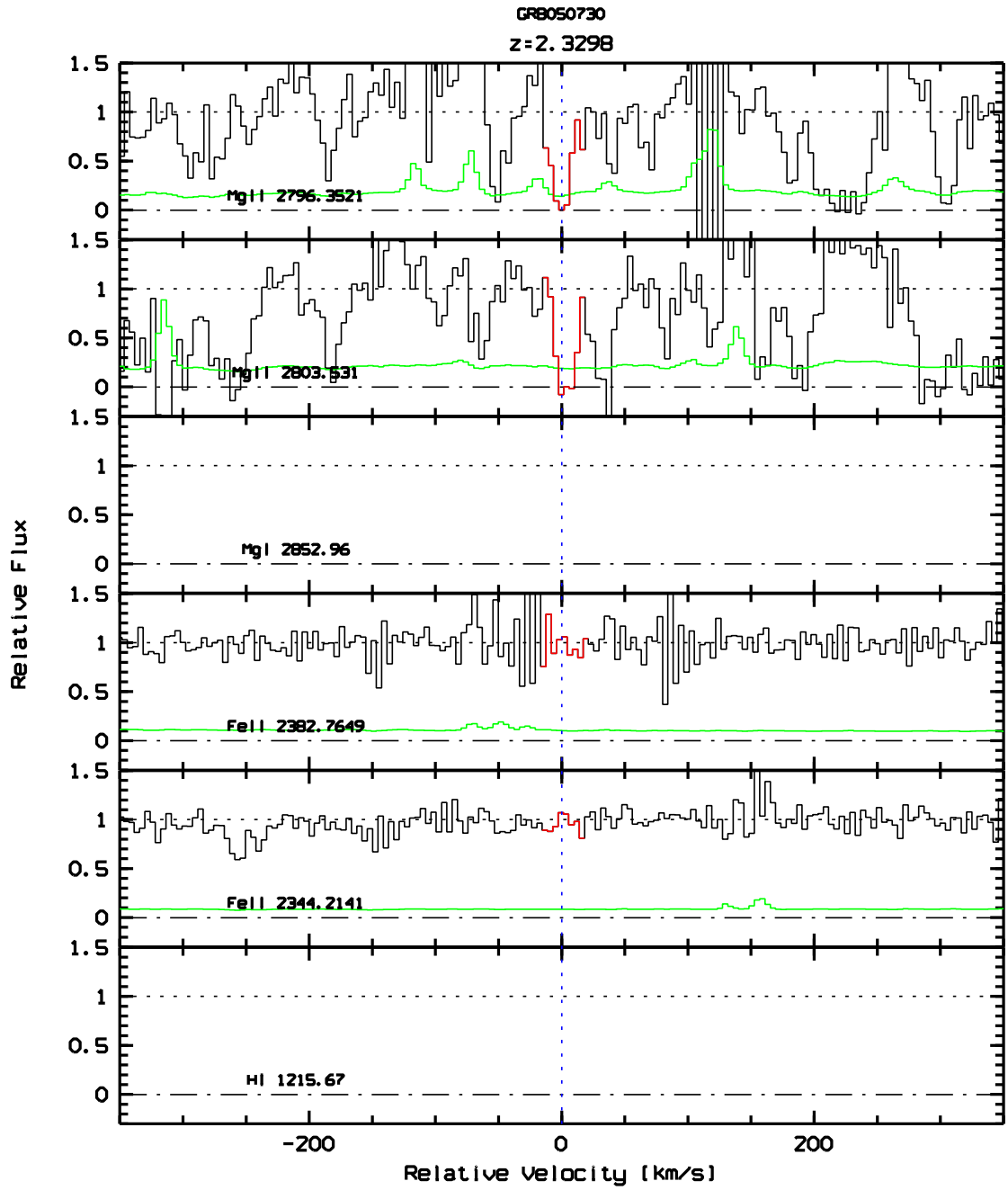


Figure 4.38 Absorption velocity profile of Mg II absorption system at $z_{abs} = 2.3298$. This system is a dubious one and will be only used to obtain an upper limit value on number density.

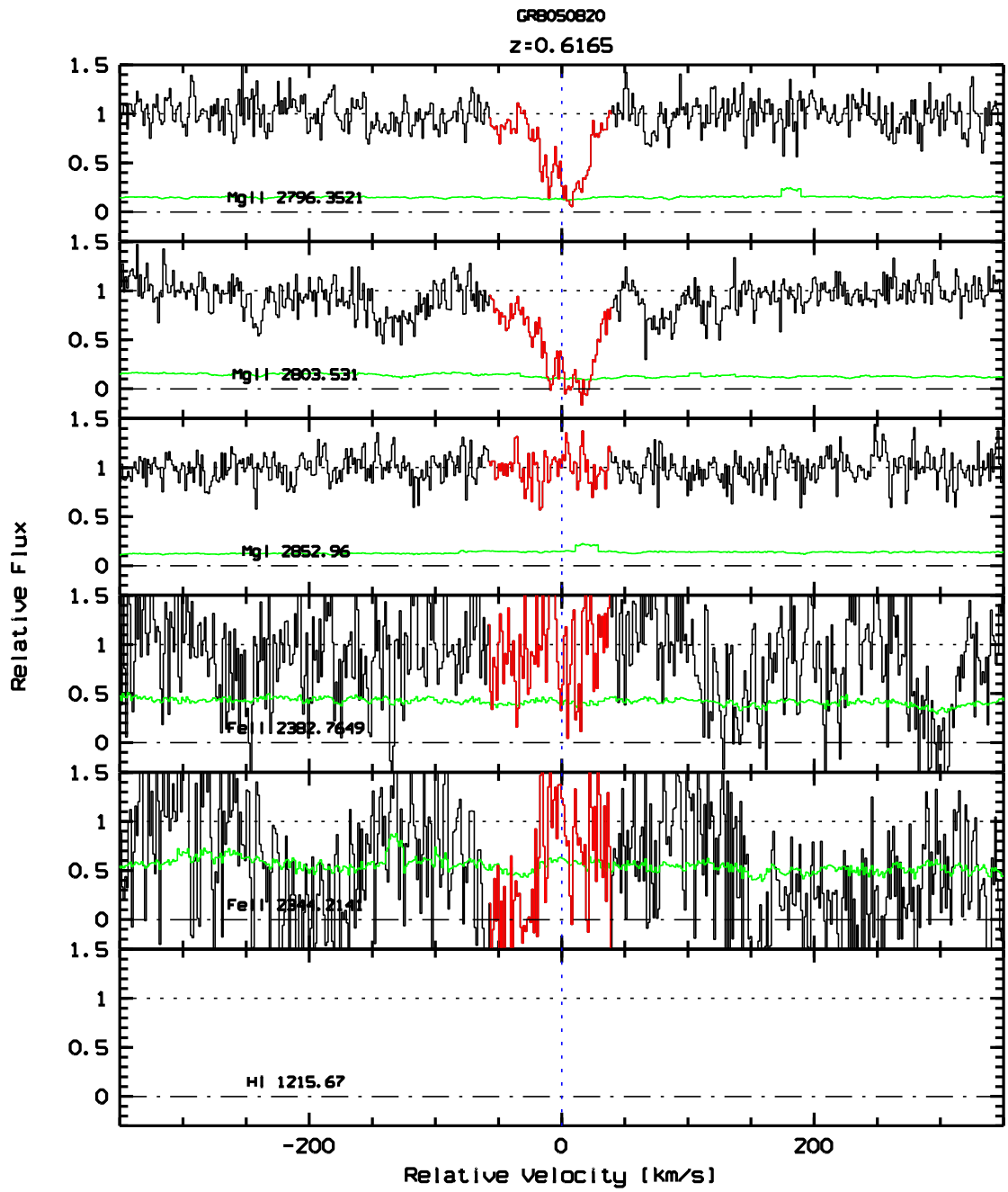


Figure 4.39 Absorption velocity profile of Mg II absorption system at $z_{abs} = 0.6165$. This system is a dubious one and will be only used to obtain an upper limit value on number density.

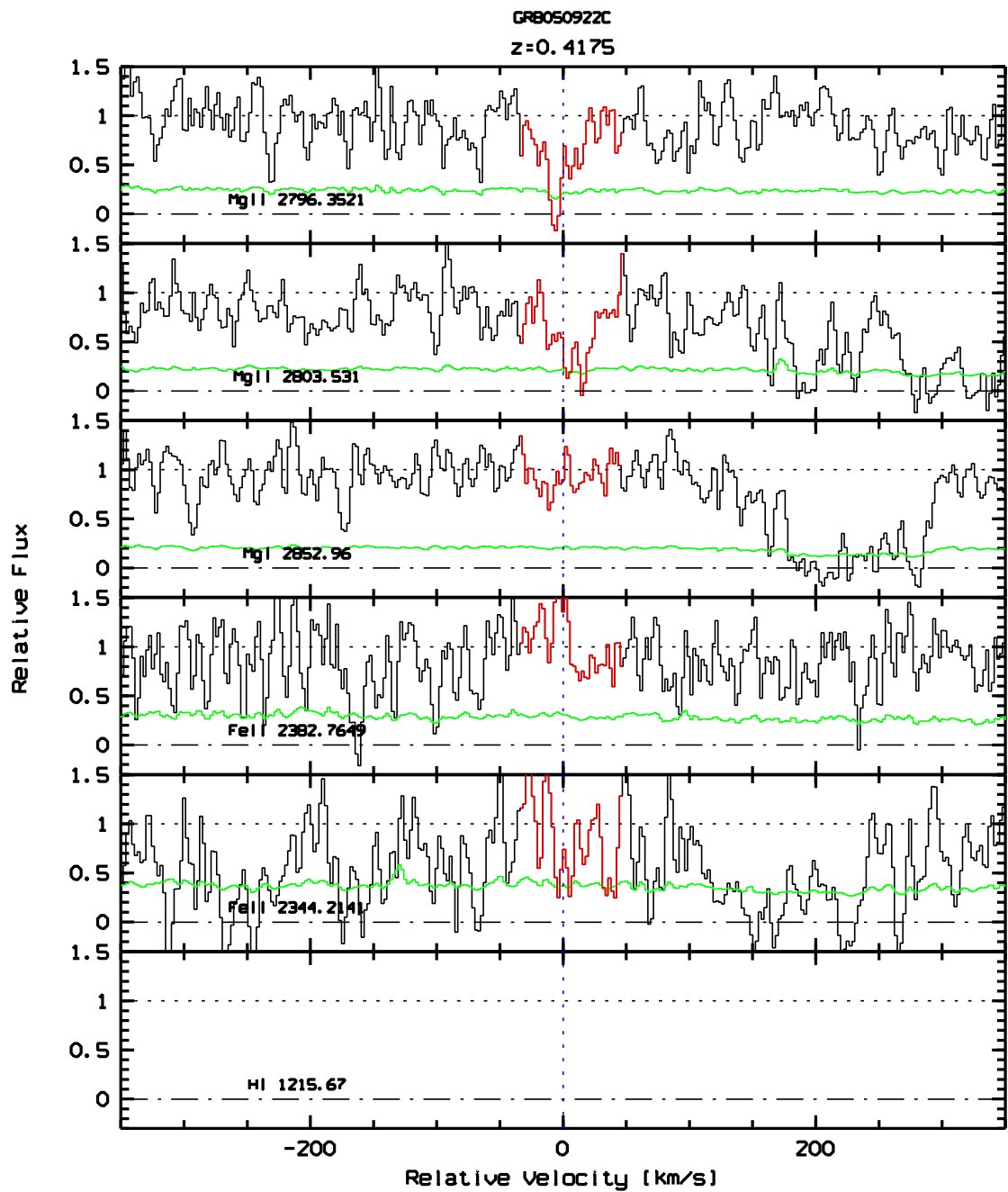


Figure 4.40 Absorption velocity profile of Mg II absorption system at $z_{abs} = 0.4175$. This system is a dubious one and will be only used to obtain an upper limit value on number density.

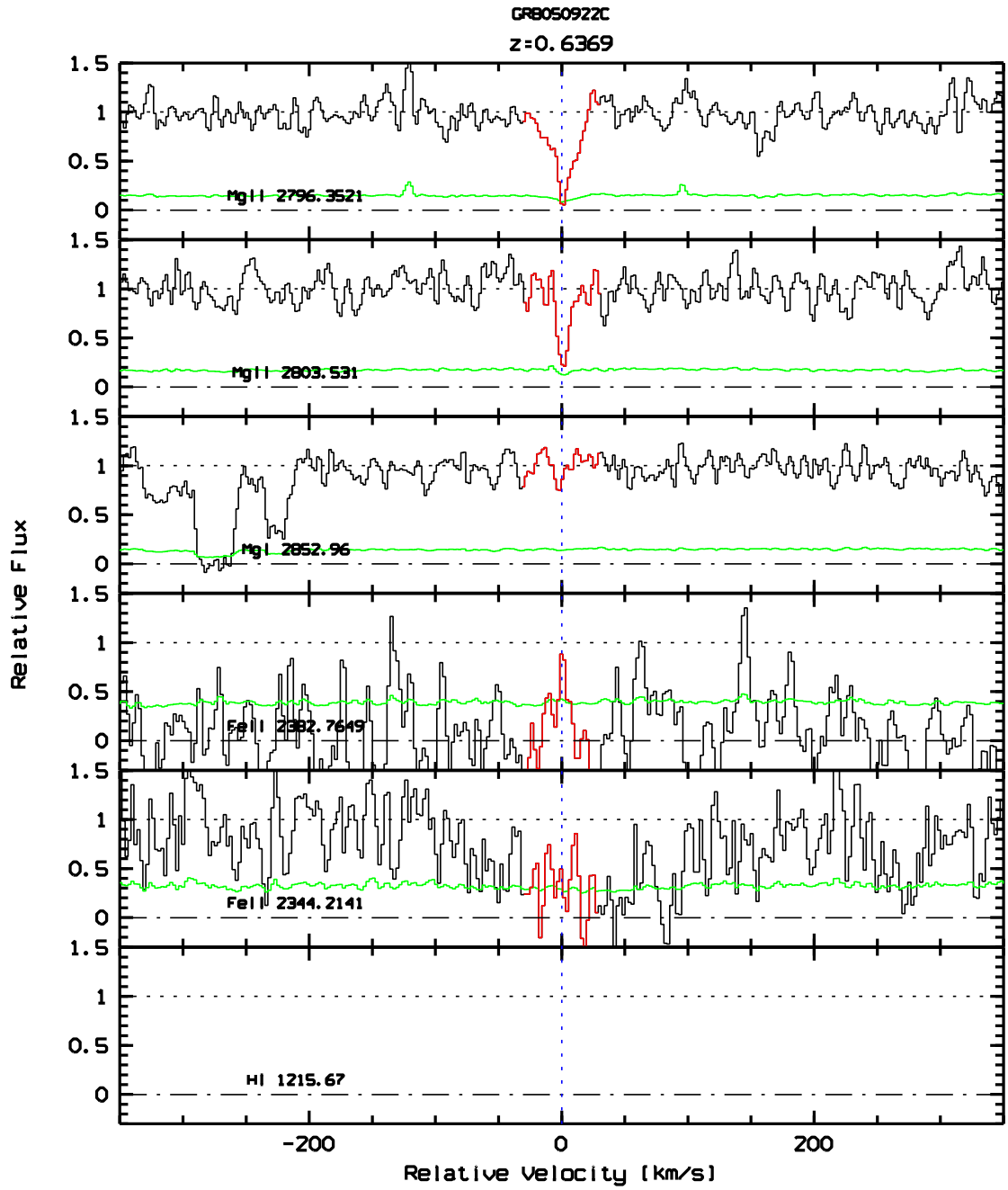


Figure 4.41 Absorption velocity profile of Mg II absorption system at $z_{abs} = 0.6369$. This system is a dubious one and will be only used to obtain an upper limit value on number density.

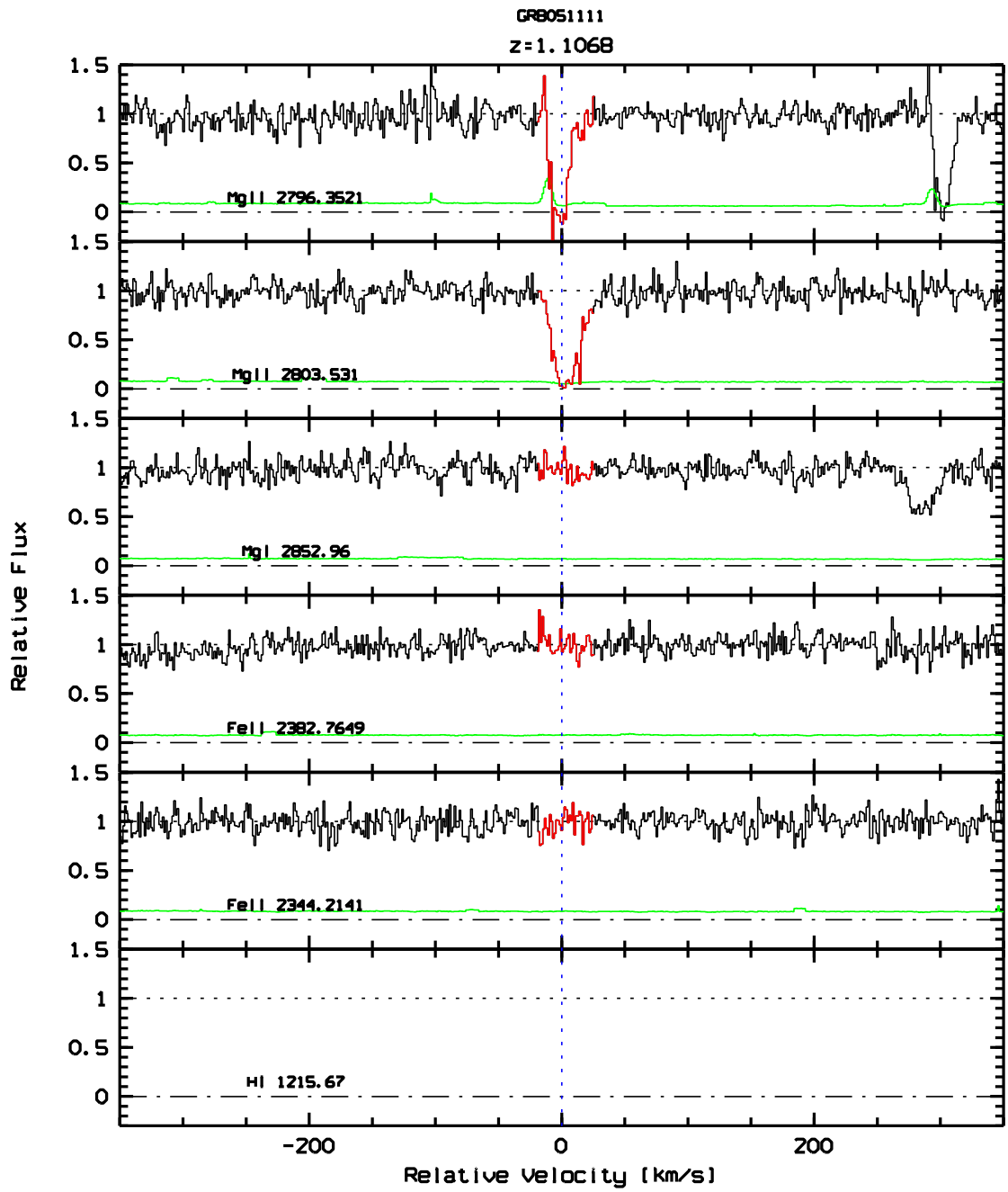


Figure 4.42 Absorption velocity profile of Mg II absorption system at $z_{abs} = 1.1068$. This system is a dubious one and will be only used to obtain an upper limit value on number density.

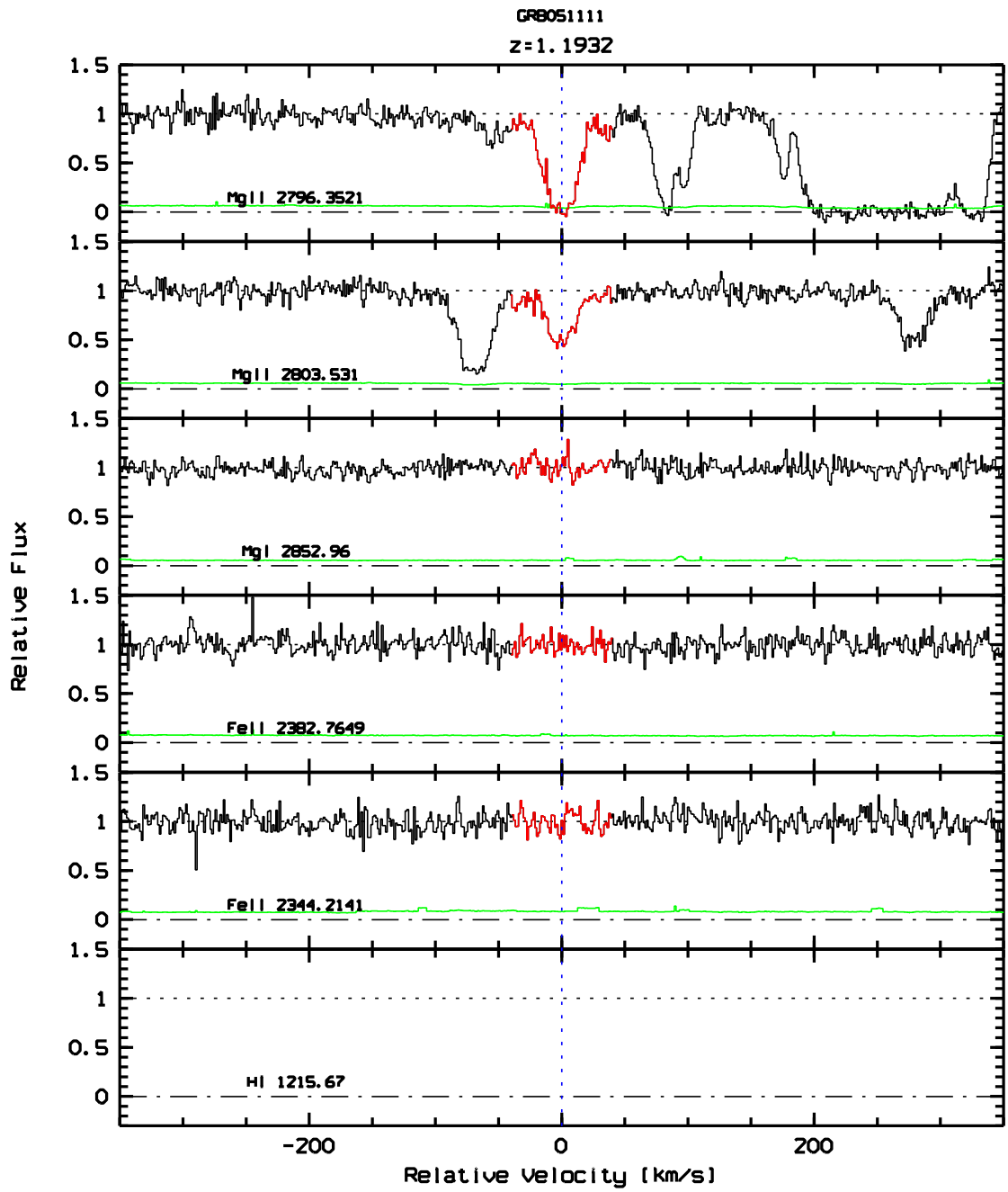


Figure 4.43 Absorption velocity profile of Mg II absorption system at $z_{abs} = 1.1933$. This system is a dubious one and will be only used to obtain an upper limit value on number density.

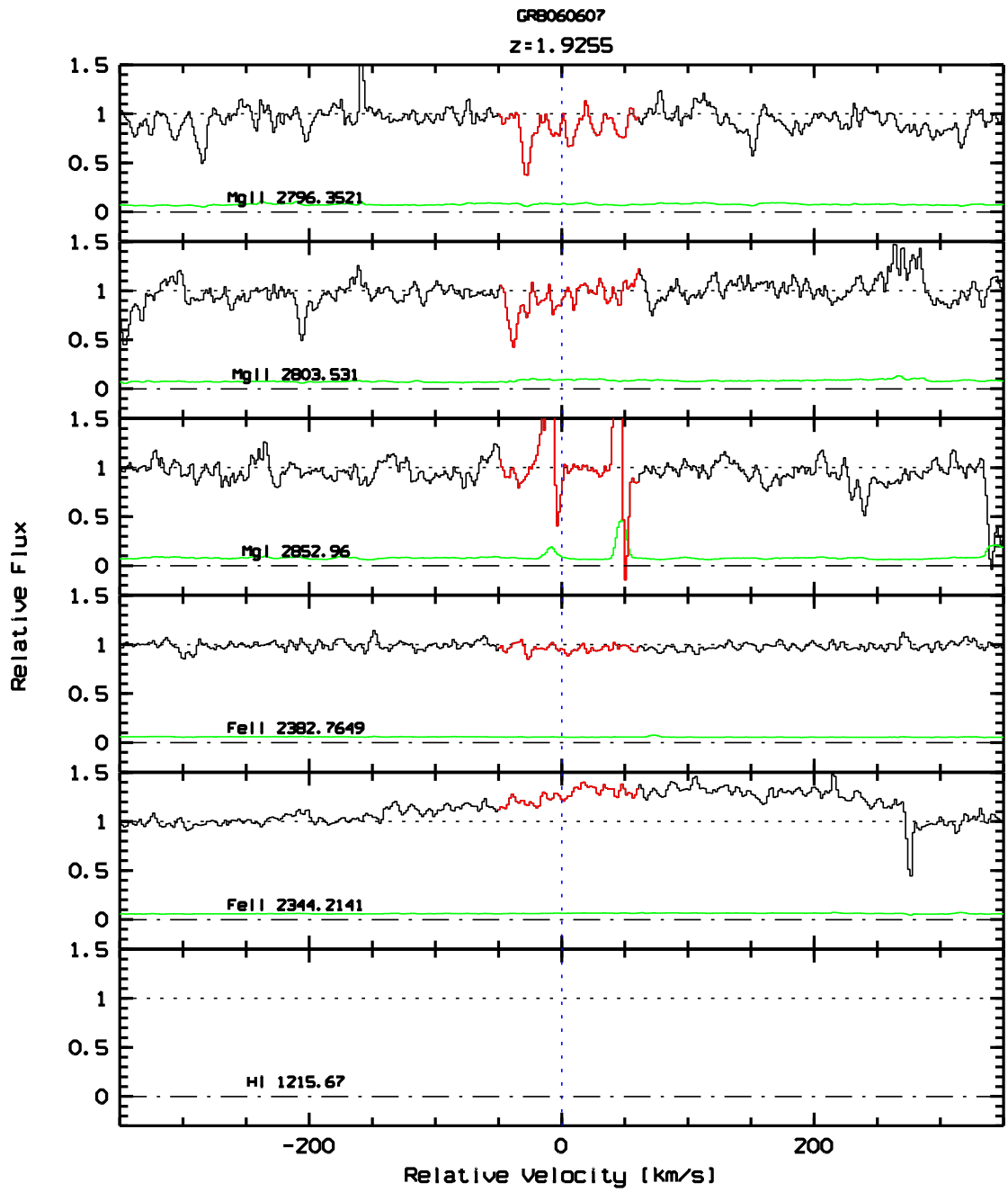


Figure 4.44 Absorption velocity profile of Mg II absorption system at $z_{abs} = 1.9255$. This system is a dubious one and will be only used to obtain an upper limit value on number density.

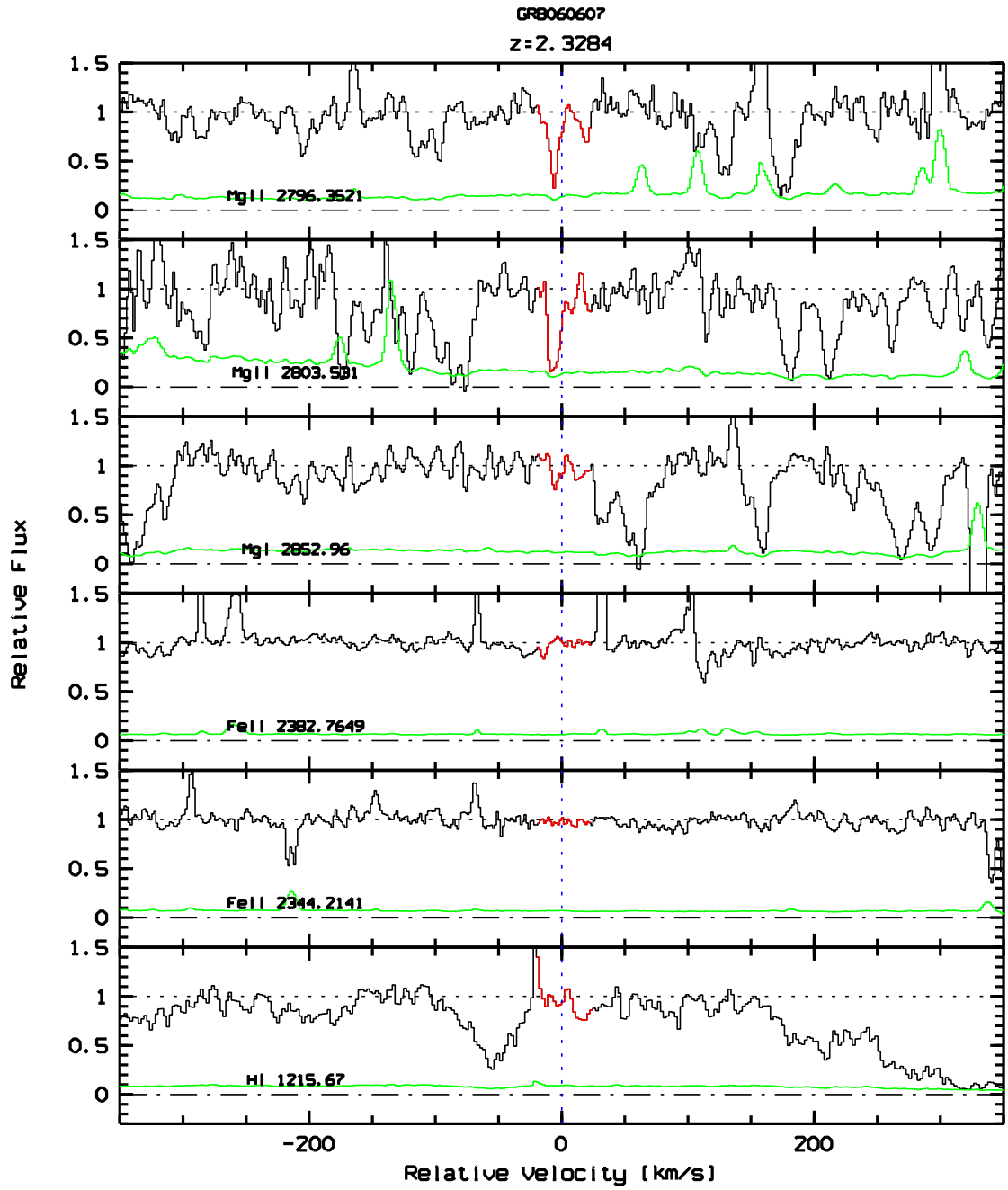


Figure 4.45 Absorption velocity profile of Mg II absorption system at $z_{abs} = 2.3284$. This system is a dubious one and will be only used to obtain an upper limit value on number density.

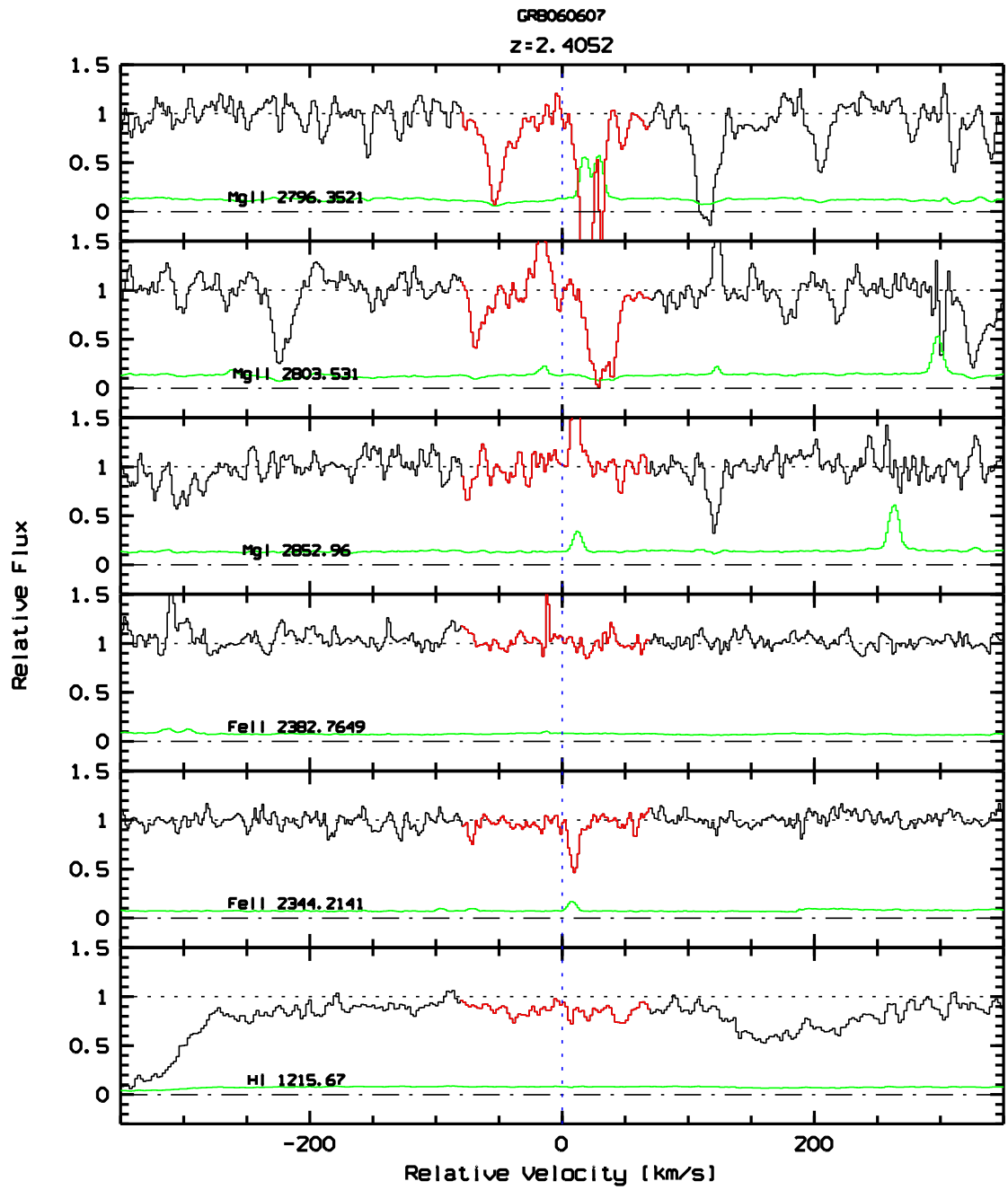


Figure 4.46 Absorption velocity profile of Mg II absorption system at $z_{abs} = 2.4052$. This system is a dubious one and will be only used to obtain an upper limit value on number density.

Chapter 5

Redshift Path Density

According to the formalism described in Lanzetta et al. (1987), the redshift path density, $g(W, z)$, is defined as the number of lines of sight whose absorption lines with rest equivalent width greater or equal to W at an absorption redshift z , could be detected in the survey.

This number is used to compensate for inhomogeneities in the different spectra of a sample, either due to differences in signal-to-noise, or in the redshift coverage for a given transition (e.g., Mg II, C IV).

A convenient way to get this function is in terms of pixels (as in section 3.1.1). Let λ_i and λ_0 be the wavelength of the i th pixel and the rest wavelength of a given transition, respectively, then the redshift corresponding to that transition is $z_i = \lambda_i/\lambda_0 - 1$. Therefore, it is possible to write the redshift path density of the survey at the j th rest equivalent width, W_j , and k th redshift, z_k , as,

$$g(W_j, z_k) = \sum_n H(z_k - z_n^{min}) H(z_n^{max} - z_k) H(W_j - W_k^{min})$$

where H is the Heaviside step function, z_n^{min} and z_n^{max} are the minimum and maximum redshift covered for the n th GRB for the given transition, respectively, and W_k^{min} is the minimum rest frame equivalent width that the line at redshift z_k that can be detected at a given significance level. Finally, the sum is over all GRB spectra in the sample.

5.1 Determination of W^{min} as a Function of Wavelength

To calculate the minimum rest frame equivalent width of a line that can be detected for a given redshift z and significance level sl , a W^{min} spectrum was created.

From each GRB spectrum we have the normalized flux of pixel j , I_j , and its uncertainty or noise, σ_{I_j} . Therefore, the associated W^{min} of the j th pixel can be written as,

$$W_j^{min} = \frac{sl \lambda_j \sigma_{I_j}}{(1+z) R}$$

where λ_j is the wavelength of pixel j and R is the spectral resolution. This equation is analogous to say that the uncertainty on W is,

$$\sigma_W = \frac{FWHM}{\langle S/N \rangle}$$

where $FWHM$ is the spectral resolution (in wavelength units) and $\langle S/N \rangle$ is the average signal-to-noise ratio over a given spectral range, except that, the former expression was corrected by redshift and the signal-to-noise ratio is treated in pixel units assuming that $(\frac{S}{N})_j = \frac{1}{\sigma_{I_j}}$.

As an example, Figure 5.1 shows the W^{min} spectrum as a function of redshift for the C IV and Mg II transitions for the same GRB and a 5σ significant level.

This spectrum was not smoothed in order to take into account the effect produced by spectral zones with low signal-to-noise (e.g., see the zones in Figure 5.1 over the reference W_{min}^{ref} value) or in other words, to not overestimate the redshift path density. It is clear that W_{min} varies with redshift and for different transitions, having direct impact in the determination of the redshift path density.

5.2 Redshift Path as a Function of Equivalent Width

To determine the survey completeness, i.e., the W_{min} values at which the redshift path density is maximized, it is useful to compute the function,

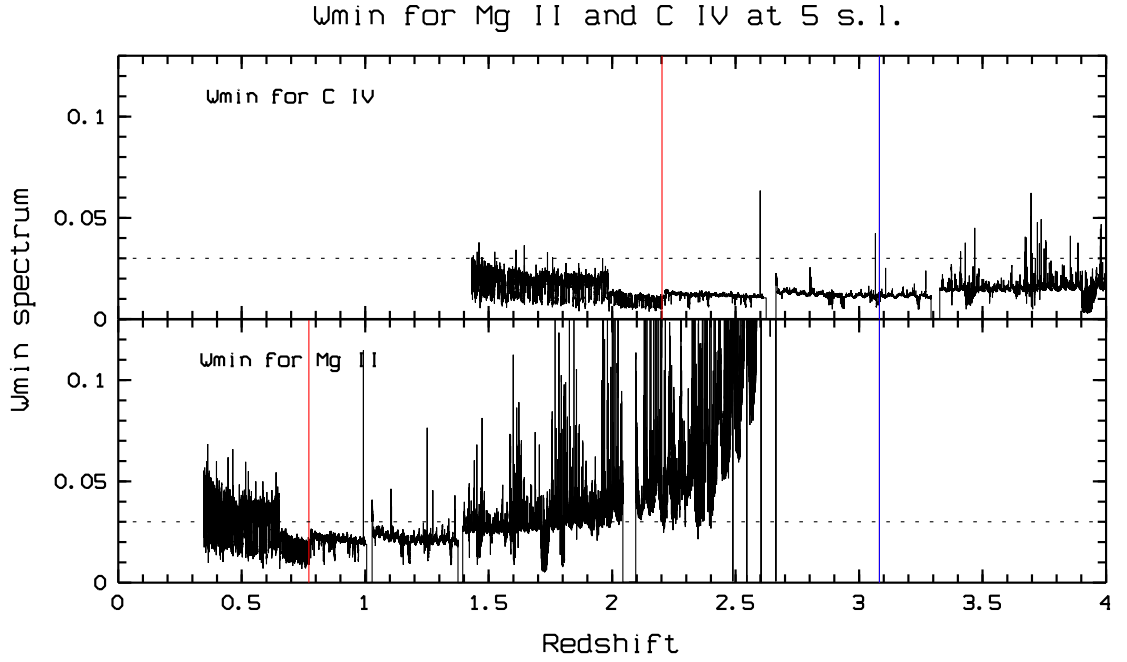


Figure 5.1 Minimum equivalent width spectrum for the C IV and Mg II transitions as a function of redshift both at 5σ significance level for GRB060607. Blue and red lines correspond to the redshift of the GRB and the associated position of the Ly α , transition respectively. Dotted lines show a reference value of $W_{min}^{ref} = 0.03 \text{ \AA}$. It is clear how W_{min} varies with redshift and for different transitions with direct impact in the determination of the redshift path density.

$$g(W) = \int_0^{\infty} g(W, z) dz$$

or its discrete form,

$$g(W_j) = \sum_k g(W_j, z_k) \delta z$$

where δz is the grid resolution in redshift and the sum is over the redshift interval analyzed. This function gives the total redshift path covered by the survey for a given W_j .

5.3 Redshift Path as a Function of Redshift

The number of lines of sight covered by the survey between redshift z and $z + dz$ for a given W_{min} can be obtained from $g(W_{min}, z)$. Thus, the total redshift path covered by the survey between $z = 0$ and $z = z_k$, namely $\Delta Z(z_k)$, can be written as a cumulative function of $g(W_{min}, z)$,

$$\Delta Z(z_k) = g(W_{min}|z < z_k) = \sum_{i=0}^k g(W_{min}, z_i) \delta z$$

Therefore, the total redshift path between z_1 and z_2 with $z_1 < z_2$ can be calculated simply from $\Delta Z(z_2) - \Delta Z(z_1)$. This value gives the total redshift path for a given redshift bin between z_1 and z_2 .

5.4 Removal of Telluric Lines Zones

As mentioned in Section 4, spectral zones blueward of Ly α and within 5000 km s $^{-1}$ from each GRB redshift were removed from the survey in order to improve the results. Likewise, because of the presence of many telluric lines certain spectral zones were also removed from the search of intervening systems. I removed the zones between 6860 – 7000 Å and 7590 – 7690 Å which have high contamination of sky lines. I refer the reader to the High Resolution Spectral Atlas of Telluric Lines by Catanzaro (1997) for further details about contaminated spectral zones.

5.5 Redshift Path for the Mg II Sample

Figure 5.2 shows the redshift path for the Mg II GRB sample as a function of rest-frame equivalent width. It is clear that the survey is very incomplete at $W_{min} < 0.05$ Å hence I cannot compare directly with previous high resolution surveys which have used $W_{min} = 0.02$ Å (Narayanan et al., 2007). Therefore I excluded systems in previous surveys with rest-frame equivalent width smaller than our W_{min} . As mentioned, I chose a $W_{min} = 0.07$ Å for the Mg II survey which gives a completeness above a 96% (see Figure 5.2).

Figure 5.3 shows the equivalent width spectrum for the Mg II sample as a function of redshift. This figure is useful to visualize the total redshift path covered by the survey as a function of both equivalent width and redshift simultaneously. The dotted line shows how the completeness is nearly

total about $W_{min} = 0.07 \text{ \AA}$.

Adopting this $W_{min} = 0.07 \text{ \AA}$ for Mg II I can obtain the number of lines-of-sight and its cumulative redshift path covered by the survey as a function of redshift, as shown in Figure 5.4.

5.6 Redshift Path for the C IV Sample

Figure 5.5 shows the redshift path for the C IV GRB sample as a function of rest-frame equivalent width. It is clear that the GRB survey is complete at $W_r \geq 0.15 \text{ \AA}$. This limit is the same as used by previous QSO surveys (Steidel, 1990) for this kind of studies.

Figure 5.6 shows the equivalent width spectrum for the C IV sample as a function of redshift. This figure is useful to visualize the total redshift path covered by the survey as a function of both equivalent width and redshift simultaneously.

Figure 5.7 shows the redshift path as a function of redshift for a given W_{min} value. In this case I use $W_{min} = 0.15 \text{ \AA}$ which corresponds to the same limit used in previous surveys.

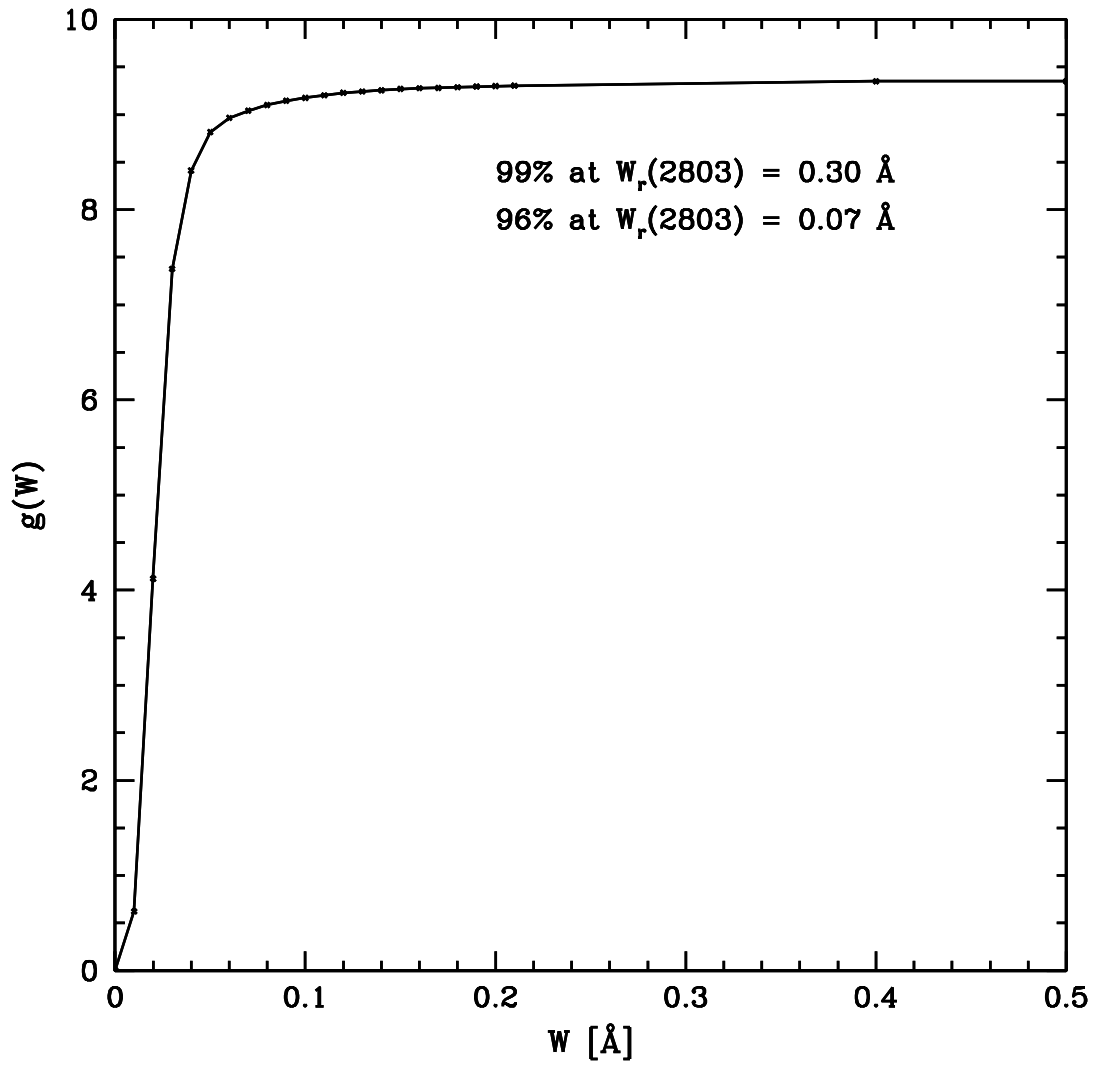


Figure 5.2 Cumulative redshift path of the Mg II GRB survey as a function of rest-frame equivalent width.

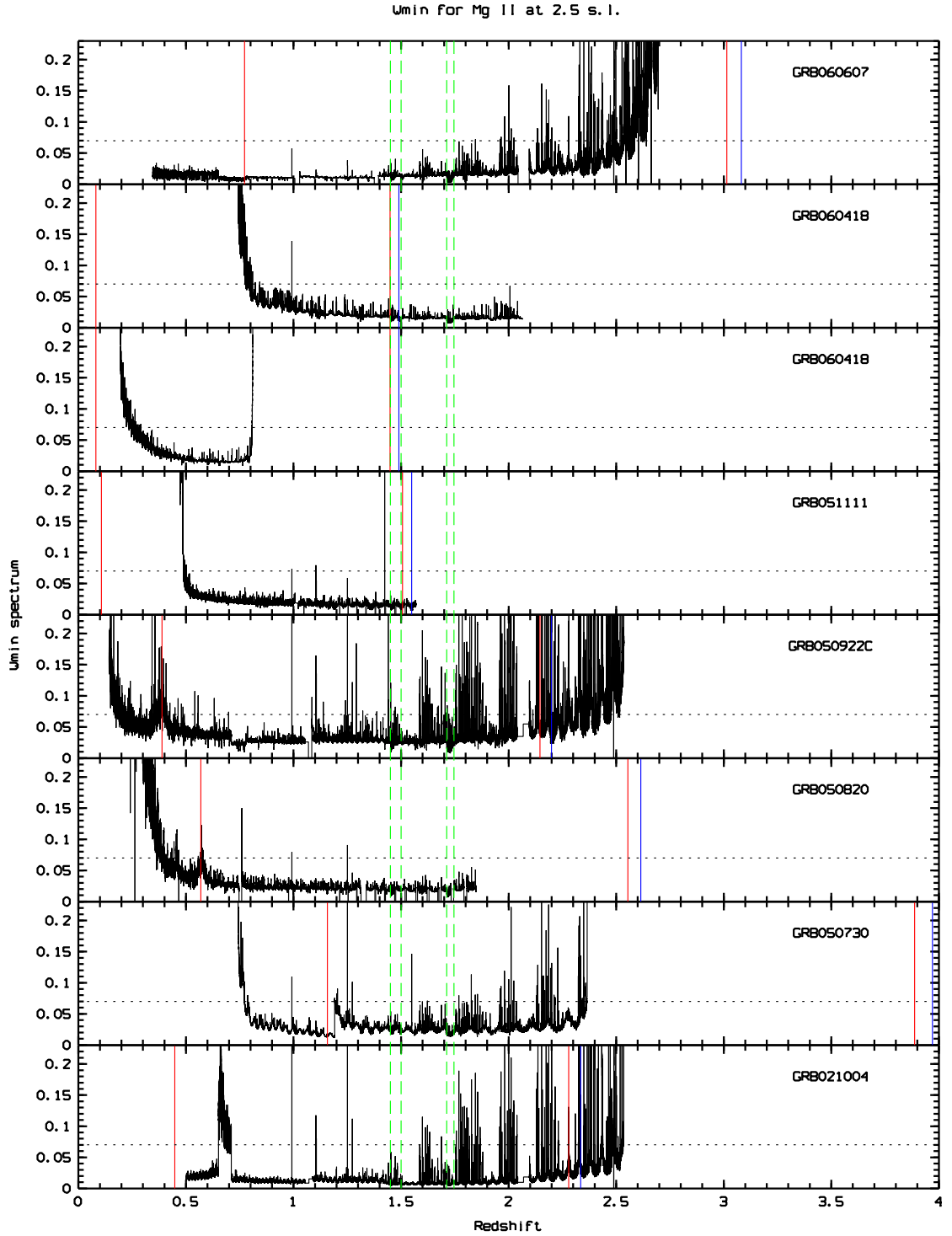


Figure 5.3 Minimum equivalent width spectrum for Mg II as a function of redshift at the 2.5σ significance level. Blue lines correspond to each GRB redshift. Red lines correspond to $\text{Ly}\alpha$ transition and 5000 km s^{-1} from the GRB redshift (used to remove source contamination). Green lines show sky line contamination zones which were excluded from the redshift coverage. Dotted lines show a reference value of $W_{min}^{ref} = 0.07 \text{ \AA}$ which was used in further analysis.

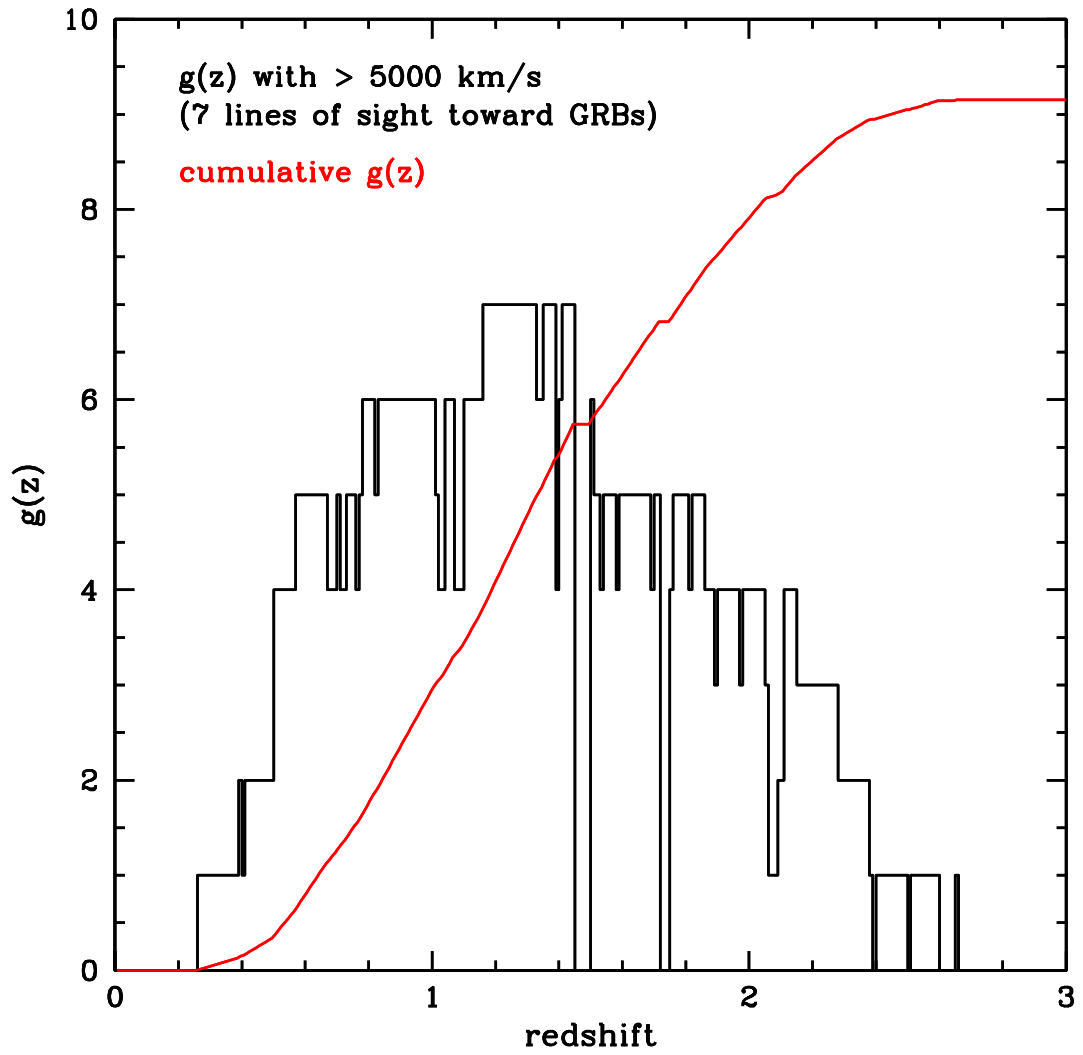


Figure 5.4 Number of lines of sight in the Mg II survey and cumulative redshift path as a function of redshift for $W_{min} = 0.07 \text{ \AA}$.

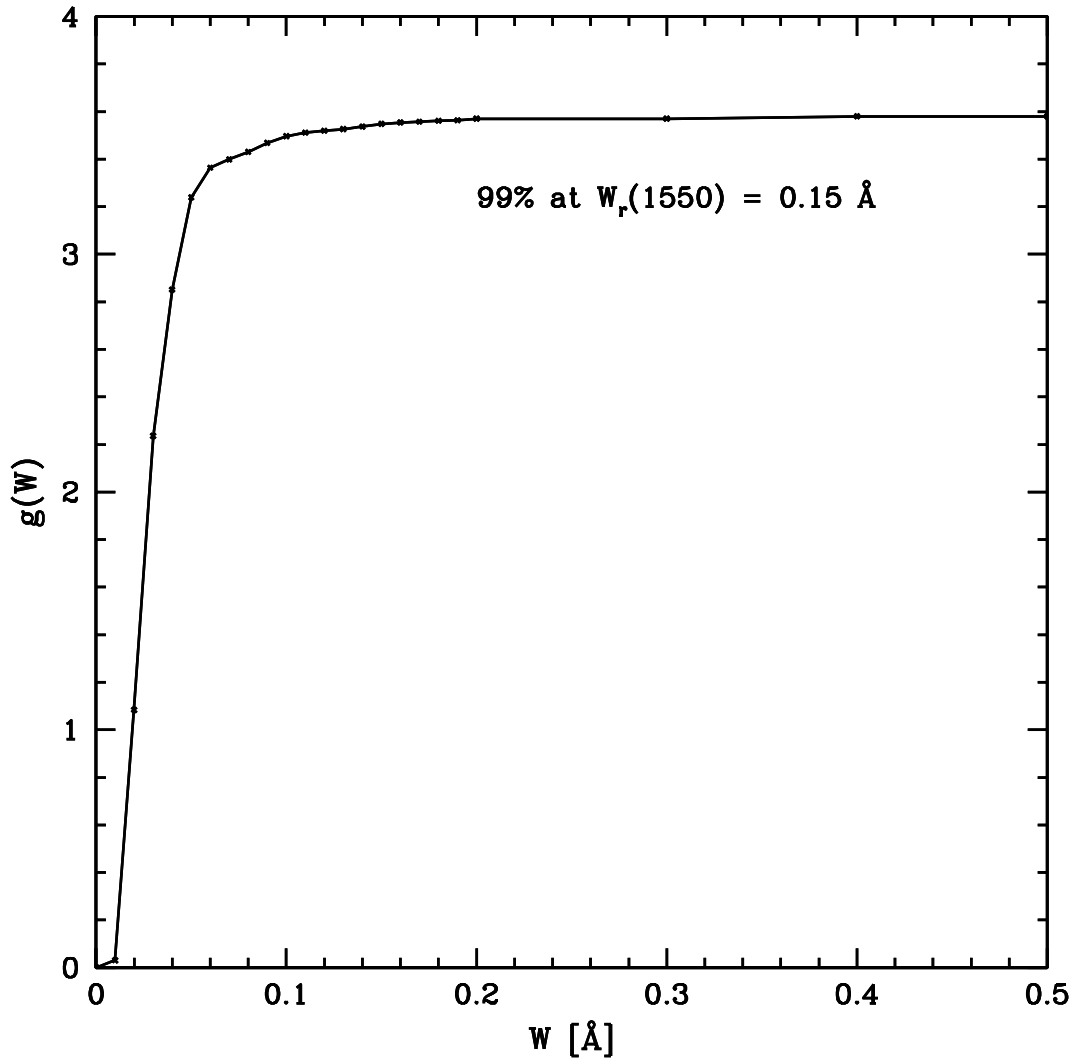


Figure 5.5 Cumulative redshift path of the C IV GRB survey as a function of rest-frame equivalent width.

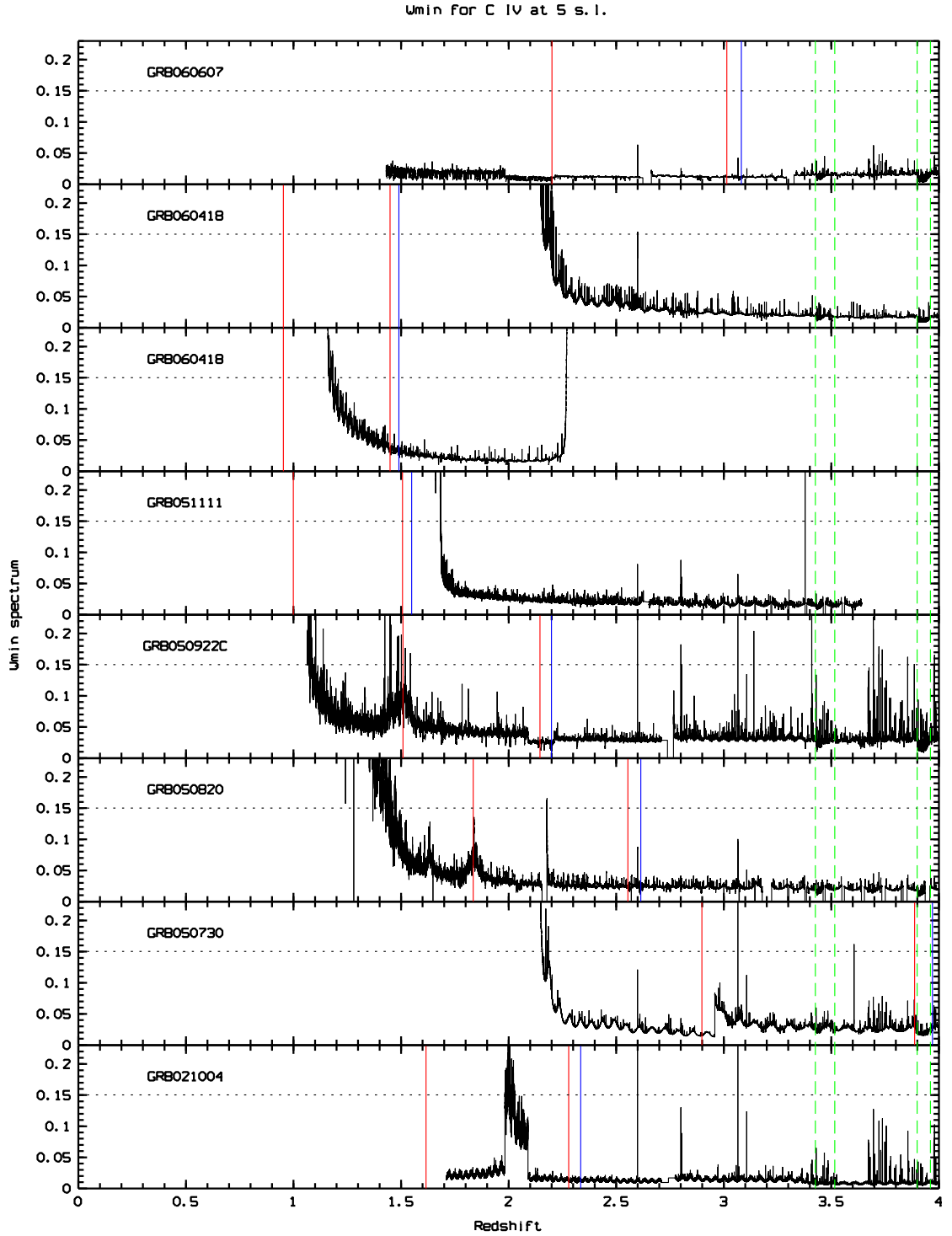


Figure 5.6 Minimum equivalent width spectrum for C IV as a function of redshift at the 5σ significance level. Blue lines correspond to each GRB redshift. Red lines correspond to Ly α transition and 5000 km s^{-1} from the GRB redshift (used to remove source contamination). Green lines show sky line contamination zones which were excluded from the redshift coverage. Dotted lines show a reference value of $W_{min}^{ref} = 0.15 \text{ \AA}$ which was used in further analysis.

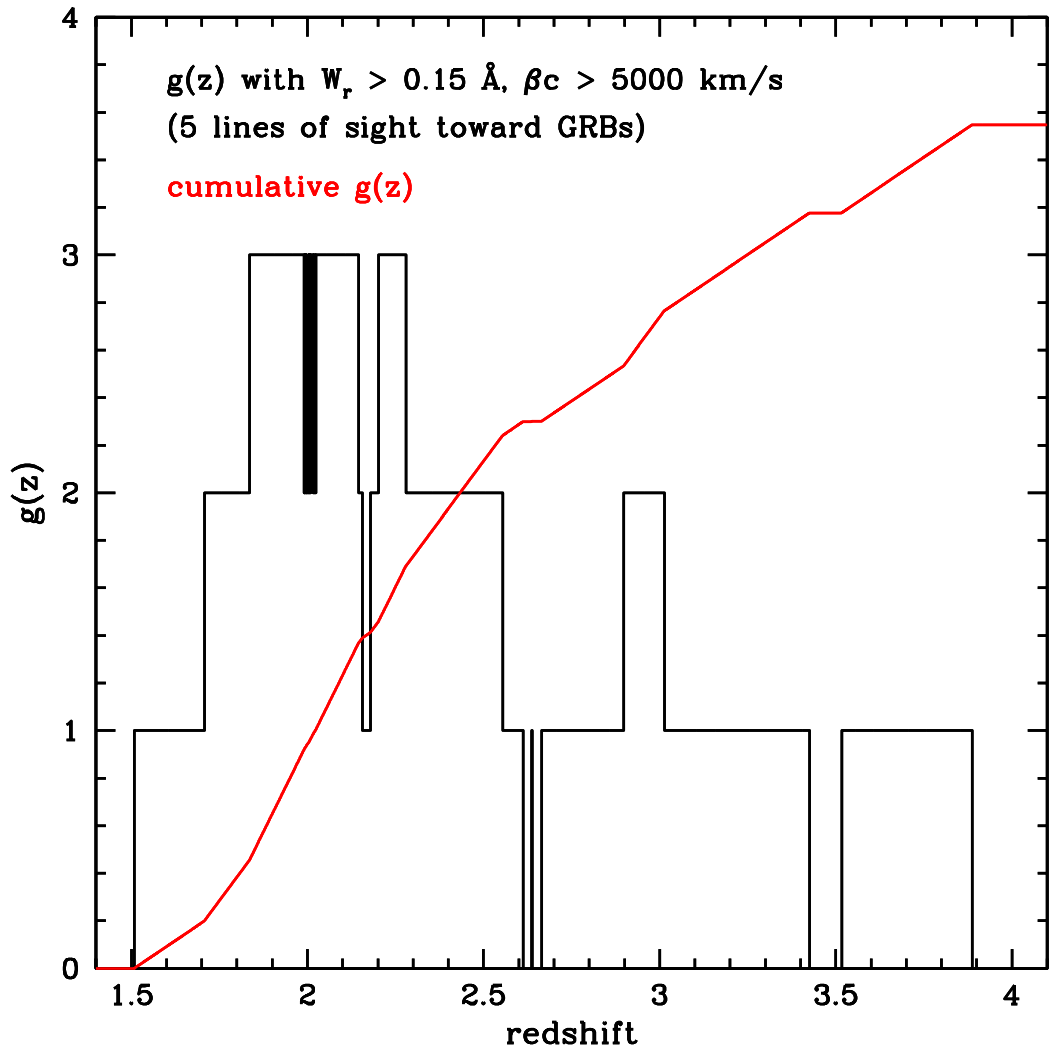


Figure 5.7 Number of lines of sight in the C IV survey and cumulative redshift path as a function of redshift for $W_{min} = 0.15 \text{ \AA}$.

Chapter 6

Redshift Number Density

6.1 Definition

The redshift number density, dN/dz , is the number of absorbers per unit redshift. By definition,

$$\frac{dN}{dz} = \frac{N_{abs}}{\Delta z},$$

where N_{abs} is the number of absorption systems observed in the redshift path Δz . As shown in Chapter 5, the redshift path is a function of both redshift and equivalent width, therefore N_{abs} is directly related to Δz in the sense that each detected system has a given equivalent width. For this reason there are two ways to calculate the redshift number density, either a direct calculation or one weighting different redshift paths. These definitions can be used directly for different redshifts bins without any extra consideration.

6.1.1 Direct Calculation

If there is an unbiased survey defined by a single W_{min} value it is possible to obtain the redshift number density directly from its definition, i.e.,

$$\frac{dN}{dz}(W_{min}) = \frac{N_{abs}(W_r > W_{min})}{\Delta z(W_{min})}.$$

In this case the whole spectral range used to search systems must have enough signal-to-noise ratio to permit detections with $W_r > W_{min}$.

6.1.2 Calculation Weighting Different Redshift Paths

If it is necessary to perform surveys at equivalent widths limits which fall near the completeness of the survey, the redshift number density can be calculated as the sum of all detected systems, each one divided by its own redshift path, i.e.,

$$\frac{dN}{dz} = \sum_i^{N_{abs}} \frac{1}{\Delta z(W_r^i)},$$

where W_r^i is the rest-frame equivalent width for the i th detected system. This approach takes into account the fact that it is easier to find systems with greater equivalent widths ($\Delta z(W_1) \geq \Delta z(W_2)$ for $W_1 > W_2$). Strictly speaking this formalism gives a more meaningful redshift number density than a direct calculation. However since Δz has an 'asymptotic' behavior at equivalent widths closer to the survey completeness, the differences between redshift paths for different equivalent widths are negligible.

I use both methods for the calculations of redshift path density for the *weak* Mg II population. For *strong* Mg II and C IV I use only the direct calculation because the equivalent width limits for those samples are greater than the equivalent width completeness.

6.2 Error Estimation

It is very important to have meaningful error estimates for the redshift number density because these numbers will have direct impact on the results and the comparison with other surveys. The conclusions may be affected, especially due to the small number statistics, if the errors are underestimated.

To estimate the error in dN/dz I assume a Poissonian distribution in the number of absorbers N_{abs} in a given redshift bin Δz^{bin} . I do not assume the usual approximation:

$$\sigma_{N_{abs}} = \sqrt{N_{abs}},$$

which is typically used for Poissonian distributions. Instead, I take into account the fact that N_{abs} is usually small, under which circumstances the Poissonian distribution is asymmetric with different upper and lower limits. According to the study of confidence limits for small numbers (Poissonian and Binomial distributions) by Gehrels (1986) there are good approximations for these limits although the best values come from numerical results. For that reason, to obtain the errors associated with our redshift number density calculation, I assign the upper and lower limits correspond to 1σ confidence level of a Gaussian statistic, ($1\sigma = 0.8413$) $1\sigma_{N_{abs}}^+$ and $1\sigma_{N_{abs}}^-$ respectively, obtained directly from the Gehrels (1986) tables. For instance, these limits can be approximated by,

$$\sigma_{N_{abs}}^+ \approx \sqrt{N_{abs} + \frac{3}{4}} + 1,$$

and

$$\sigma_{N_{abs}}^- \approx \sqrt{N_{abs} - \frac{1}{4}},$$

Despite that I do not use these analytics expressions, it is interesting to note that the $\sigma_{N_{abs}}^+$ is considerably incremented (at least in one unit) while the $\sigma_{N_{abs}}^-$ is nearly the same when comparing both with the usual approximation $\sqrt{N_{abs}}$.

Finally, the error associated to the redshift path determination is neglected. This is because the error in redshift number density value is dominated by the uncertainty in N_{abs} . Following previous notation, the redshift number density uncertainty obtained from a direct calculation, can be written as,

$$\sigma_{dN/dz}^{+,-} = \frac{1\sigma_{N_{abs}}^{+,-}}{\Delta z^{bin}}.$$

On the other hand, to estimate the error in dN/dz obtained by weighting different redshift for each system equivalent width, the literature gives the following expression (e.g., Lanzetta et al., 1987),

$$\sigma_{dN/dz}^2 = \sum_i^{N_{abs}} \frac{1}{\Delta z^2 (W_r^i)},$$

which corresponds to a symmetric error and is the analogous to $\sigma = \sqrt{N}$. To correct this underes-

timination of the error I use,

$$\sigma_{dN/dz}^{+,-} = \frac{1\sigma_{N_{abs}}^{+,-}}{\langle \Delta z^{bin} \rangle},$$

where $\langle \Delta z^{bin} \rangle$ is calculated by dividing the total number of systems by the redshift number density value, i.e., $\langle \Delta z^{bin} \rangle = \frac{N_{abs}}{dN/dz}$.

Chapter 7

Results

7.1 Results on Mg II

As already said the study on Mg II in GRB spectra is motivated by the significant overabundance of *very* strong systems ($W_r \geq 1 \text{ \AA}$) reported by Prochter et al. (2006b). Because of there seems to be two Mg II populations: weak ($W_r < 0.3 \text{ \AA}$) and strong ($W_r > 0.3 \text{ \AA}$), each one showing different equivalent width distributions (see Chapter 2) it is important to investigate the incidence of these absorption systems at lower W_r values. Here, I will compare my results on these two populations of absorbers separately.

Table 7.1. Specifications of the Strict $dN/dz|_{\text{GRB}}^{\text{MgII}}$ for each Equivalent Width Range.

W_r Range [\AA]	N_{abs}^{strict}	Δz	$dN/dz _{\text{GRB}}^{strict}$	$dN/dz _{\text{QSO}}^{\text{MgII}}$
$0.07 \leq W_r(2803)$ and $W_r(2796) < 0.3$	4	9.039	$0.44^{+0.35}_{-0.21}$	$0.709^{+0.109}_{-0.095}$
$0.3 \leq W_r(2796)$	15	9.4	$1.60^{+0.53}_{-0.41}$	0.783 ± 0.033
$0.6 \leq W_r(2796)$	11	9.46	$1.16^{+0.47}_{-0.35}$	0.489 ± 0.015
$1.0 \leq W_r(2796)$	9	9.46	$0.95^{+0.43}_{-0.31}$	0.278 ± 0.010

Note. — For comparison the last column shows the resulting $dN/dz|_{\text{QSO}}^{\text{MgII}}$ from previous surveys results: Narayanan et al. (2007) for the weak Mg II population ($W_r < 0.3 \text{ \AA}$) and Nestor et al. (2005) for the strong Mg II population ($W_r > 0.3 \text{ \AA}$).

Table 7.2. Specifications of the Relaxed $dN/dz|_{\text{GRB}}^{\text{MgII}}$ for each Equivalent Width Range.

W_r Range [Å]	$N_{abs}^{relaxed}$	Δz	$dN/dz _{\text{GRB}}^{relaxed}$	$dN/dz _{\text{QSO}}^{\text{MgII}}$
$0.07 \leq W_r(2803)$ and $W_r(2796) < 0.3$	11*	9.039	$1.22^{+0.49}_{-0.36}$ *	$0.709^{+0.11}_{-0.10}$
$0.3 \leq W_r(2796)$	19*	9.4	$2.02^{+0.58}_{-0.46}$ *	0.783 ± 0.033
$0.6 \leq W_r(2796)$	11	9.46	$1.16^{+0.47}_{-0.35}$	0.489 ± 0.015
$1.0 \leq W_r(2796)$	9	9.46	$0.95^{+0.43}_{-0.31}$	0.278 ± 0.010

Note. — * These numbers must be considered as upper limits due to the presence of many unreal systems. For comparison the last column shows $dN/dz|_{\text{QSO}}^{\text{MgII}}$ from previous surveys results: Narayanan et al. (2007) for the weak Mg II population ($W_r < 0.3$ Å) and Nestor et al. (2005) for the strong Mg II population ($W_r > 0.3$ Å).

Table 7.3. Comparison between $dN/dz|_{\text{GRB}}^{\text{MgII}}$ for very strong Mg II systems ($W_r > 1$ Å) obtained from our survey and Prochter et al. (2006b).

Survey	N_{abs}	Δz	$dN/dz _{\text{GRB}}^{\text{MgII}}$
This work	9	9.46	$0.95^{+0.43}_{-0.31}$
This work ($z < 2$)	8	8.14	$0.98^{+0.45}_{-0.34}$
Prochter et al. (2006b)	14	15.5	$0.90^{+0.31}_{-0.24}$

Note. — We obtain the same result as Prochter et al. (2006b). Our result is based on 7 high resolution GRB spectra while Prochter et al. (2006b) used 14 GRB spectra. Both surveys have in common 5 GRB spectra (namely GRB021004, GRB050730, GRB050820, GRB051111 and GRB060418) while our survey have 2 new spectra (GRB050922C and GRB060607). Our survey extends beyond $z = 2$ in contrast with Prochter et al. (2006b) survey which was performed $z < 2$.

7.1.1 Weak Mg II Absorption Systems

Due to the short Δz available to obtain the number density, I use only one redshift bin across the whole redshift coverage of our survey ($0.25 < z < 2.59$). I find that $dN/dz|_{\text{GRB}} = 0.44_{-0.21}^{+0.35}$ for $W_r < 0.3 \text{ \AA}$ in the *strict* sample. This number is consistent with $dN/dz|_{\text{QSO}} = 0.71_{-0.10}^{+0.11}$ obtained by Narayanan et al. (2007) results based on 55 systems with $W_r(2803) \geq 0.07 \text{ \AA}$ and $W_r(2796) < 0.3 \text{ \AA}$ in a total redshift path $\langle \Delta z \rangle = 77.596$ ¹ between $0.4 < z < 2.4$ ². These results are summarized in Table 7.1 (first row) and shown in Figure 7.1. I find that the incidence of weak Mg II absorbers along GRB sightlines is less than twice that one along QSOs at almost 99% confidence level. If I include insecure systems (which satisfy the *relaxed* criteria) the number density increases by a factor of ~ 2.7 ($dN/dz|_{\text{GRB}} = 1.22_{-0.36}^{+0.49}$). This upper limit is still consistent within 1σ with $dN/dz|_{\text{QSO}}$ (see first row of Table 7.2). These results show that there is no significant difference between the redshift number density of weak Mg II measured in sightlines to QSOs and GRBs. In other words, an overabundance of weak Mg II towards GRB sightlines is very unlikely and can be ruled out.

Alternative Results

As discussed in Section 6 there is another way to obtain the redshift number density when W_{min} is below the completeness of the survey, namely weighting by different redshift paths.

Based on the four systems with $W_r(2803) \geq 0.07 \text{ \AA}$ and $W_r(2796) < 0.3 \text{ \AA}$ found in the Mg II sample, the redshift number density turns out to be,

$$\begin{aligned} \frac{dN}{dz_{weak}} &= \frac{1}{\Delta z(0.093 \text{ \AA})} + \frac{1}{\Delta z(0.114 \text{ \AA})} + \frac{1}{\Delta z(0.130 \text{ \AA})} + \frac{1}{\Delta z(0.129 \text{ \AA})} \\ \frac{dN}{dz_{weak}} &= \frac{1}{9.145} + \frac{1}{9.203} + \frac{1}{9.242} + \frac{1}{9.242}. \end{aligned}$$

This yields a $dN/dz|_{\text{GRB}} = 0.43_{-0.21}^{+0.34}$, which is somewhat lower but similar to the value obtained by direct calculation. Therefore the conclusions mentioned above do not change.

If I use the *worst scenario* mentioned in Section 4.3 (namely, use W_r^{pixel} instead of W_r^{gauss} for good fits and viceversa for poor fits) the number of weak Mg II systems in our sample would be

¹See notation defined in Section 6.2.

²There is a difference between my redshift coverage and that of Narayanan et al. (2007). If I restrict the redshift range to that of Narayanan et al. (2007), the result does not change significantly, i.e., four systems in $\Delta z = 8.733$ imply $dN/dz|_{\text{GRB}} = 0.46_{-0.22}^{+0.36}$.

five instead of four implying a $dN/dz|_{\text{GRB}} = 0.55^{+0.37}_{-0.24}$, which is still consistent with the previous result, i.e., no overdensity.

7.1.2 Strong Mg II Absorption Systems

Given that Nestor et al. (2005) do not give information for different redshift bins I will compare directly with their full sample (see their Table 1) which has a redshift range of $0.366 < z < 2.269$ using the same W_r limits used by these authors. Although there is a difference between our redshift coverage and that of Nestor et al. (2005), it is possible to perform comparisons for different equivalent width ranges.

Systems with $W_r(2796) \geq 0.3 \text{ \AA}$

I find that $dN/dz|_{\text{GRB}} = 1.60^{+0.53}_{-0.41}$ which is inconsistent with the QSO result at the 68% confidence level. Since $dN/dz|_{\text{QSO}} = 0.783 \pm 0.033$ I find an overabundance of about ~ 2 in sightlines to GRBs. The QSO/GRB discrepancy is not too significant even considering the number density obtained from unreal systems (which satisfied the *relaxed* criteria) in which case I find an overabundance of ~ 2.6 at less than 99% confidence level as upper limit ($dN/dz|_{\text{GRB}} = 2.02^{+0.58}_{-0.46}$). If I restrict the analysis to the same redshift coverage used by Nestor et al. (2005) the numbers do not change significantly, i.e., 13 systems in $\Delta z = 8.74$ imply a $dN/dz|_{\text{GRB}} = 1.49^{+0.54}_{-0.41}$. Therefore these values are consistent with an overabundance of absorbers toward the GRB sightlines though not too significant (only 1σ). It is important to note that this QSO/GRB discrepancy is far away from the factor of ~ 4 times found by Prochter et al. (2006b) in systems with $W_r(2796) \geq 1.0 \text{ \AA}$. These results are summarized in Tables 7.1 and 7.2 (second rows) for the strict and relaxed samples, respectively. Figure 7.2 shows the comparison between our GRB results and that from QSO.

Systems with $W_r(2796) \geq 0.6 \text{ \AA}$

I find that $dN/dz|_{\text{GRB}} = 1.16^{+0.47}_{-0.35}$ which is inconsistent with the QSO value at almost the 95% confidence level. In this case I also find an overabundance (a factor of ~ 2.4) in sightlines to GRBs, given that the number density of QSO is $dN/dz|_{\text{QSO}} = 0.489 \pm 0.015$. It is important to note that at this equivalent width level there are no differences between the *relaxed* and *strict* samples. If I take into account the differences between redshift ranges for our survey and that of Nestor et al. (2005) the overabundance is still significant at the 95% c.l. (11 systems in $\Delta z = 8.8$ imply a $dN/dz|_{\text{GRB}} = 1.25^{+0.50}_{-0.37}$). These values are all consistent with a significant overabundance of systems toward GRBs when compared with QSOs sightlines. Moreover, this overabundance seems

to be greater than that found in systems with $W_r(2796) \geq 0.3 \text{ \AA}$. These results are summarized in Table 7.1 (third row) and shown in Figure 7.3.

Systems with $W_r(2796) \geq 1.0 \text{ \AA}$

This is the limit used by Prochter et al. (2006b) which included low resolution data. In order to corroborate their result I also calculated the number density for these *very* strong Mg II absorption systems. I find $dN/dz|_{\text{GRB}} = 0.95^{+0.43}_{-0.31}$ which is consistent with Prochter et al. (2006b) who found a $dN/dz|_{\text{GRB}}^{\text{previous}} = 0.90^{+0.31}_{-0.24}$ from 14 systems in a total redshift path $\Delta z = 15.5$ (their sample is composed by 14 GRB spectra with low and high spectral resolutions). My result is based on 7 GRB with high resolution spectra (see Section 2): a subsample of 5 GRBs used by Prochter et al. (2006b) (namely GRB021004, GRB050730, GRB050820, GRB051111 and GRB060418) and 2 new ones (GRB050922C and GRB060607). Both GRB surveys have different redshift coverage. While Prochter et al. (2006b) survey was performed for $z < 2$ our survey extends beyond $z = 2$. If I restrict the analysis to $z < 2$ the result remains the same. Table 7.3 shows these results and comparisons.

These values are inconsistent with previous results on the redshift number density in QSO sightlines and show a significant overdensity of systems in sightlines to GRBs (a factor of ~ 4)³. Our survey yields an overabundance which is significant at the 95% confidence level, while Prochter et al. (2006b) found a significance greater than 99.9%. If I restrict the analysis to match the redshift coverage used by Nestor et al. (2005) i.e., between redshift $0.366 < z < 2.269$, the discrepancy between results from QSOs and GRBs is incremented⁴. These results are summarized in Table 7.1 (fourth row). In conclusion, I confirm the result by Prochter et al. (2006b) albeit at a factor of $\sim 3.2 - 3.4$ only when compared with Nestor et al. (2005) results.

Alternative Results

At this equivalent width limit differences on the redshift number density obtained from a direct calculation or weighting by different redshift paths are negligible.

If I use the *worst case* mentioned in Section 4.3 the result does not change significantly. In fact, for the Strict Sample I would obtain 15 systems instead of 16 for $W_r(2796) \geq 0.3 \text{ \AA}$, 13

³If I compare with Nestor et al. (2005) the overabundance is a factor of $\sim 3.2 - 3.4$ only. If I use the same survey to compare with previous surveys used by Prochter et al. (2006b), which parameterized the incidence of very strong Mg II per unit redshift as $dN/dz|_{\text{QSO}}(z) = -0.026 + 0.374z - 0.145z^2 + 0.026z^3$, the overabundance could be greater than 4 for $z = 1$.

⁴Nine systems in $\Delta z = 8.74$ imply $dN/dz|_{\text{GRB}} = 1.03^{+0.47}_{-0.34}$

Table 7.4. Specifications of the $dN/dz|_{\text{GRB}}^{\text{MgII}}$ for each Equivalent Width Bin.

W_r Bin [\AA]	N_{abs}	Δz	$dN/dz _{\text{GRB}}$	$dN/dz _{\text{QSO}}^{\text{MgII}}$
$0.3 \leq W_r(2796) < 0.6$	4	9.4	$0.43^{+0.34}_{-0.20}$	0.294 ± 0.036
$0.3 \leq W_r(2796) < 0.6$	8*	9.4	$0.85^{+0.42}_{-0.29}$ *	0.294 ± 0.036
$0.6 \leq W_r(2796) < 1.0$	2	9.46	$0.21^{+0.28}_{-0.14}$	0.211 ± 0.018
$1.0 \leq W_r(2796)$	9	9.46	$0.95^{+0.43}_{-0.31}$	0.278 ± 0.010

Note. — * These numbers must be considered as upper limits due to the presence of many unreal systems. For comparison the last column (see Section 7.1.3 for details about calculation of this numbers) shows the resulting $dN/dz|_{\text{QSO}}^{\text{MgII}}$ from Nestor et al. (2005).

systems instead of 12 for $W_r(2796) \geq 0.6 \text{ \AA}$ and 8 systems instead of 9 for $W_r(2796) \geq 1.0 \text{ \AA}$. These changes only affect the results by $\sim 10\%$ and the conclusions remain the same.

7.1.3 Equivalent Width Distribution

It is interesting to note that the data are consistent with an increase of $dN/dz|_{\text{GRB}}$, ranging from no overabundance with respect to QSOs sightlines for $W_r < 0.3 \text{ \AA}$ to a factor of $\sim 3-4$ overabundance for $W_r \geq 1 \text{ \AA}$. Given the fact that there is a known overabundance of Mg II systems toward GRB sightlines for $W_r > 1 \text{ \AA}$, the results obtained for lower W_r limits (e.g., $W_r > 0.3 \text{ \AA}$ and $W_r > 0.6 \text{ \AA}$) could be affected by this overabundance. Since I do not find significant differences in the redshift number density between QSOs and GRBs for weak Mg II systems, one way to assess whether the overabundance is effectively observed at equivalent widths lower than 1 \AA , is to perform comparisons of dN/dz for different equivalent width bins at $W_r < 1 \text{ \AA}$.

Table 7.4 shows dN/dz for the strong Mg II sample using different equivalent width bins. For the weak Mg II sample I use the previous result directly. The QSO values were obtained from Nestor et al. (2005), assuming that the differences between redshift paths are negligible, in the following way:

$$\frac{dN}{dz}(W_r^a < W_r < W_r^b) = \frac{dN}{dz}(W_r^a < W_r) - \frac{dN}{dz}(W_r^b < W_r).$$

I find that for systems with $W_r < 1 \text{ \AA}$ the results from GRB and QSO sightlines are consistent. Figure 7.5 shows dN/dz values for different W_r bins. It is clear that only systems with $W_r > 1 \text{ \AA}$ show an overabundance of systems toward GRBs while the rest is 1σ consistent with previous QSO results.

From the equivalent width distribution I conclude that previous discrepancies that I found for systems with $W_r > 0.3 \text{ \AA}$ and $W_r > 0.6 \text{ \AA}$ were produced by the strong overabundance of systems with $W_r > 1.0 \text{ \AA}$.

It is interesting to note that equivalent width distribution for GRBs shows the opposite trend than that for QSOs, i.e., I found more strong than weak Mg II systems. However, due to small number statistics involved this trend cannot be taken as significant. In fact, the weakest and strongest W_r bins are consistent between them with 1σ . However as mentioned, our result is in agreement with Prochter et al. (2006b) (see blue point in Figure 7.5) for systems with $W_r \geq 1 \text{ \AA}$ where an overabundance of systems in GRB sightlines is found compared with the expected value from QSOs surveys.

7.1.4 Comments on the Upper Limits

As mentioned in Section 3.6 I use a set of *relaxed* criteria which is highly contaminated by unreal systems. This is done to improve the significance on the result of this work, i.e., that I did not find an overabundance of weak Mg II systems toward GRBs compared to previous results from QSOs.

Given the fact that our GRB spectral sample is small and the signal-to-noise ratio is not too high, taking into account unreal systems as *real* ones and finding that the redshift number densities obtained from these numbers are still consistent with the QSO results (at least for weak systems⁵) guarantees that it is very unlikely to find future discrepancies using large datasets. Moreover, an overabundance of a factor of ~ 4 on weak systems toward GRBs compared with QSO (as found for very strong systems) is even more unlikely.

Finally these values must not be taken as real (or meaningful) results but only as upper limits. I refer to the reader to Figures 4.36 - 4.46 to see what kind of systems were included in the *Relaxed* Samples. Viewing their velocity profiles it is possible to note that these numbers are very overestimated.

7.2 C IV Results

For the Statistical Sample I find $dN/dz|_{\text{GRB}}(z \sim 1.5) = 2.2^{+2.8}_{-1.4}$, $dN/dz|_{\text{GRB}}(z \sim 2.5) = 2.3^{+1.8}_{-1.1}$ and $dN/dz|_{\text{GRB}}(z \sim 3.5) = 1.1^{+2.6}_{-0.9}$. The choice of redshift bins is arbitrary; I used three bins of 1 redshift unit between $z = 1$ and $z = 4$. Table 7.5 shows the specific results for each redshift.

⁵As is shown in Table 7.4 for systems with $0.3 \text{ \AA} < W_r < 0.6 \text{ \AA}$ if there is an overabundance toward GRB this should not be significant.

Table 7.5. Specifications of the $dN/dz|_{\text{GRB}}^{\text{CIV}}$ for each Bin from the Statistical Sample.

Redshift Bin	N_{abs}	Δz	$dN/dz _{\text{GRB}}^{\text{CIV}}$	$dN/dz _{\text{QSO}}^{\text{CIV}}$
[1, 2[2	0.93	$2.2^{+2.8}_{-1.4}$	$2.7^{+0.5}_{-0.4}$
[2, 3[4	1.74	$2.3^{+1.8}_{-1.1}$	$2.5^{+0.4}_{-0.4}$
[3, 4[1	0.90	$1.1^{+2.6}_{-0.9}$	$1.1^{+0.7}_{-0.4}$
[1, 4[7	3.57	$2.0^{+1.1}_{-0.7}$	$2.4^{+0.3}_{-0.2}$

Note. — For comparison the fifth column shows the resulting $dN/dz|_{\text{QSO}}^{\text{CIV}}$ for same bins from Steidel (1990).

I find that $dN/dz|_{\text{GRB}}$ decreases with redshift in the range between $z = 1$ and $z = 4$ as in QSO surveys. In Figure 7.6 I compare $dN/dz|_{\text{GRB}}$ with $dN/dz|_{\text{QSO}}$ using our binning. It can be seen that, within the errors, our result on C IV matches the Steidel (1990) and Misawa et al. (2002) ones (according to Misawa et al., the fact that these two previous results do not match each other would be due to a statistical accident). On the other hand, if I only use one redshift bin between $z = 1$ and $z = 4$ I find that the incidence of C IV absorbers along the GRB sightlines is less than twice that along QSOs (Steidel 1990 sample) at the 95% confidence level, i.e., a large overabundance is unlikely (even taking into account the 2 dubious systems excluded from the Statistical Sample). Therefore, there is no significant difference between the GRB and QSO statistics in our sample.

7.2.1 Equivalent Width Distribution

While the change in $dN/dz|_{\text{GRB}}^{\text{CIV}}$ for $W_r(1548) \geq 0.15 \text{ \AA}$ may be modest, as argued above, it is possible that an enhancement in $dN/dz|_{\text{GRB}}^{\text{MgII}}$ will imply a C IV equivalent width *distribution* that is very different from that toward QSOs, e.g., a much higher incidence of $W_r(1548) > 1 \text{ \AA}$ (as found in Mg II sample). Figure 7.7 presents a histogram of the equivalent widths for my analysis and that of Steidel (1990) with arbitrary binning. I performed a K-S test on the un-binned distributions of rest frame equivalent widths that rules out the null hypothesis (of similar distributions) at only the 1% c.l. Therefore, there is no indication of possible differences between equivalent width distributions of C IV absorbers toward GRBs and QSOs although the small number statistic this result can be taken as not significant.

7.3 Summary of the Results

I summarize our results as follow:

- (1) I do not find any discrepancy in weak Mg II systems ($W_r < 0.3 \text{ \AA}$) between QSO and GRB sightlines.
- (2) I do not find any discrepancy in strong Mg II systems for the equivalent width range $0.3 \text{ \AA} \leq W_r < 1.0 \text{ \AA}$ between QSO and GRB sightlines.
- (3) I find a significant overabundance of very strong Mg II systems ($W_r \geq 1.0 \text{ \AA}$) in GRB sightlines compared to previous results from QSOs.
- (4) I do not find any discrepancy in strong C IV systems ($W_r > 0.15 \text{ \AA}$) between QSO and GRB sightlines.

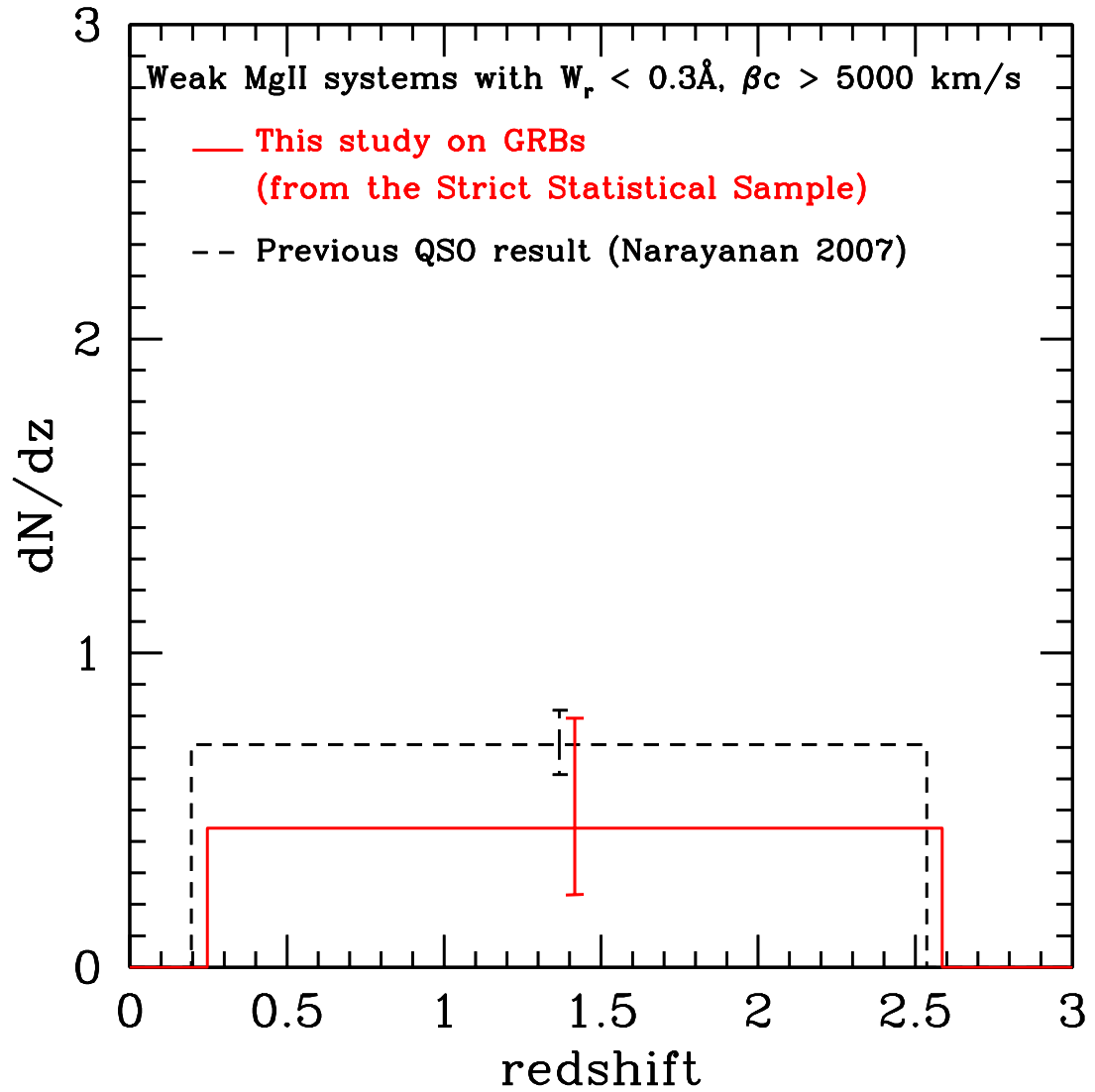


Figure 7.1 Redshift number density for weak Mg II ($0.07 \text{ \AA} \leq W_r(2803) \text{ and } W_r(2796) < 0.3 \text{ \AA}$) absorption systems in our GRB Statistical Sample. As a comparison (dashed line) we show the result obtained from the QSO survey by Narayanan et al. (2007) using the same equivalent width limits. The bins have been slightly offset in redshift for clarity.

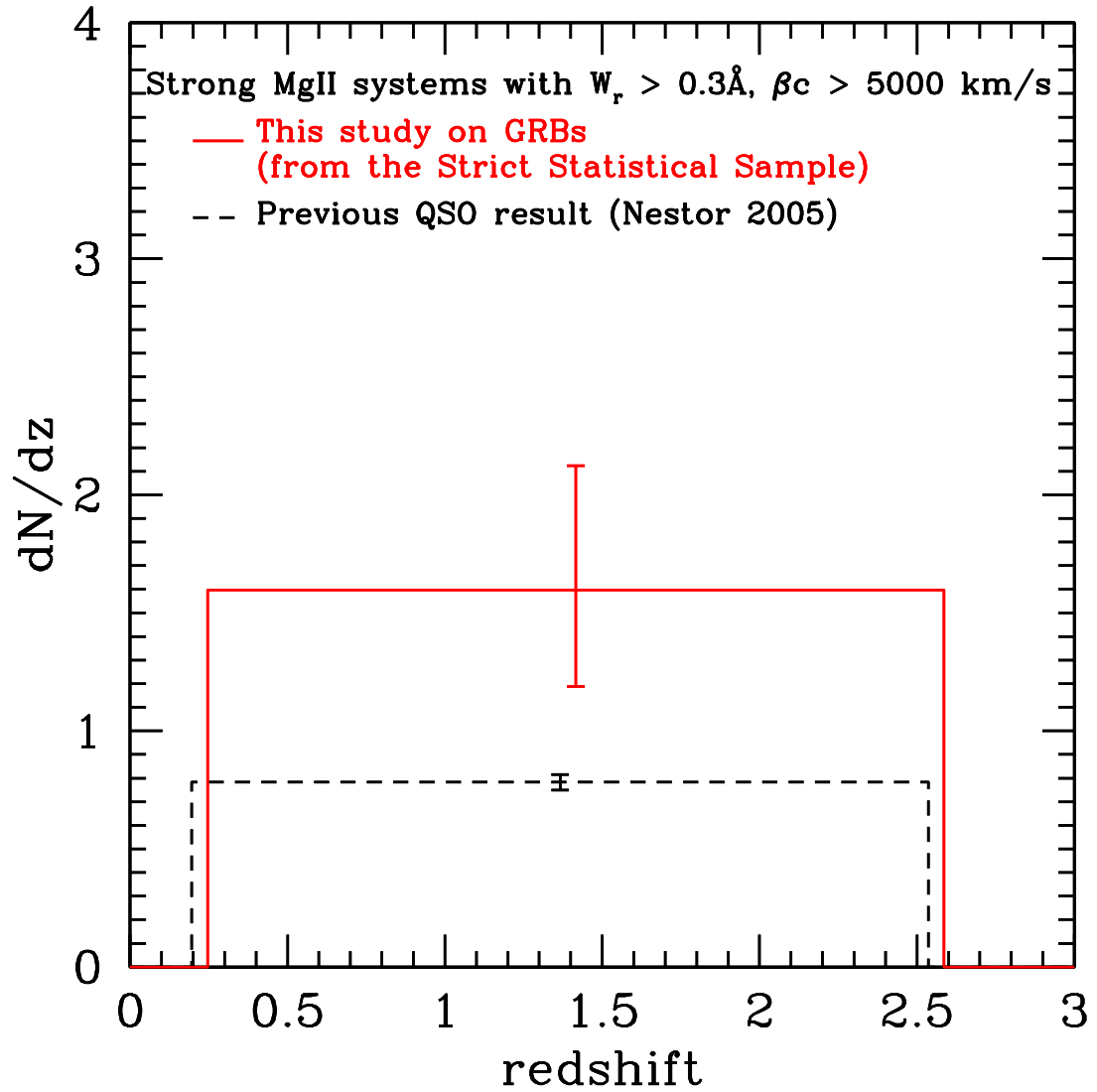


Figure 7.2 Redshift number density for strong Mg II absorption systems with $W_r(2796) \geq 0.3\text{ \AA}$ in our GRB Statistical Sample. As a comparison (dashed line) we show the result obtained from the QSO survey by Nestor et al. (2005) using the same equivalent width limit. The bins have been slightly offset in redshift for clarity.

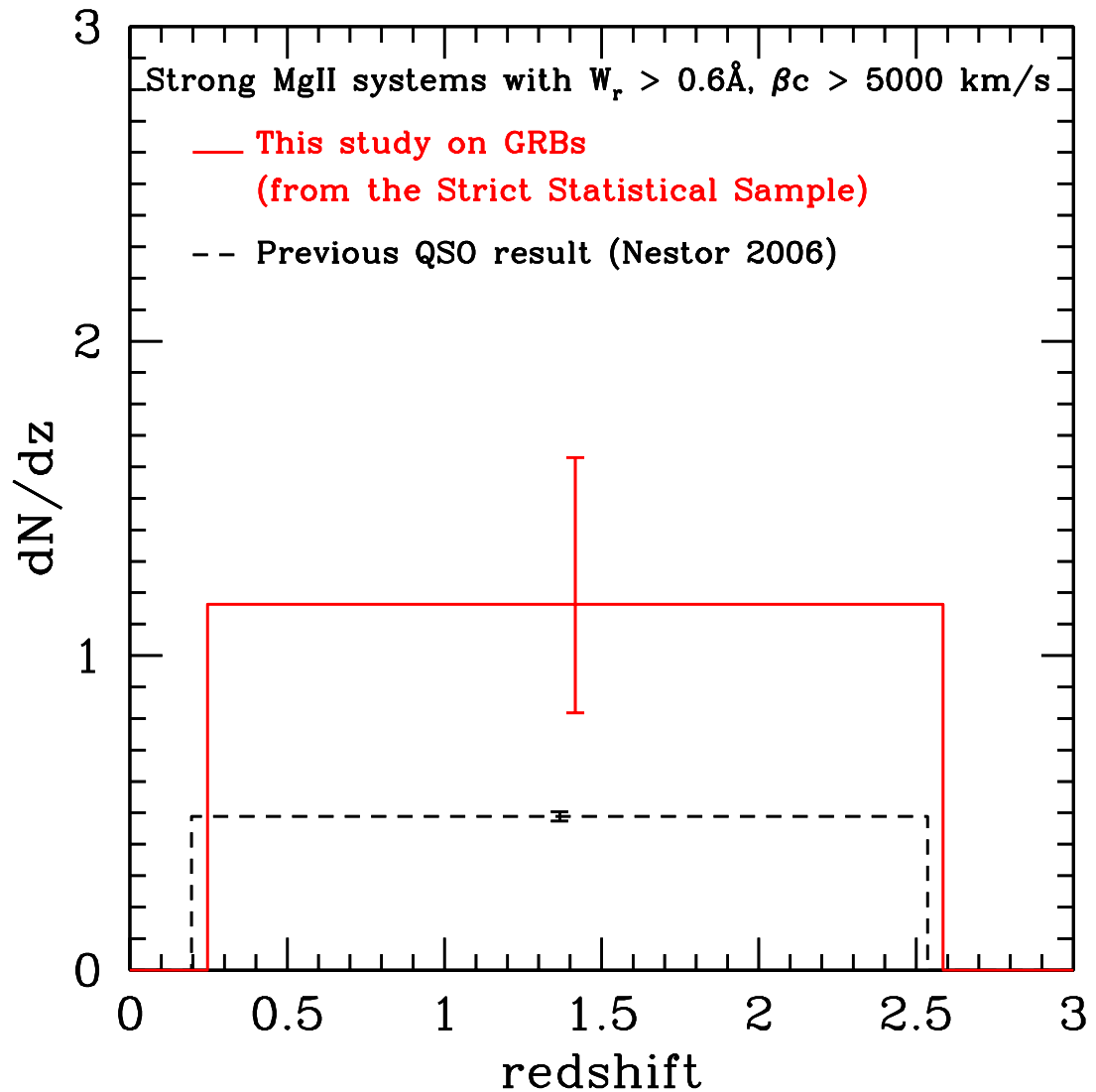


Figure 7.3 Redshift number density for strong Mg II absorption systems with $W_r(2796) \geq 0.6 \text{ \AA}$ in our GRB Statistical Sample. As a comparison (dashed line) we show the result obtained from the QSO survey by Nestor et al. (2005) using the same equivalent width limit. The bins have been slightly offset in redshift for clarity.

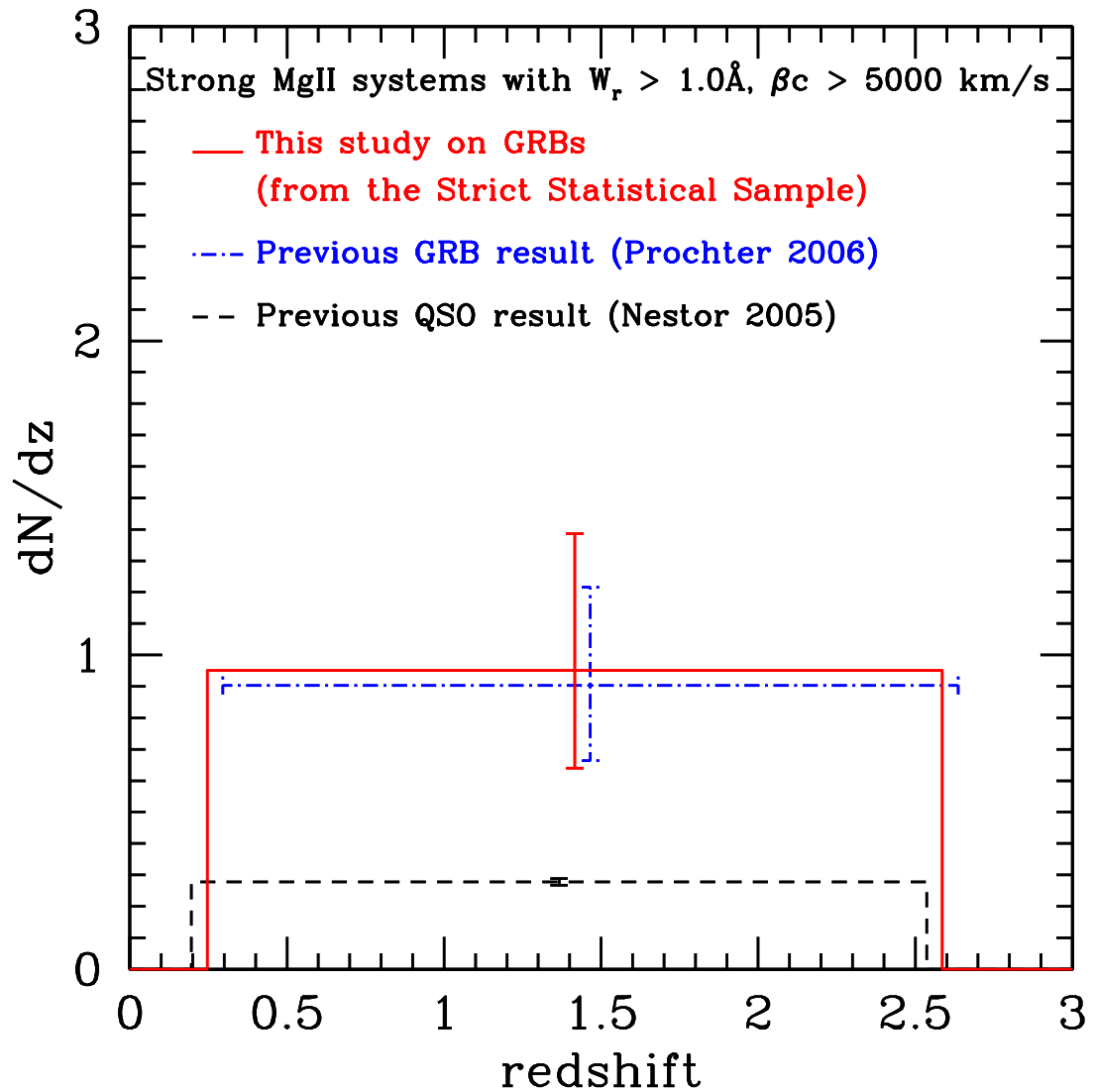


Figure 7.4 Redshift number density for strong Mg II absorption systems with $W_r(2796) \geq 1.0 \text{ \AA}$ in our GRB Statistical Sample. As a comparison (black dashed line) we show the result obtained from the QSO survey by Nestor et al. (2005) using the same equivalent width limit. Also we show the previous GRB result by Prochter et al. (2006b) (blue dashed line) which is consistent with our result. The bins have been slightly offset in redshift for clarity.

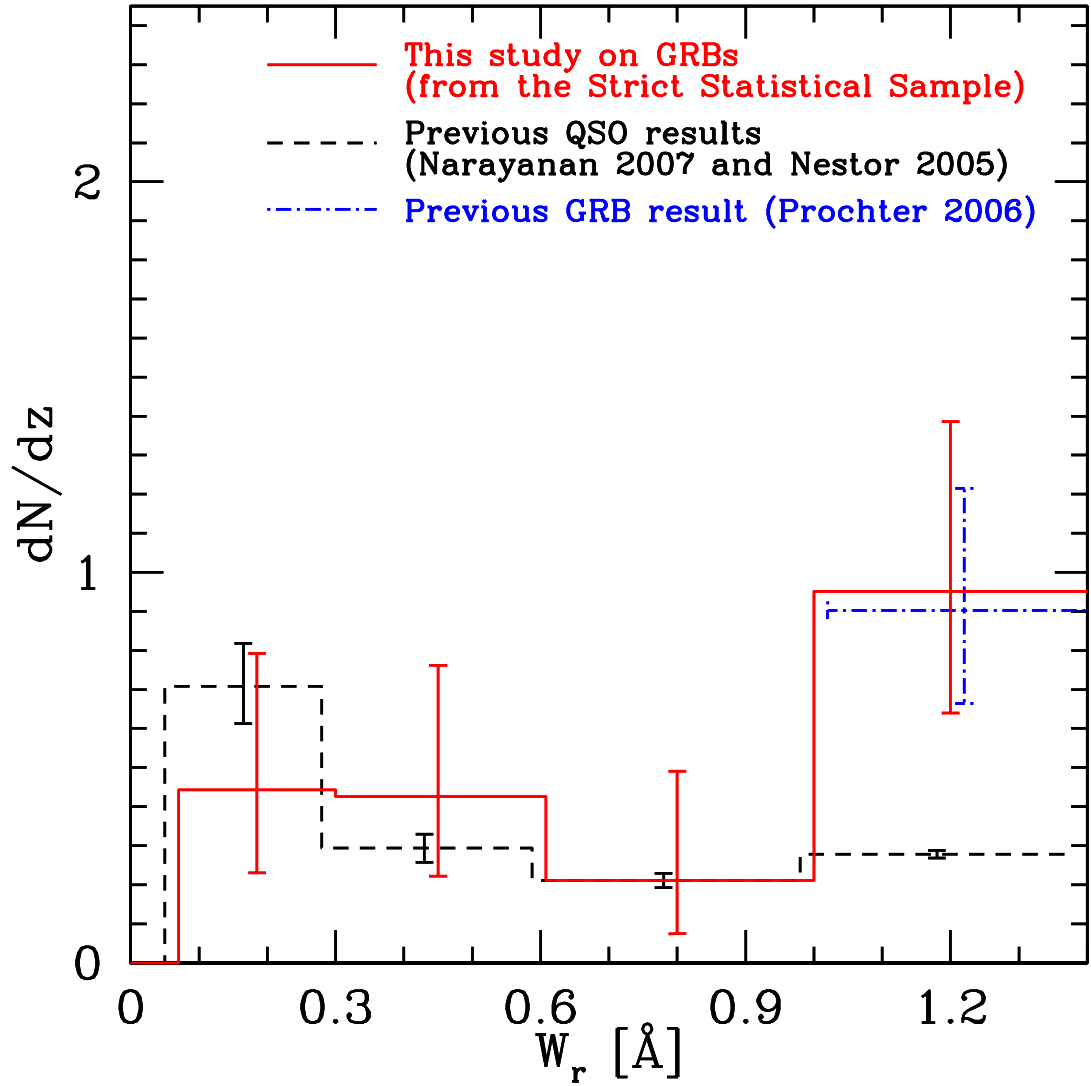


Figure 7.5 Redshift number density of Mg II absorption systems in our GRB Statistical Sample for different equivalent width bins (see Table 7.4 for details). As a comparison we show the results obtained from the QSO surveys by Narayanan et al. (2007) (first bin) and Nestor et al. (2005) (the rest of the bins) using the same equivalent width limit (black dashed line). Also we show the previous GRB result by Prochter et al. (2006b) (blue dashed line) which is consistent with our result. The bins have been slightly offset in W_r for clarity.

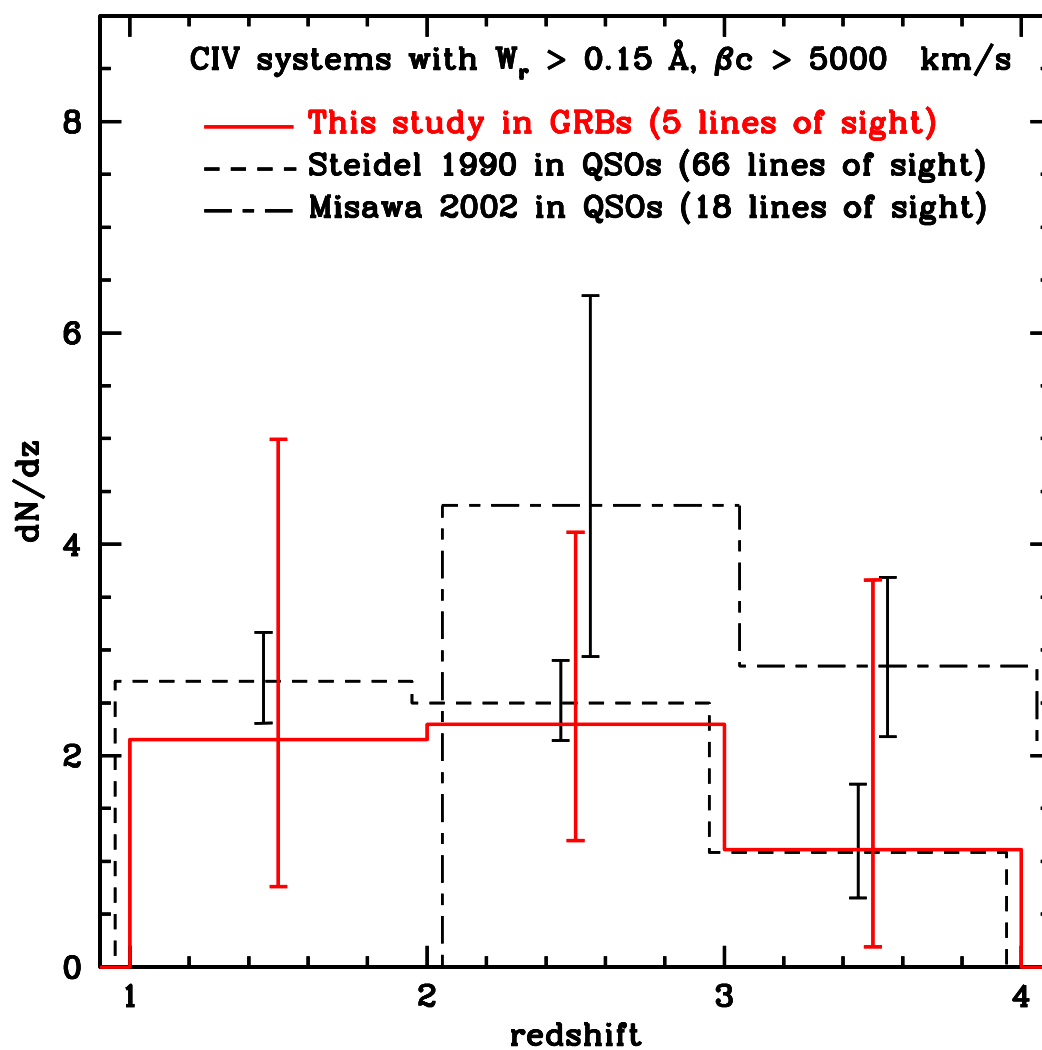


Figure 7.6 Distribution of the number of C IV absorption systems per unit redshift in our GRB Statistical Sample. As a comparison (dashed line) we show results from QSO survey by Steidel (1990) and Misawa et al. (2002) using the same binning as that for the GRB-C IV analysis. The bins have been slightly offset in redshift for clarity.

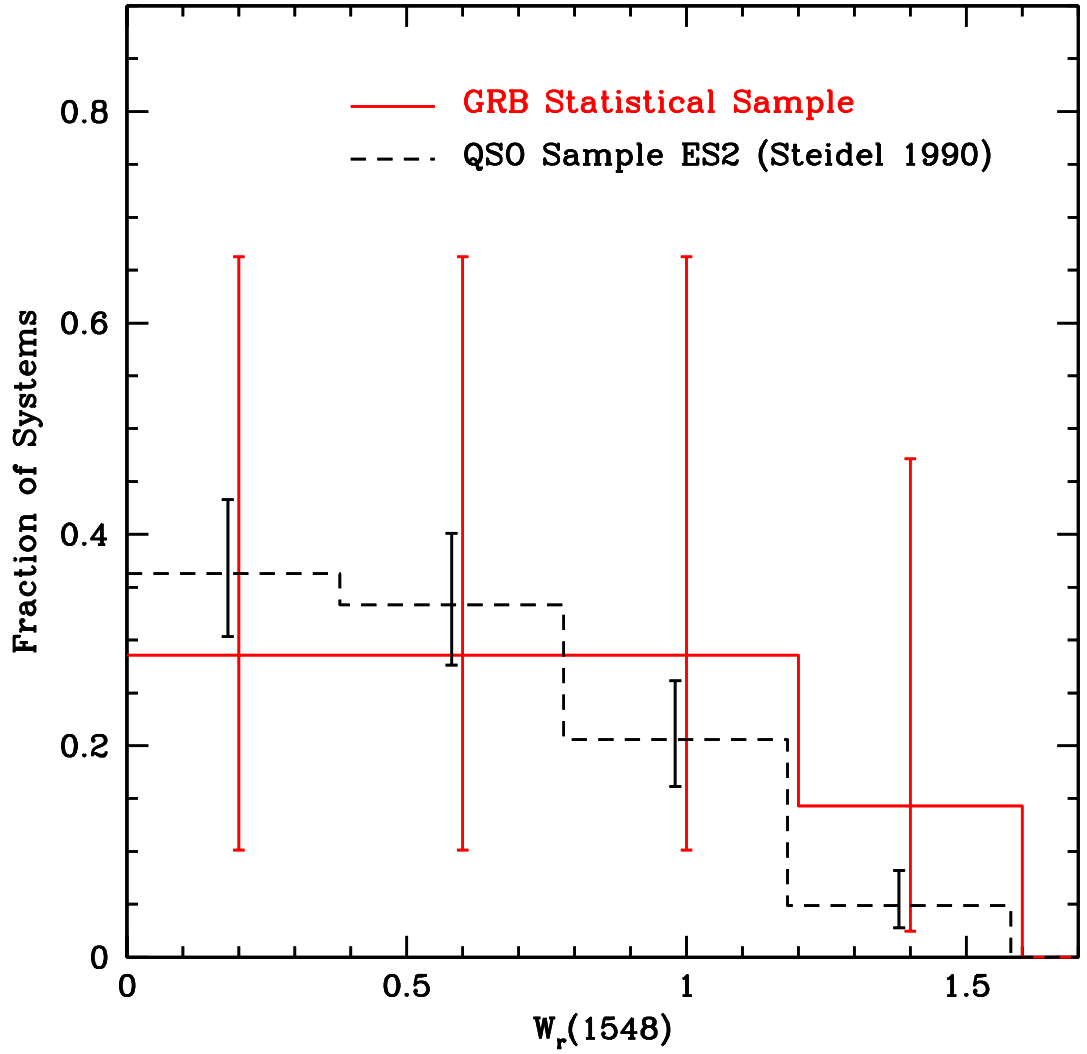


Figure 7.7 Distribution of rest-frame equivalent widths $W_r(1548)$ from the C IV Statistical Sample of GRB absorption systems compared with those from Steidel (1990) for QSO absorption systems (dashed line). The bins have been slightly offset in $W_r(1548)$ for clarity.

Chapter 8

Discussion of the Results

The results of my analysis can be summarized as follows: (1) the incidence of Mg II ($W_r < 1.0 \text{ \AA}$) and C IV absorbers ($W_r \geq 0.15 \text{ \AA}$) along GRB sightlines is consistent with that is observed along QSO sightlines, while (2) *very strong* Mg II absorbers ($W_r \geq 1.0 \text{ \AA}$) show a significant overabundance (a factor of ~ 3.4) along GRB sightlines compared with the same statistic along QSO sightlines. In the following sections I will discuss possible explanations and their consequences.

8.1 C IV versus Very Strong Mg II

The result obtained for C IV systems is already published (Tejos et al., 2007). The majority of the following discussion of this Section can be also found in that paper. The result for strong Mg II is in Prochter et al. (2006b) and it is confirmed in this thesis.

The main result is that the incidence of C IV systems in GRB sightlines conforms that one for QSO. Note that the same conclusion is reached out by Sudilovsky et al. (2007) using similar data (although these authors used a smaller total redshift path and a lower equivalent width cutoff than ours).

Quantitatively, I can set a 95% upper limit of $dN/dz|_{\text{GRB}}^{\text{CIV}} < 2dN/dz|_{\text{QSO}}^{\text{CIV}}$ over the redshift interval $z \sim 2$ to 4. This mean that even at 2σ level C IV toward GRBs cannot be two times more frequent than toward QSOs. At the surface, this result lies in stark contrast to the incidence of strong Mg II absorbers at $z < 2$ where Prochter et al. (2006b) find a *lower limit* $dN/dz|_{\text{GRB}}^{\text{MgII}} > 2dN/dz|_{\text{QSO}}^{\text{MgII}}$ (confirmed by our results) at the 99.9% significance level.

Are these two results contradictory? The fact that I do not find any discrepancy of the redshift number density for intervening C IV systems with $W_r \geq 0.15 \text{ \AA}$ between QSO and GRB spectra must be taken carefully. A direct comparison between C IV and Mg II systems is not appropriate. There are several factors that make the two absorption line samples disjoint as I will comment in the following.

First, C IV may probe a distinct gas phase than Mg II in the intergalactic medium owing to its substantially higher ionization potential. The ionization potential of C IV is 47.9 eV compared with the 15 eV for Mg II. This is reflected in the statistics obtained in QSO surveys. For example, at $z = 2$, $dN/dz|_{\text{QSO}}^{\text{MgII}} \approx 0.4$ (Prochter et al., 2006a) and $dN/dz|_{\text{QSO}}^{\text{CIV}} \approx 2.5$ (Steidel, 1990), i.e., C IV systems are $\times 6$ more abundant than Mg II for the W_r thresholds relevant to our study. In other words, there are plenty of C IV (weak) systems that do not show strong Mg II absorption. Likewise, C IV and Mg II absorption line samples show different kinematics (Churchill et al., 2000). In short, C IV and Mg II absorption systems arise in different gas phases.

A second important difference between the two statistics is the redshift coverage of both absorption line samples. The Mg II absorbers are surveyed at $z < 2$ while most of the pathlength surveyed here for C IV absorption has $z > 2$. While there is no indication that the $dN/dz|_{\text{GRB}}^{\text{MgII}}$ enhancement is declining with increasing redshift, there are possible reasons to expect such an effect (e.g., gravitational lensing, see Section 8.4). If that were the case the Mg II enhancement would vanish at the redshifts probed with C IV. Unfortunately, there are not current Mg II absorption line samples beyond $z > 2.2$ to test it. In short, both samples are disjoint in redshift (different cosmic epochs).

On the other hand, it is expected that nearly every strong Mg II absorber will also exhibit C IV absorption. Furthermore, many of these will have an equivalent width in excess of 0.15 \AA (e.g., Churchill et al., 1999a). Therefore, if the enhancement in $dN/dz|_{\text{GRB}}^{\text{MgII}}$ continues beyond $z = 2$, a certain bias to larger $dN/dz|_{\text{GRB}}^{\text{CIV}}$ should be expected. However, since there is not a one-to-one correspondence between $W_r \geq 1 \text{ \AA}$ Mg II absorbers and $W_r \geq 0.15 \text{ \AA}$ C IV absorbers, such possible bias is diluted in the much more numerous statistics of C IV (indeed, none of the C IV absorbers in our Statistical Sample which have enough coverage shows *strong* Mg II absorption¹; e.g., $z_{\text{CIV}} = 1.568, 1.989, 2.009$ from GRB050922C). Even if I assume that $dN/dz|_{\text{GRB}}^{\text{MgII}} = 4 dN/dz|_{\text{QSO}}^{\text{MgII}}$ and that each system also has $W_{\text{CIV}} > 0.15 \text{ \AA}$, the effect on $dN/dz|_{\text{GRB}}^{\text{CIV}}$ is less than 50% (at most $(dN/dz|_{\text{GRB}}^{\text{CIV}})/(dN/dz|_{\text{QSO}}^{\text{CIV}}) = 9/6$ given that $(dN/dz|_{\text{GRB}}^{\text{MgII}})/(dN/dz|_{\text{QSO}}^{\text{MgII}}) = 4/1$ and $(dN/dz|_{\text{QSO}}^{\text{CIV}})/(dN/dz|_{\text{QSO}}^{\text{MgII}}) = 6/1$).

In summary, there is no fundamental conflict between observing an enhanced incidence of strong Mg II absorbers along GRB sightlines without a corresponding enhancement of C IV absorbers in the same data.

¹I will later comment about weak Mg II and C IV found at the same redshift. See Section 8.1.1.

Table 8.1. Mg II-C IV Sample

GRB	z_{abs}^{MgII}	$W_r^{pixel}(2796)$	$W_r^{gauss}(2796)$	z_{abs}^{CIV}	$W_r^{pixel}(1548)$	$W_r^{gauss}(1548)$
		$W_r^{pixel}(2803)$	$W_r^{gauss}(2803)$		$W_r^{pixel}(1550)$	$W_r^{gauss}(1550)$
GRB050922C	1.56689	0.102 ± 0.008	0.109 ± 0.017	1.56843	0.989 ± 0.031	0.885 ± 0.053
		0.049 ± 0.008	0.059 ± 0.011		0.600 ± 0.029	0.538 ± 0.058
GRB060607	2.27840	0.171 ± 0.015	0.128 ± 0.024	2.27853	0.479 ± 0.017	0.477 ± 0.027
		0.044 ± 0.017	0.044 ± 0.016		0.366 ± 0.017	0.373 ± 0.022
		0.293 ± 0.015	0.310 ± 0.015		0.164 ± 0.004	0.171 ± 0.008
		0.286 ± 0.017	0.282 ± 0.019		0.093 ± 0.004	0.100 ± 0.008

Note. — Systems with Mg II and C IV absorption lines found in our GRB survey.

8.1.1 C IV Systems and their Mg II Counterparts

As mentioned above, none of the statistical C IV systems with enough redshift coverage ($z_{CIV} = 1.568, 1.989, 2.009$ from GRB050922C) have strong Mg II counterparts. However I did find three C IV-Mg II systems considering W_r limits below the statistical definitions. These are: $z_{abs} = 1.568, 2.009$ from GRB050922C and $z_{abs} = 2.279$ from GRB060607. Table 8.1 summarizes their individual information and Figures 8.1 to 8.3 show their velocity profiles.

The C IV-Mg II systems were not used in the analysis of this thesis. These systems are shown for completeness. Any of them could be useful for future surveys or studies.

8.2 Weak versus Strong Mg II

The fact that I do not find any discrepancy on intervening redshift number density for systems with $W_r < 1.0 \text{ \AA}$ between QSO and GRB spectra opens the question of why there is an overabundance only for very strong Mg II absorption systems. The answer to this question is not clearly revealed by these low number statistics; however, I will discuss possible explanations.

In principle, there are two main possibilities to explain this discrepancy: (1) it could be attributed to intrinsic differences in the properties of the absorbers themselves (the real nature of the absorption systems is still unknown) or (2) due to a bias effects in the QSO and GRB samples. Even, it could be produced by both effects simultaneously.

Considering that there are two known different Mg II populations in QSO surveys (weak and strong) which are separated by an equivalent width cutoff near $W_r \sim 0.3 \text{ \AA}$ (see Figure 1.8), the discrepancy between the QSO and GRB results does not appear to be due to intrinsic differences between the properties of the absorbers in each population (environments and/or relative number

densities). If that were the case, one would expect differences also for Mg II systems in the range $0.3 \text{ \AA} < W_r < 1.0 \text{ \AA}$.

Even more, assuming the standard picture of the absorbers, being larger than galaxies (absorbers as galaxy haloes with sizes of $\sim 10 - 100 \text{ kpc}$) it is difficult to believe that the discrepancy is due to a contamination of a different type of absorbers in GRB sightlines. In that case, it is more likely to think of a bias effect between the samples. Therefore, the observed overabundance of very strong Mg II ($W_r > 1 \text{ \AA}$) and the lack of it for weak Mg II ($W_r < 1 \text{ \AA}$), would be due to the total integrated mass densities (total masses, impact parameter from host galaxies) of the intervening absorbers, suggesting that the GRB/QSO discrepancy should arise in the galaxies that host the strong absorbers. In the following sections I will comment about explanations such as dust extinction and/or gravitational lensing (Prochter et al., 2006b; Porciani et al., 2007) effects.

On the other hand, the possibility of a contamination due to a different type of absorption systems cannot fully ruled out a priori. Thus, it would be also possible to attribute the GRB/QSO discrepancy to a different nature of the absorbers (although this scenario appears more unlikely than a bias selection effect). In this context, I will also discuss the possibilities of an association between the Mg II systems and GRBs themselves (Prochter et al., 2006b; Porciani et al., 2007), and differences between GRBs and QSOs beam sizes compared to the length of hypothetical Mg II systems *cores* (with sizes smaller than a pc) proposed by Frank et al. (2007).

8.3 Dust Extinction

The effect of dust extinction in magnitude selected samples is always an important element to be considered. In the case of absorption lines surveys dust extinction could affect the number density because dusty absorbers could obscure the background sources. Assuming that dust is more abundant in high density zones, which are mainly associated with smaller impact parameters from the centers of galaxies, it might be possible that some faint QSO behind galaxies are not observed while this effect does not occur with GRBs (which are intrinsically brighter than QSO). Various absorption line surveys have tried to assess QSO obscuration and reddening by the absorbers (e.g., Ellison et al., 2001; York et al., 2006; Ménard et al., 2008; Ellison & Lopez, 2009). The majority of these have concluded that dust bias in QSO surveys is not important. The CORALS² survey (Ellison et al., 2001) for instance, has found no significant differences between dN/dz from optical SDDS and from radio-selected QSOs (radio-selected sources are expected not to be affected by dusty absorbers). This implies that dust extinction would not play an important role in the study of intervening systems³. Reddening by absorbers in QSO sightlines is also not observed, York et al.

²Complete Optical and Radio Absorption Line System.

³However, there are some evidence of this selection bias, specially in sightlines with DLA (Fall & Pei, 1993; Ellison et al., 2004; Smette et al., 2005) using optical selected samples.

(2006) have found an average color excess in SDSS QSOs of only $E(B - V) < 0.01$ magnitudes for sightlines with Mg II $W_r(2796) < 1.5 \text{ \AA}$ systems. Therefore, at this equivalent widths dust obscuration does not appear to explain the discrepancy of very strong Mg II ($W_r(2796) > 1.0 \text{ \AA}$) as was pointed out by Prochter et al. (2006b). Porciani et al. (2007) also discussed this possibility and concluded that dust obscuration can not fully explain this discrepancy. These authors found that the chance, after correction by possible dust obscuration in QSO sightlines, to find 14 absorbers in a $\Delta z = 15.5$ due to a statistical fluctuation is less than 1.5%.

An interesting aspect was pointed out by Sudilovsky et al. (2007). They claimed that more than half of the Prochter et al. (2006b) sample is composed by systems with $W_r(2796) > 1.5 \text{ \AA}$ where dust extinction could be more important. Recently, Ménard et al. (2008) used ~ 7000 Mg II systems with $W_r(2796) > 1 \text{ \AA}$ from SDSS (Data Release 4) to parameterize the average color excess in these QSO sightlines as $\langle E(B - V) \rangle(W_r) = C(W_r)^\alpha$, with $C = (0.8 \pm 0.1) \times 10^{-2}$ and $\alpha = 1.88 \pm 0.17$. This parameterization is valid for systems with $1 \text{ \AA} < W_r(2796) < 6 \text{ \AA}$ in the redshift range $0.4 < z < 2$. This result is in agreement with York et al. (2006) and give us reference color excess values of $\langle E(B - V) \rangle(W_r = 2 \text{ \AA}) = 0.03 \pm 0.006$ and $E\langle(B - V)\rangle(W_r = 2.5 \text{ \AA}) = 0.04 \pm 0.008$ in QSO sightlines. It is true that Prochter et al. (2006b) sample is dominated by systems with $W_r(2796) > 1.5 \text{ \AA}$ however, only one of these has $W_r(2796) > 2.5 \text{ \AA}$.

More recently, Sudilovsky et al. (2009) also studied this bias effect applying an empirical relationship between dust column density and Mg II rest-frame equivalent width to simulate QSOs sightlines and to model the underlying number of QSOs that must be present to explain the published magnitude distribution of SDSS QSOs. They concluded that this bias is likely to reduce the discrepancy only by $\sim 10\%$.

Therefore, I conclude that the hypothesis of dust extinction, alone, does not explain the discrepancy between strong Mg II intervening systems in GRB and QSO sightlines.

The main difference between dust obscuration and gravitational lensing biases is that the former implies that the dN/dz for QSOs is *underestimated* while the later implies that the dN/dz for GRBs is *overestimated*. A scenario of dust lowering the statistics of strong systems only in QSOs sightlines looks somehow puzzling. If that were the case, it would mean that what we observe toward GRBs is the unbiased (thus 'real') equivalent width distribution. When combined with our results for weak systems, such a distribution looks quite atypical; compare for instance, with the same distribution of Ly α lines (e.g., Paschos et al., 2008), for which dust bias should not exist. Thus, if the observed QSO/GRB discrepancy were fully explained by a dust bias, it should open a new and more conceptual problem.

8.4 Gravitational Lensing

There are two sources of gravitational lensing amplification: macrolensing and microlensing. Gravitational lensing is an important effect that could affect the statistics on dN/dz between GRB and QSO sightlines. Since gravitational lensing can magnify background sources it is possible that the current GRB samples are incomplete being biased toward sightlines with intervening galaxies which have magnified a fraction of the current observed GRBs. The reason is that it is easier to obtain GRB optical afterglow spectroscopy for the brightest events than the rest.

8.4.1 Macrolensing

Macrolensing is produced by a great concentration of mass, like a galaxy or a cluster of galaxies, located between the source and the observer. It is known from QSO sightlines that samples of strong intervening systems are affected by macrolensing (e.g., Smette et al., 1997; Ménard et al., 2008). Indeed, it has been even possible to observe separated images for the same QSO and to identify the lens galaxy (strong lensing). However, the majority of macrolensing in QSO corresponds to weak lensing (just one amplified image). Likewise, only a few GRBs in every thousand detections are expected to be strongly lensed by galaxy-sized halos (Porciani & Madau, 2001).

The amplification effect is more intense at lower impact parameters from the lens and reaches a maximum when the lens is located at the half distance between the source and the observer. In terms of redshift, for sources typically at $z_s \lesssim 1$ the maximum effect would be at $z_l^{max} \sim z_s/2$ while for sources at $z_s \gg 1$ the maximum would be at $z_l^{max} \sim 0.7$ (e.g., Smette et al., 1997). As it was pointed out by Sudilovsky et al. (2007) if macrolensing is an important factor, the strong Mg II sample would follow this trend. This behavior is not seen in the GRB samples where the majority of the absorption systems are at quite different redshift than the "expected" ones indicating that macrolensing would not be an important factor to explain the QSO/GRB discrepancy. However, given the low number of the systems in the GRBs samples, this conclusion is not particularly strong.

There are several evidences supporting this scenario (Prochter et al., 2006b). For instance, the strong Mg II absorbers reside in relatively massive dark matter halos $M \sim 10^{12} M_\odot$ (Bouché et al., 2004; Lundgren et al., 2009). Also, nearly every GRB sight line shows a Mg II system with $W_r(2796) \geq 0.5 \text{ \AA}$ and the luminosities of low-redshift ($z < 0.5$) GRBs appear to be significantly lower than those of the high-redshift events (Kann et al., 2006). Porciani et al. (2007) found that optical GRB afterglow with more than one strong Mg II are, on average, 1.7 times brighter than the rest (using data from Nardini et al., 2006). These authors found that there is a 10% chance that this result is due to random fluctuations and therefore could be an indication of weak macrolensing bias although, on the other hand, Sudilovsky et al. (2007) did not find any correlation using similar

data from Kann et al. (2006) for the GRB afterglows magnitudes.

Obviously, further deep late-time imaging observations of GRB fields must be carried out in order to identify the absorbing galaxies and possibly look for impact-parameter/line-strength correlations. In this context, from HST⁴ imaging of GRB host galaxies, Chen et al. (2009) recently found that every GRB field with known strong Mg II absorbers⁵ shows galaxies at angular separations $\Delta\theta < 2$ arcseconds of the GRB sightline, while no galaxy is seen (at least brighter than AB(R) = 28 mag) in GRB fields without strong Mg II absorbers⁶ at the same small angular separation. Likewise, Jakobsson et al. (2004) found several foreground galaxies at small impact parameters from the line-of-sight toward the GRB030429. These results favor the macrolensing scenario, especially considering that the strong Mg II absorption systems found in GRB050820A and GRB060418 appear at $z_l \sim 0.7$ (where the effect of lensing is maximum for sources at $z_s > 1$) making them good lens candidates. Very recently, Pollack et al. (2009) identified a galaxy associated to the Mg II absorber at $z = 0.656$ in the sightline toward GRB060418. They also found indications of an association between small impact parameter galaxies and the other two strong Mg II absorbers in the same sightline. However, the majority of the candidate galaxies found in GRB fields have not been spectroscopically identified yet.

In conclusion, despite that it is not clear whether macrolensing is producing the QSO/GRB discrepancy or not, it appears as a better candidate effect than dust obscuration.

8.4.2 Microlensing

Contrary to macrolensing, microlensing is produced by compact objects like stars or MACHOs⁷ when the source and the lens have comparable sizes. The microlensing effect is not spatially resolved and it is observationally detected as a magnification of the source within a timescale of days. This magnification is maximized when the impact parameter between the source and the lens is equal to the Einstein radius of the compact object.

In the case of GRBs afterglows, this effect could be present. This is because, according to the fireball model, the optical emission of GRBs afterglows are expected to be produced in a ring with typical sizes of 10^{14-15} cm which are comparable with Einstein radius of compact solar mass objects at cosmological distances (see Porciani et al., 2007; Frank et al., 2007, and references therein). Likewise, this effect could be more important for the GRBs than QSOs (assuming that GRBs beam sizes are smaller than QSOs beam sizes). However, whether this effect would be important or not it is not clear. For instance, Porciani et al. (2007) argued that, in the standard

⁴Hubble Space Telescope

⁵4 GRB fields: GRB060418, GRB021004, GRB050820A, GRB060206.

⁶3 GRB fields: GRB011211, GRB000926, GRB030323.

⁷Massive Compact Halo Objects.

cosmological scenario, only a few percent of the GRB afterglows should be affected by microlensing (in the most optimistic assumption that 20% of the dark matter is in MACHOs). On the other hand, they also argued that in the presence of a cosmological population of small dark matter clumps, the expectation of the Swift microlensed afterglows should be $\sim 30\%$ (assuming that all the dark matter is in miniclusters).

Microlensing also has a dependence in the impact parameter from galaxies (like in the macrolensing case), in the sense that the surface density of stars (and MACHOs) is greater in the center than in the outskirts of galaxies. Therefore, the microlensing optical depth should also follow the same behavior, then, assuming that microlensing is an important effect, there will be more probability to find microlensed sources associated with larger equivalent widths.

Summarizing, either macro or microlensing could be affecting the GRB statistics. Both scenarios remain in agreement with our results on Mg II and C IV intervening absorption systems. On the one hand, the observed excess of strong Mg II could be interpreted as being associated to the galaxy which produce the lensing effect because the Mg II redshift coverage includes the redshift where the effect is maximized, z_l^{max} . On the other hand, in the case of C IV this z_l^{max} is not surveyed, then, this effect should not be observed.

It is important to keep exploring the feasibility of the gravitational lensing bias effect in the current GRBs samples. In this context, Tejos et al. (2009) used a sample of 8 GRBs echelle spectra (namely the 7 used in this thesis and the GRB080810) to carry out the same study presented here. This new sightline does not show any Mg II system with $W_r(2803) \geq 0.07 \text{ \AA}$ (note that Mg II-free sightlines are expected from QSO surveys). Consequently, they found that the results of this thesis remain the same (see Section 7.3) although the significant overdensity is reduced from a factor of ~ 3.5 to a factor of ~ 3 only. This number allowed them to speculate about the fraction f_l of magnified GRBs that otherwise would not have been spectroscopically observed. Considering only systems with $W_r \geq 1 \text{ \AA}$ they estimated that $f_l \sim 50\%$ to reproduce the factor of 3 enhancement. Note that this argument becomes unrealistic for a factor of ~ 4 enhancement, for which f_l would approach $\approx 100\%$. Similarly, an enhancement factor of ~ 2 (still consistent with their result at the 1σ c.l.) would require $f_l \sim 30\%$. These numbers allow lensing bias to provide, at least qualitatively, a viable explanation to the QSO/GRB discrepancy.

8.5 Are the Mg II Absorbers Related to GRB?

Mg II related to the GRB itself was proposed by Prochter et al. (2006b). However, these authors discarded this scenario for two reasons (see Table 1 and Figure 1 in their paper):

1. If the lines would be associated with the GRB itself, these should have very high relative radial velocities with respect to the source (at least $\sim 50000 \text{ km s}^{-1}$) and,
2. The velocity profiles of the lines are not wide enough to be consistent with the expected high radial velocities assumed in (1), as observed in broad absorption lines (BALs).

The results presented here also disfavor this scenario. First, the line profiles of the $W_r < 1 \text{ \AA}$ Mg II systems show no indication of broad and shallow absorption troughs, characteristic of BAL QSOs⁸. Second, I do not find any discrepancy in dN/dz for these systems between GRBs and QSOs. If some of the Mg II systems were intrinsic to the GRB it would be expected to find an overabundance also in the weakest ones. Indeed, an overabundance of strong C IV would be expected too, and that is also not observed. Third, many of the Mg II systems show Mg I, implying that the gas must be far away from the GRB itself (see Prochaska et al., 2006).

More recently, Cucchiara et al. (2009) also tested this possibility and they did not find any important difference in the properties of the strong Mg II systems found in GRB spectra compared with the intervening ones in QSOs.

In conclusion, the discrepancy observed in strong Mg II systems between GRBs and QSOs spectra can not be due to a misidentification of intervening systems. For further discussion about the possibility to associate Mg II systems to the GRB itself and its environment, I refer the reader to Porciani et al. (2007) and Cucchiara et al. (2009).

8.6 Different Beam Sizes of the Sources and Partial Beam Coverage

As mentioned in Section 1.6, GRBs and QSOs are entirely different phenomena each one with its own size scales. Thus, it is possible that GRBs are several times smaller than QSOs. From this assumption Frank et al. (2007) proposed a geometric solution for the GRB/QSO discrepancy. This solution is based on the different GRB and QSO beam sizes, both comparable, to the Mg II absorber characteristic size.

In their model, Frank et al. (2007) consider the Mg II systems as clumpy clouds having a spherical core of radius r_0 with constant density ρ_0 surrounded by an extended zone with densities following a power law $\rho(r) = (r/r_0)^{-k}$. This is a toy model which, in principle, could explain the overabundance of strong systems in sightlines to smaller beam sizes sources. They argued that GRB optical afterglows beam sizes are 10^{14-15} cm while QSOs beam sizes are greater than

⁸However, note that very shallow systems would not, in most cases, be detected in our GRB spectral sample.

$\sim 3 \times 10^{16}$ cm (note that $1 \text{ pc} = 3.1 \times 10^{18}$ cm). Thus, if the cloud cores have typical sizes of $\sim 5 - 10 \times 10^{15}$ cm (comparable with GRBs and QSOs beam sizes, much smaller than galaxies), it would explain the discrepancy. Considering the case of strong systems, the QSOs beam (assumed bigger than the core) would pass through both the dense core and the extended diluted material, while in the case of the GRB beam (assumed smaller than the core) would pass only through the core with a minimal contribution of the more diluted material. Therefore, the statistics of dN/dz could be affected showing more strong systems toward GRBs than QSOs for a same population of intervening absorbers.

As mentioned, this model must be taken only as a global picture which in the case of finding favor evidences it would need refinement. The observational consequences related with this model would be the following:

1. Time variability of the GRBs absorption lines strength due to the fact that the GRBs beam sizes evolve (according to the fireball model).
2. Similar behavior in both the incidence of strong Mg II systems and time variability of the absorption lines strength between blazars and GRBs (blazars are also variable objects and, according to the unified model for AGN, are several times smaller than QSOs).
3. A lack of weak Mg II in GRB sightlines (compared with QSO sightlines). On the one hand, this geometrical solution favors an overabundance of strong systems toward smaller beam sizes while, on the other hand, weak systems are affected in an inverse manner.
4. Different incidence of Mg II in QSO spectral zones associated with different intrinsic sizes (e.g., Broad Lines Regions versus continuum zones).
5. Different incidences of Mg II in QSOs with different intrinsic luminosities (it is believed that the size of the QSO continuum zone is dependent on the luminosity).
6. Mg II systems seen in the spectra of lensed QSOs should be seen evolving (microlensing effect should be important).
7. Since the denser zone (which could saturate the line) is diluted by the extended material, there could be a presence of apparently unsaturated Mg II systems in QSO sightlines with unexpected doublet ratios (e.g., 1:1).

Currently, this geometrical model is severely discarded because none of its predictions have been observed confidently. For example, Hao et al. (2007) recently reported time variability (\sim hours) of intervening Fe II and Mg II in GRB060206 sightline. However, this claim was ruled out later by Thöne et al. (2008) and Aoki et al. (2009) who did not find any significant variation of these lines in the same GRB using spectra with higher signal-to-noise ratio. Likewise, a possible

variation in the strength of absorption lines in a blazar was reported by Peterson et al. (1977). An excess of Mg II absorbers in blazars was reported by Stocke & Rector (1997) although in this case, the overabundance is not as significant as in GRB sightlines. Due to the lack of both strong emission lines and host DLAs, redshift measure of blazars is more complicated than for QSOs or GRBs, and currently only few of them have been used to survey intervening absorption systems. Thus, none of these results can be taken (confidently) as a prove in favor of this model.

An important test was performed by Pontzen et al. (2007). They looked for differences in the equivalent width distribution of Mg II over QSO continuum regions and C III emission line regions from SDSS QSOs. They argued that these differences should be detectable but are not observed in the current data. This result represents an important counterevidence of the model.

Porciani et al. (2007) also exposed several reasons against this scenario. One of these points is concerning to the equivalent width distribution. This function appears self-consistent between GRBs and QSOs sightlines for $W_r \geq 1 \text{ \AA}$ (see their Figure 3). According to this model, a flatter distribution of Mg II equivalent widths along GRBs would be expected which is not observed (our result also shows consistency at $W_r < 1 \text{ \AA}$). Additionally, these authors noted that there are theoretical and observational estimation suggesting that QSO beams could be smaller than the GRB ones (see also Frank et al., 2007).

Another consequence of the geometrical model noticed by Porciani et al. (2007) is that a fraction of weak systems in QSO spectra should have $DR \approx 1$. From the Narayanan et al. (2007) sample it is possible to find this fraction to be $\approx 5\%$. Due to the smaller GRB beam sizes, the same fraction in GRB spectra is expected to be lower than this value. In contrast, we find that 2 out of 5 systems with $W_r^{2796} < 0.3 \text{ \AA}$ show $DR \approx 1$ (taking larger equivalent widths values would include saturated lines). Shin et al. (2006) also found a weak Mg II system with $DR \sim 1 : 1$ in GRB030226. This result goes in the opposite direction and therefore, though not significant, does not support the geometrical model.

Our result on dN/dz of weak Mg II systems, appears particularly interesting because despite that there is a consistency between QSO and GRB sightlines, the mean dN/dz value in GRBs is below the observed in QSOs. This could be an evidence favoring this geometrical solution (see the third point of the observational consequences of this model) although not significant. Duplicating the redshift path for $W_r < 0.3 \text{ \AA}$ in the GRB sample, it would be possible to reduce enough the error bars to discriminate whether this suggested underabundance of weak Mg II systems in GRBs is real or not.

Before concluding, it is important to note that the sizes proposed by Frank et al. (2007) (i.e., $\sim 10^{-4} - 10^{-3} \text{ pc}$) for strong Mg II systems are several times smaller than the smallest of the characteristic sizes estimation inferred from resolved QSOs pairs, i.e., $\sim 1 - 100 \text{ pc}$ (e.g., Smette et al., 1995; Lopez et al., 1999).

In conclusion, there are many evidences against this model. Despite the presence of few indications in favor, the geometrical model is currently ruled out by the present data.

8.7 Summary of the Discussion

I discussed possible explanations for the discrepancy of strong Mg II systems between QSOs and GRBs sightlines reported by Prochter et al. (2006b) in light of our new results as well as from related literature. A bias selection effect in the current GRB samples appears more likely than intrinsic differences in the nature of the absorbers themselves. In view of the weak Mg II result, it is suggested that the GRB/QSO discrepancy should arise in the galaxies that host the strong absorbers. Explanation such a dust obscuration in Mg II host galaxies appears improbable, while a gravitational lensing effect (albeit perhaps not unique) seems to be in best agreement with our observations. Effects associated to the GRB itself phenomenon or the geometrical solution proposed by Frank et al. (2007) are ruled out by the current data. Despite these new results the problem opened by Prochter et al. (2006b) remains unsolved.

8.8 Outlook

To fully understand why there is an overabundance of strong intervening Mg II systems towards GRB sightlines compared to that from QSO sightlines it is necessary to increase the GRB spectral sample observed at both high and low spectral resolution. Although the signal to noise is an important factor that could be improved, I consider that the current S/N values are enough to help address the discrepancy which is only seen for the very strong Mg II systems ($W_r > 1 \text{ \AA}$). This kind of systems are well probed by low resolution spectrographs. Thus, in principle, the first step should be to increase the GRB redshift path from a low-resolution GRB spectral sample. Indeed, there is a Spanish and an ESO group which will publish new samples of GRB soon.

At the same time of the spectroscopic observations of GRB afterglows, there will be also important to obtain deep imaging of the GRB fields in order to look for the galaxies that could produce the absorption features in the GRB spectra as well as spectroscopic confirmation of these galaxies.

The next step should be to increase the current high resolution GRB sample in order to corroborate the results on C IV and weak Mg II systems. Also high resolution data will be useful to study the strong Mg II population in greater detail.

If these results are confirmed in larger surveys and can be explained by a bias effect in the samples, these results could be used to constrain the dust reddening or mass of the intervening galaxies hosting the absorbers using samples selected by one or another kind of absorption systems. Very rapid and deep spectroscopy of 'dark' bursts will be important to test the gravitational lensing bias scenario. On the other hand, if the discrepancy between strong Mg II between GRBs and QSOs cannot be explained by bias effect one may use the contrasting results to infer characteristics of the absorbers themselves. For example, if the $dN/dz|_{\text{GRB}}^{\text{MgII}}$ enhancement is to be explained by the geometric differences between the GRB and QSO beams, then one would conclude that, on the one hand, the C IV absorbers are significantly larger than the Mg II clouds and the QSO beam size while, on the other hand, Mg II are significantly smaller than galaxy halos.

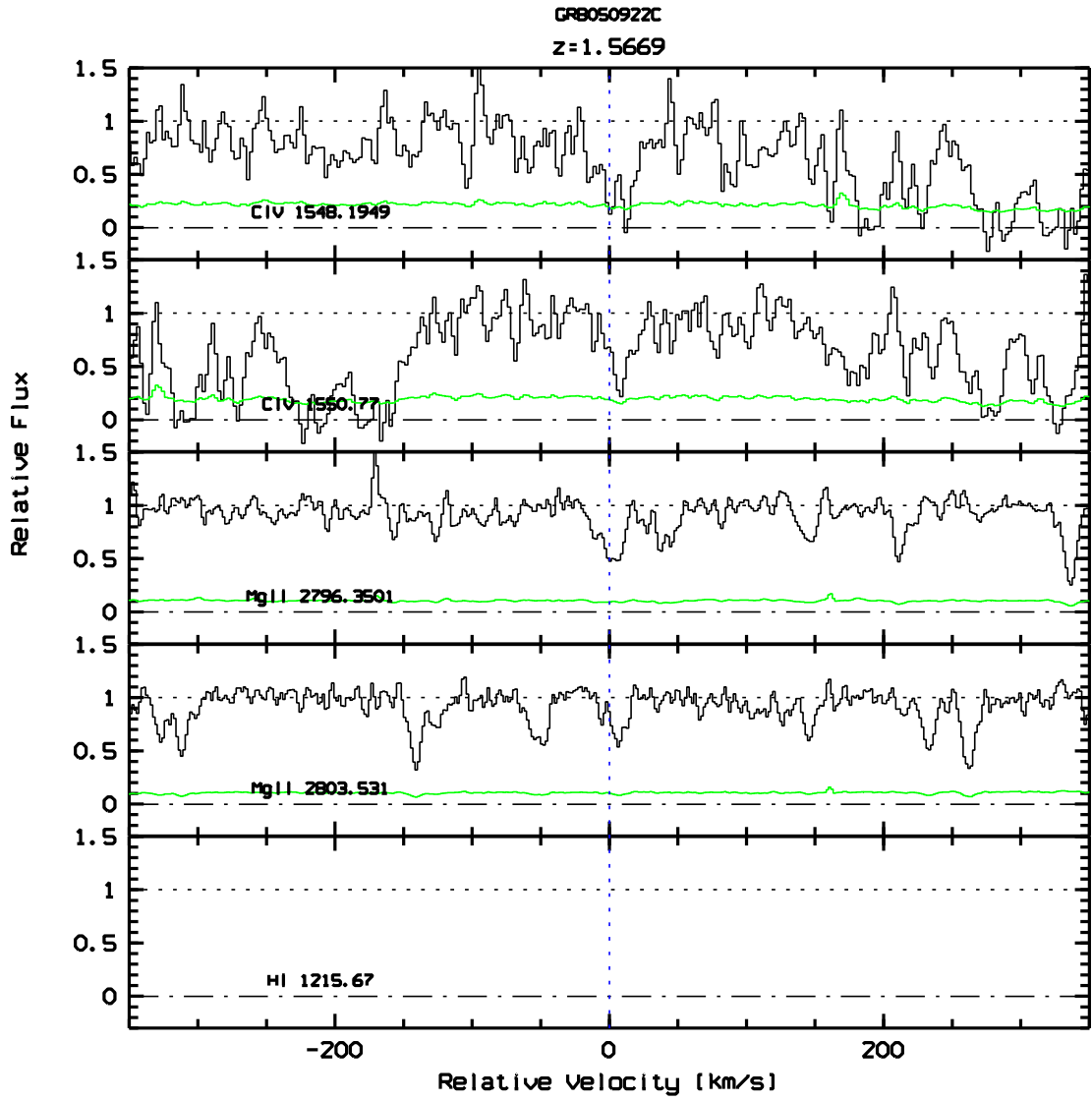


Figure 8.1 Absorption velocity profile of C IV-Mg II absorption system at $z_{abs} = 1.567$.

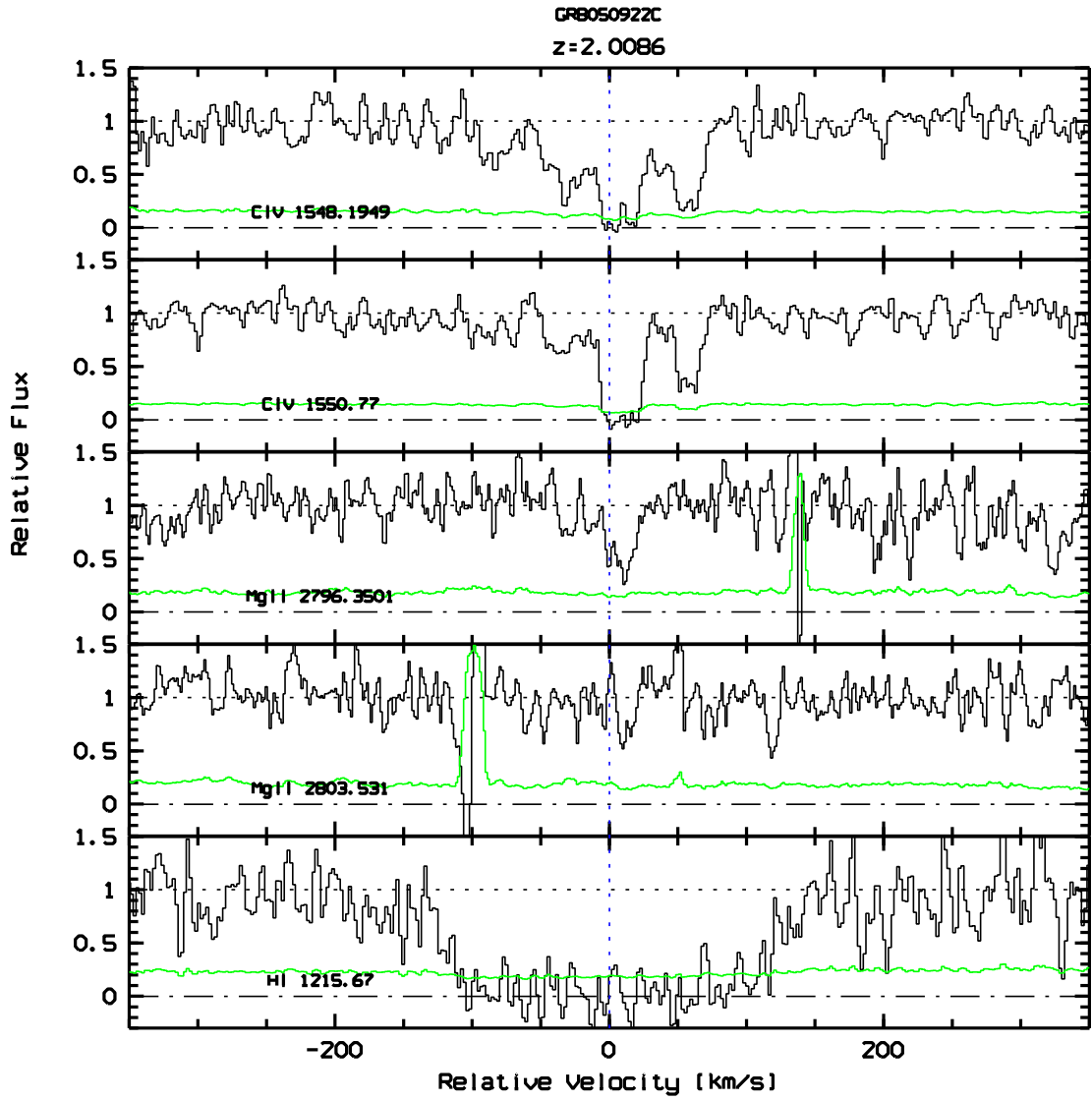


Figure 8.2 Absorption velocity profile of C IV-Mg II absorption system at $z_{abs} = 2.009$.

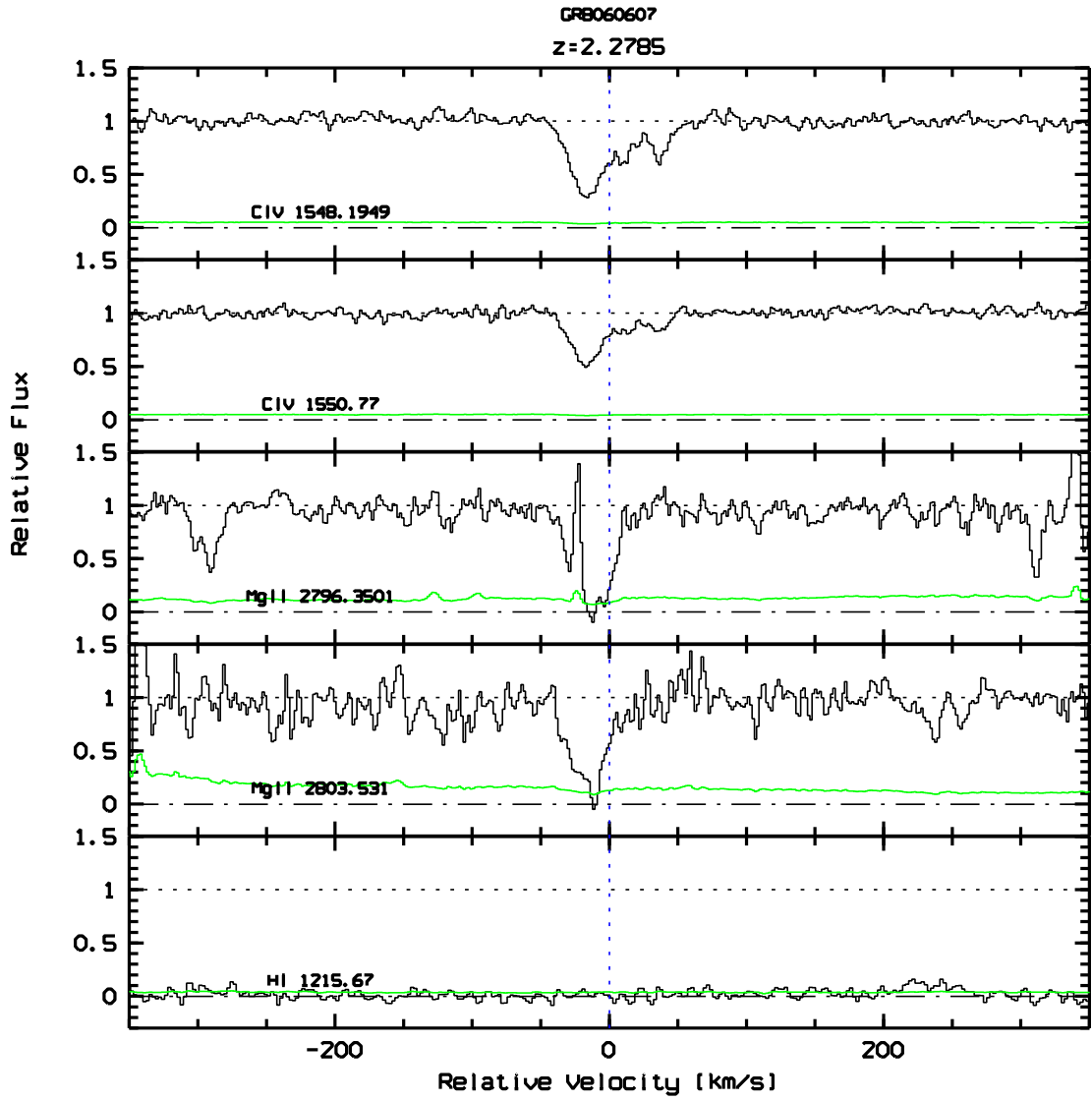


Figure 8.3 Absorption velocity profile of C IV-Mg II absorption system at $z_{abs} = 2.785$.

References

- Aoki, K., Totani, T., Hattori, T., Ohta, K., Kawabata, K. S., Kobayashi, N., Iye, M., Nomoto, K., & Kawai, N. 2009, PASJ, 61, 387
- Bechtold, J. 2001, ArXiv Astrophysics e-prints
- Bernstein, R., Shectman, S. A., Gunnels, S. M., Mochmacki, S., & Athey, A. E. 2003, in Presented at the Society of Photo-Optical Instrumentation Engineers (SPIE) Conference, Vol. 4841, Instrument Design and Performance for Optical/Infrared Ground-based Telescopes. Edited by Iye, Masanori; Moorwood, Alan F. M. Proceedings of the SPIE, Volume 4841, pp. 1694-1704 (2003)., ed. M. Iye & A. F. M. Moorwood, 1694–1704
- Bouché, N., Murphy, M. T., & Péroux, C. 2004, MNRAS, 354, L25
- Burbidge, E. M., Lynds, C. R., & Stockton, A. N. 1968, ApJ, 152, 1077
- Catanzaro, G. 1997, Ap&SS, 257, 161
- Cen, R. & Ostriker, J. P. 2006, ApJ, 650, 560
- Chen, H.-W., Perley, D. A., Pollack, L. K., Prochaska, J. X., Bloom, J. S., Dessauges-Zavadsky, M., Pettini, M., Lopez, S., Dall’aglio, A., & Becker, G. D. 2009, ApJ, 691, 152
- Chen, H.-W., Prochaska, J. X., Bloom, J. S., & Thompson, I. B. 2005, ApJ, 634, L25
- Churchill, C. 2008, QSO Absorption Lines Studies: Ultraviolet and Optical Spectroscopy
- Churchill, C., Steidel, C., & Kacprzak, G. 2005, in Astronomical Society of the Pacific Conference Series, Vol. 331, Extra-Planar Gas, ed. R. Braun, 387–+
- Churchill, C. W., Mellon, R. R., Charlton, J. C., Jannuzi, B. T., Kirhakos, S., Steidel, C. C., & Schneider, D. P. 1999a, ApJ, 519, L43
- . 2000, ApJ, 543, 577
- Churchill, C. W., Rigby, J. R., Charlton, J. C., & Vogt, S. S. 1999b, ApJS, 120, 51
- Ciardi, B. & Loeb, A. 2000, ApJ, 540, 687

- Cucchiara, A., Jones, T., Charlton, J. C., Fox, D. B., Einsig, D., & Narayanan, A. 2009, *ApJ*, 697, 345
- Davé, R., Cen, R., Ostriker, J. P., Bryan, G. L., Hernquist, L., Katz, N., Weinberg, D. H., Norman, M. L., & O’Shea, B. 2001, *ApJ*, 552, 473
- Dekker, H., D’Odorico, S., Kaufer, A., Delabre, B., & Kotzlowski, H. 2000, in Presented at the Society of Photo-Optical Instrumentation Engineers (SPIE) Conference, Vol. 4008, Proc. SPIE Vol. 4008, p. 534-545, Optical and IR Telescope Instrumentation and Detectors, Masanori Iye; Alan F. Moorwood; Eds., ed. M. Iye & A. F. Moorwood, 534–545
- Eichler, D., Livio, M., Piran, T., & Schramm, D. N. 1989, *Nature*, 340, 126
- Ellison, S. L., Churchill, C. W., Rix, S. A., & Pettini, M. 2004, *ApJ*, 615, 118
- Ellison, S. L. & Lopez, S. 2009, ArXiv e-prints
- Ellison, S. L., Yan, L., Hook, I. M., Pettini, M., Wall, J. V., & Shaver, P. 2001, *A&A*, 379, 393
- Fall, S. M. & Pei, Y. C. 1993, *ApJ*, 402, 479
- Fiore, F., D’Elia, V., Lazzati, D., Perna, R., Sbordone, L., Stratta, G., Meurs, E. J. A., Ward, P., Antonelli, L. A., Chincarini, G., Covino, S., Di Paola, A., Fontana, A., Ghisellini, G., Israel, G., Frontera, F., Marconi, G., Stella, L., Vietri, M., & Zerbi, F. 2005, *ApJ*, 624, 853
- Frank, S., Bentz, M. C., Stanek, K. Z., Mathur, S., Dietrich, M., Peterson, B. M., & Atlee, D. W. 2007, *Ap&SS*, 312, 325
- Fukugita, M., Hogan, C. J., & Peebles, P. J. E. 1998, *ApJ*, 503, 518
- Gehrels, N. 1986, *ApJ*, 303, 336
- Greenstein, J. L. & Schmidt, M. 1967, *ApJ*, 148, L13+
- Griem, H. R. 1974, *Spectral line broadening by plasmas* (Pure and Applied Physics, New York: Academic Press, 1974)
- Gunn, J. E. & Peterson, B. A. 1965, *ApJ*, 142, 1633
- Hao, H., Stanek, K. Z., Dobrzycki, A., Matheson, T., Bentz, M. C., Kuraszkiewicz, J., Garnavich, P. M., Howk, J. C., Calkins, M. L., Worthey, G., Modjaz, M., & Serven, J. 2007, *ApJ*, 659, L99
- Jakobsson, P., Hjorth, J., Fynbo, J. P. U., Weidinger, M., Gorosabel, J., Ledoux, C., Watson, D., Björnsson, G., Gudmundsson, E. H., Wijers, R. A. M. J., Möller, P., Pedersen, K., Sollerman, J., Henden, A. A., Jensen, B. L., Gilmore, A., Kilmartin, P., Levan, A., Castro Cerón, J. M., Castro-Tirado, A. J., Fruchter, A., Kouveliotou, C., Masetti, N., & Tanvir, N. 2004, *A&A*, 427, 785
- Kann, D. A., Klose, S., & Zeh, A. 2006, *ApJ*, 641, 993

- Kitchin, C. R. 1995, *Optical astronomical spectroscopy* (Bristol: IOP Publishing, —c1995)
- Klebesadel, R. W., Strong, I. B., & Olson, R. A. 1973, *ApJ*, 182, L85+
- Lamb, D. Q. & Reichart, D. E. 2000, *ApJ*, 536, 1
- Lanzetta, K. M., Wolfe, A. M., & Turnshek, D. A. 1987, *ApJ*, 322, 739
- Ledoux, C., Vreeswijk, P., Smette, A., Jaunsen, A., & Kaufer, A. 2006, *GRB Coordinates Network*, 5237, 1
- Lopez, S., Barrientos, L. F., Lira, P., Padilla, N., Gilbank, D. G., Gladders, M. D., Maza, J., Tejos, N., Vidal, M., & Yee, H. K. C. 2008, *ApJ*, 679, 1144
- Lopez, S., Maza, J., Masegosa, J., & Marquez, I. 2001, *A&A*, 366, 387
- Lopez, S., Reimers, D., Rauch, M., Sargent, W. L. W., & Smette, A. 1999, *ApJ*, 513, 598
- Lundgren, B. F., Brunner, R. J., York, D. G., Ross, A. J., Quashnock, J. M., Myers, A. D., Schneider, D. P., Al Sayyad, Y., & Bahcall, N. 2009, *ApJ*, 698, 819
- Ménard, B., Nestor, D., Turnshek, D., Quider, A., Richards, G., Chelouche, D., & Rao, S. 2008, *MNRAS*, 385, 1053
- Metzger, M. R., Djorgovski, S. G., Kulkarni, S. R., Steidel, C. C., Adelberger, K. L., Frail, D. A., Costa, E., & Frontera, F. 1997, *Nature*, 387, 878
- Misawa, T., Tytler, D., Iye, M., Storrie-Lombardi, L. J., Suzuki, N., & Wolfe, A. M. 2002, *AJ*, 123, 1847
- Narayanan, A., Misawa, T., Charlton, J. C., & Kim, T.-S. 2007, *ApJ*, 660, 1093
- Nardini, M., Ghisellini, G., Ghirlanda, G., Tavecchio, F., Firmani, C., & Lazzati, D. 2006, *A&A*, 451, 821
- Nestor, D. B., Turnshek, D. A., & Rao, S. M. 2005, *ApJ*, 628, 637
- Paschos, P., Jena, T., Tytler, D., Kirkman, D., & Norman, M. L. 2008, *ArXiv e-prints*
- Peterson, B. M., Strittmatter, P. A., Williams, R. E., & Coleman, G. D. 1977, *ApJ*, 218, 605
- Piranomonte, S., D’Elia, V., Ward, P., Fiore, F., & Meurs, E. J. A. 2006, *Nuovo Cimento B Serie*, 121, 1561
- Pollack, L. K., Chen, H. ., Prochaska, J. X., & Bloom, J. S. 2009, *ArXiv e-prints*
- Pontzen, A., Hewett, P., Carswell, R., & Wild, V. 2007, *MNRAS*, 381, L99
- Porciani, C. & Madau, P. 2001, *ApJ*, 548, 522
- Porciani, C., Viel, M., & Lilly, S. J. 2007, *ApJ*, 659, 218

- Prochaska, J. X., Chen, H.-W., & Bloom, J. S. 2006, *ApJ*, 648, 95
- Prochaska, J. X., Chen, H.-W., Bloom, J. S., Dessauges-Zavadsky, M., O'Meara, J. M., Foley, R. J., Bernstein, R., Burles, S., Dupree, A. K., Falco, E., & Thompson, I. B. 2007, *ApJS*, 168, 231
- Prochter, G. E., Prochaska, J. X., & Burles, S. M. 2006a, *ApJ*, 639, 766
- Prochter, G. E., Prochaska, J. X., Chen, H.-W., Bloom, J. S., Dessauges-Zavadsky, M., Foley, R. J., Lopez, S., Pettini, M., Dupree, A. K., & Guhathakurta, P. 2006b, *ApJ*, 648, L93
- Rauch, M. 1998, *ARA&A*, 36, 267
- Rees, M. J. & Meszaros, P. 1992, *MNRAS*, 258, 41P
- Rigby, J. R., Charlton, J. C., & Churchill, C. W. 2002, *ApJ*, 565, 743
- Rybicki, G. B. & Lightman, A. P. 1979, *Radiative processes in astrophysics* (New York, Wiley-Interscience, 1979. 393 p.)
- Salvaterra, R., Della Valle, M., Campana, S., Chincarini, G., Covino, S., D'Avanzo, P., Fernandez-Soto, A., Guidorzi, C., Mannucci, F., Margutti, R., Thoene, C. C., Antonelli, L. A., Barthelmy, S. D., De Pasquale, M., D'Elia, V., Fiore, F., Fugazza, D., Hunt, L. K., Maiorano, E., Marinoni, S., Marshall, F. E., Molinari, E., Nousek, J., Pian, E., Racusin, J. L., Stella, L., Amati, L., Andreuzzi, G., Cusumano, G., Fenimore, E. E., Ferrero, P., Giommi, P., Guetta, D., Holland, S. T., Hurley, K., Israel, G. L., Mao, J., Markwardt, C. B., Masetti, N., Pagani, C., Palazzi, E., Palmer, D. M., Piranomonte, S., Tagliaferri, G., & Testa, V. 2009, *ArXiv e-prints*
- Sargent, W. L. W., Boksenberg, A., & Steidel, C. C. 1988, *ApJS*, 68, 539
- Shin, M.-S., Berger, E., Penprase, B. E., Fox, D. B., Price, P. A., Kulkarni, S. R., Soderberg, A. M., West, M. J., Cote, P., & Jordan, A. 2006, *ArXiv Astrophysics e-prints*
- Smette, A., Claeskens, J.-F., & Surdej, J. 1997, *New Astronomy*, 2, 53
- Smette, A., Robertson, J. G., Shaver, P. A., Reimers, D., Wisotzki, L., & Koehler, T. 1995, *A&AS*, 113, 199
- Smette, A., Wisotzki, L., Ledoux, C., Garcet, O., Lopez, S., & Reimers, D. 2005, in *IAU Colloq. 199: Probing Galaxies through Quasar Absorption Lines*, ed. P. Williams, C.-G. Shu, & B. Menard, 475–477
- Steidel, C. C. 1990, *ApJS*, 72, 1
- Stocke, J. T. & Rector, T. A. 1997, *ApJ*, 489, L17+
- Sudilovsky, V., Savaglio, S., Vreeswijk, P., Ledoux, C., Smette, A., & Greiner, J. 2007, *ApJ*, 669, 741
- Sudilovsky, V., Smith, D., & Savaglio, S. 2009, *ArXiv e-prints*

- Tejos, N., Lopez, S., Prochaska, J. X., Bloom, J. S., Chen, H.-W., Dessauges-Zavadsky, M., & Maureira, M. J. 2009, ArXiv e-prints
- Tejos, N., Lopez, S., Prochaska, J. X., Chen, H.-W., & Dessauges-Zavadsky, M. 2007, *ApJ*, 671, 622
- Thöne, C. C., Wiersema, K., Ledoux, C., Starling, R. L. C., de Ugarte Postigo, A., Levan, A. J., Fynbo, J. P. U., Curran, P. A., Gorosabel, J., van der Horst, A. J., Llorente, A., Rol, E., Tanvir, N. R., Vreeswijk, P. M., Wijers, R. A. M. J., & Kewley, L. J. 2008, *A&A*, 489, 37
- Tripp, T. M. & Bowen, D. V. 2005, in *IAU Colloq. 199: Probing Galaxies through Quasar Absorption Lines*, ed. P. Williams, C.-G. Shu, & B. Menard, 5–23
- Tytler, D. 1987, *ApJ*, 321, 49
- van de Hulst, H. C. & Reesinck, J. J. M. 1947, *ApJ*, 106, 121
- Vogt, S. S., Allen, S. L., Bigelow, B. C., Bresee, L., Brown, B., Cantrall, T., Conrad, A., Couture, M., Delaney, C., Epps, H. W., Hilyard, D., Hilyard, D. F., Horn, E., Jern, N., Kanto, D., Keane, M. J., Kibrick, R. I., Lewis, J. W., Osborne, J., Pardeilhan, G. H., Pfister, T., Ricketts, T., Robinson, L. B., Stover, R. J., Tucker, D., Ward, J., & Wei, M. Z. 1994, in *Presented at the Society of Photo-Optical Instrumentation Engineers (SPIE) Conference, Vol. 2198, Proc. SPIE Instrumentation in Astronomy VIII*, David L. Crawford; Eric R. Craine; Eds., Volume 2198, p. 362, ed. D. L. Crawford & E. R. Craine, 362–+
- Wolfe, A. M., Turnshek, D. A., Smith, H. E., & Cohen, R. D. 1986, *ApJS*, 61, 249
- Woosley, S. E. 1993, *ApJ*, 405, 273
- York, D. G., Adelman, J., Anderson, Jr., J. E., Anderson, S. F., Annis, J., Bahcall, N. A., Bakken, J. A., Barkhouser, R., Bastian, S., Berman, E., Boroski, W. N., Bracker, S., Briegel, C., Briggs, J. W., Brinkmann, J., Brunner, R., Burles, S., Carey, L., Carr, M. A., Castander, F. J., Chen, B., Colestock, P. L., Connolly, A. J., Crocker, J. H., Csabai, I., Czarapata, P. C., Davis, J. E., Doi, M., Dombeck, T., Eisenstein, D., Ellman, N., Elms, B. R., Evans, M. L., Fan, X., Federwitz, G. R., Fiscelli, L., Friedman, S., Frieman, J. A., Fukugita, M., Gillespie, B., Gunn, J. E., Gurbani, V. K., de Haas, E., Haldeman, M., Harris, F. H., Hayes, J., Heckman, T. M., Hennessy, G. S., Hindsley, R. B., Holm, S., Holmgren, D. J., Huang, C.-h., Hull, C., Husby, D., Ichikawa, S.-I., Ichikawa, T., Ivezić, Ž., Kent, S., Kim, R. S. J., Kinney, E., Klaene, M., Kleinman, A. N., Kleinman, S., Knapp, G. R., Korienek, J., Kron, R. G., Kunszt, P. Z., Lamb, D. Q., Lee, B., Leger, R. F., Limmongkol, S., Lindenmeyer, C., Long, D. C., Loomis, C., Loveday, J., Lucinio, R., Lupton, R. H., MacKinnon, B., Mannery, E. J., Mantsch, P. M., Margon, B., McGehee, P., McKay, T. A., Meiksin, A., Merelli, A., Monet, D. G., Munn, J. A., Narayanan, V. K., Nash, T., Neilsen, E., Neswold, R., Newberg, H. J., Nichol, R. C., Nicinski, T., Nonino, M., Okada, N., Okamura, S., Ostriker, J. P., Owen, R., Pauls, A. G., Peoples, J., Peterson, R. L., Petravick, D., Pier, J. R., Pope, A., Pordes, R., Prosapio, A., Rechenmacher, R., Quinn, T. R., Richards, G. T.,

- Richmond, M. W., Rivetta, C. H., Rockosi, C. M., Ruthmansdorfer, K., Sandford, D., Schlegel, D. J., Schneider, D. P., Sekiguchi, M., Sergey, G., Shimasaku, K., Siegmund, W. A., Smees, S., Smith, J. A., Snedden, S., Stone, R., Stoughton, C., Strauss, M. A., Stubbs, C., SubbaRao, M., Szalay, A. S., Szapudi, I., Szokoly, G. P., Thakar, A. R., Tremonti, C., Tucker, D. L., Uomoto, A., Vanden Berk, D., Vogeley, M. S., Waddell, P., Wang, S.-i., Watanabe, M., Weinberg, D. H., Yanny, B., & Yasuda, N. 2000, *AJ*, 120, 1579
- York, D. G., Khare, P., Vanden Berk, D., Kulkarni, V. P., Crotts, A. P. S., Lauroesch, J. T., Richards, G. T., Schneider, D. P., Welty, D. E., Alsayyad, Y., Kumar, A., Lundgren, B., Shanidze, N., Smith, T., Vanlandingham, J., Baugher, B., Hall, P. B., Jenkins, E. B., Menard, B., Rao, S., Tumlinson, J., Turnshek, D., Yip, C.-W., & Brinkmann, J. 2006, *MNRAS*, 367, 945